Functional Dyes as Tools for Neurophysiology

James Edward Reeve

Lady Margaret Hall

University of Oxford

A thesis submitted in partial fulfillment of the requirements for the degree of

Doctor of Philosophy

Trinity Term 2012

Functional Dyes as Tools for Neurophysiology

James Edward Reeve, Lady Margaret Hall, University of Oxford

D.Phil. Thesis, TT 2012

The aim of the project described in this thesis is to synthesise new functional molecules which interact with light for neurophysiological applications. In particular, I describe a family of amphiphilic porphyrins with large first hyperpolarisabilities which are used as SHG contrast agents and voltage-sensitive probes. In addition I detail a methodological microscopy tool and a novel caged form of a neuronal ion-channel antagonist.

Chapter 1 introduces the key concepts underlying the use of dyes as SHG contrast agents. In particular it focuses on aspects of molecular design, covering both the amphiphilicity and nolinearity required by the target molecule. It covers quantification of the nonlinear properties of SHG stains, then surveys a number of examples which showcase the flexibility of SHG imaging as a biomedical technique.

Chapter 2 describes a family of amphiphilic porphyrins with large first hyperpolarisabilities. Working from the structure-property relationships identified in Chapter 1, we fully characterise these dyes and demonstrate that they can be used in SHG imaging. We demonstrate that these molecules may also be tuned by complexation of a metal ion which can modulate their photophysical and solubility behaviour.

Chapter 3 provides a description of how to determine the orientational distribution of dipolar dyes in a membrane by multiphoton microscopy. We measure the signal intensity of the dye in a model membrane system then find distributional moments which lead to the distribution itself.

Chapter 4 explores whether off-axis contributions to the first hyperpolarisability tensor can significantly augment the dominant on-axis contribution from the main dipolar charge-transfer band. We synthesise and characterise a series of *cis*-donor *cis*-acceptor porphyrin compounds and explore their biophysical characteristics.

Chapter 5 is the culmination of this project and after discussing method development, goes on to show how we measure the voltage sensitivity of an amphiphilic porphyrin SHG dye. We compare the archetypal porphyrin dye chromophore with three commercially available styryl dyes and demonstrate that our dye has greater sensitivity and a more rapid response.

Chapter 6 describes a side project, the use of a photolabile cage to protect MK801, a neuronal ion-channel antagonist. By developing a water soluble photolabile cage using molecular design techniques, we are able to release MK801 in neurons with precise spatiotemporal control, allowing us to pinpoint the locus of two key neurophysiological processes.

Acknowledgements

First and foremost, I would like to thank Professor Harry Anderson for his supervision over the five years I have spent in his research group. He has always been consistently dedicated to each and every project, provided insightful and though-provoking encouragement and keen eye for spotting the patterns and interconnectivity which make science sing.

The unrivalled community of the HLA group must also be a reciepient of my thanks, from the support, humour and advice from post-docs old and new, to the first questions from a part II. Special thanks are directed towards my original supervisors, Dr. Hazel Collins and Dr. Karl Thorley who taught me what it was to be in G2. To the SHG subgroup, for the dedication and inspiration which you gave and to my four part IIs: Tom, Sally, Phil and Kuoren, thanks for being there, putting up with me and asking me the hard questions. Thanks to some great friends in the lab, who always made it worth coming in: Phil B, Rage and Marsi especially.

This interdisciplinary project would be nowhere without its collaborators, so it also falls to me to thank everyone working with me to make voltage-sensitive SHG imaging a reality. The others in the group, Tom, Hazel, Igor, James W, Ismael and Jan, Wojciech and Alex, great work guys, we're nearly there. Those PIs that have provided me with advice and encouragement, especially Profs. Hagan Bayley, William Barford, Tony Wilson and Ole Paulsen. Many thanks to those in other groups too – to Koen, Javier and Kurt in Leuven and to Michael and Antonio in Cambridge. Thanks to the NMR staff for some fantastic carbons and especially to Charlie in the PTCL wokshop for invaluable teaching and assistance in the machine shop.

Thanks to friends and surrogate family here in Oxford, to a fantastic MCR community and to all those at LMH that made a college a home.

My personal and final thanks go to three wonderful people who taught me that without love, all of this is nothing. Thanks mum and dad for absolutely everything, and to my wife, Sian, who made all this work worthwhile.

Contents

Note to the Reader

This thesis has been assembled as a series of standalone chapters, which use their own axis convention and Greek symbols. Some chapters began life as academic publications, therefore axis conventions and symbols are preserved to maintain coherence with other literature in the field. Each chapter contains standalone reference and figure numbering.

Glossary of Abbreviations

SHG	Second harmonic generation	**α**	Polarisability
1PF	One-photon fluorescence	**β**	First hyperpolarizability
2PF	Two-photon fluorescence	**γ**	Second hyperpolarizability
HRS	Hyper-Rayleigh scattering	$\chi^{(n)}$	n^{th}-order bulk nonlinear susceptibility
EFISHG	Electric field-induced second harmonic generation	$t_{1/2}$	Half-life
THG	Third harmonic generation	$\Delta S/S$	Fractional signal change
CARS	Coherent anti-Stokes Raman spectroscopy	**HOMO**	Highest occupied molecular orbital
NLO	Nonlinear optical	**LUMO**	Lowest unoccupied molecular orbital
AM	Amplitude modulation	**(N)IR**	(Near) infrared
CT	Charge-transfer	**UV**	Ultraviolet
TDM	Transition dipole moment	**GUV**	Giant unilamellar vesicle
LB	Langmuir-Blodgett	**HLB**	Hemispherical lipid bilayer
GUI	Graphical user interface	**DIB**	Droplet interface bilayer
Nd:YAG	Neodymium-doped yttrium aluminum garnet laser	**TFA**	Trifluoroacetic acid
Ti:Sapp	Titanium-sapphire laser	**TEG**	Triethylene glycol
PMT	Photomultiplier tube	**DPhPC**	1,2-diphytanoyl-sn-glycero-3-phosphocholine
MPM	Multiphoton microscopy	**POPC**	1-palmitoyl-2-oleoyl-sn-glycero-3-phosphocholine
N.A.	Numerical aperture	**TICT**	Twisted intramolecular charge-transfer

***epi*–**	above the specimen	**DMEM**	Dulbecco's modified eagle's medium
Blue/Red-shift	Spectral shift to shorter / longer wavlength	**aCSF**	Artificial cerebrospinal fluid
FPGA (card)	Field-programmable gate array (card)	**DMSO**	Dimethyl sulfoxide
PDF	Probability density function	**SK-OV-3 (cells)**	Human epithelial ovarian adenocarcinoma cells
RMS	Root-mean square	**HeLa (cells)**	Human epithelial cervical adenocarcinoma cells
(E) G/Y FP	(Enhanced) Green/Yellow fluorescent protein	**AP**	Action potential
***meso*-position**	methylene position of porphyrin	**(E/I) PSP**	(Excitatory/Inhibitory) Post-synaptic potential
Ar	Aryl	**VSD**	Voltage-sensitive dye
MALDI	Matrix-assisted laser desorption ionization	**LTP**	Long-term potentiation
HRMS	High resolution mass spectrometry	**LTD**	Long-term depression
ESI^+	Electrospray ionisation	**MNI**	4-Methoxy-7-nitroindolinyl
NMDA (receptor)	N-methyl D-aspartate (receptor)	**NVOC**	6-Nitroveratryloxycarbonyl
MK801	Dizocilpine (INN)	**ATP**	Adenosine-5'-triphosphate
GABA	γ-Aminobutyric acid		

Chapter 1

Introduction: Design of Dyes for SHG Imaging

Summary

Nonlinear optical imaging has revolutionised microscopy for the life sciences.* Second harmonic generation (SHG), and its younger sibling of two-photon excited fluorescence (2PF), are techniques that can produce high resolution images from deep inside biological tissues. Second harmonic light is generated by the coherent scattering of an ensemble of aligned chromophores in a focused, pulsed laser beam. SHG is only generated at the focal spot, because of its quadratic intensity dependence, reducing the background signal, and requires ordered chromophores, so is highly structure-specific. In contrast to two-photon fluorescence, the physical process that creates the signal does not require the formation of excited states, allowing elimination of harmful photochemistry. While the SHG of native proteins and biopolymers is well known, the use of exogenous dyes can provide SHG contrast from areas without a sufficiently high intrinsic quadratic hyperpolarisability, β. Dyes for SHG primarily target lipid bilayers; a trait that, combined with sensitivity to transmembrane potential, allows monitoring of action potentials in a variety of excitable cells, most importantly mammalian neurons. This introduction summarises the principles of SHG imaging and explores approaches for maximising the SHG signal from a biological specimen. I survey methods of optimising the optical set-up and enhancing β of a dye whilst maintaining biological compatibility, the focus of

*Most of this chapter has already been published as a "perspectives" review article: J. E. Reeve, H. L. Anderson, K. Clays, *Phys. Chem. Chem. Phys.*, 2010, 12, 13484-13498

chapters 2–4. I cover the key molecular design concepts which guided our structural considerations, lay out the photophysical groundwork for SHG imaging and detail the empirical measurement of molecular β. In conclusion, I examine novel applications of SHG imaging such as transmembrane potential sensitivity (which we develop in chapter 5) and highlight other promising directions for the development of the field.

1.1 Second Harmonic Generation

Second harmonic generation (SHG) occurs when an intense focused coherent laser beam passes through a medium of high quadratic hyperpolarisability, generating light of twice its frequency. A strong effect requires high bulk hyperpolarisability, available through an ensemble of molecules with ordered first hyperpolarisabilities; no signal is evolved from an isotropic solution (except for weak hyper-Rayleigh scattering (HRS) which results from random statistical deviations from an isotropic solution). SHG is useful, not just for imaging biological structures, but also for probing the electrical potential across membranes, as it can be easily detected by commercially available microscopes. Since, in contrast to fluorescence microscopy, SHG does not rely on the formation of excited states, it is possible to avoid harmful photochemistry.

SHG has been used for a number of non-microscopy applications, for example the production of a 532 nm laser by the frequency doubling of a pumped Nd:YAG crystal laser at 1064 nm. As such, it is a widely used tool in the laboratory, providing access to laser wavelengths that would be otherwise unavailable, as well as a compact green source for laser pointers. The field of optical communications also takes an active interest in SHG, using it as the basis of many optical elements such as all-optical switches, phase-shifters as well as other non-reciprocal optical devices.[1]

The nonlinear optical phenomenon of SHG was first observed from quartz by Franken *et al*. in 1961, made possible by the demonstration of the pulsed ruby laser by Maiman in the previous year.[2] Interestingly, when these findings were reported, the spot on the spectrographic plate representing SHG was mistakenly removed by the copy editor prior to publication and the image has not been corrected to this day (Figure 1).[3]

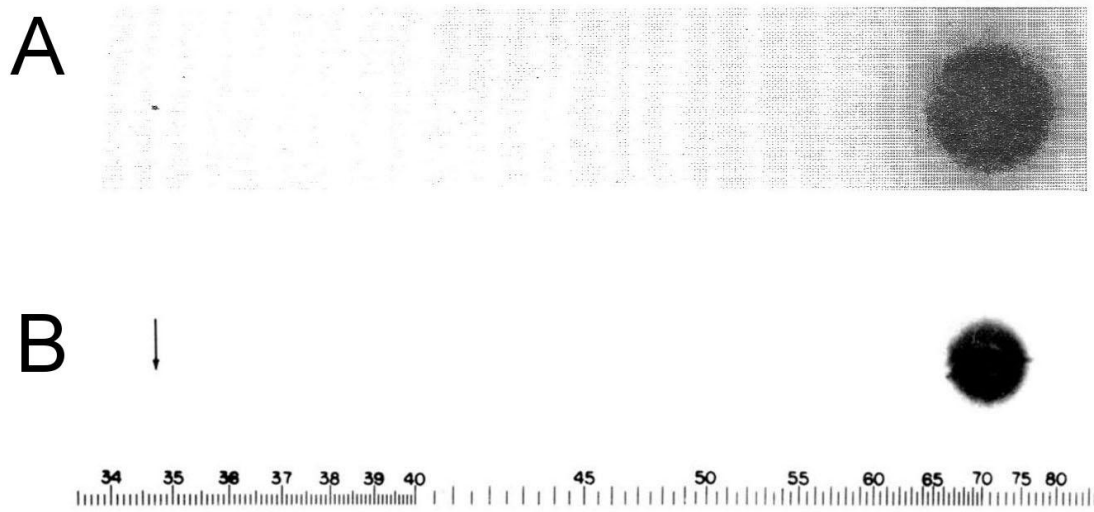

Figure 1 (A) The original photographic plate submitted to Phys. Rev. Lett. in 1961, clearly showing the spots of frequency doubled light on the left and (B) the figure as it appeared in print (and as it appears today) following editing, with the absence of a SHG spot (below arrow). The graduated scale represents wavelength (nm/10). Original plates kindly provided by Professor Allan E. Hill, author, and Prof. Martin Blume, editor-in-chief emeritus of Physical Review Letters. Copyright 1961 by The American Physical Society.[3]

Before the development of two-photon fluorescence (2PF) microscopy, Hellwarth and Christensen applied the principle of SHG in the first case of nonlinear optical microscopy.[4] Laser light at 1064 nm was used to detect structural inhomogeneities in a ZnSe crystal. Although no optical aberrations could be observed by eye, the frequency-doubled light (532 nm) allowed micron-scale crystalline platelets to be identified.

The first dedicated SHG microscope was described by Sheppard *et al.* in 1977.[5] In 1986, Freund *et al.* performed the first SHG microscopy experiments on rat tail tendon, revealing the structure and polarity of connective tissue.[6] This experiment set the stage for a large number of SHG investigations that exploit the intrinsic hyperpolarisability of native proteins and biopolymers to generate a second harmonic signal.[7]

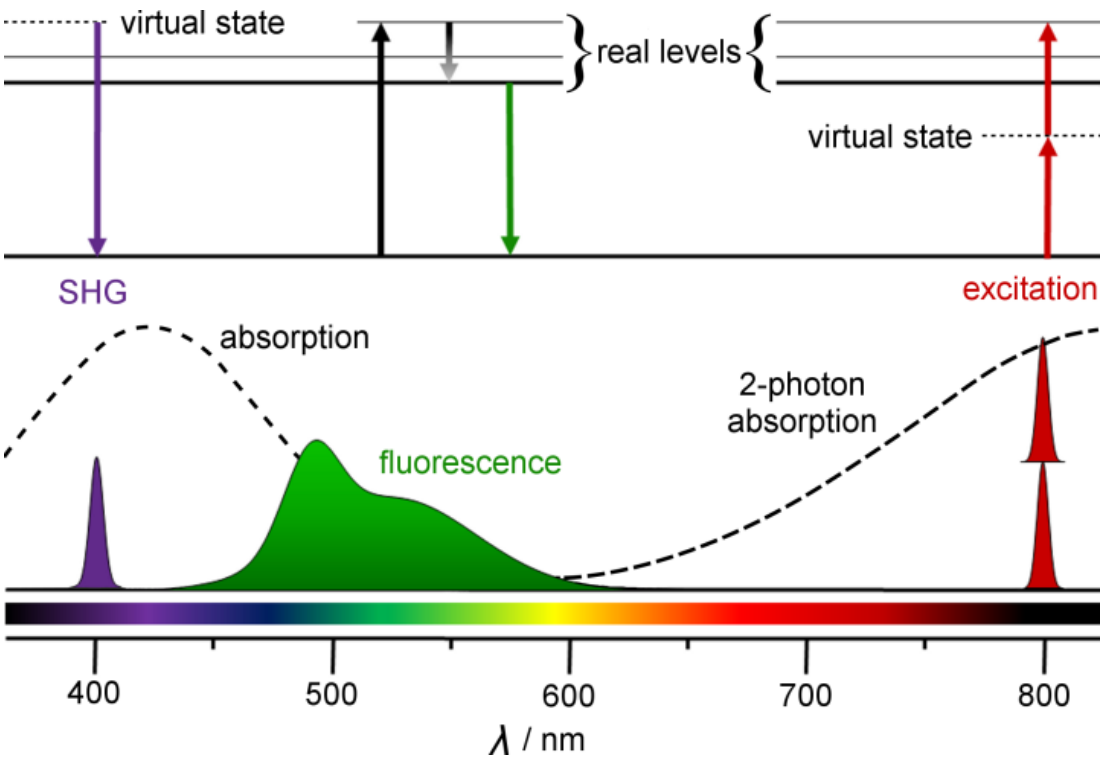

Figure 2 Diagram showing the energy levels of real states (solid) and virtual states (dashed) and the relevant transitions between them.

The use of exogenous dyes can provide SHG contrast in tissues that do not have sufficiently high intrinsic bulk hyperpolarisabilities.[8-10] Most effort has been directed towards SHG contrast agents for cellular lipid bilayers.[11-15] Biological membranes provide a scaffold that may induce order in a dye population. Dyes aligned within a membrane are sensitive to any transmembrane electric field due to reorganization of electron density, so changes in membrane potential can be monitored by SHG. A large body of research has culminated in the ability to probe action potentials of neural networks *via* SHG. Most current work on measuring action potentials uses fluorescent calcium indicators or voltage-sensitive fluorescent probes. SHG has potential to provide reduction of photodamage and an increase in spatial resolution over fluorescence microscopy. The use of SHG allows neurophysiologists to quantitatively observe potential changes in neural networks over long periods of time. An ultimate goal of neurophysiological SHG microscopy is to record excitatory and inhibitory post-synaptic potentials which are in the range of 10-20 mV, an order of magnitude lower than the 110 mV action potentials which can currently be

measured optically.

This thesis is limited in its scope to the design and application of exogenous SHG dyes. While SHG microscopy of inorganic samples has been performed, it is not easily transferrable to a biological setting.[4, 16] I examine the factors that affect the ability of dyes to generate second harmonic light when introduced into a biological environment. In order to compare dyes, I expand on how the molecular first hyperpolarisability of chromophores can be accurately determined by HRS. I will then explore the molecular design and engineering of optimal dipolar SHG chromophores. As dye molecules must be spatially ordered to produce SHG, I survey known probes which are designed to align in the natural acentrosymmetry of cellular membranes. Finally, I illustrate the power of this technique and the advantages conferred by recent advances in dyes for second harmonic imaging of membrane potential.

1.2 Multiphoton Microscopy

Nonlinear optical microscopy relies on either coherent, instantaneous scattering of laser light or absorption of multiple photons, followed by fluorescence. Second, third[17, 18] and higher harmonic generation, as well as coherent anti-Stokes Raman scattering (CARS),[19-22] generate light at specific wavelengths whereas two, three and higher photon absorption result in emission of Stokes-shifted fluorescence. Nonlinear scattered light retains phase, polarisation and directional information after interaction with the sample. The structure as well as the size or ordering of the specimen may be elucidated while also providing a method of separating scattered light from any background.[23] When absorbed (and subsequently emitted), photons do not retain this information and, as they populate an electronically excited state, they may trigger damaging photochemistry.

1.2.1 Scattering Techniques

While second and third harmonic generation produce light at twice or three times the

fundamental laser frequency respectively, the mechanisms that cause scattering in each case are distinct. SHG requires the area within the focal spot to have a non-zero second order susceptibility ($\chi^{(2)}$) whereas third harmonic generation (THG) requires an interface between two regions of different third order susceptibility ($\chi^{(3)}$) to scatter light.[17] Both second and third harmonic generation microscopies are zero-background techniques, as scattering of light from isotropic regions does not occur. SHG microscopy is therefore useful for the study of highly structured regions as described in this perspective, and may visualise both intrinsic and extrinsic harmonogens. THG microscopy, on the other hand is ideal for imaging interfaces and edges that are otherwise invisible to light microscopy such as subcellular lipid bodies.[17, 18, 24] Although THG is limited to structural imaging (it does not respond to changes in static electric field), the low phototoxicity and orthogonality of this technique with intrinsic chromophores allows long-term imaging *in vivo*.[24, 25]

CARS is a $\chi^{(3)}$ scattering phenomenon in which a signal is produced when molecular vibrations which resonate at the frequency-difference between two coincident lasers are present within the focal spot.[19-21] Unlike SHG and THG, CARS is not a zero-background technique as a non-resonant CARS signal is also generated from the media which must be separated from the resonant CARS signal of the molecular vibrations under investigation. Relatively weak signals in comparison to SHG and THG can also lead to slow image acquisitions, as long as 10 ms per pixel.[21] The uptake of CARS in the scientific community has been slow, primarily due to the difficulty of synchronising two lasers into the same focal spot: however, recent advances by Xie and coworkers are improving its accessibility.[26] CARS can also be used without the introduction of contrast agents, which avoids perturbation of biological systems and scatters light both backwards and forwards depending upon the thickness of the sample.[19] An unique advantage of CARS is that the localisation of any molecule may be studied, though it can be difficult to assign the vibrations that are producing resonant CARS in an image with particular chemical species,

especially in complex biological systems.[19]

THG and CARS can reveal the distribution of structure and biomolecules that would otherwise be elusive, while SHG is only selective for interfaces which allow ordering of molecules. However, SHG imaging is the only scattering technique that allows monitoring of transmembrane potential.

1.3 Theory of SHG

In nonlinear microscopy, one-photon excited fluorescence (1PF), 2PF and SHG operate in parallel. These phenomena are the wavelength-dependent competing optical effects of absorption to a real (electronically excited) state (1PF and 2PF) and scattering through interaction with a virtual state (SHG). These interactions are summarised in Figure 2.

Absorption can occur via one-photon excitation if the total energy difference between the two real states is provided by a single photon of wavelength λ_{abs}. It is also possible for this energy to be provided by the simultaneous absorption of two photons of half the energy, resulting in two-photon absorption.[27] After excitation, relaxation to the lowest vibrational level of the first electronic excited state occurs. After a certain excited-state lifetime, a photon can be emitted around the fluorescence wavelength λ_{em} (where $\lambda_{em} > \lambda_{abs}$) returning the chromophore to the ground state. Typically, the energy difference between ground and first excited electronic state is such that an energetic ultraviolet or blue photon has to be absorbed, e.g. at 400 nm. Two-photon absorption is then possible for near-infrared (NIR) photons, e.g. at 800 nm. Fluorescence occurs at a slightly lower energy than the excitation, resulting in e.g. green fluorescence at 500–600 nm.

As well as transitions to real states with finite lifetimes, there are scattering phenomena

involving interaction with virtual states. Linear scattering generates light at the fundamental frequency ω (i.e. the frequency of the incident light) while nonlinear hyper-Rayleigh scattering (HRS) generates light at the second harmonic frequency 2ω. With the constructive interference of an ensemble of individual nonlinear scattering centers, SHG can be produced at 2ω. In biological experimental setups, near-IR light (at 700–900 nm) can penetrate most deeply through scattering tissue. Therefore we focus on hyper-Rayleigh scattering and SHG in the blue spectral region (e.g. with excitation at 800 nm and SHG at 400 nm).

The efficiency of SHG from a chromophore is primarily determined by the molecular second-order nonlinear polarisability, or first hyperpolarisability, β. If the molecule is placed in a strong oscillating electric field (E), such as that of a laser beam, then the oscillating dipole moment μ_{ind}, induced by this field can be expressed as a series expansion, Equation (1)

$$\mu_{ind} = \alpha E + \beta E^2 + \gamma E^3 \ldots \quad \text{(Eq. 1)}$$

where α is the linear polarisability, responsible for among other things, linear Rayleigh scattering, β is the second-order nonlinear polarisability and γ is the third-order nonlinear polarisability (which can be neglected here, but determines factors such as the efficiency of two-photon absorption). Consider the effect of a sinusoidally varying temporal dependence for E, i.e. Equation (2)

$$E(t) = E_0 \sin(\omega t) \quad \text{(Eq. 2)}$$

with E_0 the amplitude of the impinging field and ω the optical frequency. From Equations (1) – (3), it is clear that the second-order nonlinear response generates, besides the static component, a Fourier component of the induced dipole moment oscillating at the second

harmonic frequency 2ω and proportional to the value of the first hyperpolarisability β

$$\sin^2(\omega t) = \frac{1}{2}(1 - \cos(2\omega t)) \quad \text{(Eq. 3)}$$

Transforming the oscillating induced dipole moment of an individual molecule to the resulting intensity of the scattered light by taking the square, shows that the hyper-Rayleigh scattering light intensity at the second harmonic frequency is proportional to this hyperpolarisability squared.

It is possible to estimate the molecular zero-frequency first hyperpolarisability β_0 from three molecular properties using Oudar's two state model, Equation (4):[28, 29]

$$\beta_0 \propto (\mu_{ee} - \mu_{gg}) \frac{\mu_{ge}^2}{E_{ge}^2} \quad \text{(Eq. 4)}$$

where μ_{gg} and μ_{ee} represent the ground and excited state dipole moments respectively, μ_{ge} is the transition dipole moment of the charge-transfer (CT) transition, and E_{ge} represents the transition energy. β_0 is maximised when the oscillator strength of the CT transition is high and the difference in dipole moment between the ground and excited states is large. The lower the energy of the CT state, the greater its contribution to the quadratic hyperpolarisability. However, an upper limit on the static hyperpolarisability of chromophores seems to exist, which links static beta to the number of polarisabile electrons in the molecule, a relationship which has been investigated theoretically by Kuzyk.[30]

In practice, the zero-frequency hyperpolarisability β_0 is normally too low to give a useful SHG intensity, but can be enhanced by resonance with allowed transitions between real states. Resonance enhancement of β can be estimated by application of a two-level quantum model proposed by Oudar and Chemla in 1977,[28] which shows excellent agreement with experimental results. Their model states:

$$\beta_\lambda \approx \beta_0 \frac{\omega_{ge}^4}{(\omega_{ge}^2 - \omega^2)(\omega_{ge}^2 - 4\omega^2)} \quad \text{(Eq. 5)}$$

where β_λ is the resonance enhanced first hyperpolarisability, $h\omega$ is the energy of the laser photon used to generate SHG and $h\omega_{ge}$ is the energy difference between the ground and the CT state. The result of this phenomenon is that the first hyperpolarisability is significantly enhanced when studied at the wavelength, or double the wavelength, of the CT band (i.e. β_{max} exists at $\lambda = \lambda_{max}$ and $\lambda = 2\lambda_{max}$).

A study by Beratan and coworkers has provided an approach to predicting the frequency dependent first hyperpolarisability based on an absorption spectrum and very few hyperpolarisability measurements.[31] First excited state energies and dipole moments were extracted from linear absorption data, allowing calculation of transition dipole moments using the Thomas-Kuhn sum rules. By employing a sum-over-states expression which considers three-level contributions to β (rather than the two of Oudar's model), SHG spectra may be calculated and the optimum SHG wavelength found for any dye. More recent work has expanded the approach to porphyrin chromophores, overcoming the difficulty presented by additional low-energy absorption bands by comparing simulated spectra with real data. Interestingly, this work confirmed the presence of sharp oscillations of the β spectrum within the biological transparency window, underlinining the importance of resonance enhancement within SHG imaging.[31]

1.4 Experimental Aspects of Measuring the First Hyperpolarisability, β

1.4.1 Hyper-Rayleigh Scattering

Although non-coherent HRS is a weak effect, it provides a useful route to the measurement of β without the requirement to order the chromophore. For the purpose of characterising

the magnitude of the molecular second-order nonlinear response of a chromophore dissolved in an isotropic solvent, it may be assumed that there are no specific phase relations between individual molecules. They can therefore be treated as individual uncorrelated scattering centers. This translates into the linear relation between total HRS intensity $I_{HRS}^{2\omega}$ and number density N of the chromophore in solution. In practice, a high-intensity laser is focused on a dye solution and the HRS light is detected after a bandpass filter. The slope of this linear function is the square of the first hyperpolarisability (and a proportionality constant G, determined by theoretical and experimental factors, Equation 6).

$$I_{HRS}^{2\omega} = GN\beta^2 I_0^2 \qquad \text{(Eq. 6)}$$

By comparing slopes for a plot of $I_{HRS}^{2\omega}$ vs I_0^2 for the unknown and reference compound, it is possible to experimentally determine the first hyperpolarisability for new chromophores.[33] This treatment is valid for simple chromophores with a major CT resonance along the molecular dipolar z-axis contributing to the electronic response. The first hyperpolarisability third-rank tensor is then dominated by a single β_{zzz} component. For molecules with more complex symmetry, other tensor elements may contribute and additional experiments, such as measurement of the HRS depolarisation ratio, are needed to retrieve more tensor components. However, it becomes rapidly too complicated to deduce additional information from this incoherent scattering phenomenon. HRS does not give any information on the sign of β, that is, whether β_{zzz} is directed parallel or antiparallel with the molecular axis. Even for a single CT transition, β may be negative or positive, with the sign depending on the wavelength of investigation. With the inclusion of additional energy-level contributions to the molecular hyperpolarisability, additional complexity in the wavelength-dependent β spectrum is generated.

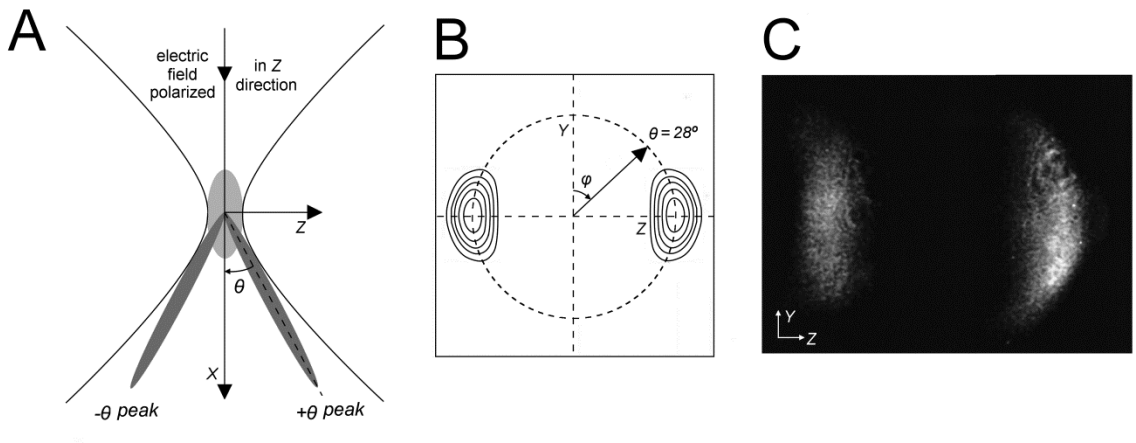

Figure 3 (a) The fundamental driving frequency is only strong enough to generate SHG in the focal spot. SHG is emitted in two lobes at an angle θ away from the beam direction (X). (b) The lobes are structurally well defined and only occur on the axis of the polarised light. (c) Lobes of SHG recorded on a photographic plate in the ZY plane show the calculated lobe structure agrees well with experiment. Reprinted from *J. Opt. Soc. Am. B.*, Moreaux *et al.*, 17, 1685-1694, Copyright 2000, with permission from the Optical Society of America.[32]

Another experimental intricacy with HRS is that the incoherent signal is often convolved with 2PF, especially for chromophores designed for combined SHG and 2PF microscopy. A demodulation technique in the frequency domain has been developed based on the delay between fluorescence and scattering in the time domain.[34] At high amplitude modulation frequencies, the fluorescence contribution is demodulated and out of phase with the scattering. The simultaneous fitting of both intensity and phase data then allows for the accurate determination of the first hyperpolarisability from fluorescence-free scattering.[35]

1.4.2 Other Techniques for Measuring β

For neutral, dipolar chromophores exhibiting a CT transition, it is possible to apply a static electric field to partially orient the molecules through the interaction of their dipole moment with the field. This induces specific phase relations between the molecules, resulting in the coherent generation of a second harmonic in the forward direction. Hence this technique is termed electric-field-induced second harmonic generation (EFISHG).[36] Since a third static field is involved, it is actually the third-order polarisability γ that is probed. This γ contains a small isotropically averaged $<\gamma>$ and a dominating orientational contribution (Equation 7):

$$\gamma = \langle\gamma\rangle + \frac{\mu \cdot \beta_{zzz}}{5kT} \qquad \text{(Eq. 7)}$$

The latter is the vector dot product, and for CT molecules, this product can be written as the product of the dipole moment μ times the dipolar diagonal tensor element β_{zzz}. The experimental result of an EFISHG measurement is often expressed as a $\mu\beta_{zzz}$. Without knowledge of the value of the dipole moment, it is not possible to derive a value for β_{zzz}. This points to one of the shortcomings of the EFISHG technique: The inherent limitation to neutral and dipolar molecules. Many interesting chromophores for second-order nonlinear optical applications deviate from the dipolar and neutral paradigms. More specifically, octopolar molecules also exhibit non-centrosymmetry and, therefore, second-order nonlinear responses which may not be probed through EFISHG. Ionic molecules cannot be oriented in an electric field, but are useful molecular design motifs, since charges impose large asymmetries in the electron distribution of chromophores, thereby strongly enhancing the second-order nonlinear response. Despite the ability of EFISHG to probe the sign of measured β, there has been a distinct evolution in screening technique for molecular second-order nonlinear optics from EFISHG to HRS.

Apart from these two solution-based techniques, there are a number of solid-state approaches that profit from the alignment of chromophores. The advantage is the larger signal from chromophores with strongly improved specific phase relations.[37] The prototypical example is the non-centrosymmetric bulk crystal, an intermediate being the thin-layer Langmuir-Blodgett (LB) film for amphiphilic molecules. LB films are a convenient, robust model for amphiphilic dyes in a membrane. The influences of tilt angle, number density and local field factors are similar to biological membranes and may be probed more consistently in LB films.

1.4.3 Directionality of SHG

Depending on the phase relations between the chromophores in the focal volume, SHG can be observed in reflection or transmission channels. For very thin samples, or for a tightly focused beam, a second-order signal is only generated from a narrow slice of chromophores. In this limit, reflection or transmission SHG are equally useful. An interaction over an appreciable length causes destructive interference of the backward SHG, reducing its intensity.

SHG is emitted with a high degree of structure in two well defined lobes at an angle θ from the hyperpolarisability tensor of the chromophore, which may be observed experimentally (Figure 3). The structure of the output light is due to the Gouy phase shift (the phenomenon of a Gaussian beam gaining a phase of π when passing through a focal point). The structure of these lobes can give information on the orientation of the membrane under inspection.[32]

1.4.4 Relating the First Hyperpolarisability, β to SHG Efficiency

The intensity of SHG at any particular wavelength is determined by three parameters: (1) the individual molecular first hyperpolarisability, dominated by β_{zzz}, along the molecular *z*-axis of the chromophore; (2) the relative orientation of the chromophore with respect to

the polarisation of the incoming laser light; and (3) the overall symmetry of the ensemble of chromophores. The first, microscopic, condition is the most fundamental: A centrosymmetric dye is not amenable to SHG. The other two dependences of the SHG intensity provide more information than 2PF: The orientation of the dipolar chromophore with respect to the polarisation of the light can be deduced (Figure 3), and centrosymmetric arrangements of dipolar molecules can be extracted from the difference image with 2PF.[38] The relationship between the molecular hyperpolarisability β_{zzz} and the efficiency of SHG can be quantified in terms of the macroscopic second-order susceptibility along the laboratory Z-axis $\chi^{(2)}_{ZZZ}$, Equation (8)

$$\chi^{(2)}_{ZZZ} = Nf\beta_{zzz}\langle\cos^3\alpha\rangle \qquad \text{(Eq. 8)}$$

where N is the number density, f is the global local field factor related to the refractive index, n, by $f = (n^2 + 2)/3$, β_{zzz} is the major hyperpolarisability tensor element, parallel with the polarisation of the laser light and $\langle\cos^3\alpha\rangle$ is an orientation factor with α the angle between the molecular z-axis and the laboratory Z-axis (Z is defined as the electric field vector of the incident light). By expanding this convention to consider SHG at angles from alignment with polarisation, it is possible to deduce the molecular orientational distribution of a chromophore (see Chapter 3). For example, to a rough approximation, RH237 (**1a**, originally synthesised by Rina Hildesheim)[39] is found to have an average tilt angle, α, of 36° away from the laboratory Z-axis in a lipid bilayer membrane (Figure 4).[40]

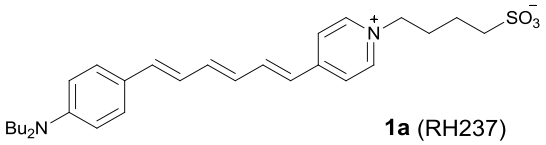

1a (RH237)

As the orientation factor $\langle\cos^3\alpha\rangle$ approaches unity, e.g. for amphiphilic chromophores ordered in membranes, SHG gains power and directionality.

The sum of the HRS from chromophores inside the focus only has a linear dependence on N as in Equation (6). However, the constructive phase relation between oriented chromophores gives rise to SHG as opposed to isotropic HRS.

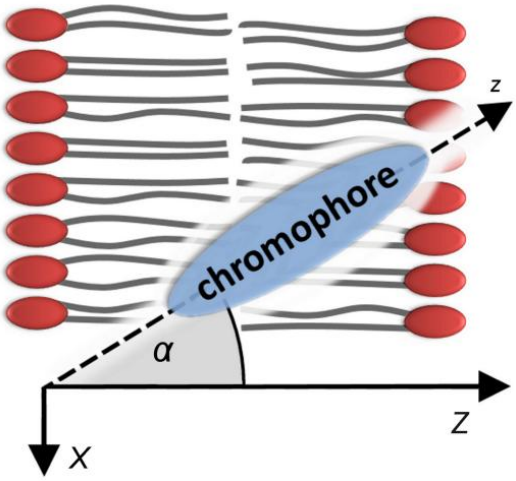

Figure 4 Definition of α, tilt angle of a chromophore relative to the membrane normal (vertical arrow). For example, with **1a**, the ensemble average tilt angle, α, is 36°. *X* is the beam direction, *Z* represents the electric field vector of the light and *z* is the molecular z-axis.[40]

By considering a constructive summation of the scattered fields over all the chromophores in the focal volume, as in Equation (9), we see that the SHG in the forward direction scales with the square of the number density (N^2).

$$I_{SHG} = G(Nf\beta_{zzz}\langle\cos^3\alpha\rangle)^2 I_0^2 \qquad \text{(Eq.9)}$$

SHG intensity from a focal volume element can be simplified and rewritten to depend on the following variables:

$$I_{SHG} \propto \Theta_2 N^2 \beta^2 I_0^2 \qquad \text{(Eq. 10)}$$

Thus, SHG power is quadratically dependent on the number density of chromophores, N, intensity of the laser light, I_0, and first hyperpolarisability, β. There is a linear dependence on the phase coherence over the focal cross section, Θ_2.[10] A large first hyperpolarisability, β, and high labelling density, N, are crucial factors for a good SHG image. The quadratic dependence on chromophore number density is in contrast to 1PF, 2PF and HRS which scale linearly with N. Therefore, although SHG produces less signal than 2PF at low N, at sufficient labeling density the signal strengths become comparable.

1.4.5 Molecular Requirements

The design of a dye for SHG imaging requires fine tuning of a number of molecular properties. In order to optimise the signal, a chromophore should have a high molecular first hyperpolarisability, β, at the wavelength of illumination. Current commercially available probes (such as FM4-64, **1b**) have $\beta_\lambda \approx 1000 \times 10^{-30}$ esu in the biological tissue transparency window (700 – 900 nm).[41]

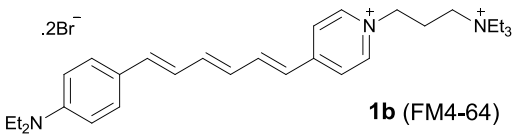

1b (FM4-64)

Values of at least 300×10^{-30} esu are required for an easily detectable SHG signal with current microscopy technology, given sufficient dye concentration. To compete with the current state of the art, chromophores should have a resonance enhanced β exceeding 1500×10^{-30} esu.

Biologically useful SHG dyes have CT bands at approximately the wavelength (one-photon enhancement), and half the wavelength (two-photon enhancement), of the live tissue transparency window (800–900 nm).

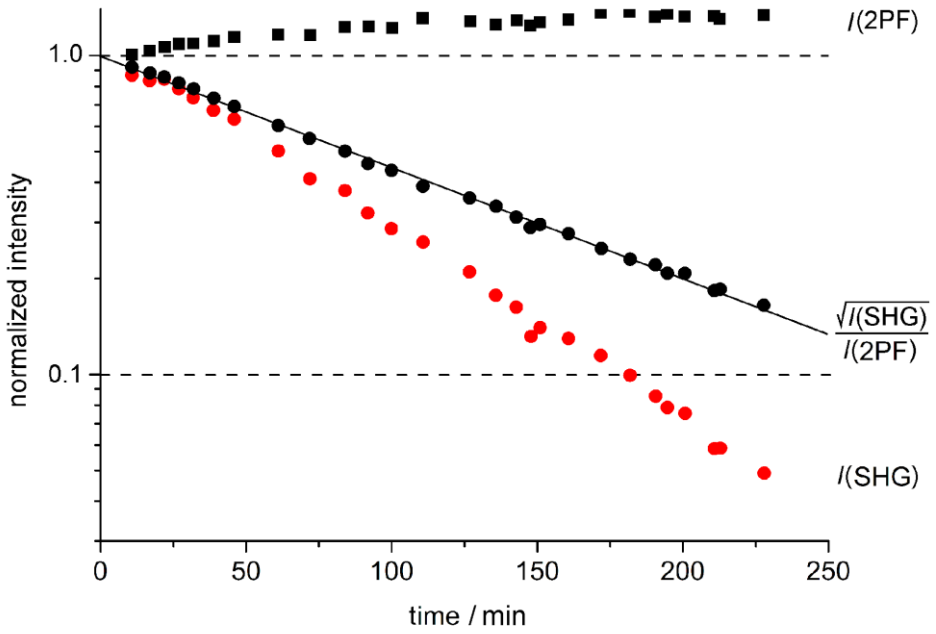

Figure 5 The dynamics of di-6-ASPBS (an analogue of **1a**) absorbed into the outer leaflet of a giant unilamellar vesicle (GUV) membrane. SHG (red circles) decays over time since flip-flop causes destructive interference of the signal. The local concentrations are monitored by 2PF levels (black squares), against which the SHG can then be normalised to find the fraction of molecules which are asymmetrically organised (black circles). The time constant for flip-flop of di-6-ASPBS is about 2 hours. Reprinted from *Biophys. J.*, Moreaux *et al.* 80, 1568-1574, Copyright 2001, with permission from Elsevier.[42]

This allows for resonance enhancement of β. While it is easier to compare static hyperpolarisabilities, β_0, from molecule to molecule (since β_0 is independent of CT transition wavelengths), it is the resonance enhanced hyperpolarisability, $\beta_{\lambda,}$ that is of most relevance to signal generation (governed by Equation 5). While resonance enhancement is inherently difficult to design into a molecule, it has been shown that the β_λ spectrum resulting from this resonant phenomena may be calculated from an absorption spectrum, with application of the Thomas-Kuhn sum rules (as mentioned above).[31]

The chromophore should have a high affinity for the biological membrane it is designed to probe, to maximise number density. At number densities of approximately one dye molecule per 100 lipids, SHG signal strength is observed using current multiphoton scanning microscopes. Number densities of this level are readily achieved with conventional styryl dyes, as well as newer derivatives.

Over time, dyes switch between leaflets of a membrane through a process called flip-flop, which reduces the overall bulk hyperpolarisability of the bilayer. The half-life of dye flip-flop can be measured by monitoring the decay of an SHG signal normalised against a 2PF signal in an asymmetrically labeled bilayer (Figure 5).[42] A dye should accumulate in membranes within 5 minutes and flip-flop slowly, with a half-life of over an hour, to ensure that the time window for experiments is sufficiently long.[43] Pixel intensities in an SHG image of 5 times above background are usually sufficient, and have been found to be as high as 20 for some commercially available SHG probes.[9]

Injection of SHG dyes into neurons can be troublesome due to their tendency to precipitate and block the tip of the micropipette (diameter ca. 1 μm). If a dye is not water-soluble it may need to be formulated with an organic solvent, e.g. DMSO, lipids or block copolymers such as pluronic F127.[9, 44]

1.4.6 Optimising Optics for SHG Microscopy

While optimising dyes for SHG, we must consider the equipment that will be needed to conduct SHG microscopy. The most striking, and often the most limiting, aspect of SHG microscopy is the forward propagation of SHG light. This is in contrast with one- and two-photon fluorescence which are emitted isotropically. Forward-only propagating SHG is easily distinguished from 2PF, which appears equally in both transmission and epi channels. The numerical aperture (*N.A.*) of a lens is defined as $N.A. = n \sin \varphi_{obj}$ (n is the refractive index, 1.0 for air, 1.3 for water and 1.5 for oil lenses, Figure 6). Typically in multiphoton (2PF) microscopy, a high *N.A.* objective is used to enhance the signal intensity. Higher *N.A.* optics have smaller focal spots, leading to greater resolution and greater nonlinear effects.

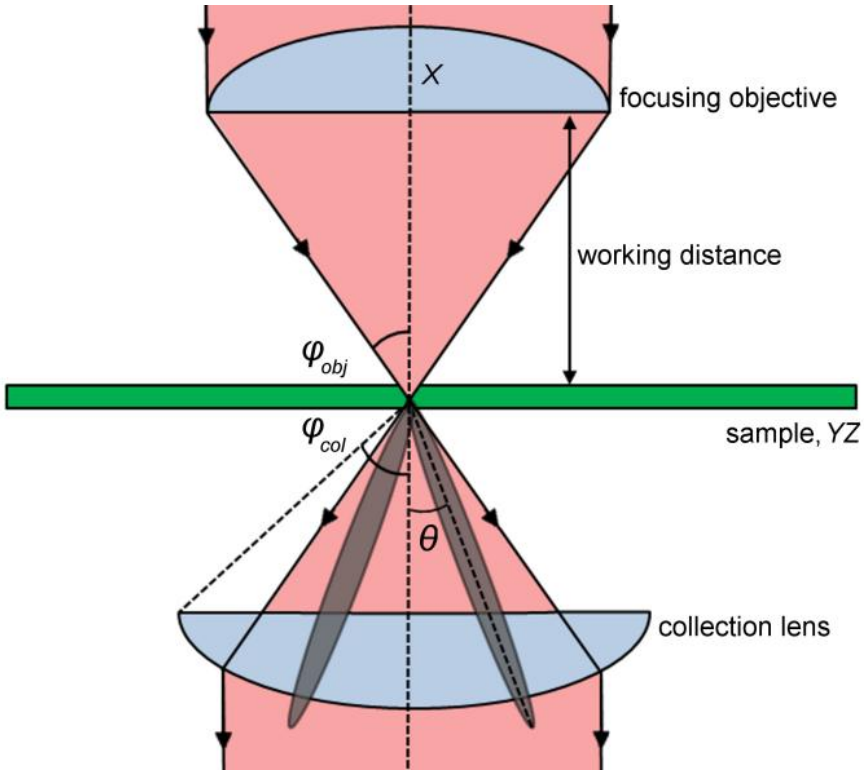

Figure 6 The focusing of a laser beam upon a nonlinear optical medium generates second harmonic light in two lobes. *X*, *Y* and *Z* coordinates are consistent with Figures 3 and 4.

Unlike 2PF, SHG signal intensity does not increase with the numerical aperture of the focusing objective. The consequence of a higher *N.A.* is a tighter focus which increases the light intensity at the focal cross section ($I_0 \propto (N.A.)^2$). Similarly, the phase coherence across the focus ($\Theta \propto (N.A.)^2$) improves but the number of molecules in the focal point is reduced by a factor of ($N \propto (N.A.)^{-3}$). When these terms are substituted into the previous expression for SHG intensity, Equation (10) gives Equation (11) [45]:

$$I_{SHG} \propto (N.A.)^2[(N.A.)^{-3}]^2[(N.A.)^2]^2 \cong (N.A.)^0 \qquad \text{(Eq. 11)}$$

The lack of *N.A.* dependence of SHG essentially comes down to the reduction in the number of oscillators in the focal volume and is a consequence of the fact that SHG depends on N^2 whereas 2PF depends on *N*. While the numerical aperture of the objective does not affect the SHG signal detected, the *N.A.* of the collection lens is critical. The *N.A.* of the collector must be higher than that of the focusing objective (i.e. $\varphi_{col} > \varphi_{obj}$, Figure 6), otherwise the

lobes of SHG (at θ) fall outside of the collector, and fail to reach the detector (since $\theta \propto \varphi_{obj}$).[32]

For tissue imaging, the optimum laser wavelengths lie within the biological transmission window, 700–900 nm. Illuminating the specimen in this window permits good depth penetration and low phototoxicity. Below this range, light is scattered by cellular structures and absorbed by natural chromophores like hæmoglobin while above this range there is absorption by water. Femtosecond pulsed Ti:Sapphire lasers are commonly used since they may be tuned across the range of 700–900 nm. The wavelength of investigation should also be modulated to exploit the resonance enhancement of SHG dyes. This can be simple with a Ti:Sapphire laser, which can be tuned to the wavelength of maximum SHG.

When designing an SHG imaging system for biological applications, it is necessary to consider the properties of the laser source such as the average power, individual pulse energy and pulse peak intensity. An individual pulse carrying energy above a threshold leads to heat-induced formation of bubbles or photo-ionisation in the focal spot. SHG and 2PF intensity scale with the inverse of the pulse duration for a constant average laser power in the range 400 fs to sub-20 fs.[46] Thus ideal pulses are short so that a combination of high peak intensity and low pulse energy is achieved. Photodamage may also be decreased without reduction of SHG signal by increasing repetition rate and reducing pulse energy (at constant laser power).[47] It is therefore desirable to use a laser source with pulse energy below the damage threshold, combined with a short pulse duration and high repetition rate (e.g. 2 GHz).

1.5 Molecular Design

Any molecule lacking a center of inversion can exhibit SHG; however, several criteria must be satisfied to achieve a useful quadratic hyperpolarisability (β). The highest quadratic hyperpolarisabilities are exhibited by molecules consisting of electron donors and acceptors linked by highly polarisable π-conjugated bridges, to provide a low energy CT state, a high oscillator strength and a large change in dipole moment in the excited state (Equation 4). It is also essential that molecules are ordered, so that the CT vectors point in the same direction. Without order, individual molecular hyperpolarisabilities cancel and only HRS is generated. This section will survey different approaches to maximising the molecular first hyperpolarisability and examine methods for inducing order. While design of a conjugated π-system to maximise β is a challenge that has attracted considerable interest over the last decade,[11, 12, 14, 48-51] few attempts have been made to convert novel high-β harmonogens into dyes for biological applications. We will concentrate on dipolar molecules as these are most suited to biological imaging.

1.5.1 Optimising the Bridge

A good bridge will provide coupling between donor and acceptor with a high oscillator strength.[52-54] The bridge must provide the basis for a low energy CT transition as it dictates the size of the starting HOMO-LUMO gap which can then be reduced by the addition of suitable donors and acceptors. In order to create a dye with a large first hyperpolarisability, a good approach is to choose a highly polarisable bridge and attach donors and acceptors which maximise β for that bridge.

Polymethine bridges have dominated SHG dye chemistry due to their strong π-conjugation and ease of synthesis. Almost all dipolar molecules used for biological imaging of membranes consist of a polymethine bridge flanked by aromatic (or polyaromatic) donors and acceptors. Hyperpolarisability tends to increase with bridge length (Figure 7),[55] hence

the success of extended polymethine chromophores such as FM4-64 (**1b**, developed by the groups of Lewis and Loew).[56] However, as the bridge length increases, the solubility of the dyes in aqueous media becomes worse and stability to photodamage and nucleophiles is reduced. Acetylene bridges (such as in **2**) have similar nonlinear optical properties to polymethine bridges, though they have not been widely investigated. Therien and coworkers applied the predictions of Oudar's two-level model to porphyrinic bridges.[37, 52-54] The synthesis of a library of push-pull porphyrin chromophores led to understanding of the relationship between structure and hyperpolarisability.

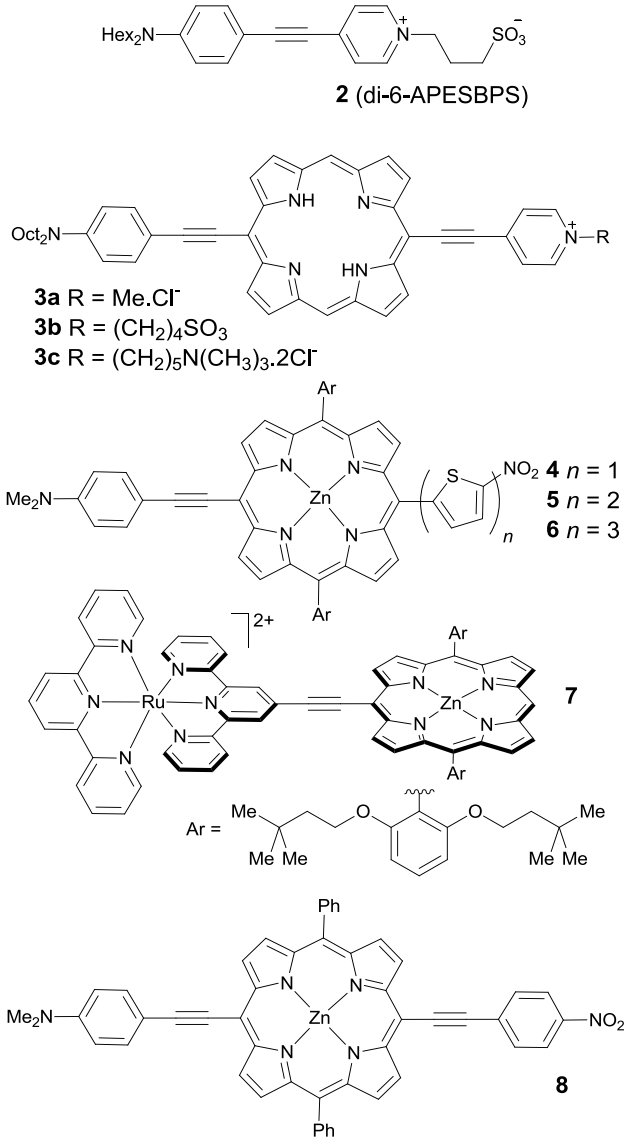

Donor-π-acceptor porphyrins (**3**–**8**) have strong CT transition oscillator strengths (along the long molecular axis). The porphyrin bridge also leads to a very low HOMO-LUMO gap, maximising each factor in Oudar's model (Equation 4). Porphyrins exhibit some of the largest resonance enhanced hyperpolarisabilities recorded by HRS. The use of porphyrin bridges in dyes for SHG imaging has led to order of magnitude increases in signal strength. The application of porphyrin chromophores as π-bridges is detailed within this thesis, and allowed me to image bilayers with high SHG contrast. However, poor aqueous solubility limited further application of these dyes. In particular we found that the inclusion of octyl chains prevented proper seal formation when patch-clamping neurons.[14, 57] The versatile coordination properties of porphyrins allow for inclusion of a metal cation, which modulates the electronic structure of the chromophore and can be used to adjust the solubility. Metalation can be used to tune the absorption bands of a porphyrin, to exploit resonance enhancement at different driving frequencies. The porphyrin Soret band has a high oscillator strength, and typically lies between 400 and 420 nm, such that resonance enhancement between 800 and 840 nm is directly inside the transparency window of biological tissues.

Fluorene and oligophenylene bridges have also been investigated,[11, 12, 55] but are less hyperpolarisable than polymethine bridges, due to weaker π-conjugation and greater loss of aromaticity upon charge-transfer.

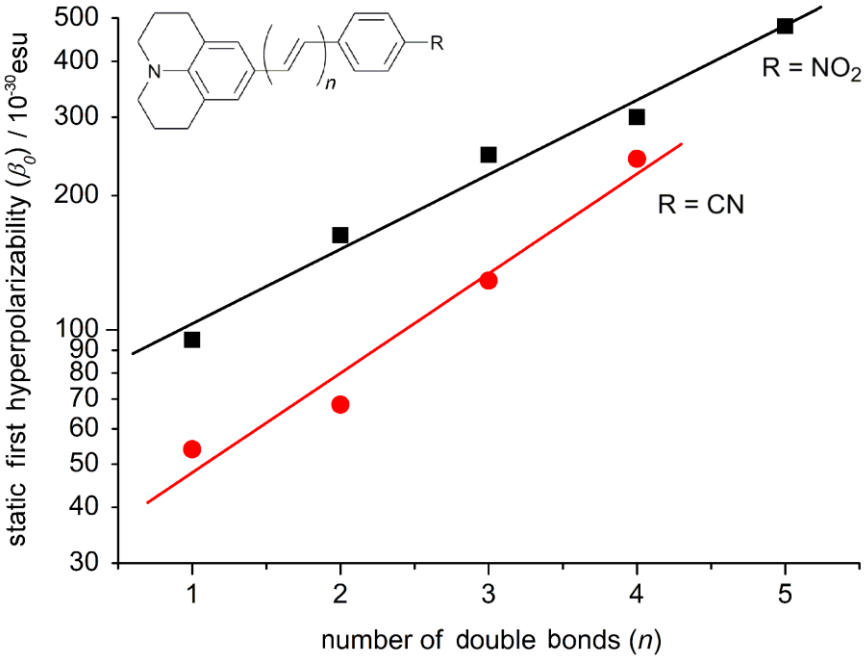

Figure 7 As the number of double bonds is increased, the bridge is elongated and the oscillator strength increases, increasing the static hyperpolarisability, β_0. The static hyperpolarisability, β_0, is calculated using Oudar's two-state model. The ground and excited state dipoles were found by taking electro-optical absorption measurements, and the transition dipole found by numerical integration of the absorption band. Reprinted from *Chem. Phys.*, Alain *et al*. 245, 51-71, Copyright 1999, with permission from Elsevier. [55]

Both Marder and Ratner note that CT chromophores with one aromatic and one quinoidal ring have smaller ground state to excited state energy gaps because electron transfer from the donor to the acceptor involves no net change in aromaticity, as illustrated for compounds **9** and **10** (Figure 8).[50, 58, 59] This is reflected in the β_0 values for these chromophores; **10** has nearly twice the quadratic hyperpolarisability of **9** (Table 1).

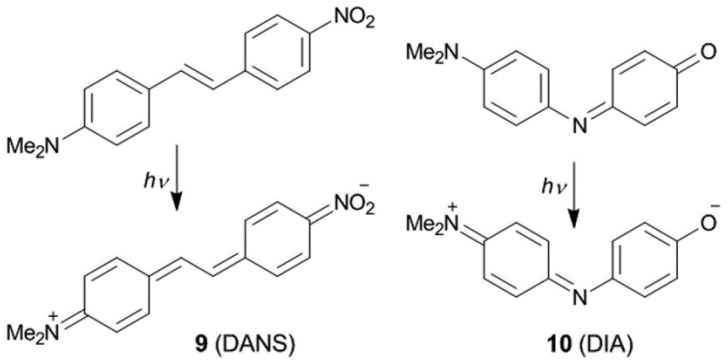

Figure 8 The CT transition of **9** results in the loss of aromatic stabilisation whereas the CT transition of 10 has no net change in aromaticity.[59]

1.5.2 Donor and Acceptor

Suitable donors and acceptors must be chosen to optimise β for a particular bridge to achieve a strong, low-energy CT transition.[50, 54, 59-61] Marder and coworkers postulate that each factor in the two-level model has a characteristic maximum which is a function of the degree of bond-length alternation, so that maximisation of β requires some compromise in the molecular design. Their findings can be reduced to three cases: The first (Figure 9, left), when donors and acceptors have little Coulombic energy difference, molecules have very strong through bridge coupling, resulting in a high oscillator strength and small HOMO-LUMO gap. However the dipole moment change between ground and CT states is small and reduces β. The limiting case is a symmetrical chromophore such as a cyanine.

In the case where donors and acceptors are strong (Figure 9, right), and have a large Coulombic energy difference (such as the amine and nitro combination in **9**), the dipole moment of the CT state is stronger, but the CT transition oscillator strength is low due to poor π-overlap. The HOMO-LUMO gap is also increased due to asymmetrical (and energetically costly) charge separation.

The case which maximises β is a balance of these factors which can be found by judiciously choosing donor and acceptor for a given bridge (Figure 9, center). A dipole moment change exists from the ground to excited state, but the transition energy is not too costly (thus the transition makes a large contribution to β given a sum-over-states approximation), and the oscillator strength is still high.

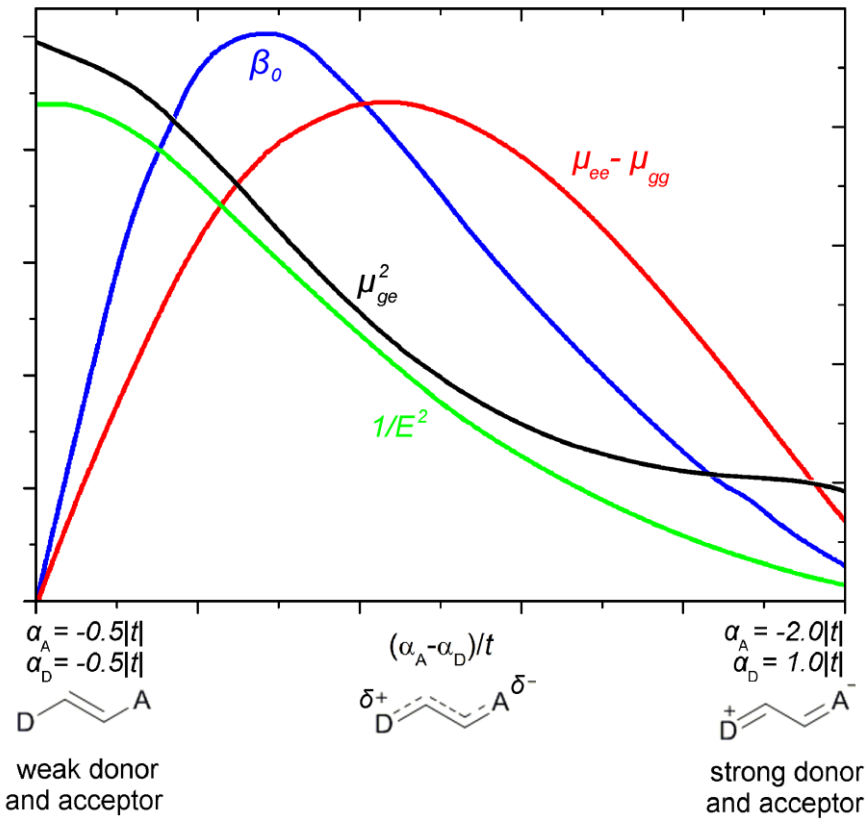

Figure 9 β_0 is maximised at certain Coulombic energy differences between donor and acceptor for a particular bridge. α_A and α_D are the Coulombic potentials of the donor (D) and acceptor (A) respectively and *t* is the exchange matrix element between the bridge orbitals. From *Science*, Marder *et al.*, 252, 103-106. Reprinted with permission from AAAS.[50, 59]

1.5.3 Achieving Chromophore Alignment in Biological Systems

Without a driving force for the chromophores to order, the ensemble average of the first hyperpolarisability tensors (Equation 8) will be low, and the SHG signal will be weak. Biological systems contain many membrane and interfacial structures which provide asymmetric environments for ordering chromophores. For the labeling density required for SHG, lipid membranes provide the best surface at which to organise due to their scale and ability to rapidly incorporate amphiphilic dyes.

1.5.4 Amphiphilic Dyes

The traditional approach to an amphiphilic molecule is *via* the attachment of hydrophobic moieties to one end of the molecule and hydrophilic functional groups (such as the sulfonate in **1a** and **14a**, the quaternary amine in **1b** or the quaternary ethanolamine in **11** and **12**) to the other. This gives a structure that will insert into lipid bilayers in one direction, and will not quickly diffuse through the bilayer. The choice of polar and nonpolar groups subtly affects the biological localisation of the dyes. Long aliphatic chains lead to a higher partitioning into cellular membranes, however they retard diffusion into the bilayer due to the lack of aqueous solubility. Longer alkyl chains also slow dye flip-flop as they increase the energy required for reorientation.

The purpose of a polar head group is to anchor the dye in the aqueous phase so that it cannot diffuse through the membrane or flip-flop. In order to undergo a rearrangement of this sort, the head group must first be desolvated, which is enthalpically expensive for highly polar functionalities. The incorporation of high charge density will also confer greater aqueous solubility to the dye, especially when combined with a hydrophilic counterion.

Typically, at least two charges are required on the polar headgroup of the molecule,[62] although some dyes that use neutral sugar groups show reasonable membrane leaflet retention due to the anchoring effect of solvation. Barsu *et al*. investigated a number of neutral headgroups that gave good membrane localisation.[11]

1.5.5 Chiral SHG Chromophores

Chiral dyes cannot exist in a centrosymmetrical arrangement; therefore enantiomerically pure dyes may diffuse into both leaflets of a lipid membrane and still produce SHG. However, if the chiral dyes diffuse into both sides of a membrane and equal quantities are

aligned antiparallel, the bulk molecular hyperpolarisability of each side of the membrane will generate two SHG signals that are approximately 180° out of phase, and so cancel. The inclusion of chiral groups does enhance SHG, but may instead invoke additional contributions from off-axis hyperpolarisability tensors which are generally weaker than the primary β_{zzz} component. If this is the case, the SHG signal from a symmetrically doped bilayer should show minimal modulation upon the application of a static electric field, in comparison to dyes doped asymmetrically into a membrane. One class of chiral harmonogen, binaphthylstyryl dyes with two orthogonal chromophores were synthesised by Yan *et al* (Figure 10, 12 and 13) [63] and may align with one chromophore in the membrane and one on the surface. A second family of chiral SHG dyes consists of a normal amphiphilic structure with a chiral polar group attached. Auxiliaries that have been used include sugars[64] and molecules derived from amino acids such as L-proline.[49]

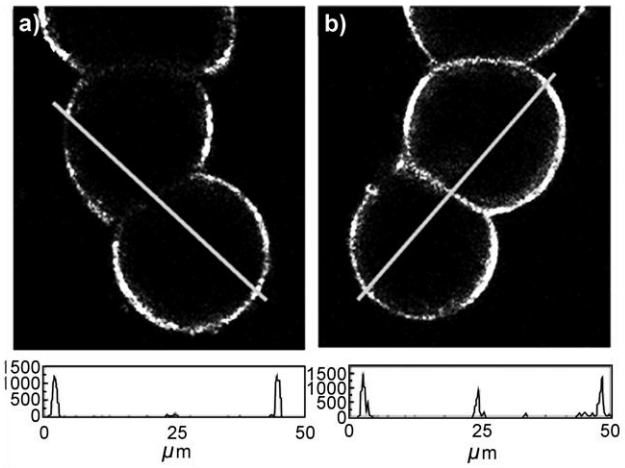

Figure 10 SHG images of cells stained with (a) racemic dimer (**11±**), and (b) chiral dimer (**11**) when illuminated with circularly polarised light. Intensity of line scans through cell-cell junctions are shown on plots below, demonstrating that the chiral dye (**11**) is capable of SHG in a symmetrical bilayer environment whereas the racemate (**11±**) is not. Reprinted in part with permission from *J. Am. Chem. Soc.*, Yan *et al*., 2006, 128, 11030-11031. Copyright 2006 American Chemical Society.[63]

1.5.6 Supramolecular modification of dyes

SHG dyes have been attached to proteins or other cellular structures either coordinatively[64] or covalently. Salafsky used the PyMPO dye (**13**) which was covalently conjugated to

proteins to elucidate the tilt angle of proteins absorbed onto surfaces.[51, 65] Gold nanoparticles have been coordinatively attached to proteins, allowing for the enhancement of SHG from membrane bound dyes by exploiting surface plasmon resonance.[64]

Once synthesised, the usefulness of SHG dyes may be increased by supramolecular complexation. The inclusion of dyes in molecular hosts such as cyclo-γ-dextran (a 1,6-α linked sugar based macrocycle) or amylose helices can enhance hyperpolarisability by enforcing planarity on the molecule.[9, 66, 67] The inclusion of hydrophobic dyes in cyclodextrins is a common method of aiding solubility in aqueous media.

Table 1 Photophysical properties of dyes referenced in this chapter

Dye	λ_{max} / nm (solvent)	β_0 / 10^{-30} esu (λ / nm)[c]	β / 10^{-30} esu (λ / nm)[d]	References
1a,b[b]	500 (MeCN)	310 (1300) 370 (800)	900 (1300) 1085 (800)	9, 40, 68
3	448, 643, 723 ($CHCl_3$) 437, 629, 707 (DMF)	-	2300 (800) 5800 (840) 8000 (840)[e] 3700 (1064)	14
4	456, 580, 640 (THF)	-	480 (800)[f] 2400 (1300)[f]	54
5	457, 583,641 (THF)	-	345 (800)[f] 2200 (1300)[f]	54
6	458, 579, 641 (THF)	-	510 (800)[f] 4350 (1300)[f]	54
7	428, 567, 639 (MeCN)	-	2100 (1064) 5100 (1300)	37, 69
8	450, 680 ($CHCl_3$)	800[a]	4933 (1064)	52
9	430 ($CHCl_3$)	55 (1907)	73 (1907)	59
10	590 ($CHCl_3$)	106 (1907)	190 (1907)	59
11	473	-	-	44, 63, 70
12[b]	449	600[a]	-	62, 63
13	415	-	-	51, 65
14a,b[b]	542 ($CHCl_3$)	600[a]	-	9, 71-73

a) Wavelength not provided b) From model chromophore c) Wavelength which β_0 is calculated from d) In $CHCl_3$ unless otherwise specified. e) In *N*,*N*-dimethylformamide f) In tetrahydrofuran

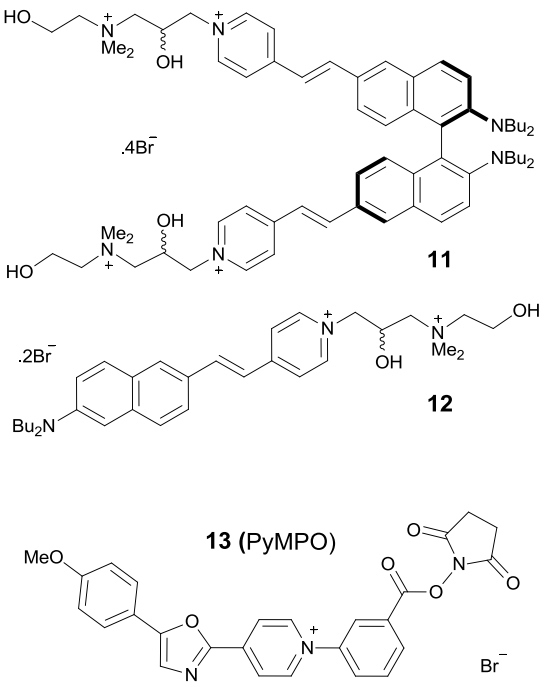

1.5.7 Probes Introduced by Genetic Modification

The recipients of the 2008 Nobel Prize, Shimomura, Chalfie and Tsien, developed fluorescent probes that can be incorporated into organisms by genetic engineering.[74] Green fluorescent protein (GFP) consists of 238 amino acids arranged to form a beta-barrel around a central chromophore. The quadratic nonlinear optical properties of GFP and a number of engineered proteins have been investigated.[75, 76] An effort has also been made to elucidate the relationship between structure and quadratic hyperpolarisability of EYFP (enhanced yellow fluorescent protein) and DsRed (*Discosoma sp.* red fluorescent protein).[13] The chromophore of these fluorescent proteins is highly conserved (Figure 11b); modifications are made through small functional group changes in remote positions or by introducing other π-systems in close proximity to the chromophore.

The resonance enhanced β of EGFP was found to be highest in the series EGFP, EYFP and DsRed (λ_{em} = 507, 527, 583 nm, $\beta_{HRS,800}$ = 107, 37, 81 × 10^{-30} esu respectively). According to a two-level model, we can expect that the quadratic hyperpolarisability should decrease

through this series as the energy of the CT transition increases. EYFP was found to have a low β which can be explained by molecular modeling of the protein. The close centrosymmetrical proximity of a tyrosine residue (Figure 11a) and the chromophore of EYFP cancels a large part of the molecular hyperpolarisability. The engineering of fluorescent proteins with extended chromophores may lead to new FPs with higher quadratic hyperpolarisabilities. For example, zFP538 contains a novel three-ring chromophore which has a close interaction between two aromatic residues that should enhance its SHG response.[77]

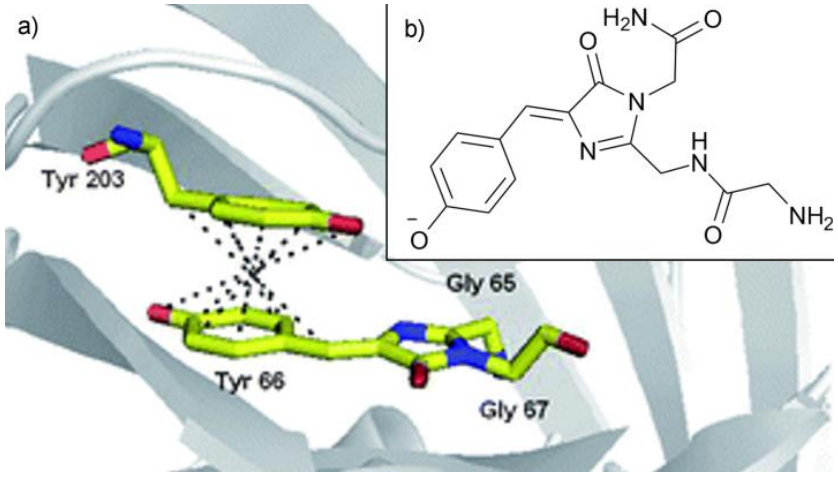

Figure 11 Representation of the encapsulated chromophore in EYFP (a), showing the center of inversion symmetry around the phenolic tyrosine residue. (b) Molecular structure of the EYFP chromophore.[13]

1.5.8 Reducing Phototoxicity

Extensive testing of the dipolar dye FM4-64 (**1b**) by Webb and coworkers has revealed that a significantly problematic aspect of SHG imaging of neuronal action potentials is photodamage.[78] High photodamage is symptomatic of the low signal-to-noise ratio of current SHG dyes. New dyes with a stronger SHG signal should allow for lower laser power and less photodamage. Sacconi *et al.* found that the amount of photodamage increased linearly with the dye concentration, and was proportional to the cube of the peak laser intensity. Protocols were developed to maximise the labeling density at constant

concentration, since the SHG signal intensity increases with the square of the dye number density. Higher labeling density allowed the use of much lower light intensity which led to reduced photodamage. The presence of antioxidants or oxygen scavenging enzymes (such as Oxyrase®)[79] reduced the phototoxic effect of laser illumination by about a factor of 5 (Figure 12).[78] These results indicate that two-photon excited production of singlet oxygen is the main mechanism of photodamage with this dye.

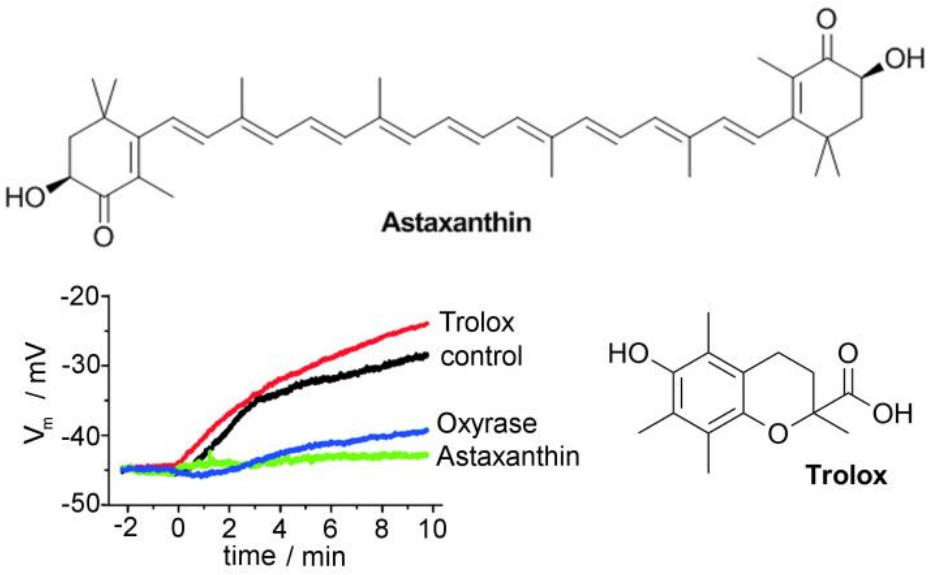

Figure 12 Imaging with FM4-64 (**1b**) in the presence of oxygen reducing agents such as Oxyrase[79] or antioxidants such as Astaxanthin (above) reduces the photodamage (below) inflicted on cells and increases the experimental timeframe. Reprinted in part from *Proc. Natl. Acad. Sci. U.S.A.*, Sacconi *et al.*, 2006, 103, 3124-3129. Copyright (2006) National Academy of Sciences, U.S.A.[78]

The use of antioxidants does not address the root cause of photodamage: photochemistry resulting from two-photon excitation. It is difficult to avoid populating excited states as resonance enhancement of SHG signal occurs in the same region as strong two-photon absorption. It is not viable to irradiate the sample away from absorption bands where only the β_0 contributes to the bulk hyperpolarisability, because β_0 is too low.

The approach to limiting photodamage I describe in this thesis involves the complexation of open-shell divalent metal ions to a porphyrin-based SHG dye.[14] Since the generation of

optical harmonics does not require excitation of the molecule, it is possible to quench any excited states and still observe a SHG signal. Open-shell transition metal cations (e.g. Ni^{2+}, Cu^{2+}) allow for the formation of excited states that have very fast non-radiative relaxation mechanisms. With such fast removal of excited states, the dye has little chance to undergo damaging photochemical reactions, reducing phototoxicity. In the same vein, attachment of stable organic radicals should also provide relaxation pathways through mixing with the first excited state or electron transfer.[80]

Avoiding phototoxicity requires rapid relaxation of excited states once formed (as with the previous examples) or prevention of their formation. It is possible to either tune two-photon absorption bands out of regions where SHG resonance enhancement is high, or to increase the β/γ ratio.[60] This may be achieved by altering the donor-acceptor pair, substituting heteroatoms or modification of the chromophore; however this will inevitably affect the SHG efficiency.

1.6 Applications of SHG Microscopy

Creative application of SHG microscopy may solve a wide range of problems in the life sciences. Due to the inherent differences in the physical processes that lead to SHG and fluorescence, the effects provide complementary information. SHG can provide information on the local organisation of a structure. The intensity of the SHG signal from a particular point in the cell is dependent on the dye organisation and labeling density. In order to study changes in organisation of part of a biological sample, the SHG may be normalised against 2PF (as illustrated in Figure 5).

1.6.1 Structural Imaging

In work such as that by Millard *et al*.,[81] the ratio of SHG to 2PF is plotted as a function of time during exocytosis at fertilisation of an egg of the sea urchin *Lytechinus pictus* (Figure 13). Eggs are dyed with di-8-ANEPPS (*N*-octyl form of **14a**), and the sample shows constant SHG and 2PF levels until exocytosis begins. Exocytosis is triggered by a calcium wave that propagates around the egg from the point of fertilisation, significantly changing the structure of the membrane which has two effects on the signal from the localised dye. The SHG decreases as dyes arranged antiparallel in the microvilli emit SHG out of phase, reducing the overall SHG from the membrane (Figure 13). The 2PF will simultaneously increase, since a reduced dye density in the membrane results in less dye-dye self-quenching. The sum of these effects leads to a marked change in the SHG/2PF ratio. The orthogonality of the signal from these two effects allows Millard *et al*. to follow the wave of exocytosis around the membrane.

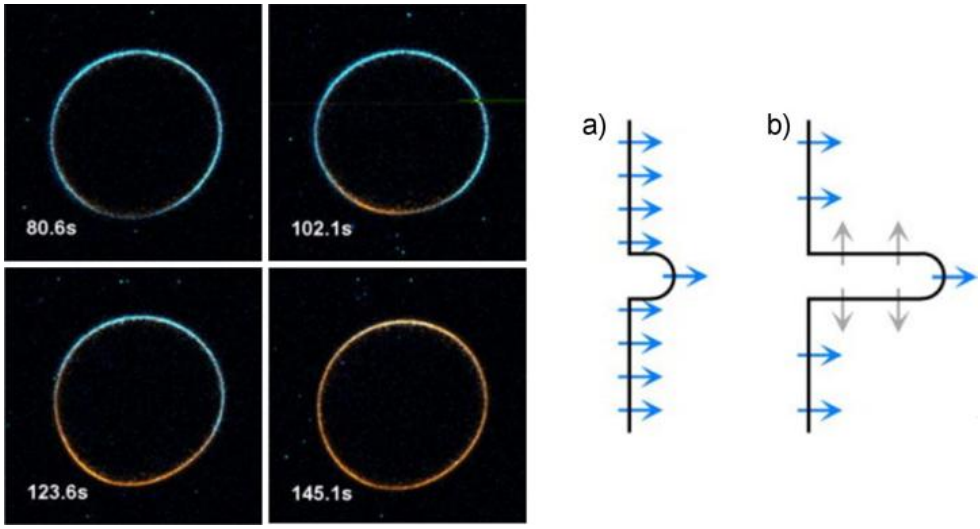

Figure 13 (left) SHG (blue) and 2PF (orange) microscopy with di-8-ANEPPS (*N*-octyl form of **14a**) of an egg undergoing exocytosis, from the point of fertilisation until the entire egg has been covered in microvilli. (right) Prior to exocytosis (a), the membrane has only small microvilli, and SHG can be produced from most parts of the membrane. Following fusion (b), SHG cancels in regions of the membrane where probes are aligned antiparallel. Reprinted from *Biophys. J.*, Millard *et al*. 88, L46-L48, Copyright 2005, with permission from Elsevier.[81]

1.6.2 Voltage-Sensitive Imaging

Probes for membrane potential are sensitive to the electric field within a membrane. Electric fields change the efficiency of SHG via a number of mechanisms, each occurring at a different rate. The fastest, an electro-optical effect sees the hyperpolarisability modulated by the application of a field. This changes β instantaneously, and is ideal for probing the fast (~1 ms) changes of neuron synaptic potentials.

The response of dyes is highly dependent on the experimental system used (Table 2). Biological membranes often have slower response times than model membranes. The lipid and protein concentration as well as thickness of biological membranes is vastly different to the oxidised cholesterol often used in hemispherical lipid bilayers (HLBs) or the pure lipid bilayers of giant unilamellar vesicles (GUVs).[56, 82] For example, commercially available dye di-4-ANEPPS (**14a**, developed by Loew and coworkers)[71] has a 40% SHG change per 100 mV in a cultured neuron and only a 2% SHG change per 100 mV *ex vivo*.[9, 66] Dyes that are to be used for neuronal or cardiac voltage sensitive imaging require an SHG response on the millisecond timescale and greater than 10% / 100 mV change in SHG signal. Dyes that do not meet these requirements will suffer a poor temporal resolution or low signal-to-noise respectively.

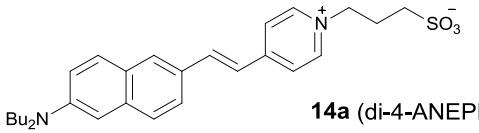

14a (di-4-ANEPPS)

The main application of amphiphilic, highly polarisable dyes (such as di-4-ANEPPS (**14a**) and FM4-64 (**1b**) which have been well characterised in terms of their kinetic and overall response to electric fields)[9, 44, 73, 83] has been the probing of membrane potential transients by fluorescence and SHG microscopy. In 1PF microscopy, electric field sensitivity is evolved from a Stark shift under the application of an external electric field. The static field

perturbs the energy level of the electronic states, causing a shift in the absorption and emission spectrum which can be detected with the correct implementation of a bandpass filter. This microscopy technique cannot be applied to the deep tissue imaging of brain slices due to poor transparency and high photodamage at fluorescence wavelengths. The use of SHG allows photodamage to be avoided, only generates signal from cellular membranes, and provides deep tissue penetration of the excitation light. While exploring methods of limiting photodamage in SHG microscopy, Sacconi and Dombeck[78] took recordings from different points in a cultured neuron. They were able to monitor action potentials at multiple points in a neurite (Figure 14). However, this technique requires refinement before we have the ability to monitor action potentials on a trial-by-trial basis: This study required $n = 20$ traces which were averaged to obtain the traces presented in Figure 14. This is typically a very difficult task since neurites have low damage tolerance thresholds. Measurements at each position were taken with a 4 second lag time between scans to allow time for the cell to recover. Recording from an *ex vivo* brain slice is more difficult, however the recent advance of random access SHG microscopy has allowed membrane potential recording simultaneously from multiple neurons in a brain tissue slice.[84]

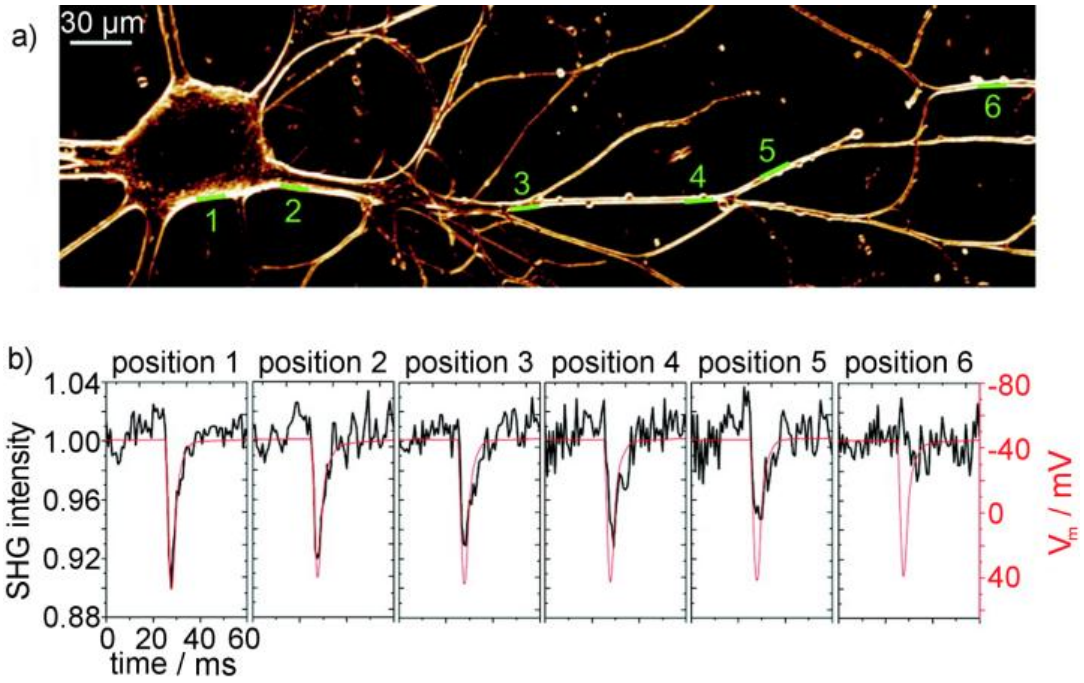

Figure 14 (a) SHG image of a cultured squid neuron showing six positions of interest at which line scans of SHG intensity took place. (b) SHG intensity for a series of line scans (n = 20 trials, black) and transmembrane potential (patch clamp, red) at increasing distance from the soma, the point of greatest SHG response. At larger distances from the soma, SHG signal is lower but action potentials are still easily observed until position 6. Reprinted in part from *Proc. Natl. Acad. Sci. U.S.A.*, Sacconi *et al.*, 2006, 103, 3124-3129. Copyright (2006) National Academy of Sciences, U.S.A.[78]

An advantage of SHG microscopy is that we may investigate light-activated processes without perturbing them by using infrared light. For example, Ben-Oren *et al.*[82] applied SHG microscopy to the study of membrane potential of photoreceptor cells in the eye of a living Musca fly. This task would have been unachievable by normal fluorescence microscopy as optical measurements of membrane potential in photoreceptor cells cannot be made at normal wavelengths, due to their natural photosensitivity.

Table 2 Potential Sensitivities of Dyes in Various Biological Systems

Dye	Potential sensitivity % / 100 mV	Model	Wavelength (nm)	Reference
1b	12	can[e]	1064	9
	7.5	arbs[b]	1064	9
	5	arbs[b]	900	9
	15	mns[c]	1064	40
	11	mns[c]	900	40
	10	mns[c]	850	40
2	9	GUV[d]	950	38
	6	GUV[d]	900	38
	2	GUV[d]	850	38
11	4	mn[a]	916	44
14a	43	mn[a]	950	73
	26	mn[a]	910	73
	18.5	mn[a]	850	73

a) Mouse neuroblastoma b) Acute rat brain slice c) Mouse neocortical slice d) Giant unilamellar vesicle e) Cultured *aplysia* neuron

In this experimental set-up, the photoreceptor cells were dyed with JPW 1259 (**14b**), exposed and surface-mounted. The 1064 nm Nd:YAG IR laser and 632.8 nm HeNe photoexcitation laser were directed at the sample, and a SHG detector mounted at the reflection angle of the incident fundamental beam. After appropriate controls, it was established that photoexcitation with a HeNe laser caused depolarisation of the membrane. This was detected in SHG signal changes of as much as 30%. This work sets the stage for further SHG investigation of processes that are light activated which cannot be investigated by traditional fluorescence microscopy, such as photosynthesis or the uncaging of photolyzable molecules.

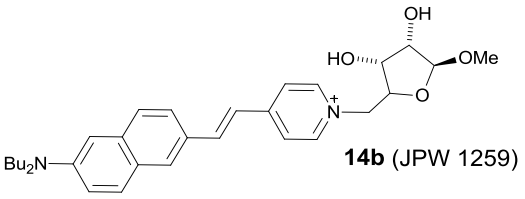

14b (JPW 1259)

The first instance of SHG from green fluorescent protein was recorded by Khatchatouriants *et al*. in 2000.[76] Three mutants of *C. elegans* were grown, each expressing a chimeric form of GFP with either DEG-2 (a subunit of the nicotinic acetylcholine receptor) or MEC-2. When excited with a Nd:YAG laser at 1064 nm, a SHG signal could be observed at 532 nm. The effect of membrane potential was investigated by application of choline to the biological tissue. DEG-2 is a choline receptor, and establishes a membrane potential upon the application of choline to neurons. In the hmIS4 mutant which contains a DEG-2/GFP chimera, SHG sensitivity to choline was observed as a 65% reduction in signal strength. In a hmIS4;4773 DEG-3 transgenic mutant which lacks choline sensitivity, no loss of second harmonic signal was observed. Similar experiments were carried out with a strain of transgenic *C. elegans* which expressed a mechanically sensitive MEC-2/GFP chimera. The animal was placed under a coverslip as in the previous experiments and SHG changed by up to 24% as a function of mechanical pressure. No readings of transmembrane potential were taken in parallel with these optical measurements.

1.7 Outlook and Scope of Thesis

Recent advances in microscopy have made SHG an increasingly popular technique. Microscopes able to take advantage of the specific characteristics of SHG (instantaneous frequency doubling, exact light conversion and forward transmission) have been built and provide unprecedented contrast.[84,85] Recording post-synaptic potentials with high spatiotemporal resolution from multiple membranes in an *ex vivo* brain slice will require a concerted effort: Developments in microscopy that increase the signal per photon input and methods of scanning more quickly in three dimensions will be required. Methods of overcoming photodamage have been suggested,[14, 78] but are in need of further development. Dyes with stronger SHG, greater signal-to-noise and rapid response to changes in potential must be developed. Advances in laser technology will also progress this field, as lasers with higher repetition rates and narrower pulses generate higher SHG with less photodamage.

This will enable microscope users to limit photodamage more effectively, permitting longer experiments.

The engineering of new chromophores with high quadratic hyperpolarisability (and voltage sensitivity) can be approached from both computational and empirical perspectives. However, due to the large number of unpredictable factors when introducing dyes into a biological setting, calculated data on chromophores can only take us so far. Research groups with synthetic specialisation are needed to design and build new chromophores for testing, with properties such as biological solubility and toxicity in mind. Many new members [11, 13, 14, 63] have been added to the library of compounds that may be used for SHG imaging, but further development is required.

This thesis presents a number of tools for new neurophysiological interventions or experiments. Chapter 2 details our family of SHG contrast agents which outperform commercially available proves. Chapter 4 explores new approaches to optimising molecular probes by taking advantage of off-axis contributions to the molecular hyperpolarisability. The distribution of angles which dyes embedded in membranes occupy is covered from a biophysical perspective through the methodology described in Chapter 3, and the voltage sensitivity of our SHG contrast agents is demonstrated in Chapter 5. Finally, Chapter 6 presents a novel tool for the inhibition of ion channels which has now been made commercially available.

1.8 References

1. K. Koynov, S. Saltiel and I. Buchvarov, *J. Opt. Soc. Am. B.*, 1997, **14**, 834-838, K. A. Stankov, V. P. Tzolov and M. G. Mirkov, *Appl. Opt.*, 1992, **31**, 5003-5009
2. P. A. Franken, A. E. Hill, C. W. Peters and G. Weinreich, *Phys. Rev. Lett.*, 1961, **7**, 118, T. H. Maiman, *Nature*, 1960, **187**, 493-494.
3. A. E. Hill, *Personal Communication*, 2009,
4. R. Hellwarth and P. Christensen, *Opt. Commun.*, 1974, **12**, 318-322.
5. C. Sheppard, J. Gannaway, R. Kompfner and D. Walsh, *IEEE J. Quantum Elect.*, 1977, **13**, 912-912.
6. I. Freund, M. Deutsch and A. Sprecher, *Biophys. J.*, 1986, **50**, 693-712.
7. Y. Fu, H. Wang, R. Shi and J.-X. Cheng, *Biophys. J.*, 2007, **92**, 3251-3259; R. M. Williams, W. R. Zipfel and W. W. Webb, *Biophys. J.*, 2005, **88**, 1377-1386.
8. P. J. Campagnola and L. M. Loew, *Nat Biotech*, 2003, **21**, 1356-1360; P. J. Campagnola, M.-d. Wei, A. Lewis and L. M. Loew, *Biophys. J.*, 1999, **77**, 3341-3349.
9. D. A. Dombeck, L. Sacconi, M. Blanchard-Desce and W. W. Webb, *J. Neurophysiol.*, 2005, **94**, 3628-3636.
10. L. Sacconi, I. Tolic-Nørrelykke, M. D'Amico, F. Vanzi, M. Olivotto, R. Antolini and F. Pavone, *Cell Biochem. Biophys.*, 2006, **45**, 289-302.
11. C. Barsu, R. Cheaib, S. Chambert, Y. Queneau, O. Maury, D. Cottet, H. Wege, J. Douady, Y. Bretonniere and C. Andraud, *Org. Biomol. Chem.*, 2009, **8**, 142-150.
12. C. Barsu, R. Fortrie, K. Nowika, P. L. Baldeck, J.-C. Vial, A. Barsella, A. Fort, M. Hissler, Y. Bretonniere, O. Maury and C. Andraud, *Chem. Commun.*, 2006, 4744-4746.
13. E. De Meulenaere, I. Asselberghs, M. de Wergifosse, E. Botek, S. Spaepen, B. Champagne, J. Vanderleyden and K. Clays, *J. Mater. Chem.*, 2009, **19**, 7514-7519.
14. J. E. Reeve, H. A. Collins, K. D. Mey, M. M. Kohl, K. J. Thorley, O. Paulsen, K. Clays and H. L. Anderson, *J. Am. Chem. Soc.*, 2009, **131**, 2758-2759.
15. T. Z. Teisseyre, A. C. Millard, P. Yan, J. P. Wuskell, M.-d. Wei, A. Lewis and L. M. Loew, *J. Biomed. Opt.*, 2007, **12**, 044001.
16. R. D. A. Hudson, A. R. Manning, J. F. Gallagher, M. H. Garcia, N. Lopes, I. Asselberghs, R. V. Boxel, A. Persoons and A. J. Lough, *J. Organomet. Chem.*, 2002, **655**, 70-88; D. Gindre, I. Ka, A. Boeglin, A. Fort and K. D. Dorkenoo, *Appl. Phys. Lett.*, 2007, **90**, 094103-094103; G. Peleg, A. Lewis, O. Bouevitch, L. Loew, D. Parnas and M. Linial, *Bioimaging*, 1996, **4**, 215-224; N. Kato, K. Saito, H. Aida and Y. Uesu, *Chem. Phys. Lett.*, 1999, **312**, 115-120.
17. Y. Barad, H. Eisenberg, M. Horowitz and Y. Silberberg, *Appl. Phys. Lett.*, 1997, **70**, 922-924.
18. J. Squier, M. Muller, G. Brakenhoff and K. R. Wilson, *Opt. Express*, 1998, **3**, 315-324.
19. J.-x. Cheng, A. Volkmer, L. D. Book and X. S. Xie, *J. Phys. Chem. B*, 2001, **105**, 1277-1280.
20. M. D. Duncan, J. Reintjes and T. J. Manuccia, *Opt. Lett.*, 1982, **7**, 350-352.
21. A. Zumbusch, G. R. Holtom and X. S. Xie, *Phys. Rev. Lett.*, 1999, **82**, 4142.
22. C. L. Evans and X. S. Xie, *Annu. Rev. Anal. Chem.*, 2008, **1**, 883-909.
23. D. Oron, D. Yelin, E. Tal, S. Raz, R. Fachima and Y. Silberberg, *J. Struct. Biol.*, 2004, **147**, 3-11.
24. D. Debarre, W. Supatto, A.-M. Pena, A. Fabre, T. Tordjmann, L. Combettes, M.-C. Schanne-Klein and E. Beaurepaire, *Nat Meth*, 2006, **3**, 47-53.
25. W. Supatto, D. Débarre, B. Moulia, E. Brouzés, J.-L. Martin, E. Farge and E. Beaurepaire, *Proc. Natl. Acad. Sci. U. S. A.*, 2005, **102**, 1047-1052.
26. M. Wei, L. Sijia, R. H. Gary and X. S. Xie, *ChemPhysChem*, 2009, **10**, 344-347.

27. G. S. He, L.-S. Tan, Q. Zheng and P. N. Prasad, *Chem. Rev.*, 2008, **108**, 1245-1330; M. Pawlicki, H. A. Collins, R. G. Denning and H. L. Anderson, *Angew. Chem., Int. Ed.*, 2009, **48**, 3244-3266; W. R. Zipfel, R. M. Williams and W. W. Webb, *Nat Biotech*, 2003, **21**, 1369-1377; H. M. Kim and B. R. Cho, *Chem. Commun.*, 2009, 153-164.
28. J. L. Oudar and D. S. Chemla, *J. Chem. Phys.*, 1977, **66**, 2664-2668.
29. J. L. Oudar and H. Le Person, *Opt. Commun.*, 1975, **15**, 258-262.
30. M. G. Kuzyk, *Phys. Rev. Lett.*, 2000, **85**, 1218; M. G. Kuzyk, *J. Mater. Chem.*, 2009, **19**, 7444-7465.
31. X. Hu, D. Xiao, S. Keinan, I. Asselberghs, M. J. Therien, K. Clays, W. Yang and D. N. Beratan, *J. Phys. Chem. C*, 2010, **114**, 2349-2359; K. De Mey, J. Perez-Moreno, J. E. Reeve, I. Lopez-Duarte, H. L. Anderson and K. Clays, *J. Phys. Chem. C*, 2012, **116**, 13781-13787.
32. L. Moreaux, O. Sandre and J. Mertz, *J. Opt. Soc. Am. B*, 2000, **17**, 1685-1694.
33. K. Clays and A. Persoons, *Phys. Rev. Lett.*, 1991, **66**, 2980; K. Clays and A. Persoons, *Rev. Sci. Instrum.*, 1992, **63**, 3285-3289; K. Clays, A. Persoons and L. De Maeyer, *Adv. Chem. Phys.*, 1994, **85**, 455-498.
34. G. Olbrechts, R. Strobbe, K. Clays and A. Persoons, *Rev. Sci. Instrum.*, 1998, **69**, 2233-2241.
35. K. Wostyn, K. Binnemans, K. Clays and A. Persoons, *Rev. Sci. Instrum.*, 2001, **72**, 3215-3220.
36. B. F. Levine and C. G. Bethea, *J. Chem. Phys.*, 1975, **63**, 2666-2682; G. R. Meredith, *Rev. Sci. Instrum.*, 1982, **53**, 48-53; K. D. Singer and A. F. Garito, *J. Chem. Phys.*, 1981, **75**, 3572-3580.
37. G. Gonella, H.-L. Dai, H. C. Fry, M. J. Therien, V. Krishnan, A. Tronin and J. K. Blasie, *J. Am. Chem. Soc.*, 2010, **132**, 9693–9700.
38. L. Moreaux, O. Sandre, M. Blanchard-Desce and J. Mertz, *Opt. Lett.*, 2000, **25**, 320-322; V. Nikolenko, B. Nemet and R. Yuste, *Methods*, 2003, **30**, 3-15.
39. A. Grinvald, R. Hildesheim, I. C. Farber and L. Anglister, *Biophys. J.*, 1982, **39**, 301-308.
40. J. Jiang, K. B. Eisenthal and R. Yuste, *Biophys. J.*, 2007, **93**, L26-L28.
41. D. R. Kanis, M. A. Ratner and T. J. Marks, *Chem. Rev.*, 1994, **94**, 195-242; The first hyperpolarisability (β) is often expressed in electrostatic units (esu). 1 esu = 3.71×10^{-21} C m^3 V^{-2},
42. L. Moreaux, O. Sandre, S. Charpak, M. Blanchard-Desce and J. Mertz, *Biophys. J.*, 2001, **80**, 1568-1574.
43. Y. Wu, F. L. Yeh, F. Mao and E. R. Chapman, *Biophys. J.*, 2009, **97**, 101-109.
44. A. C. Millard, L. Jin, J. P. Wuskell, D. M. Boudreau, A. Lewis and L. M. Loew, *J. Membr. Biol.*, 2005, **208**, 103-111.
45. A. C. Millard, P. J. Campagnola, W. Mohler, A. Lewis, L. M. Loew, G. Marriott and I. Parker, *Second Harmonic Imaging Microscopy* in *Methods Enzymol.*, 2003, 47-69, Academic Press,
46. S. Tang, T. B. Krasieva, Z. Chen, G. Tempea and B. J. Tromberg, *J. Biomed. Opt.*, 2006, **11**, 020501-020503.
47. S.-W. Chu, T.-M. Liu, C.-K. Sun, C.-Y. Lin and H.-J. Tsai, *Opt. Express*, 2003, **11**, 933-938.
48. M. Blanchard-Desce, *C. R. Phys.*, 2002, **3**, 439-448; M. Blanchard-Desce, V. Alain, P. V. Bedworth, S. R. Marder, A. Fort, C. Runser, M. Barzoukas, S. Lebus and R. Wortmann, *Chem. - Eur. J.*, 1997, **3**, 1091-1104; S. Keinan, M. J. Therien, D. N. Beratan and W. Yang, *J. Phys. Chem. A*, 2008, **112**, 12203-12207.
49. R. D. A. Hudson, A. R. Manning, J. F. Gallagher, M.-H. Garcia, N. Lopes, I. Asselberghs, R. Van Boxel and A. Persoons, *Tetrahedron Lett.*, 2002, **43**, 8375-8378.
50. S. R. Marder, L.-T. Cheng, B. G. Tiemann, A. C. Friedli, M. Blanchard-Desce, J. W. Perry and J. Skindhøj, *Science*, 1994, **263**, 511-514.

51. J. S. Salafsky, *Chem. Phys. Lett.*, 2001, **342**, 485-491.
52. S. M. LeCours, H.-W. Guan, S. G. DiMagno, C. H. Wang and M. J. Therien, *J. Am. Chem. Soc.*, 1996, **118**, 1497-1503.
53. S. Priyadarshy, M. J. Therien and D. N. Beratan, *J. Am. Chem. Soc.*, 1996, **118**, 1504-1510.
54. T.-G. Zhang, Y. Zhao, I. Asselberghs, A. Persoons, K. Clays and M. J. Therien, *J. Am. Chem. Soc.*, 2005, **127**, 9710-9720.
55. V. Alain, S. Rédoglia, M. Blanchard-Desce, S. Lebus, K. Lukaszuk, R. Wortmann, U. Gubler, C. Bosshard and P. Günter, *Chem. Phys.*, 1999, **245**, 51-71.
56. O. Bouevitch, A. Lewis, I. Pinevsky, J. P. Wuskell and L. M. Loew, *Biophys. J.*, 1993, **65**, 672-679.
57. M. J. Therien, *Nature*, 2009, **458**, 716-717.
58. I. D. L. Albert, T. J. Marks and M. A. Ratner, *J. Am. Chem. Soc.*, 1998, **120**, 11174-11181.
59. S. R. Marder, D. N. Beratan and L. T. Cheng, *Science*, 1991, **252**, 103-106.
60. F. Meyers, S. R. Marder, B. M. Pierce and J. L. Bredas, *J. Am. Chem. Soc.*, 1994, **116**, 10703-10714.
61. S. R. Marder, C. B. Gorman, B. G. Tiemann and L. T. Cheng, *J. Am. Chem. Soc.*, 1993, **115**, 3006-3007.
62. L. Jin, A. C. Millard, J. P. Wuskell, H. A. Clark and L. M. Loew, *Biophys. J.*, 2005, **89**, L04-L06; L. Jin, A. C. Millard, J. P. Wuskell, X. Dong, D. Wu, H. A. Clark and L. M. Loew, *Biophys. J.*, 2006, **90**, 2563-2575.
63. P. Yan, A. C. Millard, M. Wei and L. M. Loew, *J. Am. Chem. Soc.*, 2006, **128**, 11030-11031.
64. G. Peleg, A. Lewis, M. Linial and L. M. Loew, *Proc. Natl. Acad. Sci. U. S. A.*, 1999, **96**, 6700-6704.
65. J. S. Salafsky, *Phys. Chem. Chem. Phys.*, 2007, **9**, 5704-5711.
66. A. C. Millard, L. Jin, A. Lewis and L. M. Loew, *Opt. Lett.*, 2003, **28**, 1221-1223.
67. J. Perez-Moreno, I. Asselberghs, K. Song, K. Clays, Y. Zhao, H. Nakanishi, S. Okada, K. Nogi, O.-K. Kim, J. Je, J. Matrai, M. De Maeyer and M. G. Kuzyk, *J. Chem. Phys.*, 2007, **126**, 074705.
68. B. J. Coe, J. A. Harris, J. J. Hall, B. S. Brunschwig, S.-T. Hung, W. Libaers, K. Clays, S. J. Coles, P. N. Horton, M. E. Light, M. B. Hursthouse, J. Garin and J. Orduna, *Chem. Mater.*, 2006, **18**, 5907-5918.
69. H. T. Uyeda, Y. Zhao, K. Wostyn, I. Asselberghs, K. Clays, A. Persoons and M. J. Therien, *J. Am. Chem. Soc.*, 2002, **124**, 13806-13813.
70. A. L. Obaid, L. M. Loew, J. P. Wuskell and B. M. Salzberg, *J. Neurosci. Methods*, 2004, **134**, 179-190.
71. E. Fluhler, V. G. Burnham and L. M. Loew, *Biochemistry*, 1985, **24**, 5749-5755.
72. J. Y. Huang and A. Lewis, *Biophys. J.*, 1989, **55**, 835-842.
73. A. C. Millard, L. Jin, M.-d. Wei, J. P. Wuskell, A. Lewis and L. M. Loew, *Biophys. J.*, 2004, **86**, 1169-1176.
74. M. Chalfie, *Angew. Chem., Int. Ed.*, 2009, **48**, 5603-5611; O. Shimomura, *Angew. Chem., Int. Ed.*, 2009, **48**, 5590-5602; R. Y. Tsien, *Angew. Chem., Int. Ed.*, 2009, **48**, 5612-5626.
75. I. Asselberghs, C. Flors, L. Ferrighi, E. Botek, B. t. Champagne, H. Mizuno, R. Ando, A. Miyawaki, J. Hofkens, M. Van der Auweraer and K. Clays, *J. Am. Chem. Soc.*, 2008, **130**, 15713-15719; A. Lewis, A. Khatchatouriants, M. Treinin, Z. Chen, G. Peleg, N. Friedman, O. Bouevitch, Z. Rothman, L. Loew and M. Sheres, *Chem. Phys.*, 1999, **245**, 133-144.
76. A. Khatchatouriants, A. Lewis, Z. Rothman, L. Loew and M. Treinin, *Biophys. J.*, 2000, **79**, 2345-2352.
77. S. J. Remington, R. M. Wachter, D. K. Yarbrough, B. Branchaud, D. C. Anderson, K. Kallio and K. A. Lukyanov, *Biochemistry*, 2004, **44**, 202-212.

78. L. Sacconi, D. A. Dombeck and W. W. Webb, *Proc. Natl. Acad. Sci. U. S. A.*, 2006, **103**, 3124-3129.
79. Oxyrase® is a commercial oxygen scavenging enzyme system.
80. E. Szajdzinska-Pietek and M. Wolszczak, *Chem. Phys. Lett.*, 1997, **270**, 527-532.
81. A. C. Millard, M. Terasaki and L. M. Loew, *Biophys. J.*, 2005, **88**, L46-L48.
82. I. Ben-Oren, G. Peleg, A. Lewis, B. Minke and L. Loew, *Biophys. J.*, 1996, **71**, 1616-1620.
83. D. A. Dombeck, M. Blanchard-Desce and W. W. Webb, *J. Neurosci.*, 2004, **24**, 999-1003.
84. L. Sacconi, J. Mapelli, D. Gandolfi, J. Lotti, R. P. O'Connor, E. D'Angelo and F. S. Pavone, *Opt. Express*, 2008, **16**, 14910-14921.
85. M. Kobayashi, K. Fujita, N. Osamu and S. Kawata, *Rev. Sci. Instrum.*, 2005, **76**, 073704.

Chapter 2

Porphyrins for Second Harmonic Generation Imaging

Summary

Amphiphilic donor-acceptor *meso*-ethynyl porphyrins* with polar pyridinium electron-acceptor head groups and hydrophobic dialkyl-aniline electron donor tail-groups have high molecular hyperpolarisabilities (as measured by hyper-Rayleigh scattering) and high affinities for biological membranes. We design this family of SHG chromophores to take advantage of the highly-polarisable porphyrin heterocycle, building on established guiding principles for the optimisation of nonlinear optical materials.

We investigate the electronic properties of this family through standard linear optical techniques and their NLO (nonlinear optical) properties through hyper-Raleigh scattering. When ordered within lipid membranes these dyes can be used for second harmonic generation (SHG) microscopy; a high intensity pulsed laser beam at 840 nm generates a strong frequency-doubled signal at 420 nm. We show that the solubility of the porphyrinic core can be controlled by the substitution of the central metal ion, or inclusion of solubilising triethylene-glycol chains. We measure the SHG generated by these dyes from droplet monolayer membranes, interpreting the intensity of SHG produced in terms of their molecular first hyperpolarisability and their number density within the membrane. Interestingly, the exctited state properties of these dyes may also be tuned: Copper(II) and nickel(II) porphyrin complexes give similar SHG signals to the free-base porphyrins, while exhibiting no detectable two-photon fluorescence (2PF).

*Part of the work in this chapter was published in: J. E. Reeve, H. A. Collins, K. D. Mey, M. M. Kohl, K. J. Thorley, O. Paulsen, K. Clays and H. L. Anderson, *J. Am. Chem. Soc.*, **2009**, 131, 2758-2759.
See also its feature in *Nature*, News and Views: M. J. Therien, *Nature*, **2009**, 458, 716-717.

2.1 Introduction

Functional imaging of the brain is an ongoing challenge that is garnering attention from many disciplines throughout the scientific community.[1-6] Recent advances in microscopy,[7-10] optics,[11, 12] biophysics,[13-16] chemistry[17-21] and neuropharmacology[22] are propelling us to a position where inter-neuron communication may be more fully understood.

Second harmonic generation (SHG) imaging is a promising technique for the imaging of the transmembrane potentials which drive neuron function.[13, 23-32] To produce signal from membranes, SHG contrast agents must have strong nonlinear optical (NLO) properties, especially a high first hyperpolarisability, β.

Voltage-sensitive styryl dyes FM4-64 (synthesised by Betz *et al.*),[33-35] RH237 (synthesised by Grinvald *et al.*)[36] and di-4-ANEPPS (developed by Loew, Lewis *et al.*)[13, 37] (Figure 1) have each been applied to SHG imaging. While they were not designed as SHG contrast agents, their donor-acceptor polyene chromophores and amphiphilic structures are sufficiently hyperpolarisable and ordered that they generate frequency-doubled light. Both di-4-ANEPPS and RH237 have been shown to be voltage sensitive[5, 36, 38] and Dombeck *et al*. have used FM4-64 to image action potentials in cultured Aplasia squid neurons with good spatial and temporal resolution.[25, 26] However, the use of these dyes to investigate real problems in neurophysiology is limited by poor signal-to-noise, requiring many repeats to obtain conclusive results.[25] Ideally, a probe would allow high signal-to-noise so that trial-by-trial recording could reveal the locus of action potentials in real time. These issues are discussed further in Chapter 5.

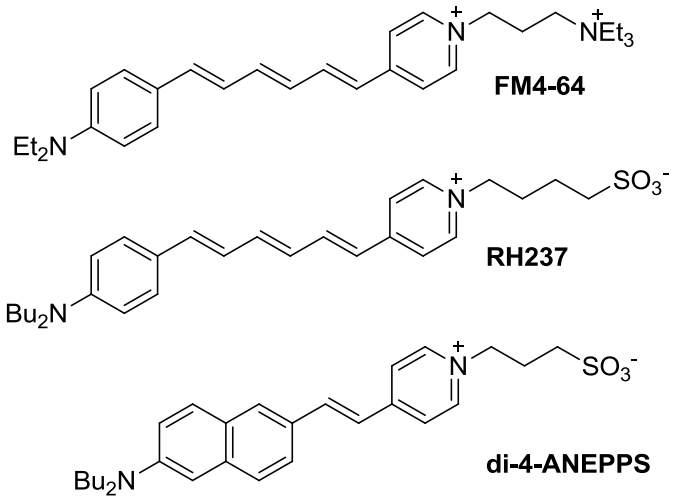

Figure 1 Styryl dyes FM4-64, RH237 and di-4-ANEPPS share the same aniline donor and pyridinium acceptor as our porphyrinic dye, however their first hyperpolarisability is significantly different due to the different π-delocalised bridge.

Amphiphilic donor-acceptor π-systems which incorporate an acetylenic porphyrin motif prove to be excellent SHG contrast agents.[20, 39-42] Our initial investigations revealed they possess molecular hyperpolarisabilities an order of magnitude greater than commercially available probes and proved that engineering of the chromophores can elicit modified photophysical behaviour and amphiphilic characteristics.[20, 21] We can further tune NLO properties through a number of molecular engineering approaches, changing the central metal, modifying the head-group or adding on water-solubilising chains. This chapter concentrates on the optimisation of a chromophore for structural imaging, whilst Chapter 5 investigates the suitability of these probes for functional, voltage-sensitive imaging.[20, 21, 30, 43-47]

Following their synthesis, we fully characterised our family of amphiphilic donor-acceptor porphyrins using a number of photophysical and biophysical methods. The linear optical properties of each dye were fully explored and assist our understanding of NLO trends. Hyper-Raleigh scattering (HRS) was then employed to gain a systematic understanding of how molecular engineering impacts quadratic hyperpolarizability.[48-52] The water-solubility of synthesised compounds showed a marked improvement on moving towards more ionic

head-groups and *meso*-aryl TEG substitution. Finally, each dye was tested for its ensemble second harmonic generating efficiency and root-mean-squared (RMS) tilt angle in membranes.[13, 53-56] We image a dye-doped monolayer of phospholipids which spontaneously encapsulate a droplet of water in oil. By fitting the angle-dependent SHG intensity around the droplet to an established model, we arrive at peak SHG powers which take into account the effect of molecular tilt.[56] We find that some dyes significantly outperform the commercially available styryl dyes, and carry them through to voltage sensitive imaging in Chapter 5.

2.2 Molecular Design

We design specialised SHG contrast agents for biological imaging by substituting the polyene of commercially available dyes (e.g. RH237 or FM4-64) for the highly polarisable acetylenic porphyrin motif. Porphyrin chromophores have been shown to have unprecedented molecular first hyperpolarisabilities, which may be attributed to a low energy first excited state, their ability to stabilise charge-separated states and their high oscillator strength. By adhering to the design principles that we set out in Chapter 1, we elaborate ethynyl porphyrin chromophores with a donor and acceptor, suitably balanced to endow optimum nonlinear optical properties.[20, 39-41, 57-59]

A quaternarised pyridine is a highly-electron deficient acceptor which, through its inherent charge, doubles as a highly polar moiety. Although not a universal head-group,[60] it is commonly used to drive amphiphilicity by imparting charge.[13, 19, 37] Similarly, aniline donors are electron rich, electrostatically neutral groups which possess two sites for alkylation, thus providing the fatty core of our molecule.

In this chapter, I document the design and synthesis of two families of amphiphilic SHG contrast agents: **1a-d.M** and **2a-d.M** (Figure 2). Firstly, we test our assumption that the porphyrinic unit flanked by a donor and acceptor grants high molecular β by HRS. To this

then-proven donor-acceptor amphiphilic porphyrin system, we make three simple modifications with the aim of establishing an optimised chromophore. We explore the role of *meso*-aryl triethylene glycol (TEG) chains in terms of water-solubility and intramembranous alignment as opposed to their *meso*-H analogues. Three different polar head-groups are also screened: (**b**) methylated, (**c**) zwitterionic and (**d**) doubly-charged pyridinium derivatives. Finally, we determine the role of metal ions in tuning hyperpolarisability, solubility and photostability.

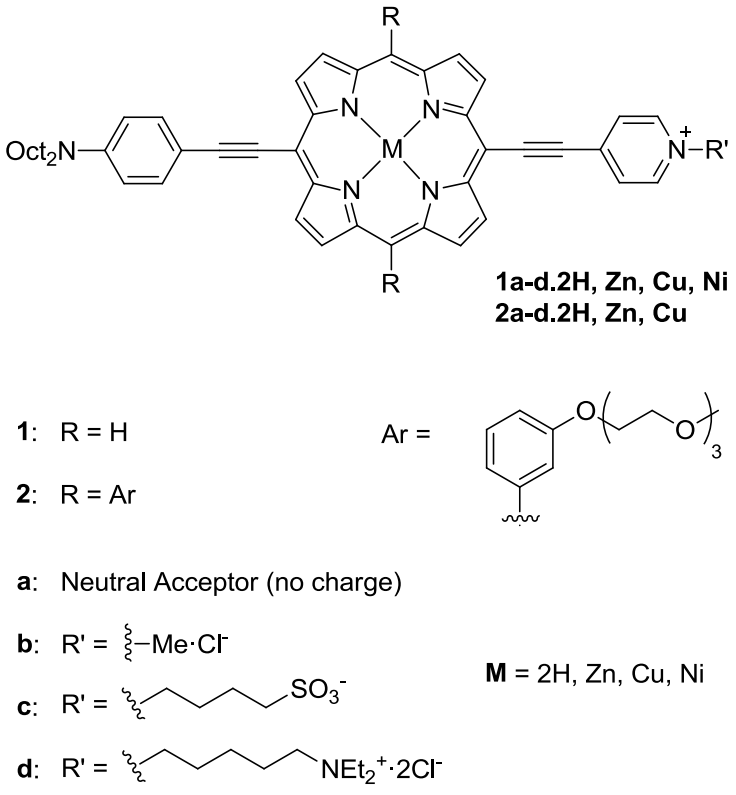

Figure 2 Porphyrinic dyes described in this chapter, which vary in terms of their *meso*-substitution (*number*), head-group (*letter*) and complexation state (*M*).

2.3 Synthesis

The set of compounds **1b-d.M** (M = Zn, 2H, Cu, Ni) and **2b-d.M** (M = Zn, 2H, Cu) were, in general, obtained from quaternarisation of key intermediate porphyrins **1a.M** and **2a.M** with the appropriate halogenated alkane or sultone derivative, respectively. This new family of amphiphilic charged porphyrins was characterised by NMR, mass spectrometry, UV-vis absorption and elemental analysis.

The preparation of compound **1a.M** is based on a convergent strategy which is derived from the common precursor compound **3**, featuring a bis-trihexylsilane-acetylene porphyrin core (see Scheme 1). Firstly, compound **3** was statistically deprotected using TBAF and the mono-deprotected porphyrin **4** was subjected to palladium-catalysed Sonogashira cross-coupling to 4-iodo-dioctylaninline followed by metallation with zinc acetate to give porphyrin **5**. Finally, compound **5** was subjected to *in situ* removal of the trihexylsilane protecting group followed by a second Sonogashira cross-coupling to 4-iodopyridine producing porphyrin **1a.Zn** in 80% yield after purification. Free-base porphyrin **1a.2H** is readily prepared in one step by demetallation of porphyrin **1a.Zn** in the presence of TFA in $CHCl_3$.

The analogous porphyrinic compounds **2b-d.M** (M = 2H, Zn, Cu), which posesses triethylene glycol substituted aryl rings at the *meso* position (rather than *meso*-H in the case of compounds **1b-d.M**) were synthesised from their parent diaryl compound (**6.M**). Bromination followed by Sonogashira cross-coupling with trihexylsilyl acetylene gave the diacetylenic intermediate **9**, which could then be subjected to the same routine of deprotection and coupling as analogous *meso*-H porphyrin **3**. Once this material was taken through to key intermediate **11**, a portion was passed on to Dr. Jan Fleischhauer for alternative quaternarisation experiments.

Simultaneously, Dr. Jan Fleischhauer designed and executed a parallel strategy, consisting of two consecutive palladium-catalysed Sonogashira couplings. His convergent approach involved coupling **7.Zn** with 4-ethynyl-substituted octylaniline or pyridine to yield key intermediate **11** before quaternarisation.

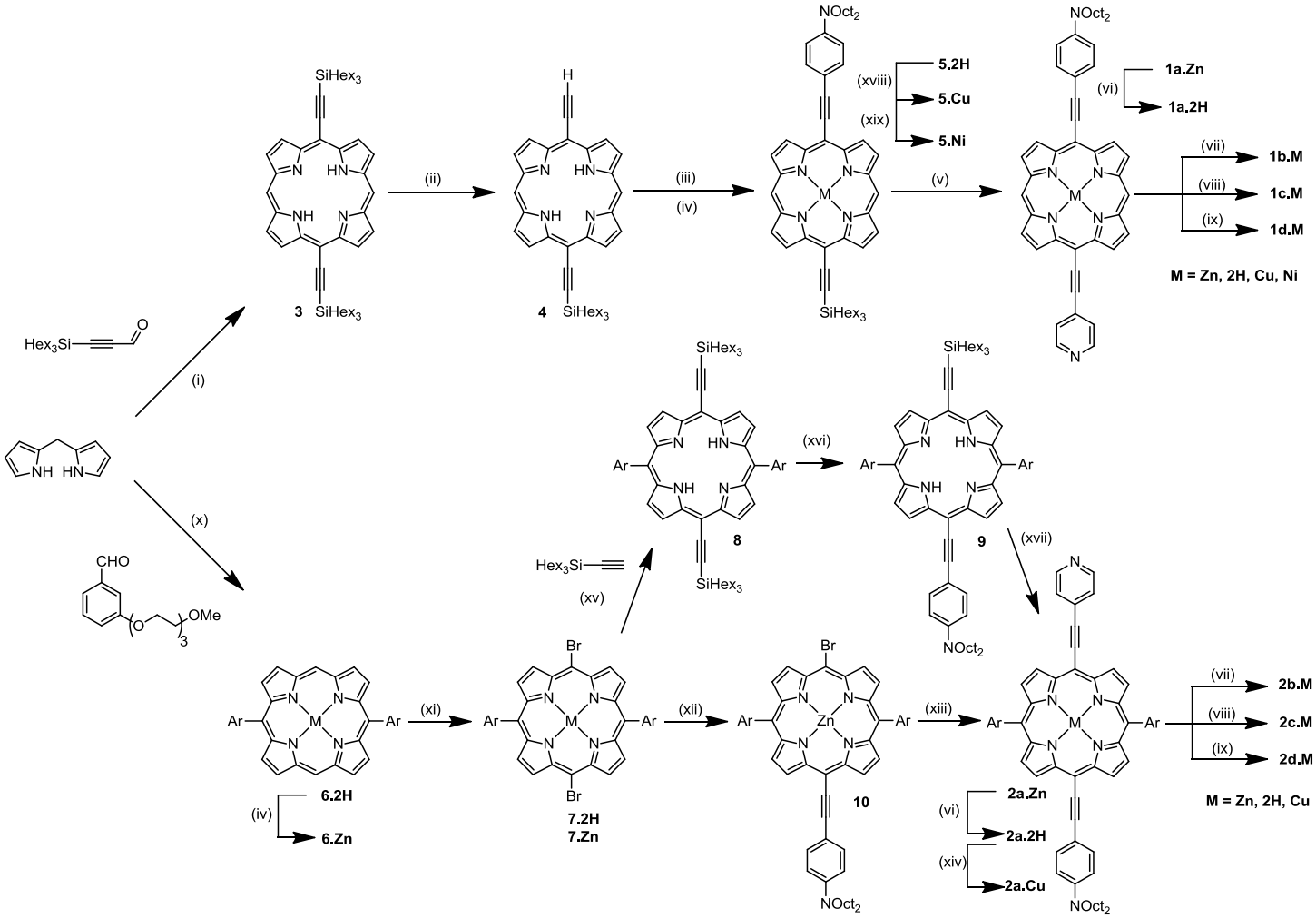

Scheme 1 Synthesis of porphyrins **1b-d.M** (M = Zn, 2H) and **2.b-dM** (M = Zn, 2H, Cu): (i) $BF_3{\cdot}OEt_2$, CH_2Cl_2 then DDQ; (ii) TBAF, $CHCl_3$; (iii) *N*,*N*-dioctyl-4-iodoaniline, $Pd_2(dba)_3$, CuI, PPh_3, PhMe, DIPA; (iv) $Zn(OAc)_2$, $CHCl_3$, MeOH; (v, via **5α.2H**) TBAF, 4-iodopyridine, $Pd_2(dba)_3$, CuI, PPh_3, PhMe, DIPA; (vi) TFA, $CHCl_3$; (vii) MeI, THF then dowex 1x8; (viii) 4-butane sultone, acetophenone; (ix) 5-iodo-*N*,*N*,*N*-triethylpentan-1-aminium, 2-pentanone; (x) TFA, CH_2Cl_2 then DDQ; (xi) NBS, $CHCl_3$, C_5H_5N; (xii) *N*,*N*-dioctyl-4-ethynylaniline, $Pd_2(dba)_3$, CuI, PPh_3, PhMe, DIPA; (xiii) 4-ethynylpyridine, $Pd_2(dba)_3$, CuI, PPh_3, PhMe, DIPA; (xiv) $Cu(OAc)_2$, $CHCl_3$, MeOH; (xv) $Pd_2(dba)_3$, CuI, PPh_3, Et_3N, PhMe; (xvi) TBAF, *N*,*N*-dioctyl-4-iodoaniline, $Pd_2(dba)_3$, CuI, PPh_3, Et_3N; (xvii) TBAF, 4-iodopyridine, $Pd_2(dba)_3$, CuI, PPh_3, Et_3N (xviii) $Cu(OAc)_2$, CH_2Cl_2, MeOH (xix) $Ni(OAc)_2$, DMF, reflux.

Quaternarisation presented a significant synthetic obstacle, imposing restrictions on the range of head-group that we could employ. A particularly challenging aspect was the quaternarisation of the zinc and copper derivatives: The free pyridine coordinates the zinc porphyrin center creating a strongly aggregating species. In these cases, combination with highly reactive methyl electrophiles (e.g. $Me_3O.BF_4$, MeOTf) would not proceed at elevated temperatures as the nucleophilicity of the lone pair is reduced by self-coordination. These zinc and copper derivatives, when not accessible through the route described in Scheme 1, were synthesised by either metal insertion to the quaternarised free-base, or by Sonogashira cross-coupling of **5** with pre-quaternarised 4-iodo *N*-methylpyridinium iodide (Scheme 2). This reaction proceeded quickly and has the additional benefit of fewer synthetic steps. While the reaction is hindered by poor solubility of the copper complexed porphyrin, the high reactivity of the extremely electron-poor pyridinium iodide to Sonogashira conditions ensured that enough product was formed for isolation and testing.

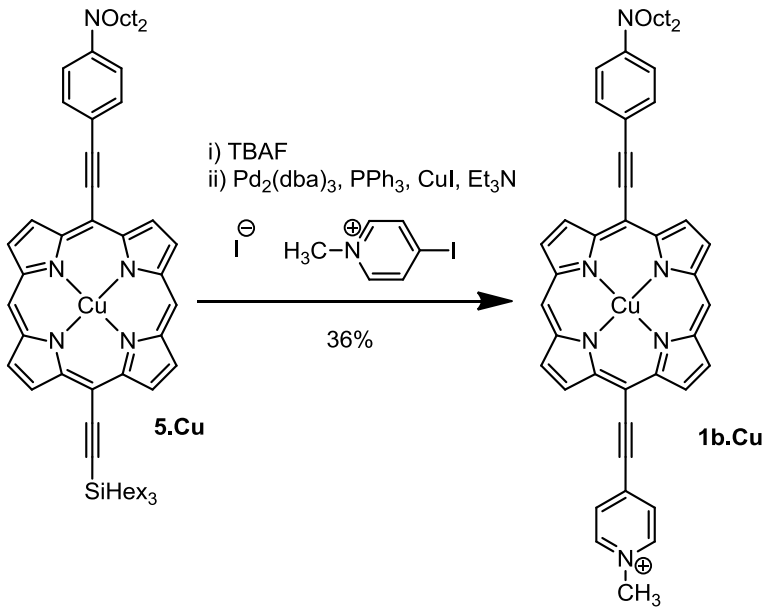

Scheme 2 Synthesis of **1b.Cu**, which is not possible via the route described for the free base or other metal complexes in Scheme 1, possibly due to aggregation, may be achieved by Sonagashira cross-coupling of **5.Cu** with 4-iodo *N*-methyl pyridinium iodide.

Following completion of the synthesis, all dyes were characterised, when soluble, the results of which are presented in Table 1, below, and are covered in more detail in the remainder of this chapter.

Table 1 Numbering scheme and photophysical data for all compounds in this Chapter.

R	R'	M	Compound	$\lambda_{max,\ abs}$ (nm)[a]	$\lambda_{max,\ em}$ (nm)[b]	Φ_f[c]	β_{zzz} (10^{-30} esu)[d]	Saturation Conc. (μM)[e]
H	None	2H	**1a.2H**	420	693	0.0063	2000	–[f]
H	Me	2H	**1b.2H**	437	684	0.0020	2500	7.1
H	Me	Zn	**1b.Zn**	452	676	0.0049	1630	48
H	Me	Ni	**1b.Ni**	433	–[g]	–[g]	650	–[f]
H	Me	Cu	**1b.Cu**	452	–[g]	–[g]	4000	–[f]
H	$(CH_2)_4SO_3^-$	2H	**1c.2H**	438	685	0.0076	2550	0.52
H	$(CH_2)_4SO_3^-$	Zn	**1c.Zn**	–[f]	674	0.0024	–[f]	0.55
H	$(CH_2)_5NEt_3^+$	2H	**1d.2H**	439	685	0.0030	1680	41
H	$(CH_2)_5NEt_3^+$	Zn	**1d.Zn**	–[f]	680	0.0058	–[f]	48
Ar	None	2H	**2a.2H**	431	674	0.0056	1240	0.21
Ar	Me	2H	**2b.2H**	446	704	0.0023	1800	18
Ar	Me	Cu	**2b.Cu**	448	682	0.00012	1040	39
Ar	Me	Zn	**2b.Zn**	–[h]	684	0.0097	1480	45
Ar	$(CH_2)_4SO_3^-$	2H	**2c.2H**	448	703	0.0024	1620	1.1
Ar	$(CH_2)_4SO_3^-$	Cu	**2c.Cu**	449	677	0.000076	730	0.035
Ar	$(CH_2)_4SO_3^-$	Zn	**2c.Zn**	–[h]	687	0.0098	1200	1.5
Ar	$(CH_2)_5NEt_3^+$	2H	**2d.2H**	447	707	0.0011	800	36
Ar	$(CH_2)_5NEt_3^+$	Cu	**2d.Cu**	449	680	0.00014	610	46
Ar	$(CH_2)_5NEt_3^+$	Zn	**2d.Zn**	461	691	0.0046	1210	37
N/A	N/A	N/A	FM4-64	562	752[i]	0.030	840	9.9
N/A	N/A	N/A	RH237	528[i]	782[i]	0.0057	–[h]	0.091
N/A	N/A	N/A	di-4-ANEPPS	497[i]	705[i]	0.042	–[h]	0.13

a) Soret (Q) band absorption maximum in *N*,*N*-dimethylformamide (see section 4.1) b) Emission maximum for lowest energy singlet emissive state. c) Fluorescence quantum yield in DMF measured relative to Zn(II) phthalocyanine in toluene (1% py), Φ_f = 0.3 (see section 4.1).[37] d) Principal component of βdirected along molecular *z*-axis, calculated from β_{HRS} at 840 nm (see section 4.2). e) Concentration of dye in pure water after 5 days (see section 5). f) Concentration too low to be accurately measured by UV-vis spectroscopy. g) No fluorescence could be detected. h) No data. i) Data from literature or supplier.

2.4 Optical Properties

2.4.1 Linear Optical Properties

The linear optical properties of a donor-acceptor ethynyl porphyrin can reveal aspects of their electronic structure. In this section, I examine the effect of three different polar head-groups, complexation of a divalent metal ion and elaboration of the chromophore with TEG-substituted aryl solubilising groups. Each of these modifications to the model chromophore alters the electronic properties of the molecule and their UV-vis absorption profiles. Furthermore, UV-vis spectra may be used through application of the Thomas-Kuhn sum rules to estimate both the magnitude and wavelength-dependence of nonlinear optical properties.[61]

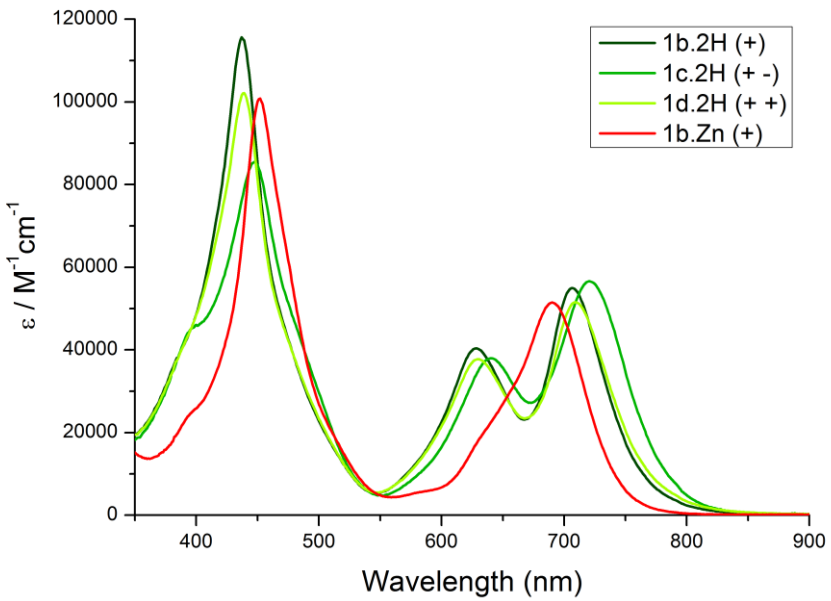

Figure 3 Comparative absorption spectra of three different polar head-groups, **1b.2H** (*dark green*) is methylated, **1c.2H** (*green*) carries a sulfonate, **1d.2H** (*light green*) bears a doubly-charged cholinic derivative. We observe that there is little change in electronic structure between the different head-groups. **1b.Zn** (*red*) is shown for comparison: whilst it is methylated like **1b.2H**, zinc complexation drastically alters its electronic properties.

In the absence of the additional solubility granted by TEG-substituted *meso*-aryl side groups we find that altering the head-group does have a small effect on the absorption properties of the

molecules. This is despite the fact that the choice of alkylation electrophile should not significantly perturb the molecule's electronic structure (Figure 3). Following comparison with the more soluble **2x.2H** and **2x.Cu** (**x** = **b**, **c**, **d**) series (where head-group substitution pattern does not affect the UV-vis spectra at all; Figure 4), we postulate that differences in aggregation state between **1b-d.2H** cause the difference in absorption spectra. This result is convenient from a molecular engineering standpoint, since it implies that we may choose from a wide range of head-groups whilst preserving the optical properties of the parent chromophore.

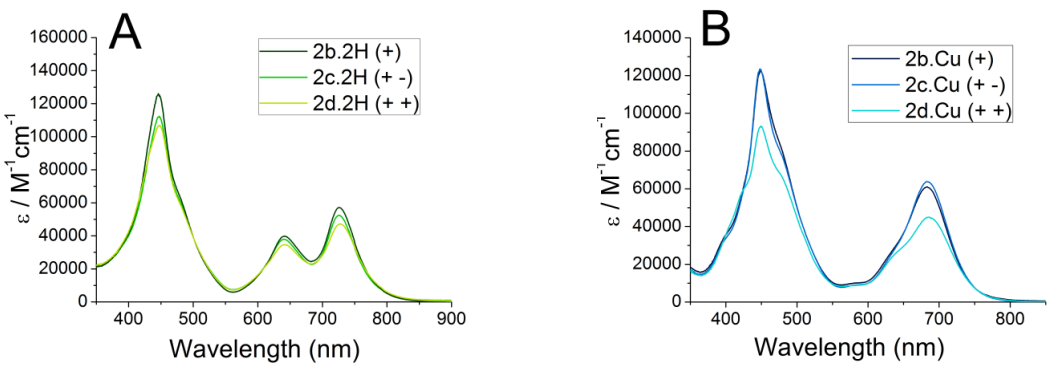

Figure 4 Absorption spectra of (A) *meso*-aryl free-base porphyrins and (B) *meso*-aryl copper porphyrins. This demonstrates that once solubilising TEG chains are included, the effect of varying the head-group is even further diminished and suggests that the effect of head-groups on UV-vis spectra seen for *meso*-H compounds **1b-d.2H** are a consequence of solubility differences.

The inclusion of zinc within the **1b.2H**, to yield **1b.Zn**, leads to significant peturbation of the UV-vis spectrum (Figure 3), specifically the coalescence of the Q-band due to the increase in symmetry on complexation (from C_s to C_{2v}). TEG-solubilised *meso*-aryl porphyrins exhibit a small red-shift over their *meso*-H counterparts. Whilst this modification to the porphyrin lies along the molecular *x*-axis, and should not significantly affect the most-important *z*-axis charge-transfer (CT) band, this perturbation of the π-electron system will have an effect on the porphyrin's NLO properties.

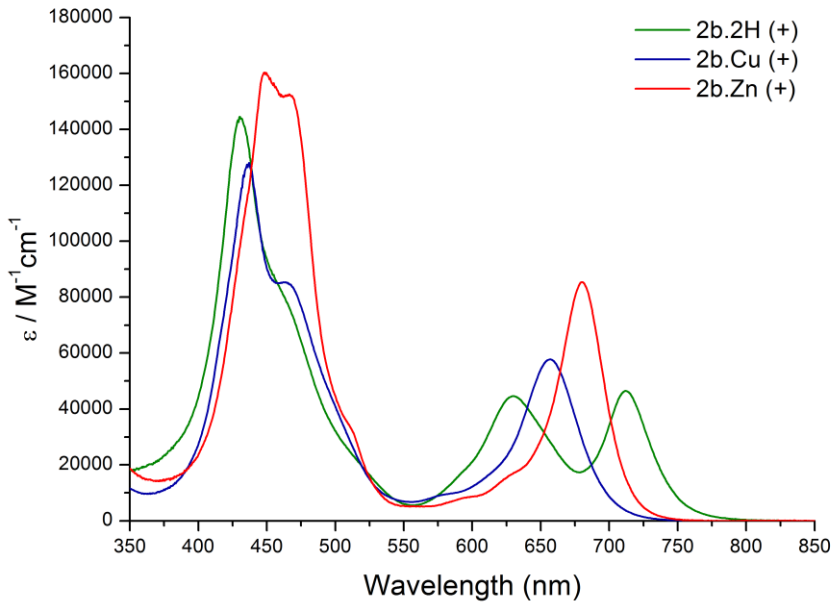

Figure 5 Comparative absorption spectra illustrating the effect of metal on the absorption characteristics of the **2b.M** family of compounds. The free-base (*green*) remains the most red-shifted, whilst inclusion of either copper (*blue*) or zinc (*red*) results in a blue-shift. The inclusion of a metal also results in consolidation of the two Q-bands of the free-base into a single Q-band.

The emissive properties of our family of compounds (Table 1) may be used to assign fluorescent signals in two-photon microscopy (2PM) as well as providing insight on their photophysics. Furthermore, we can tune the fate of some excited states of the chromophores, for example by complexation of a paramagnetic metal ion. 2PF may be expected in microscopy images of the free-base and zinc compounds, which have small but detectable quantum yields of fluorescence. Singlet excited states of copper(II) porphyrins, however, do not fluoresce strongly at room temperature which we attribute to a fast, nonradiative pathway involving the interaction of the porphyrin ring with the copper's d^9 (x^2 - y^2) electron. Intersystem crossing of the initially excited state to a ^2T state is followed by rapid spin-allowed relaxation to a $^2S_0$ ground state.[62]

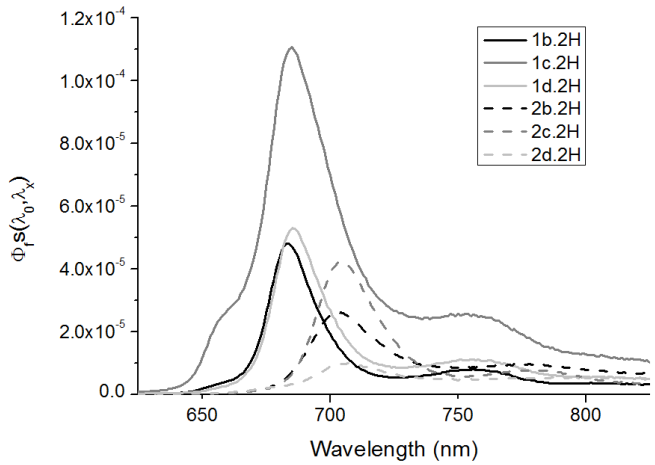

Figure 6 Fluorescence of free-base porphyrins in DMF showing little variation in the photophysical properties between head-groups. The *meso*-aryl TEG dyes (**2b-d.2H**) are red-shifted relative to their *meso*-H analogues (**1b-d.2H**).

Zwitterionic sulfonates (**c**) typically exhibit higher fluorescence quantum yields than their ionic counterparts (**b** or **d**), possibly due to the tight ion-pairing of **b** and **d** with a quenching chloride anion (Figure 6).[63, 64] Emission peak wavelengths allude to analogous trends observed in the absorption spectra. The emission of *meso*-aryl porphyrins is red-shifted (as is their absorption) due to increased conjugation between the porphyrin and its appended phenyl rings, a consequence of *meso*-Ar groups narrowing the HOMO-LUMO gap.

2.4.2 Nonlinear Optical Properties

The intensity of an SHG image is quadratically related to the molecular NLO response of the dye being imaged.[35, 65-68] A large first hyperpolarisability, β_{HRS}, dominated by β_{zzz} which is located along the molecular axis of the chromophore, is a crucial factor for a strong SHG image intensity. Hyper-Rayleigh scattering (HRS) is an incoherent second-order nonlinear scattering technique that gives a useful route to the measurement of β_{HRS} in solution without the need to order the chromophore.[30]

The molecular first hyperpolarisability, β_{HRS}, was determined by HRS measurements for compounds **1a-d.M** and **2a-d.M** in DMF solution. This work was performed at the Katholieke Universiteit Leuven in Leuven, Belgium by Dr. Ismael Lopez-Duarte and Dr. Javier Perez-Moreno as part of a collaboration with Dr. Koen Clays. HRS measurements used a femtosecond pulsed laser tuned to the IR range (most measurements are at 800 nm or 840 nm), which gives rise to a HRS signal when incident with a dilute solution of the chromophore; this can then be compared to a calibration curve of the HRS of crystal violet.

To be sure that there is no overestimation of the first hyperpolarisability due to time-delayed multiphoton fluorescence contributions, the first hyperpolarisability (β_{HRS}) was measured at different demodulation frequencies.[69] If no multiphoton fluorescence contributes to the HRS signal, then no demodulation is observed for successively higher amplitude-modulation frequencies. We have added confidence that the measurements are not convolved with fluorescence since SHG is easily distinguishable from 2PF in these compounds because the wavelength of SHG (e.g. 420 nm for measurement at 840 nm) is much shorter than fluorescence at 650–800 nm (Figure 6). For all measured compounds, a reliable value of β_{HRS} (fluorescence-free) was obtained by averaging the values at the fluorescence-free demodulation frequencies (Figure 7).

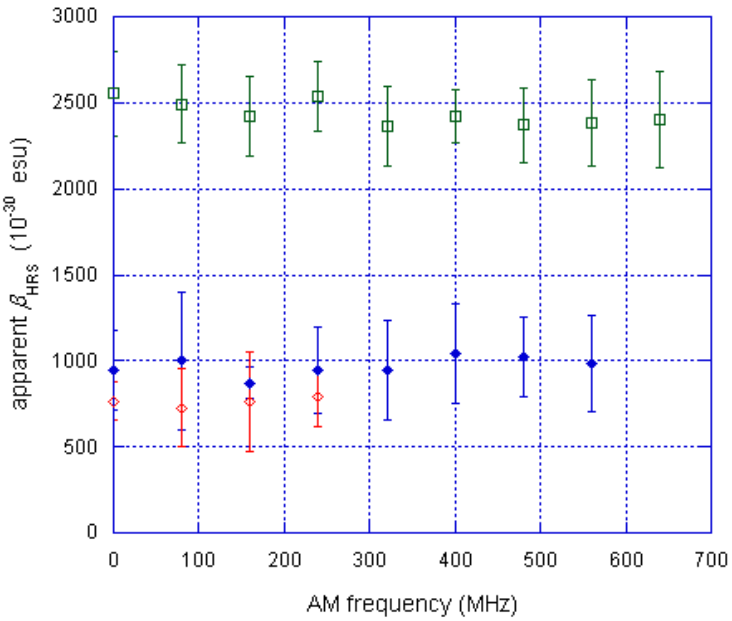

Figure 7 Apparent hyperpolarisability β_{HRS} as a function of amplitude modulation frequency for HRS measurement at 800 nm (*blue solid diamonds*); 840 nm (*green squares*) and 1300 nm (*red open diamonds*) for porphyrin **1a.2H** in $CHCl_3$. Varying the AM frequency gives no change in apparent β_{HRS}, signifying that the signal is not convoluted with (relatively) slow two-photon fluorescence.

In nearly all cases (excluding some of the blue-shifted nickel or copper derivatives), our amphiphilic porphyrins have larger β_{HRS} than commercially available styryl chromophores. This is a reflection of the greater oscillator strength, narrower HOMO-LUMO gap and the particular positioning of the porphyrin B-band in resonance with the HRS fundamental (e.g. 800 nm).[52]

Table 2 displays the values of β_{HRS}, its dominant contribution, β_{zzz}, and the wavelength of maximum absorption for the family of compounds **1a-d.M** and **2a-d.M**. An important factor controlling the magnitude of the dynamic hyperpolarisability in push-pull porphyrin-based chromophores has been shown to be the degree of B-state resonance enhancement (governed by equation 1).

$$\beta \propto \frac{\omega_{ge}^4}{\left(\omega_{ge}^2 - \omega^2\right)\left(\omega_{ge}^2 - 4\omega^2\right)} \qquad \text{(Eq. 1)}$$

Where $h\omega_{ge}$ is the energy difference between the ground and excited CT state and ω is the energy of the driving field. For these compounds, this value is largely determined by the proximity of the B-band λ_{max} value to the second harmonic wavelength of 400 nm, which is in resonance when performing experiments at 800 nm (Figure 8).[70] Since the position of the B-band maximum is sensitive to both the complexed metal and, to a lesser extent the inclusion of *meso*-aryl substituents, small structural modifications have a pronounced effect on measured dynamic first hyperpolarisability.

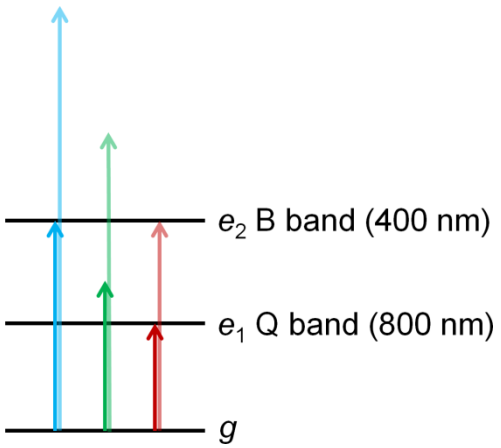

Figure 8 Energy level diagram of the ground state and the simplified electronic structure of a typical porphyrin system. Three conditions of SHG resonance are shown, (blue) resonance of the driving field (solid arrow) with one band, the B band produces a maxima in equation 1 which leads to a strong SHG response. If neither the driving wavelength nor *double* the driving wavelength (pale arrows) are in resonance with a band, then only the static portion of the hyperpolarizability contributed towards any SHG (green). If both the driving force and double the driving force are in resonance (red), the case at 800 nm with many donor-acceptor porphyrins, an even stronger maxima is expected.

As we have seen, the introduction of aryl *meso*-substituents in the porphyrin core produced a small but consistent red-shift in both B- and Q-bands, thus leading to a lower resonant enhancement from the B-band transition which shifts out of resonance. Compounds **1a.2H** (β_{zzz} = 2000 × 10^{-30} esu, λ_{max} = 420 nm) versus **2a.2H** (β_{zzz} = 1240 × 10^{-30} esu, λ_{max} = 431 nm) or **1b.2H** (β_{zzz} = 2500 × 10^{-30} esu, λ_{max} = 437 nm) versus **2b.2H** (β_{zzz} = 1800 × 10^{-30} esu, λ_{max} = 446 nm) follow this trend, with *meso*-Ar porphyrins showing diminished NLO properties.

Upon alkylation, we move from **1a.2H** (β_{zzz} = 2000 × 10^{-30} esu) to **1b.2H** (β_{zzz} = 2500 × 10^{-30} esu) and **1c.2H** (β_{zzz} = 2500 × 10^{-30} esu), finding that the pyridinium acceptor head-group leads to a larger first hyperpolarisability than a pyridine. This trend is rationalised in terms of the pyridinium's increased electronic acceptor strength over the uncharged pyridine. Unexpectedly, **1d.2H** shows lower HRS response than both **1b.2H** and **1c.2H,** a result that is not accounted for in our current structure-function models. As expected, the hyperpolarisability decrease upon metallation of the macrocycle reflects the decrease in oscillator strength, increase in HOMO-LUMO gap and a shift away from resonance.

Table 2 Linear and Nonlinear Optical Data for Porphyrin Chromophores **1a-d.M** and **2a-d.M** at 800 nm in DMF

Compound	$\lambda_{max,\ abs}$ (nm)	β_{HRS} (10^{-30} esu)	β_{zzz} (10^{-30} esu)
1a.2H	420	828.65 ± 0.03	2000 ± 300
1b.2H	437	1040.02 ± 0.03	2500 ± 400
1b.Zn	452	674.31 ± 0.03	163 ± 240
1b.Ni	433	270 ± 10	650 ± 25
1b.Cu	452	1650 ± 50	4000 ± 100
1c.2H	438	1056.86 ± 0.03	2550 ± 400
1c.Zn	–[a]	–[a]	–[a]
1d.2H	439	696.65 ± 0.03	1680 ± 250
1d.Zn	–[a]	–[a]	–[a]
2a.2H	431	513.51 ± 0.04	1240 ± 200
2b.2H	446	733.29 ± 0.03	1800 ± 250
2b.Cu	448	430 ± 15	1040 ± 30
2b.Zn	–[b]	610 ± 20	1480 ± 45
2c.2H	448	670.77 ± 0.03	1600 ± 250
2c.Cu	449	300 ± 15	730 ± 20
2c.Zn	–[b]	500 ± 15	1200 ± 35
2d.2H	447	333.32 ± 0.06	800 ± 120
2d.Cu	449	253.95 ± 0.06	610 ± 90
2d.Zn	461	500.89 ± 0.05	1210 ± 180
FM4-64	562	350 ± 10	840 ± 25

a) Saturation concentration too low to be accurately measured by UV-vis spectroscopy. b) No data.

No 2PF was observed at any of the second-harmonic wavelengths in any of these experiments, (indeed, emission only extends to $\lambda > 640$ nm) as evidenced by a constant value for the hyperpolarisability for increasing AM frequencies. This result allows simultaneous stimulation of both SHG and 2PF with the same laser wavelength which may then be separated with appropriate filters in the detection channels (e.g. a 400 nm notch filter for SHG stimulated at 800 nm and a 600 – 700 nm bandpass filter for 2PF).[20]

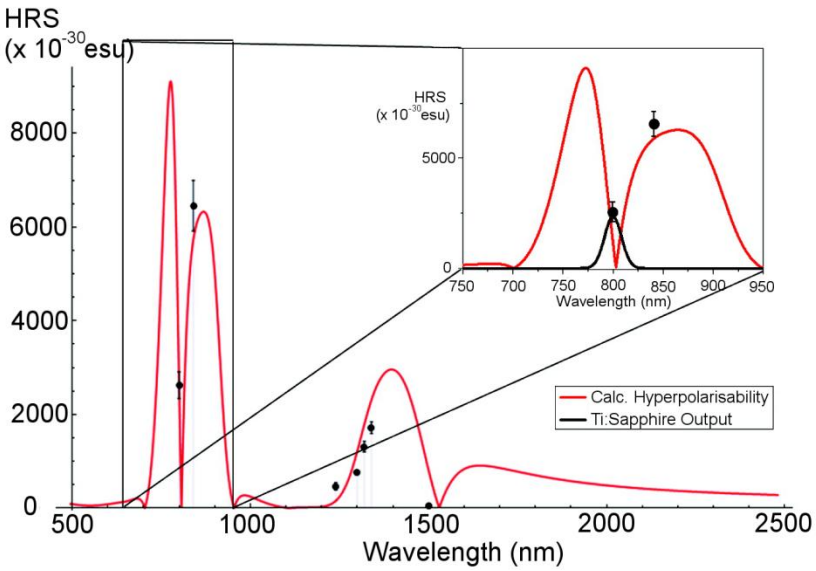

Figure 9 The calculated first hyperpolarisability spectrum derived from the absorption spectrum of porphyrinic dye **1b.2H** (red line) with wavelength-dependent experimental values of the first hyperpolarisability (black circles). These calculations reveal wavelength-dependent SHG will be a product of the wavelength-dependent hyperpolarisability and the uncertainty-broadened Ti:Sapphire laser output (black line). Reprinted with permission from K. De Mey, *et al*., *The Journal of Physical Chemistry C*, 2012, **116**, 13781-13787. Copyright (2012) American Chemical Society.

We may also simulate a wavelength-dependent β-spectrum from the linear absorption spectrum of **1b.2H** (Figure 3) through application of the Thomas-Kuhn sum rules and comparison of the calculated fit to experimental data points (Figure 9).[61] This technique holds promise for the prediction of β-spectra without the need to perform HRS, and may even be used as a predictive tool for NLO properties. There is also interest in the group in applying the same methodology to the extraction of the wavelength-dependent voltage-sensitivity, a metric which could be used to select the best wavelength to perform SHG imaging.

In conclusion, the NLO attributes lend this series of amphiphilic push-pull porphyrins to SHG imaging microscopy with laser excitation at 800–840 nm. We also expect the free-base and zinc complexes to be suitable for 2PF imaging. The remaining factors which will determine the success of these dyes as SHG contrast agents are their supermolecular partitioning behaviour in membranes and water-solubility, which is tested in the following sections.

2.5 Water-Solubility

Inclusion of *meso*-aryl triethylene glycol solubilising groups was designed to increase the dyes' water-solubility for patch clamping applications (where a solution is required to pass through a 1 μm aperture, so that traces of precipitate can be particularly problematic).[71, 72] We quantified the difference in water-solubility between *meso*-aryl and *meso*-H porphyrin dyes by finding their saturation concentrations in water. Each dye was formulated as a 10 mM stock in DMSO which was diluted 100 times with water to mimic the preparation of a solution for neuronal imaging. Following sonication and upon standing for 120 hours, the solutions were filtered through a 200 nm nylon membrane and the saturation concentration of the resulting solution was determined through UV-vis absorption spectroscopy (Figure 10).

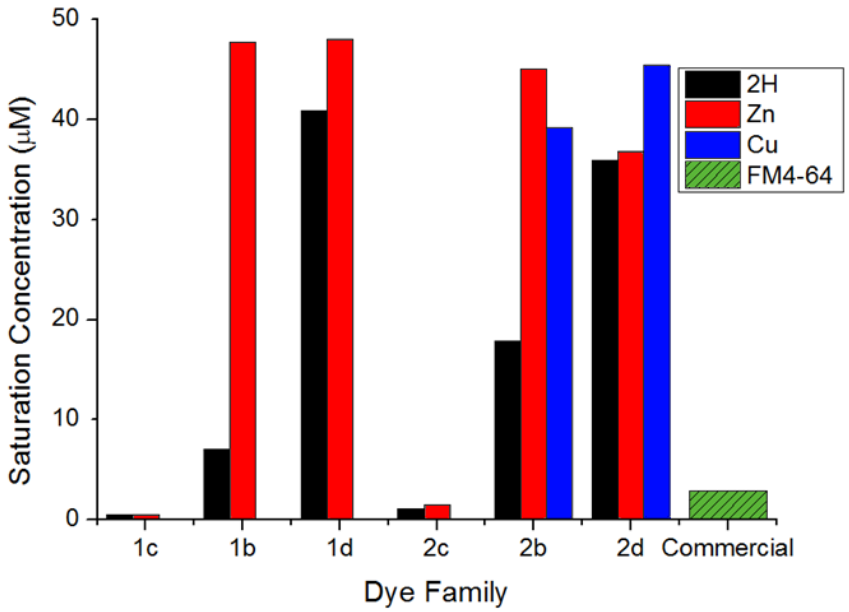

Figure 10 Solubility of porphyrinic dyes **1b-d.M** and **2b-d.M** and commercially available dye FM4-64 at equilibrium saturation concentration after 120 hours.

Zwitterionic dyes have the poorest solubility in water, a consequence of lacking an overall charge. We also find that the singly- and doubly-charged dyes have good water-solubility, with little difference between them in terms of saturation concentration. Our inclusion of *meso*-aryl triethylene glycol chains has augmented the solubility, doubling the saturation concentration for some dye classes (e.g. **1b.2H→2b.2H** and **1c.Zn→2c.Zn**). However, inclusion of these chains does not adequately solubilise the dyes with zwitterionic sulfonate head-groups. The central metal ion can also be used to augment water-solubility, though only in the absence of other dominating factors (such as the head-group). For example, different metals have little effect on the more soluble **2d** type compounds, whereas the poorly solubilised **2b** class are significantly more soluble when zinc(II) is complexed. It is possible that coordinating ligands in the metal complexes prevent molecular aggregation into micelles or large hydrophobic aggregates.

We measured the solubility of three commercially available dyes and found that in most cases, our dyes outperform even the most soluble styryl dye: FM4-64. Sulfonate derivatives RH237 and di-4-ANEPPS are all but insoluble, even as metastable solutions while FM4-64 is comparable to our dyes as a metastable solution, but is essentially sparingly soluble at equilibrium. Normally, these commercially available dyes are prepared as formulations with agents such as Pluronic F127 or polysorbate 20.[26]

2.6 Imaging in Membranes

Each of the synthesised dyes was progressively investigated through a number of model membrane systems. Advancement through these membrane models represents a transition from a very general but biologically remote membrane model to the specific case of staining neurons within an intact brain slice, the precise and final mode of their application. The most general system, droplet monolayers on the surface of water in oil, provides an interface at which dyes may orient and as such is suitable for observing SHG from a wide variety of chromophores: Including those dyes which may not otherwise produce SHG in bilayer membranes. Model membranes with increasing biological relevance also have lower tolerances to phototoxicity or low amphiphilicity. Biological intricacies also offer myriad complications that may cause absence of signal from a dye which was otherwise thought to be an excellent SHG harmonogen.[73] Additionally, biological imaging is more time intensive, less reproducible and more mechanically sensitive than simple biophysical models (such as the droplet monolayer), therefore I select dyes for biological imaging based on careful consideration of their photophysical, biophysical and solubility characteristics.

The second harmonic generation output of a dye aligned in a membrane is influenced by several biophysical factors in addition to its hyperpolarisability. As has been discussed previously, the SHG from an ensemble of dyes is also dependent on their density and

alignment at an interface. By generating SHG at the water-oil interface we can characterise our dyes in terms of the bulk hyperpolarisability and therefore intensity of SHG that they are capable of generating as an ensemble. We can simplify contributions of molecules to the ensemble hyperpolarisability by making a number of assumptions. We expect that chromophores are highly ordered in a membrane and that they do not interact physically yet scatter coherently in the focal volume of the laser. Molecular hyperpolarisabilities are assumed to lie along a well-defined molecular axis that is predominantly directed normal to the plane of the membrane. We therefore arrive at equation 2, the relation for SHG intensity, P_{SHG},

$$\boldsymbol{P_{SHG} \propto \Theta_2 I^2 \beta^2 N^2 F(\theta, \varphi)} \qquad \text{(Eq. 2)}$$

where Θ, and I (phase coherence over the focal volume and laser intensity respectively) are terms which relate only to the experimental set-up in use. $\boldsymbol{F(\theta, \varphi)}$ accounts for the angular displacement between the excitation beam and the ensemble of chromophores. The first hyperpolarisability, β, is a molecular quantity that is known for each molecule under investigation, and so can be factored in at will. We may therefore interpret results from our surface monolayer technique as giving information on two molecular quantities: the number density, N, and the root mean square tilt angle of the ensemble of dyes away from the membrane normal, φ.

2.6.1 Droplet Imaging

A small droplet (⌀ = 50 μm) of water introduced into a bath of lipid–such as 1,2-diphytanoyl-sn-glycero-3-phosphocholine (DPhPC) or 1-palmitoyl-2-oleoyl-sn-glycero-3-

phosphocholine (POPC)–in oil is rapidly encapsulated by a self-assembled monolayer.[56] This lipid-coated phase boundary allows the incorporation of amphiphilic dyes, simulating a cellular bilayer. The SHG from these dyes is most easily probed by confocal scanning multiphoton microscopy, and the circular image obtained may be used to extract the SHG power and its angular intensity variation relative to the laser polarisation (Figure 11). Since the form of $\boldsymbol{F}(\boldsymbol{\theta},\boldsymbol{\varphi})$ is highly dependent on how a dye is aligned within membranes, it is possible to predict the distribution of tilt angles from an image of this kind. Furthermore, as tilt angle increases, the power of SHG radiated decreases; therefore we must take this $\boldsymbol{F}(\boldsymbol{\theta},\boldsymbol{\varphi})$ into account to find the total SHG power from the tilt-attenuated SHG power.

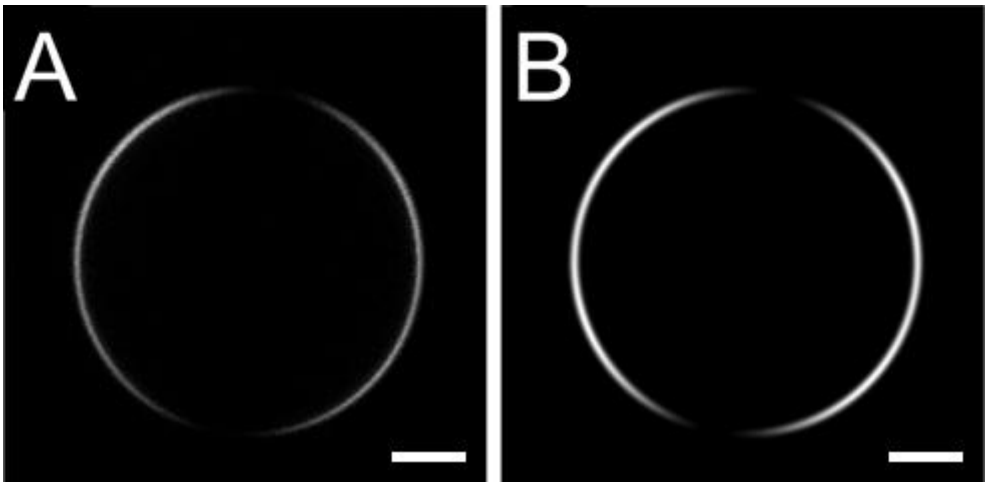

Figure 11 (A) SHG image of di-4-ANEPPS absorbed into a droplet monolayer of DPhPC on the surface of a water droplet in oil and (B) Modelled SHG power which takes the molecular tilt, and angular displacement away from polarisation into account. Scale bar 10 μm. For further information, see Chapter 3.

The advantage of this technique is its generality: it can be used for any amphiphilic molecule (whereas LB films must be grown, and Therien's surface-bound α-helix bundles[57, 74] require a metal with a vacant coordination site). Consequently, we are able to probe the SHG generated by each of our dyes, taking into account tilt angle in the membrane and compare those values to commercially available compounds.

SHG losses due to the optical set-up (e.g. SHG which falls outside of the collection optics or attenuation of laser strength by the curvature of the phase boundary) are independent of the compound tested. Therefore, while this technique does not collect all SHG produced, nor ensure optimum conditions for generation, it is useful for benchmarking SHG from an ensemble of dyes.

SHG intensities were recorded from most synthesised dyes as well as commercially available dyes FM4-64, di-4-ANEPPS and RH237. Dyes which could not be satisfactorily dissolved in the oil phase or incorporated within a lipid gel were not imaged. Nearly all porphryrinic dyes were superior SH generators than the commercially available compounds, the strongest (**2b.2H**) having SHG 20 times stronger than RH237. The trend in SHG does not mirror the trend in β_{zzz}, which confirms that the amphiphilic structure of the dyes and their incorporation into membranes is as important as their NLO properties (Table 3).

Table 3 Molecular first hyperpolarisabilities, β and SHG intensity (P_{SHG}) recorded during microscopy of each dye adsorped into a surface monolayer of DPhPC at the interface between a water droplet in oil. Tilt-attenuation is accounted for, and pertinent results are depicted graphically in Figure 12.

Compound	β_{zzz} (10^{-30} esu)	P_{SHG}[a], (counts)
1b.2H	2500	283
1b.Zn	1630	38
1d.2H	1680	589
2b.2H	1800	504
2b.Cu	1800	104
2c.2H	1600	774
2c.Cu	–[b]	119
2d.Cu	610	274
2d.Zn	1210	74

[a]Extracted from polar fits performed on at least six images of water droplets in oil under identical microscopy conditions [b]No data

The SHG intensity from an ensemble of free-base porphyrin dyes is consistently stronger than from their metalloporphyrin analogues. In the case of family **2**, free-base porphyrins generate five to eight times more SHG signal than their copper(II) counterparts. **1b.2H** generates SHG nine times more effectively than **1b.Zn**. While the β_{HRS} found for metalloporphyrins is consistently lower than free-base porphyrins, the variation in SHG cannot be accounted for solely by this difference. We may therefore infer that this discrepancy in SHG is due to higher number density of free-base porphyrins. We observe in Figure 12 that Zn complexes are typically the worst SH generators as an ensemble system. Consequently, we should avoid the design of SHG dyes based on a (porphyrinato) zinc(II) moiety.

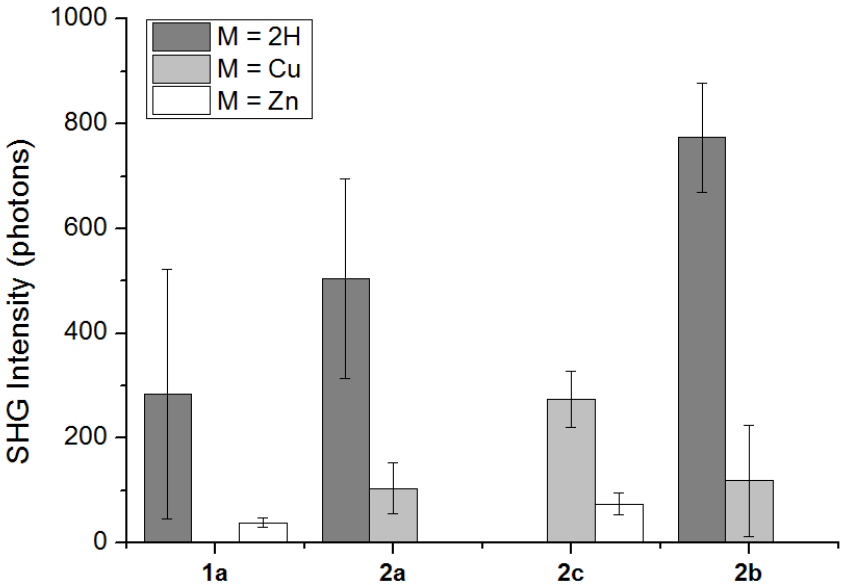

Figure 12 SH generated by different dyes in the droplet monolayer system, after accounting for tilt-attenuation of SHG. There is a strong trend demonstrating that ensemble SHG is greater from free-base porphyrins (M = 2H) rather than from metalloporphyrins (M = Cu, Zn). This could be due to disparities in the number density of packing, the RMS tilt angle or reduced dispersion factors for metalloporphyrins.

The role of the head-group in determining the membrane-affinity of a dye is significantly less important than the central metal ion (Figure 13). Generally, head-groups with a greater local charge (in the order **b** < **c** < **d**) are marginally better second harmonic generators. The doubly charged '**d**' class of compounds have the greatest SHG from membranes. From these two sets of graphs, we can also see that in general, *meso*-aryl compounds tend to perform slightly better in terms of the SHG generated than their *meso*-H counterparts. Since *meso*-H porphyrins typically have higher β values due to increased resonance enhancement at imaging wavelengths, this difference is attributable to either an increased number density, or to better alignment in the membrane.

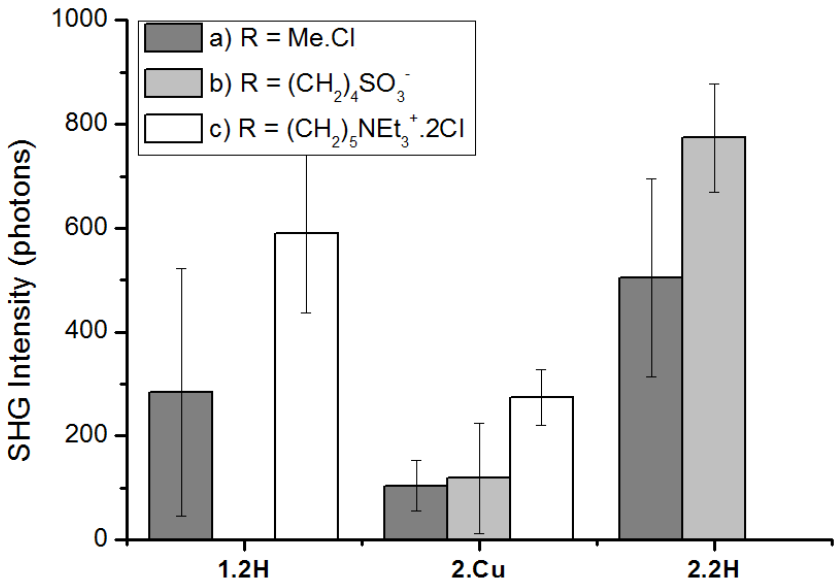

Figure 13 Graph demonstrating SHG from various head-groups, greater SHG is observed from head-groups with a greater charge.

2.6.2 *In Vitro* Cell Imaging

Given the excellent performance and aqueous solubility of **1d.2H**, we carried it through to *in vitro* testing, with the aim of imaging the plasma membranes of cultured cells. Proof-of-principle SHG images of **1d.2H** incorporated within the cellular membrane of SK-OV-3 cells were obtained via SHG microscopy, which was performed jointly with Dr. H. A. Collins. A portion of **1d.2H** from a 5 mM DMSO stock solution was added to the bath to make the concentration up to 10 μM, then the dish was incubated for one minute. SHG images were obtained with 20 mW power at 840 nm using 100 fs pulses at 80 Hz. Simultaneous wide-field images confirmed that the bulk of the signal arrives from the plasma membrane (Figure 14).[20]

This simple demonstration gave us the confidence that these SHG probes had the ability to stain plasma biomembranes as well as the model membranes that we discuss earlier in this chapter. Armed with this new insight, we were able to move the dye into a more sensitive but relevant cell line: *in vitro* neuronal cultures.

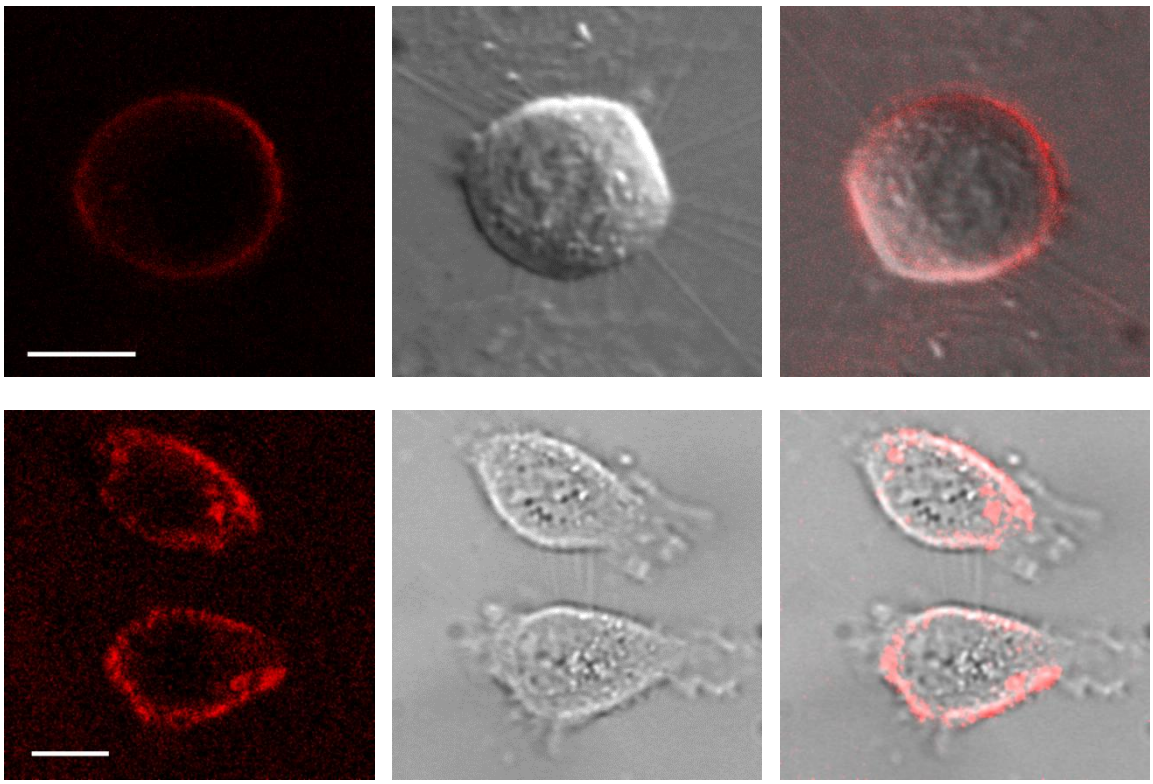

Figure 14 *In vitro* second harmonic generation imaging of porphyrin **1d.2H** in SK-OV-3 cells; SHG images (left), transmission images (centre) and the overlaid images (right), scale bar: 10 μm. The cells were seeded in 2-well coverslide chambers (Nunc) at a density of 105 cells per well in 2 mL of culture media (DMEM, Gibco). After 24 h the media on the cells was replaced with a 10 μM solution of porphyrin **1d.2H**, diluted from a 1 mM stock in DMSO. After 10 min incubation at 37 °C, the cells were washed and placed in CO_2 independent media (Gibco) and immediately imaged.

2.6.3 SHG Imaging of cultured neurons

The natural progression from SHG imaging in the cultured SK-OV-3 cell line is towards cultured primary neurons. Whilst the difference in the plasma membrane between SK-OV-3

and primary neurons is small, the demonstration that SHG may be generated from neuronal membranes is an important step towards voltage-sensitive imaging of action potentials in these membranes. Once a neuron is stained, the only advance required is attachment of an electrophysiological patch, allowing trial-by-trial SHG recording of action potentials or the external application of an artificial transmembrane potential. Although **1d.2H** was previously tested in SK-OV-3 cells, all neuronal imaging is undertaken with **1b.2H** due to its synthetic accessibility and success as a voltage-sensitive probe in Chapter 5.

We received primary cultured neurons adhered to a borosilicate glass coverslip from Dr. Gil Bub and Dr. Rebecca Burton, Department of Physiology, Anatomy and Genetics, University of Oxford. The neurons were immediately transferred to an imaging well and superfused with a solution buffered to pH 7.4. **1b.2H** was introduced from a 5 mM DMSO stock solution up to a concentration of 10 μM. The immediate precipitation of **1b.2H** upon its introduction into the well may be observed in the form of sparse dark dye particles, which in some cases obscure the neuron under investigation (Figure 15A and B). Multiphoton imaging (at 850 nm) produced SHG images from the cell plasma membranes (Figure 15D), while the two-photon mode (Figure 15C) highlighted the plasma membranes but also captured some fluorescence from inside the cytosol. Particles of precipitated dye were captured by SHG microscopy, suggesting that they contain the dye **1b.2H** in a non-centrosymmetric space-group which may therefore participate in frequency-doubling. After six full-frame exposures to 300 mW input laser light at 850 nm (20 mW at sample), the neurons experienced the consequence of phototoxicity, evidenced by apoptosis in Figure 15B. Later experiments demonstrated that by filtering the dye solution before superfusion and by cycling with an oxygenated media, cell viability is much higher and dye precipitates are not observed.

Given successful imaging, and the results presented in Chapter 5, we are confident that the combination of voltage-sensitive imaging and neuronal imaging will lead to trial-by-trial recording of transmembrane potential from neurons in both culture and *ex vivo* brain slices. Furthermore, with the sensitivity that we observe in Chapter 5, we also expect that in addition to action potentials which have previously been recorded, we may be able to record post-synaptic potentials (small, 10–30 mV transmembrane potentials which trigger the firing of action potentials). These potentials have not previously been satisfactorily spatially resolved on a single-cell level, and the ability to monitor them could lead to a new era of neurophysiology.

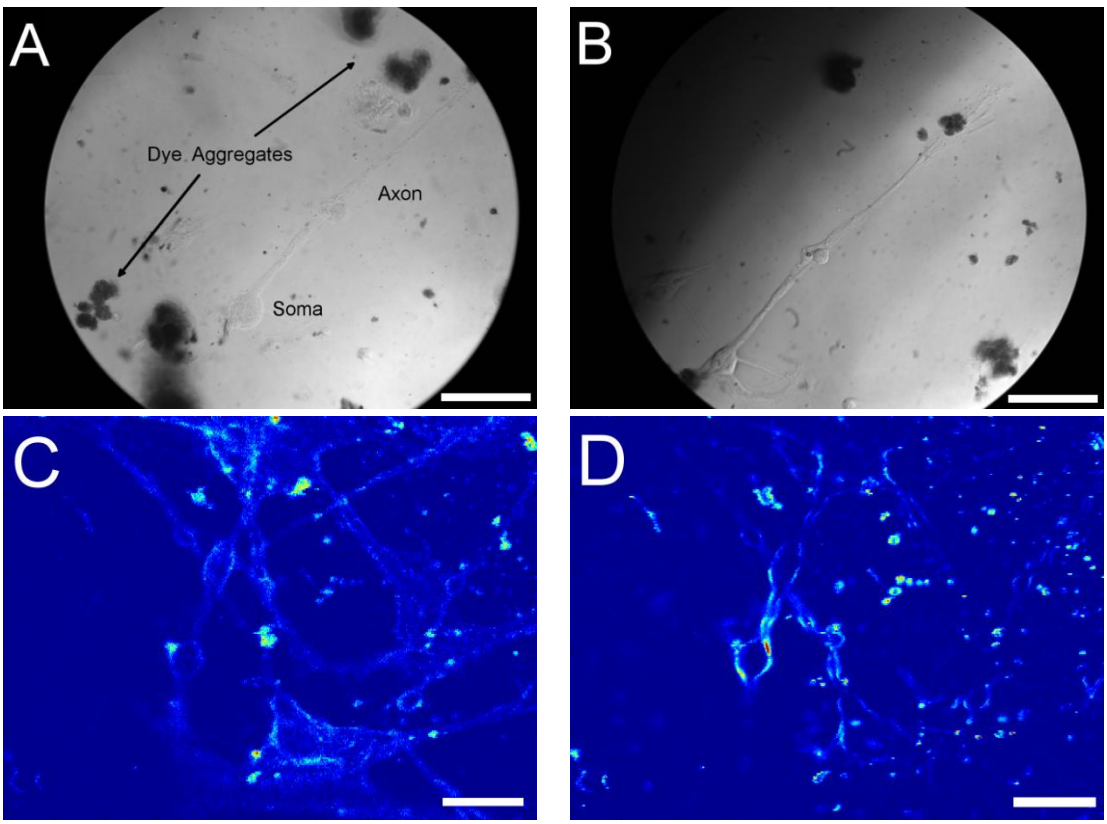

Figure 15 Light micrograph of cultured primary neuron with the soma and axon labelled both (A) before and (B) after multiphoton scanning microscopy. The neuron is stained by addition of **1b.2H** in DMSO (5 mM) to the superfusion buffer, resulting in a 10 μM solution (dye aggregates were observed). Imaging provided both (C) two-photon fluorescence images and (D) SHG images of **1b.2H** in neuronal membranes. Colourmap: JET, scale bar: 50 μm.

2.6.4 *Ex Vivo* Cell Imaging

Imaging neurons embedded within established networks is the ultimate aim for this generation of SHG dyes. Whilst the dye's affinity for plasma membranes remains unchanged in *ex vivo* neuronal preparations, imaging an individual cell deep within tissue presents a unique set of experimental challenges. Patch clamp recording is a specialised technique in which a glass micropipette backfilled with intracellular solution is used to impale a neuron at soma, with the displaced cellular membrane forming a high-resistance seal around the glass of the micropipette (Figure 16). An electrode is then introduced to the intracellular fluid which can then be used to measure the transmembrane potentials indicative of synaptic transmission.

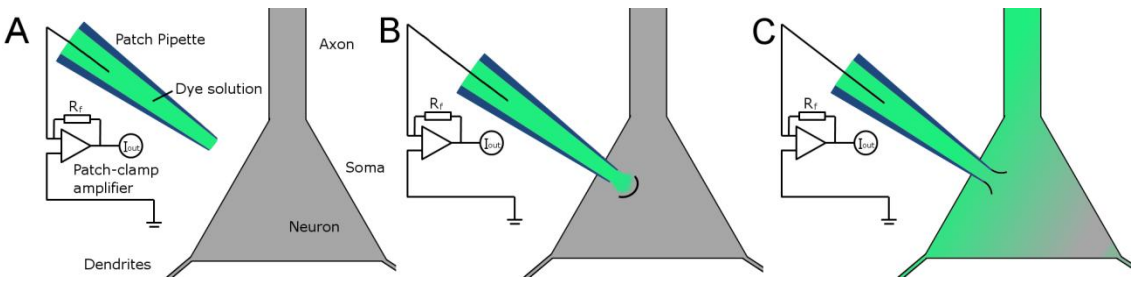

Figure 16 Process of patch clamping a neuron in whole-cell mode. The patch pipette is loaded with a dye (green) and connected to a patch clamp amplifier (A). As the patch approaches the cell soma (B), pressure applied via the pipette causes a small indentation on the cell surface. Sudden removal of pressure causes the membrane to jump back, forming a 'gigaseal' between the glass pipette and the cell membrane, an electrical contact with little or no current leakage (C). The dye is now free to diffuse into and fill the cell.

Simultaneous optical recording is possible if a stain is introduced via the patch and the experiment is carried out on a scanning microscope stage (a wide field microscope is required at the very least to locate a suitable cell and bring the patch up to the membrane surface). Once the patch forms a good seal with the membrane, a slight positive pressure on the cell via the patch introduces a small quantity of dye into the cell's interior. This dye, suitably aligned in the inner leaflet of the neuron's cellular membrane can then generate SHG when irradiated under

scanning multiphoton microscopy. In the following experiment, we attempt to image a neuron from an acute horizontal slice via multiphoton microscopy through the introduction of **1b.2H** via patch pipette. SHG images of porphyrin dye **1b.2H** were obtained from the soma of neurons within established, 400 μm thick acute neuronal slices, demonstrating the power of SHG to penetrate deep inside biological tissue. Colocalisation of the SHG signal with biological membranes can be observed in the transmission overlay, producing one of very few SHG images to be obtained from a neuron within an intact brain slice. However, more work will be reqired to match the finest exemplars of neuronal SHG imaging which are taken from *in vitro* neuronal cultures and avoid scattering of output SHG by the tissue slice (Figure 17).

Two experimental hurdles prevented acquisition of high-quality neuronal SHG images and therefore limit the scope of porphyrin chromophores in their current incarnation. Firstly, **1b.2H** is not sufficently water-soluble for patch application as a 10 μM solution, even when formulated with DMSO. Particles of precipitate formed, even after the aqueous solution was passed through a 0.1 μm porosity filter, blocking the 1 μm aperature of the patch pipette leading to a failed patching attempt. The related second hurdle is that the greasiness of the *N*-octyl chains which cause surfactant-like behaviour at the site of patching, preventing formation of a tight seal between the membrane and patch clamp pipette.[75] A leak at this site is both cytotoxic and leads to noisy electrophysical recordings, unsuitable for measuring transmembrane potential. At this point, we decided to halt patch-clamping of neurons from intact neuronal networks, and concentrate on fully characterising the chromophore before attempting to redesign the amphiphilicity of the dye to achieve biological compatibility.

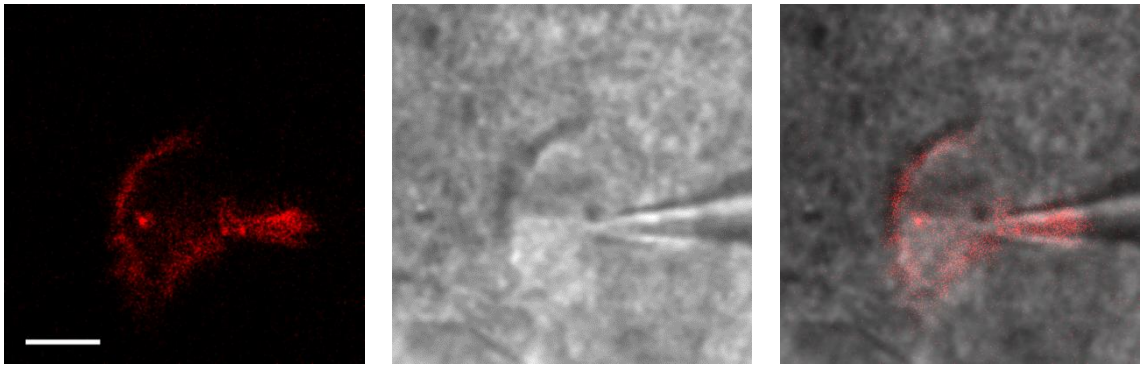

Figure 17 *Ex vivo* second harmonic generation imaging of porphyrin **1c·2H** in principal cells of rat neocortex. SHG image (left) and the corresponding transmission image (centre) with their overlay (right), scale bar: 10 µm. SHG can be seen from somatic cell membranes and from the glass-buffer interface inside the patch-clamp pipette.

The aim of this neuronal imaging was to establish whether dye **1b.2H** is suitable for use via patch-clamp application. Given the stated outcome, the goals for molecular redesign within the parameters of constructing a dye for patch-clamp application become clear. The dye must be sufficiently water-soluble for application at 10 µM without precipitating over time, and our octyl chains must be removed or trimmed down to prevent lysing of the cell membrane at the site of seal formation.

2.7 Biological Properties and Phototoxicity

Photobleaching and biological photodamage are common limitations when undertaking optical imaging.[76, 77] SHG promises to evade these problems, because (unlike fluorescence) it does not depend on the population of excited states. [20, 30, 78, 79] One- and two-photon excitation may occur in parallel with SHG, but any effect which rapidly relaxes the excited state competes with photochemical degradation, and quenches fluorescence, without directly reducing the SHG intensity. Metallation of porphyrin-based SHG dyes may enable the photochemical behaviour to be modified, without strongly affecting the SHG. Open-shell metalloporphyrins, such as

copper(II) and nickel(II) complexes, have extremely short excited-state lifetimes under normal conditions, resulting in quenched fluorescence, low singlet oxygen yields, and low phototoxicity; we therefore decided to test these metal complexes with irradiation centred around 655 nm (Figure 18).[20, 62]

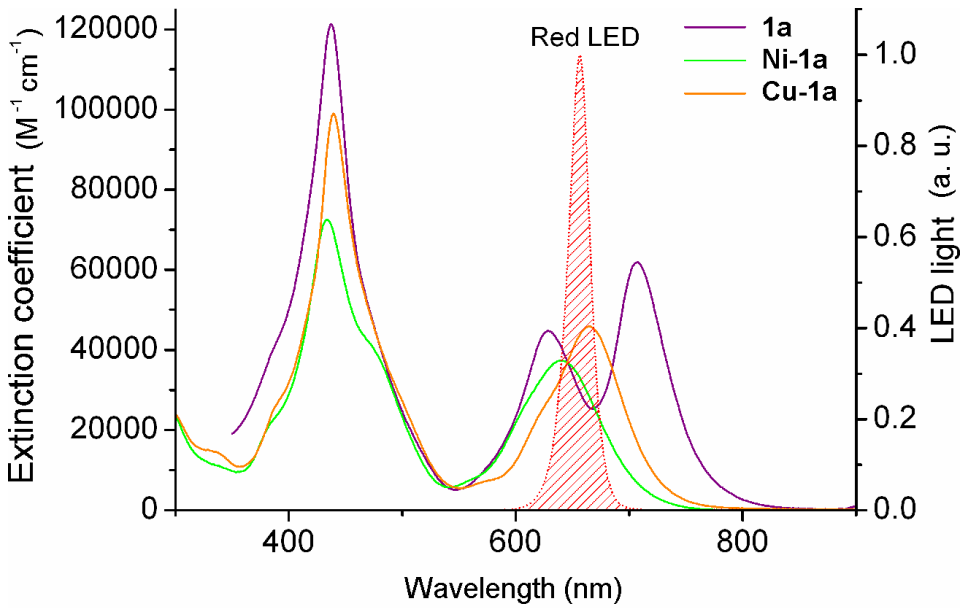

Figure 18 Absorption spectra (ε/M^{-1} cm^{-1} vs. λ/nm) of **1b.2H**, **1b.Ni** and **1b.Cu** in DMF. The emission spectrum of the red LEDs used in the phototoxicity experiments is also included for comparison.

2.7.1 Results

The phototoxicities of the free-base, copper and nickel porphyrin **1a.M** complexes were compared in human cervical epithelial carcinoma (HeLa) cells with irradiation at 657 nm (after dye uptake) using previously reported methodology (Figure 19).[80] We assume that the dyes accumulate similarly in the cells, as the porphyrin framework is the same for each compound. Figure 19 shows only minimal difference in extinction coefficient at 657 nm, the wavelength of irradiation.

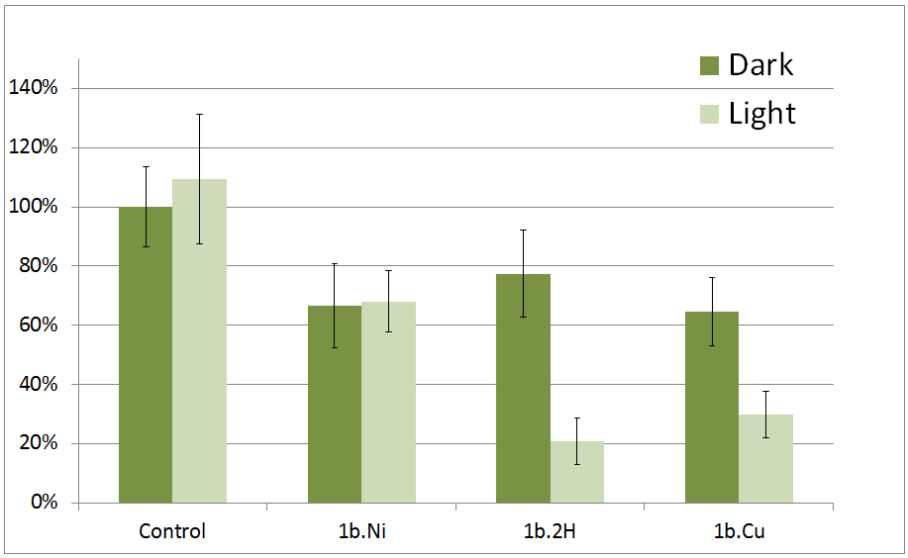

Figure 19 Typical outcome of a cell viability assay (see experimental) using porphyrins **1b.Ni**, **1b.2H** and **1b.Cu** on HeLa cells with 657 nm irradiation for 30 minutes. The drop in cell viability that all porphyrins exhibit demonstrates that exposure to any dye results in cell mortality of approximately 30%. Most importantly, nickel complex **1b.Ni** shows no phototoxicity, whereas its free-base and copper analogues (**1b.2H** and **1b.Cu** respectively) are harmful to cells when subjected to illumination. Cells were exposed to a 10 μm solution of each dye in the absence of light for one hour prior to light exposure.

Table 4 gives the ratio of the cell viability without irradiation (cells treated with the dye but maintained in the dark) to the cell viability with irradiation (657 nm, 3.2 mW, 30 min exposure). For the free-base porphyrin (**1a.2H**) the cell viability is reduced by approximately five-fold upon application of a light dose. As expected, the metal complexes are less phototoxic; the light dose reduces the cell viability by half with copper complex **1a.Cu**, and has no effect on the viability of cells incubated with the nickel complex **1a.Ni**. The mechanism for cell-death is unresolved, but both singlet oxygen or electron transfer photochemistry are candidates under these conditions, with these push-pull chromophores.

Table 4 Phototoxicity results using porphyrins **1b.2H**, **1b.Cu** and **1b.Ni**, on HeLa cells at 657 nm irradiation for 30 minutes.

Porphyrin	Dark/Light Cell Viability Ratio
1b.2H	5.11 ± 2.83
1b.Cu	1.94 ± 0.86
1b.Ni	0.99 ± 0.41

2.8 Conclusions

We designed and synthesised a large family of amphiphilic donor-acceptor dipolar porphyrins, and we demonstrated that these dyes have excellent nonlinear optical properties, associate well inside membranes and outperform commercially available probes as SHG stains.[20, 21] The optical and physical properties of each of the dyes are summarised in Table 1. By collating these data and examining the trends we can see the common motifs that make a good porphyrin SHG stain. The free-bases are consistently high performers and while the inclusion of *meso*-aryl solubilising groups has a small detrimental effect on the optical properties, it substantially increases their aqueous solubility. Copper and nickel porphyrins have short-lived excited states due to fast quenching but their complexation state and solubility are detrimental to their usefulness. Greater charge at the pyridinium group confers better solubility, but the inclusion of a dipositive headgroup may have a detrimental effect on the NLO properties, leaing to slightly decreased β_{zzz} values. The imaging of **1b.2H** and **1d.2H** within *in vitro* and *ex vivo* plasma membranes is successful and informative, offering guidelines for a second generation of SHG probes.

Since we find a large variation in performance across the family of dyes, and top performers in some categories are lacklustre in others, we must pick a dye which satisfies all criteria for comparison with the commercially available probes. Figure 20 demonstrates that **2b.2H** outperforms the state-of-the-art commercially available styryl dye FM4-64 in each of the key SHG dye metrics.

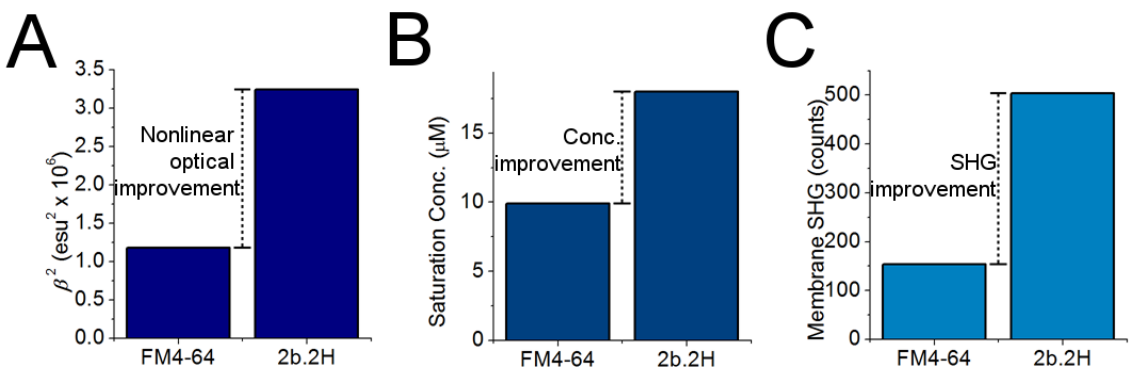

Figure 20 Porphyrinic SHG dye **2b.2H** outperforms commercially available FM4-64 in terms of (A) nonlinear optical properties with a very high acting first hyperpolarisability of 3.24 (esu^2 × 10^6) and (B) high saturation solubility which allows it to be a good SHG dye as demonstrated by (C) SHG from a model membrane, each dye (50 μm) was adsorbed into a DPhPC (1 mg/mL) monolayer formed on the surface of a droplet of water in oil (dodecane).

For a truly sucessful SHG probe, the final task is to show that its voltage-sensitivity is useful for measuring transmembrane potential in neurons or other electrically excitable cells. We examine the performance of **1b.2H** and other good SHG dyes as voltage-sensitive probes in Chapter 5: “Porphyrins as Transmembrane-Potential Sensitive Probes”.

2.9 Experimental

2.9.1 Membrane Imaging

Slice preparation and imaging was performed in collaboration with Dr. M. M. Kohl, Department of Physiology, Development & Neuroscience, University of Cambridge. Acute horizontal slices (400 µm) were prepared from postnatal day 13–20 Wistar rats of both sexes after decapitation under deep isobutane-induced anesthesia, in accordance with British Home Office regulations. Slices were maintained in an interface chamber between humidified carbogen gas (95% O_2, 5% CO_2) and standard artificial cerebrospinal fluid (aCSF) containing (in mM): 126 NaCl, 3 KCl, 1.25 NaH_2PO_4, 2 $MgSO_4$, 2 $CaCl_2$, 26 $NaHCO_3$, and 10 glucose, pH 7.2–7.4. After recovering at room temperature (20–25 °C) for at least 1 h, slices were mounted on cover slips (coated with 0.1% poly-L-lysine in double-distilled water), covered with 400 µL aCSF and kept in a chamber saturated with humidified carbogen gas at 32 °C until transferred into the recording chamber. For recordings, slices were maintained in submerged condition at 37 °C, and superfused with aCSF, bubbled with carbogen, at 2–4 mL min^{-1}. Cells with a pyramidal-shaped soma were selected for recording using infrared differential interference contrast optics. Whole-cell patch-clamp recordings were performed using glass pipettes pulled from borosilicate glass capillaries, containing (in mM): 110 K-gluconate, 40 HEPES, 2 ATP-Mg, 0.3 GTP, 4 NaCl (pH 7.2–7.3; osmolarity 270–285 mosmol L^{-1}). porphyrin **1b.2H** (10 µM) and fetal bovine serum (HyClone) were added to the internal solution and passed through a 0.22 µm filter just before patching. Pipette DC resistances were 4 to 7 MΩ. Neurons were imaged 20 minutes after establishing whole-cell configuration.

Neurons for *in vitro* imaging were obtained as mature cultures from Dr. Gil Bub of the Department of Physiology, Anatomy and Genetics, University of Oxford and SK-OV-3 cells were cultured using a previously described method.[80]

SK-OV-3 and patch clamp imaging was performed using a Leica TCS SP2 (Leica Microsystems) two-photon laser scanning microscope with a Ti:Sapphire laser at 840 nm (Mai Tai Broadband, SpectraPhysics; 100 fs pulse width; 80 MHz repetition rate). The typical laser power was 21 mW on the sample (15% power setting). Images were recorded using a 10× immersion objective with a numerical aperture (*N.A.*) of 0.3. The isotropic fluorescence and forward-propagating SHG signals were collected with external photomultiplier tubes (Leica Microsystems). The fluorescence detector was mounted in the descanned detection channel, that is, the emitted light traveled back through the pinhole following the same path as the incident excitation light, and was subsequently separated using a dichroic (525/50) and a short-pass filter (900 nm). The SHG signal, which radiates primarily in the direction of the incident light, was collected using a forward mounted non-descanned detector with narrow band-pass filters, BG3 and BG40 (Thorlabs); this combination of filters only transmits light in the wavelength range 350–450 nm. Images were acquired in framescan mode with 8-line averaging and a pixel dwell time of 2.4 µs.

Droplet interface monolayers and *in vitro* neuronal imaging were conducted on a custom-built microscope based around an Olympus BX60M upright microscope adapted with standard Linos microbench components. The light source was a Ti:Sapphire laser (Tsunami, Spectra Physics) producing 100 fs pulses centred at 850 nm. An Olympus LUMPlanFL N 40X 0.8 NA lens was illuminated at the back aperture with a 90 mW beam after passing through a 1000:1 Newport polarising beamsplitter. After passing through an excitation filter the two-photon epi-

fluorescence was filtered with a 550–650 nm bandpass filter (Semrock FF568-Di01-25x36) before being captured with a Hamamatsu H7422P series photon counting PMT. SHG emission was condensed in the forward direction, passing through an excitation filter and a 422–432 nm notch filter (Semrock FF01-427/10-25) before reaching a Sens-Tech DM0016 photon counting PMT. The alignment of the emission polariser in SHG imaging was determined using a non-linear frequency-doubling crystal.

2.9.2 Phototoxicity Studies

The adherent HeLa cells were grown in phenol red free DMEM (Gibco) supplemented with 2 mM L-glutamine (Sigma), 100 U mL^{-1} penicillin (Sigma), 100 μg mL^{-1} streptomycin (Sigma) and 10% heat-inactivated fetal bovine serum (Sigma). The cells were maintained at 37 °C in a humidified 5% CO_2 atmosphere. For the phototoxicity experiments, the cells were seeded in flat 96-well plates (Nunc) at a density of 1500 cells per well in 100 μL of culture media and irradiated 26 h later. One hour before the light dose, the media on the cells was replaced with the solution of the porphyrin in media, diluted 100 times from a 1 mM stock in DMSO. The plates were shielded from light during and after incubation. Following incubation the wells requiring light exposure were irradiated with 657 nm LEDs (3.2 mW, Dotlight GbR, Germany), then washed three times with 100 μL of media and incubated in 100 μL of media for 42 h. After this time the cell viability was determined using a proliferation assay (CellTiter 96® Aqueous, Promega) according to the manufacturer's instructions. An average background absorbance reading of the media was recorded and subtracted from the average absorbance of each replicate group before further data manipulation. Each experimental condition consisted of 5 replicates, and the experiment was repeated twice and the average ratio between the dark and light cell viability is reported in Table 4 (the errors denote one standard deviation).

2.9.3 Synthesis

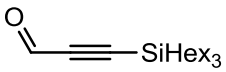

3-(Trihexylsilyl)propiolaldehyde was prepared according to an adapted literature procedure.[81] *n*-Butyllithium (1.6 M in hexanes, 3.03 mL, 4.88 mmol) was added dropwise to a stirred solution of trihexylsilylacetylene (1.50 g, 4.88 mmol) in dry THF (19.5 mL). The mixture was refluxed for 5 minutes before transfer via cannula to a stirred solution of DMF (2.25 mL, 29.08 mmol) in dry THF (19.5 mL). The mixture was refluxed for a further 5 minutes and then allowed to cool to room temperature. The reaction mixture was quenched with $HCl_{(aq)}$ (1.0 M, 10.5 mL), washed with H_2O (40 mL) and extracted with Et_2O (3 × 150 mL). The solution was dried over $MgSO_4$ and the solvent removed to give a yellow oil, (1.065 g, 65%). ^{1}H NMR (400 MHz, $CDCl_3$) δ_H 9.18 (s, 1H), 1.36 (m, 24H), 0.89 (t, 9H, J = 7.0 Hz), 0.66 (m, 6H), ^{13}C NMR (100 MHz, $CDCl_3$); δ_C 176.68, 33.11, 31.41, 23.64, 22.55, 14.10, 12.50.

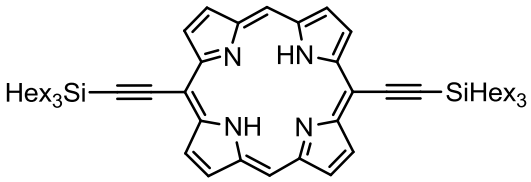

Porphyrin **3** was prepared according to an adapted literature procedure.[81] Dipyrromethane (614 mg, 4.18 mmol) was dried *in vacuo* for 1 h before addition of dry CH_2Cl_2 (238 mL) and trihexylsilyl propynal (1.4 g, 4.16 mmol). The solution was freeze-pump-thaw-degassed and $BF_3.OEt_2$ (173 μL, 1.40 mmol) was added and the mixture was stirred at room temperature for 45 minutes in the dark. After this time, DDQ (1.42 g, 6.28 mmol) was added and the mixture was stirred under air for 10 minutes. The crude mixture was passed through a large silica plug (CH_2Cl_2) and further purified by flash chromatography on silica (4:1 40–60 °C petrol ether:CH_2Cl_2). Fractions were evaporated to give **3** as a purple oil, (868 mg, 45 %). λ_{max} ($CHCl_3$)/nm (log ε) 425 (5.43), 572 (4.78), 664 (4.29). ^{1}H NMR (400 MHz, $CDCl_3$) δ_H 10.14 (s, 2H), 9.70 (d, 4H, J = 4.6 Hz), 9.31 (d, 4H, J = 4.6 Hz) 1.81 (m, 12H), 1.60 (m, 12H), 1.44 (m, 12H), 1.29 (m, 12H), 1.07 (m, 12H), 0.95 (t, 18H, J = 7.0 Hz), –2.63 (br s, 2H); *m/z* (ESI+) 923.6787 ($[M]^+$ 100%, $C_{60}H_{91}N_4Si_2^+$ requires 923.6777).

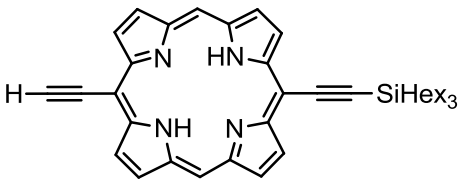

Porphyrin **4** was prepared as follows: TBAF (1.0 M in THF, 163 μL, 163 μmol) was slowly added to a stirred solution of **3** (150 mg, 163 μmol) in $CHCl_3$ (30 mL) and the reaction carefully monitored by TLC (4:1 40–60 °C petrol ether:CH_2Cl_2). When the concentrations of the starting material and bis-deprotected side-product appeared roughly equal, the reaction was quenched by

pouring directly onto a silica plug in $CHCl_3$. The monodeprotected product was obtained by flash chromatography (4:1 40–60 °C petrol ether:CH_2Cl_2) and the starting material **3** was reclaimed. The monodeprotected fractions were evaporated to dryness to give **4** as a purple wax, (42.5 mg, 43 %). λ_{max} ($CHCl_3$)/nm (log ε) 420 (5.39), 565 (4.54), 659 (4.07). ^{1}H NMR (400 MHz, $CDCl_3$) δ_H 10.00 (s, 2H), 9.64 (m, 4H), 9.23 (m, 4H) 4.22 (s, 1H), 1.85 (m, 6H), 1.63 (m, 6H), 1.46 (m, 12H), 1.10 (m, 6H), 0.97 (t, 9H, J = 7.0 Hz), –3.19 (br s, 2H).

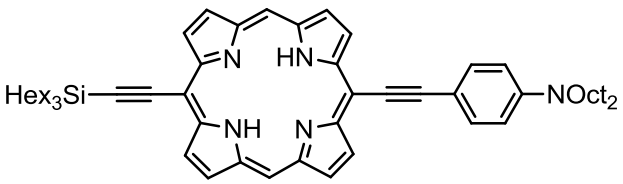

Porphyrin **5.2H** was prepared as follows: $Pd_2(dba)_3$ (33 mg, 36 μmol), PPh_3 (37.7 mg, 144 μmol), CuI (13.6 mg, 72 μmol) and **4** (229 mg, 357 μmol) were dried *in vacuo* for one hour before Et_3N (17.2 mL) was added and the mixture freeze-pump-thaw degassed. *N*,*N*-Dioctyl-4-iodoaniline (1.27 g, 2.87 mmol) was added and the mixture stirred at 40°C for 1 h under N_2. Upon completion, the mixture was passed through a silica plug (3:1 40–60 °C petrol ether: CH_2Cl_2) then purified by flash chromatography (gradient from 20:1 to 10:1 to 5:1 40–60 °C petrol ether: CH_2Cl_2) to isolate the desired product. Fractions were evaporated to dryness to give **5.2H** as purple wax, (187 mg, 55%). λ_{max} ($CHCl_3$)/nm (log ε) 422 (5.02), 608 (4.65), 686 (4.51). R_f = 0.51 (4:1 40–60 °C petrol ether:CH_2Cl_2). ^{1}H NMR (400 MHz, $CDCl_3$) δ_H 10.07 (s, 2H), 9.75 (d, 2H, J = 4.7 Hz), 9.65 (d, 2H, J = 4.7 Hz), 9.28 (m, 4H), 7.92 (d, 2H, J = 8.9 Hz), 6.81 (d, 2H, J = 8.9 Hz), 3.42 (t, 4H, J = 7.9 Hz), 1.81 (m, 6H), 1.71 (m, 4H), 1.60 (m, 6H), 1.50–1.24 (m, 32H), 1.06 (m, 6H), 0.95 (t, 9H, J = 5.4 Hz), 0.95 (t, 4H, J = 7.0 Hz), –2.37 (bs, 2H); ^{13}C NMR (100 MHz, $CDCl_3$) δ_C 133.26, 131.57, 131.03, 129.71, 111.55, 106.26, 99.80, 89.65,

51.12, 33.49, 31.93, 31.85, 29.59, 29.43, 27.36, 27.24, 24.53, 22.82, 22.76, 14.33, 14.21, 13.95; *m/z* (ESI+) 956.6961 ($[M]^+$ 100%, $C_{64}H_{90}N_5Si_1^+$ requires 956.6960).

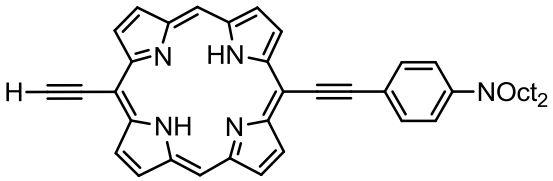

Intermediate porphyrin **5α.2H** was prepared as follows: TBAF (1.0 M in THF, 100 μL, 100 μmol) was added to a solution of **5.2H** (46 mg, 44 μmol) in CH_2Cl_2 (4 mL) and stirred for 10 minutes. The reaction mixture was passed through a silica plug (CH_2Cl_2) and evaporated to dryness to give **5α.2H** as a purple wax, (26 mg, 98%). R_f = 0.16 (4:1 40–60 °C petrol ether:CH_2Cl_2). ^{1}H NMR (400 MHz, $CDCl_3$) δ_H 10.09 (s, 2H), 9.77 (d, 2H, J = 4.5 Hz), 9.67 (d, 2H, J = 4.5 Hz), 9.31 (m, 4H), 7.93 (br s, 2H), 6.82 (br s, 2H), 4.21 (s, 1H), 3.42 (br s, 4H), 1.80–1.22 (m, 24H), 0.95 (m, 4H), −2.45 (br s, 2H); ^{13}C NMR (100 MHz, $CDCl_3$) δ_C 133.27, 132.11, 111.51, 106.62, 51.11, 31.87, 29.54, 29.38, 27.32, 27.21, 23.03, 22.69, 22.30, 21.10, 14.14.

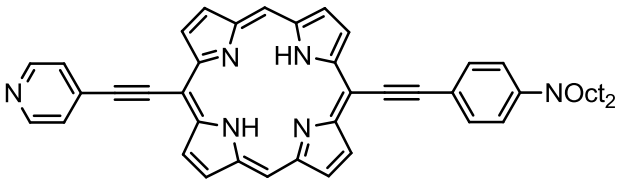

Porphyrin **1a.2H** was prepared as follows: $Pd_2(dba)_3$ (8.88 mg, 9.77 μmol), PPh_3 (10.2 mg, 39.1 μmol), CuI (3.7 mg, 20 μmol) and **5α** (187 mg, 195 μmol) were dried *in vacuo* for 1 h before Et_3N (26 mL) was added and the mixture freeze-pump-thaw degassed. 4-Iodopyridine (185 mg, 902 μmol) was added and the mixture stirred at 40°C for 3 h under N_2. Upon completion, the mixture was passed through a silica plug (CH_2Cl_2) then purified by flash chromatography (5:1 CH_2Cl_2:THF). Fractions were evaporated to dryness to give **1a.2H** as a purple wax, (127 mg, 87%). λ_{max} ($CHCl_3$)/nm (log ε) 427 (5.05), 615 (4.62), 691 (4.52). ^{1}H NMR (400 MHz, $CDCl_3$) δ_H 9.71 (s, 2H), 9.57 (s, 2H), 9.37 (s, 2H), 9.05 (m, 4H), 8.85 (d, 2H, J = 4.4 Hz), 7.91 (d, 2H, J = 8.6 Hz), 7.87 (d, 2H, J = 4.4 Hz), 6.85 (d, 2H, J = 8.6 Hz), 3.43 (t, 4H, J = 8.0 Hz), 1.8–0.8 (m, 30H), –3.36 (br s, 1H), -3.49 (br s, 1H); ^{13}C NMR (100 MHz, $CDCl_3$) δ_C 143.30, 133.27, 132.15, 130.48, 128.93, 128.36, 125.37, 111.53, 51.13, 33.29, 31.92, 31.58, 29.59, 29.43, 27.37, 27.25, 23.06, 22.74, 22.61, 15.09, 14.20, 14.16; *m/z* (MALDI-ToF) 750.99 ($[M]^+$ 100%, $C_{51}H_{54}N_6^+$ requires 750.44).

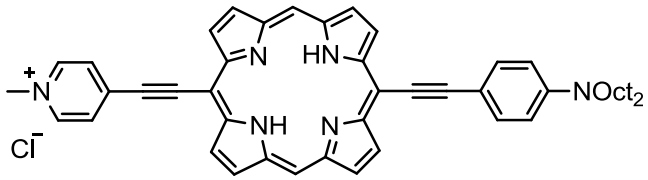

Porphyrin **1b.2H** was prepared as follows: Porphyrin **1a.2H** (10 mg, 13 μmol) in DMF (1.0 mL) was stirred and MeI (2.2 mL, 36 mmol) was added dropwise. After 15 minutes, all starting material was consumed according to TLC and the product was passed through a Dowex 1x8 200 mesh ion-exchange column (DMF). The resulting solution was precipitated from DMF with toluene, centrifuged and collected by filtration to give **1b.2H** as an amorphous dark solid, (11 mg, 55%). λ_{max} ($CHCl_3$)/nm (log ε) 448 (5.04), 643 (4.73), 723 (4.86); $\lambda_{max,em}$ ($CHCl_3$)/nm 803 (Φ_F = 0.13). ^{1}H NMR (400 MHz, DMSO-d_6) δ_H 10.44 (s, 2H), 9.86 (d, 2H, J = 4.8 Hz), 9.78 (d, 2H, J = 4.8 Hz), 9.63 (d, 2H, J = 4.8 Hz), 9.58 (d, 2H, J = 4.8 Hz), 9.19 (d, 2H, J = 6.7 Hz), 8.93 (d, 2H, J = 6.7 Hz), 7.99 (d, 2H, J = 8.9 Hz), 6.91 (d, 2H, J = 8.9 Hz), 4.43 (s, 3H), 3.5–0.8 (m, 34H), –2.26 (br s, 1H), –2.34 (br s, 1H); *m/z* (ESI+) 765.4635 ($[M]^+$ 100%, $C_{52}H_{57}N_6^+$ requires 765.4639).

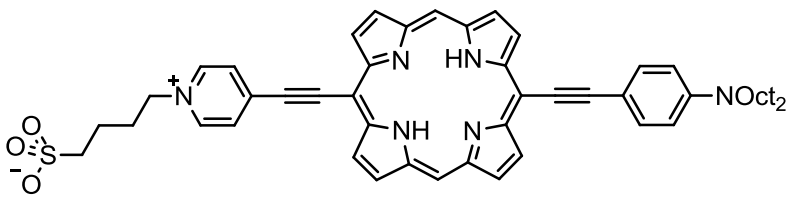

Porphyrin **1c·2H** was prepared as follows: Porphyrin **1a.2H** (30 mg, 40 μmol) and 4-butansultone (200 μL, 1.98 mmol) in DMF (3 mL) were stirred at 115 °C for 16 h. The salt was purified by SEC (4:1 THF:DMF), and then precipitated from DMF with 40–60 °C petrol ether and collected by filtration to give **1c.2H** as an amorphous dark solid. (18 mg, 51%). λ_{max} ($CHCl_3$)/nm (log ε) 467 (4.71), 645 (4.37), 726 (4.42). ^{1}H NMR (400 HMz, DMSO-d_6) δ_H 10.49 (s, 2H), 9.97 (d, 2H, J = 4.4 Hz), 9.80 (d, 2H, J = 4.1 Hz), 9.68 (d, 2H, J = 4.4 Hz), 9.60 (d, 2H,

J = 4.4 Hz), 9.33 (d, 2H, *J* = 6.8 Hz), 6.62 (d, 2H, *J* = 6.8 Hz), 8.01 (d, 2H, *J* = 8.1 Hz), 6.92 (d, 2H, *J* = 8.1 Hz), 4.72 (t, 2H, *J* = 8.2 Hz), 2.17 (m, 2H), 1.72 (m, 2H), 2.58 (m, 2H), 3.5–1.1 (m, 34H), –2.13 (br s, 2H); *m/z* (ESI+) 909.4485 ($[M]^+$ 100%, $C_{55}H_{62}N_6Na_1O_3S_1^+$ requires 909.4496).

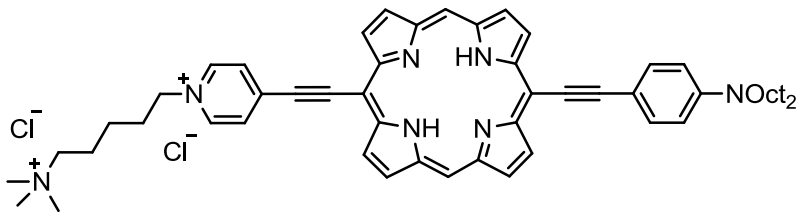

Porphyrin **1d.2H** was prepared as follows: Porphyrin **1a.2H** (25 mg, 33 μmol) and 5-iodo-*N*,*N*,*N*-trimethylpentan-1-aminium[4] (30 mg, 78 μmol) in DMF (3 mL) were stirred under Ar at 60 °C for 2 days. The reaction mixture was poured onto a Dowex column 1x8 200 mesh ion exchange column (DMF). The salt was purified by sise exclusion chromatography (9:1 THF:DMF), precipitated from DMF with 40–60 °C petrol ether to give **1d.2H** as an amorphous dark solid, (13.0 mg, 41%). $\lambda_{max}(CHCl_3)$/nm (log ε) 445 (4.57), 637 (4.22), 716 (4.24). ^{1}H NMR (400 MHz, DMSO-d_6) δ_H 10.46 (s, 2H), 9.90 (d, 2H, *J* = 4.1 Hz), 9.78 (d, 2H, *J* = 4.1 Hz), 9.66 (d, 2H, *J* = 4.5 Hz), 9.58 (d, 2H, *J* = 4.5 Hz), 9.35 (d, 2H, *J* = 6.4 Hz), 8.5 (d, 2H, *J* = 6.4 Hz), 8.5 (d, 2H, *J* = 8.8 Hz), 6.88 (d, 2H, *J* = 8.8 Hz), 4.73 (t, 2H, *J* = 7.0 Hz), 3.04 (s, 9H), 3.5-0.8 (m, 42H), –2.20 (br s, 2H).

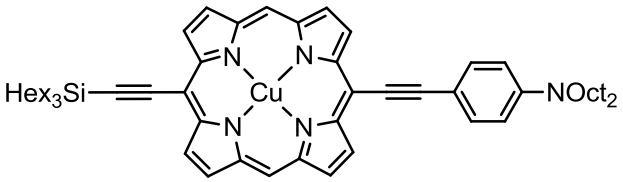

Porphyrin **5.Cu** was prepared as follows: A solution of $Cu(OAc)_2.2H_2O$ (237 mg, 1.19 mmol) in MeOH (1 mL) was added to porphyrin **5.2H** (45.4 mg, 47.4 μmol) dissolved in CH_2Cl_2 (4 mL). The mixture was stirred for 2 h at room temperature and followed by TLC (3:1 40–60 °C petrol ether: CH_2Cl_2). Upon completion the solvents were removed under reduced pressure and the product was purified by flash chromatography (6:1:0.07 40–60 °C petrol ether: CH_2Cl_2 : pyridine). Fractions were evaporated to dryness to give **5.Cu** as a purple glass, (45.0 mg, 93%). λ_{max} ($CHCl_3$)/ nm (log ε) 424 (5.20), 623 (4.72). R_f = 0.16 (3:1 40-60 °C petrol ether:CH_2Cl_2); Since copper(II) is paramagnetic, no NMR spectra were recorded. Purity was confirmed by HPLC. *m/z* (ESI+) 1017.60 ($C_{64}H_{88}CuN_5Si$, $[M]^+$, requires 1017.61, 100 %).

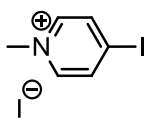

4-Iodo-*N*-methylpyridinium iodide was prepared as follows: 4-Iodopyridine (212 mg, 1.03 mmol) was dissolved in methyl iodide (2.0 mL, 32 mmol) and stirred at room temperature overnight, protected from light. The product precipitated from solution and was collected by filtration as a white powder (327 mg, 91 %). mp 210 °C with decomposition; δ_H (400 MHz, DMSO-d_6) 4.21 (s, 3H), 8.49–8.71 (m, 4 H); δ_C (100 MHz, DMSO-d_6) 48.47, 120.50, 137.55, 145.76; *m/z* ESI 219.9622 (C_6H_7IN, $[M\text{-}I^-]^+$, requires 219.9618, 100 %).

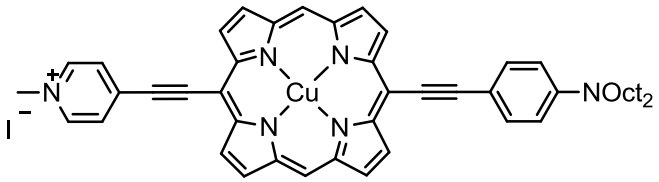

Porphyrin **1b.Cu** was prepared as follows: TBAF (1.0 M in THF, 46 μL, 46 μmol) was added to a solution of porphyrin **5.Cu** (40.0 mg, 39.3 μmol) in CH_2Cl_2 (9 mL) and stirred for 10 minutes. The reaction mixture was passed through a short flash chromatography column (CH_2Cl_2) and evaporated to dryness. The resulting porphyrin was dried *in vacuo* for 1 h with $Pd_2(dba)_3$ (1.38 mg, 1.51 μmol), PPh_3 (1.58 mg, 6.04 μmol), CuI (0.57 mg, 3.02 μmol) and 4-iodo N-methylpyridinium (69 mg, 200 μmol) before Et_3N (0.4 mL) and DMF (1.6 mL) were added and the mixture freeze-pump-thaw degassed. The reaction was followed by HPLC and was complete in 1 h. The product **1b.Cu** was precipitated from solution with PhMe, collected by centrifugation and washed with PhMe (3 × 25 mL). The powder was redissolved in NMP and layered with MeOH, the resulting precipitate was collected by centrifugation and washed with MeOH (3 × 25 mL), H_2O (2 × 25 mL), THF (2 × 25 mL) and Et_2O (3 × 25 mL). Porphyrin **1b.Cu** was obtained as a dark green powder (13.4 mg, 36%). Since copper(II) is paramagnetic, no NMR spectra were recorded. Purity was confirmed by HPLC. λ_{max} (DMF)/ nm (log ε) 439 (5.00), 664 (4.66); *m/z* ESI 826.3746 ($C_{52}H_{55}CuN_6$, $[M]^+$, requires 826.3779, 100 %).

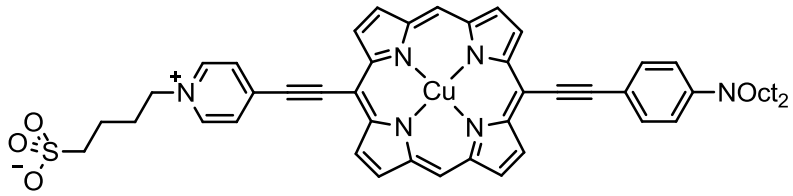

Porphyrin **1c.Cu** was prepared as follows: Porphyrin **1c.2H** (5.0 mg, 27 μmol) was stirred in $CHCl_3$ and $Cu(OAc)_2 \cdot H_2O$ (40 mg, 200 μmol) was added, the mixture was refluxed for 3 h. The product was then purified by SEC and precipitated with 40–60 °C petrol ether to yield **1c.Cu** as a dark amorphous solid. (5 mg, 94 %). Since copper(II) is paramagnetic, no NMR spectra were recorded. Purity was confirmed by HPLC. $\lambda_{max}(CHCl_3)$/nm (log ε) 437 (4.78), 664 (4.45). *m/z* (MALDI-ToF) 949.05 ($[M]^+$ 100%, $C_{55}H_{62}N_6O_3SCu^+$ requires 949.39).

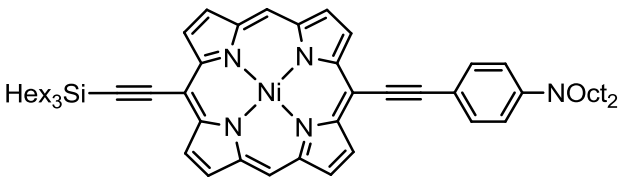

Porphyrin **5.Ni** was prepared as follows: $Ni(OAc)_2$ (100 mg, 402 μmol) was added to a solution of porphyrin **5.2H** (50 mg, 52 μmol) in DMF (5 mL) and refluxed for 1 h. The volume of DMF was reduced *in vacuo* and the solution was passed through a silica plug (4:1 40–60 °C petrol ether:CH_2Cl_2) to remove excess nickel salts. The single fraction was evaporated to dryness to give **5.Ni** as a purple wax (41 mg, 83%). R_f = 0.33 (2:1 40–60 °C petrol ether:CH_2Cl_2). ^{1}H NMR (400 MHz, $CDCl_3$) δ_H 9.56 (s, 2H), 9.55 (d, 2H, *J* = 4.4 Hz), 9.50 (d, 2H, *J* = 4.4 Hz), 8.98 (m, 4H), 7.86 (d, 2H, *J* = 8.9 Hz), 6.81 (d, 2H, *J* = 8.9 Hz), 3.40 (t, 4H, *J* = 7.9 Hz), 1.85-1.30 (m, 52H), 1.10-0.91 (m, 21H); *m/z* (MALDI-ToF) 1013.9 ($[M]^+$ 100%, $C_{64}H_{87}N_5NiSi^+$ requires 1011.6).

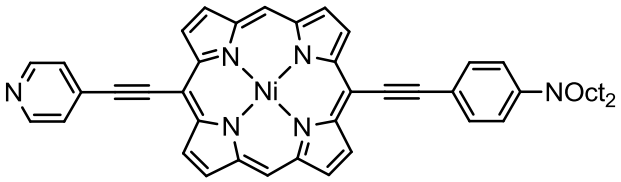

Porphyrin **1a.Ni** was prepared as follows: TBAF (1.0 M in THF, 30 μL, 30 μmol) was added to a solution of porphyrin **5.Ni** (14 mg, 1.3 μmol) in CH_2Cl_2 (3.0 mL) and stirred for 5 min. The solution was passed through a silica plug (CH_2Cl_2) and evaporated to dryness. The resulting purple solid, $Pd_2(dba)_3$ (0.63 mg, 0.69 μmol), PPh_3 (0.72 mg, 2.8 μmol) and CuI (0.26 mg, 1.4 μmol) were dried *in vacuo* for 1 h before Et_3N (3 mL) was added and the mixture freeze-pump-thaw degassed. 4-iodopyridine (15 mg, 69 μmol) was added and the mixture stirred at 40°C overnight under N_2. Upon completion, the mixture was passed through a silica plug (CH_2Cl_2) then purified by flash chromatography (4:1 CH_2Cl_2:THF). Fractions were evaporated to dryness to give **1a.Ni** as a purple wax, (7.0 mg, 63%). $\lambda_{max}(CHCl_3)$/nm (log ε) 425 (4.91), 613 (4.54). R_f = 0.38 (1:1 40–60 °C petrol ether:CH_2Cl_2). ^{1}H NMR (400 MHz, $CDCl_3$) δ_H 9.50 (d, 2H, *J* = 4.4 Hz), 9.32 (s, 2H), 9.25 (d, 2H, J = 4.4 Hz), 8.89 (br.s., 2H), 8.86 (d, 2H, *J* = 4.4 Hz), 8.81 (d, 2H, *J* = 4.1 Hz), 7.86 (d, 2H, *J* = 8.6 Hz), 7.81 (br.s., 2H), 6.81 (d, 2H, *J* = 8.6 Hz), 3.41 (t, 4H, *J* = 7.9 Hz), 1.8–0.8 (m, 30H); *m/z* (MALDI-ToF) 808.2 ($[M]^+$ 100%, $C_{51}H_{56}N_6Ni^+$ requires 806.4).

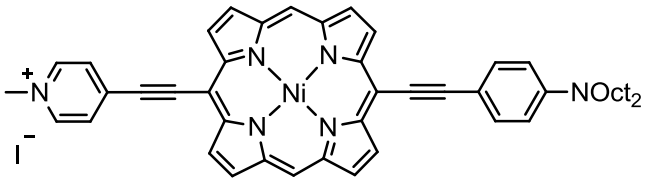

Porphyrin **1b.Ni** was prepared as follows: Porphyrin **1a.Ni** (6.0 mg, 7.4 μmol) was stirred in MeI (1.0 mL). After 6 h, all starting material was consumed according to TLC. The resulting suspension was filtered and washed with ethyl acetate (5 mL), toluene (5 mL), THF (5 mL), CH_2Cl_2 (5 mL), 40–60 °C petrol ether (5 mL) and diethyl ether (5 mL), before drying to give **1b.Ni** as an amorphous dark solid, (6.0 mg, 85%). $\lambda_{max}(CHCl_3)$/nm (log ε) 435 (4.46), 634 (4.18); ^{1}H NMR (400 MHz, DMSO-d_6) δ_H 11.08 (s, 2H), 10.92 (s, 2H), 10.72 (s, 2H), 10.57 (s, 2H), 9.54 (s, 2H), 9.13 (d, 2H, J = 6.4 Hz), 8.77 (d, 2H, J = 6.4 Hz), 7.87 (d, 2H, J = 8.6 Hz), 6.85 (d, 2H, J = 8.9 Hz), 4.36 (s, 3H), 1.7–0.8 (m, 34H); *m/z* (MALDI-ToF) 823.1 ([M]$^+$ 100%, $C_{52}H_{55}N_6Ni^+$ requires 821.4).

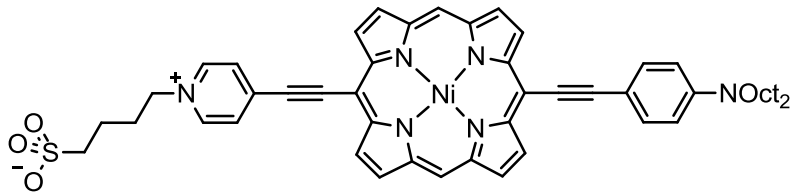

Porphyrin **1c.Ni** was prepared as follows: Porphyrin **1a.Ni** (20.0 mg, 24.8 μmol) and 4-butane sultone (400 μL, 3.96 mmol) in DMF (2 mL) were stirred at 115 °C overnight. The mixture was layered with 40–60 °C petrol ether, and the precipitate washed with ethyl acetate (5 mL), toluene (5 mL), THF (5 mL), CH_2Cl_2 (5 mL), 40–60 °C petrol ether (5 mL) and diethyl ether (5 mL), before drying to give **1b.Ni** as an amorphous dark solid (11 mg, 47%). ^{1}H NMR (400 MHz, DMSO-d_6) δ_H 11.83 (s, 2H), 11.67 (s, 2H), 11.29 (s, 4H), 9.75 (s, 2H), 9.33 (d, 2H, J = 6.9 Hz), 8.96 (d, 2H, J = 6.4 Hz), 7.96 (d, 2H, J = 8.2 Hz), 7.11 (d, 2H, J = 9.2 Hz), 4.72 (t, 2H, J = 6.9 Hz), 2.20-1.80 (m, 42H); *m/z* (MALDI-ToF) 945.5 ([M]$^+$ 100%, $C_{55}H_{60}N_6Ni_1O_3S_1^+$ requires 942.3801).

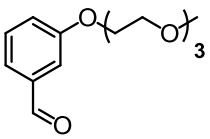

3-(2-(2-(2-Methoxyethoxy)ethoxy)ethoxy)benzaldehyde was prepared according to a literature procedure:[82] 3-Hydroxy benzaldehyde (10.6 g, 86.9 mmol), (2-(2-(2-methoxyethoxy)ethoxy)ethoxy) tosylate (27.6 g, 86.6 mmol) and K_2CO_3 (12 g, 86.9 mmol) were dissolved in MeCN (60 ml) and refluxed for 16 h under an inert atmosphere. The mixture was cooled, diluted with diethyl ether (100 ml), filtered to remove solids and the solvent evaporated. The mixture was purified by reduced pressure distillation to yield the product as a clear oil (18.579 g, 82%). R_f (CH_2Cl_2:MeOH 95:5) 0.20. b.p. 172 °C (7.2×10^{-1} mbar) FT-IR (thin film) cm^{-1}: 2877.42 (s, C-H), 1698.45 (s, C=O). ^{1}H NMR (400 MHz, $CDCl_3$) δ_H 9.97 (s, 1H), 7.46 (m, 2H), 7.40 (m, 1H), 7.22 (m, 1H), 4.20 (m, 2H), 3.89 (m, 2H), 3.75 (m, 2H), 3.69 (m, 2H), 3.65 (m, 2H), 3.56 (m, 2H), 3.38 (s, 3H); ^{13}C NMR (100 MHz, $CDCl_3$) δ_C 192.11, 159.37, 137.72, 130.03, 123.60, 122.06, 112.92, 71.91, 70.86, 70.65, 70.58, 69.59, 67.68, 59.05; *m/z* ESI 291.1 (C_6H_7IN, $[M\text{-}I^-]^+$, requires 291.12, 100 %). *m/z* (HR-FI) 268.1310 ($[M]^+$ 100%, $C_{14}H_{20}O_5^+$ requires 268.1311).

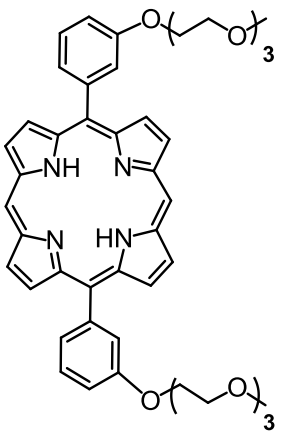

Porphyrin **6.2H** was prepared as follows: After a mixture of dipyrromethane (2.18 g, 15 mmol) in CH_2Cl_2 (2.9 L) was degassed, 3-(2-(2-(2-methoxyethoxy)ethoxy)ethoxy)benzaldehyde (4.00 g, 15 mmol) and TFA (727.3 μL, 9.5 mmol) was added by syringe under an inert atmosphere. The mixture was stirred in the dark for 3 h, DDQ (4.3 g, 19.2 mmol) was added and the mixture neutralised with NEt_3. The mixture was evaporated and poured onto a SiO_2 plug in CH_2Cl_2. The product was eluted in CH_2Cl_2:MeOH; 99:1 to yield the product as a dark solid (2.223 g, 38%). ^{1}H NMR (400 MHz, $CDCl_3$) δ_H 10.33 (s, 2H), 9.41 (d, J = 4.77 Hz, 4H), 9.12 (d, J = 4.77 Hz, 4H), 7.86 (m, 4H), 7.70 (m, 2H), 7.36 (m, 2H), 4.38 (m, 4H), 3.98 (m, 4H), 3.80 (m, 4H), 3.73 (m, 4H), 3.63 (m, 4H), 3.51 (m, 4H) 3.32 (s, 6H) -3.14 (s, 2H).

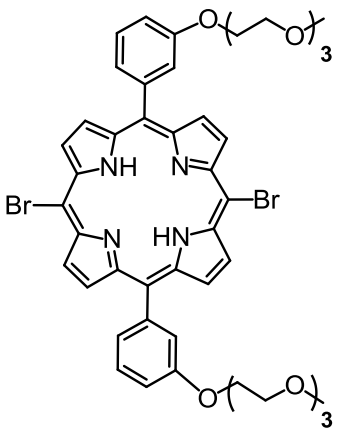

Porphyrin **7.2H** was prepared as follows: NBS (67.5 mg, 380 μmol) in $CHCl_3$ (5 mL) and pyridine (33 μL) was added dropwise to a stirred solution of porphyrin **6** in $CHCl_3$ (10 mL) and pyridine (161 μL) over 30 minutes. The solution was then stirred for a further 15 minutes and the reaction quenched with acetone (240 μL). The solvent was removed *in vacuo* and the product was eluted from a silica plug in DCM:MeOH 99:1 to obtain **7** as a dark solid (180 mg, 100%). ^{1}H NMR (400 MHz, $CDCl_3$) δ_H 9.62 (m, 4H), 8.89 (m, 4H), 7.75 (m, 4H), 7.65 (m, 2H), 7.39 (m, 2H), 4.35 (m, 4H), 3.97 (m, 4H), 3.79 (m, 4H), 3.71 (m, 4H), 3.63 (m, 4H), 3.52 (m, 4H), 3.33 (s, 6H) -2.77 (s, 2H). *m/z* (ESI+) 965.1763 ($[M+H]^+$ 100%, $C_{48}H_{47}N_4Br_2O_8^+$ requires 965.1755).

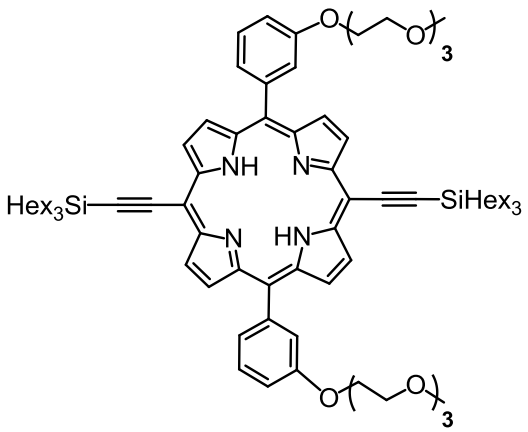

Porphyrin **8** was prepared as follows: Porphyrin **7** (2.48 g, 2.62 mmol) was dried for 1 h *in vacuo* with $Pd_2(dba)_3$ (120 mg, 131 μmol), PPh_3 (137 mg, 524 μmol) and CuI (50 mg, 268 μmol) before addition of Et_3N (25 ml) and toluene (45 ml). The mixture was freeze-pump-thaw degassed and trihexyl silyl acetylene added. The mixture was stirred at 40 °C for 3 hours when all starting material was seen to be consumed by TLC. The mixture was passed through a SiO_2 plug in DCM:MeOH 97:3 and further purified by column chromatography with DCM:MeOH 99:1 to yield porphyrin **8** as a glassy solid (3.0 g, 82 %). ^{1}H NMR (400 MHz, $CDCl_3$) δ_H 9.60 (d, J = 4.8 Hz, 4H), 8.86 (d, J = 4.55 Hz, 4H), 7.77 (m, 4H), 7.66 (m, 2H), 7.37 (m, 2H), 4.35 (m, 4H), 3.99 (m, 4H), 3.80 (m, 4H), 3.73 (m, 4H), 3.64 (m, 4H), 3.51 (m, 4H), 3.33 (s, 6H), 1.79 (m, 12H), 1.57 (m, 12H), 1.40 (m, 36H), 1.01 (m, 12H), 0.91 (m, 18H), -2.75 (s, 2H) *m/z* (MALDI-ToF+) 1400.14 ($[M+H]^+$ 100%, $C_{86}H_{126}N_4Si_2O_8^+$ requires 1399.92).

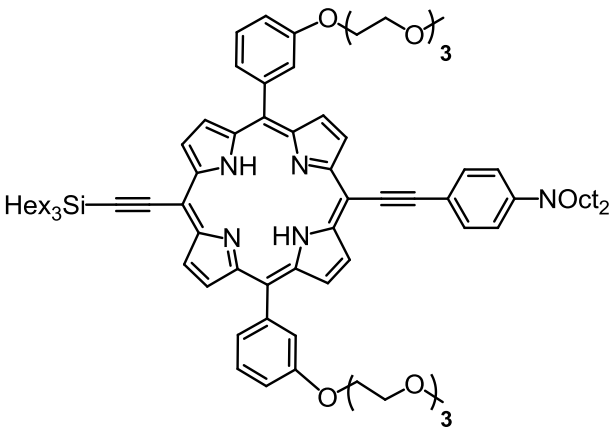

Porphyrin **9** was prepared as follows: TBAF (1.0 M in THF, 179 μL, 179 μmol) was added dropwise to a stirred solution of porphyrin **8** (130 mg, 179 μmol) in $CHCl_3$ (20 mL). When it was determined that some doubly deprotected compound was present, the reaction mixture was poured onto a SiO_2 plug to remove TBAF residues and purified by column chromatography DCM:MeOH 99:1. The dried intermediate was combined with $Pd_2(dba)_3$ (6 mg, 6.7 μmol), PPh_3 (7 mg, 27 μmol) and CuI (2.5 mg, 13.4 μmol) and substituted iodobenzene (670 μmol) before further drying for 1 h *in vacuo*. Et_3N (5 mL) was added and the reaction freeze-pump-thaw degassed. The reaction was stirred at 40 °C until deemed to have gone to completion and purified by column chromatography to yield **9** (98 mg, 54 %). ^{1}H NMR (400 MHz, $CDCl_3$) δ_H 9.66 (d, J = 4.77 Hz, 2H), 8.56 (d, J = 4.77 Hz, 2H), 8.81 (d, J = 4.77 Hz, 4H), 7.87 (d, J = 8.58 Hz, 2H), 7.76 (m, 4H), 7.63 (m, 2H), 7.38 (m, 2H), 7.29 (m, 1H), 6.80 (d, J = 8.58 Hz, 2H), 4.37 (m, 4H), 3.99 (m, 4H), 3.79 (m, 4H), 3.70 (m, 4H), 3.63 (m, 4H), 3.51 (m, 4H), 3.32 (s, 6H), 1.74 (m, 6H), 1.53 (m, 6H), 1.39 (m, 18H), 1.04 (m, 6H), 0.91 (m, 9H), -1.91 (s, 2H) ^{13}C NMR δ_c (125 MHz, $CDCl_3$) 157.8, 148.9, 148.5, 146.7, 143.2, 133.6, 131.86, 128.1, 121.8, 121.5, 144.8, 112.0, 104.3, 108.5, 101.3, 100.6, 90.8, 72.4, 71.4, 71.1, 71.0, 70.3, 68.2, 67.9, 59.5, 51.5, 33.8, 32.3, 32.2, 30.0, 29.8, 27.8, 24.9, 23.2, 14.7, 14.6, 14.3

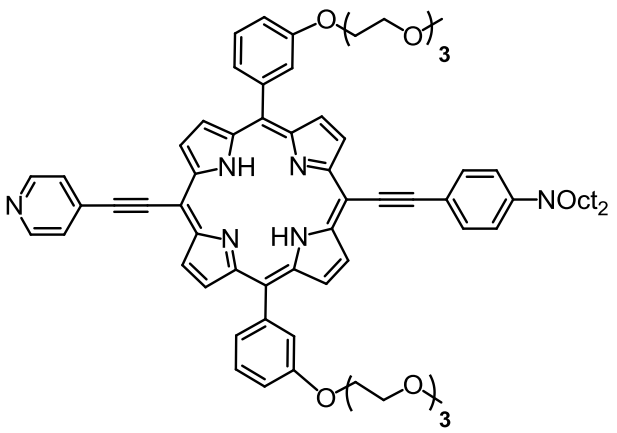

Porphyrin **2a.2H** was prepared as follows: TBAF (1.0 M in THF, 200 μL) was added to porphyrin **9** (98 mg, 68.3 μmol) in CH_2Cl_2, stirred for 5 min and passed through a silica plug. The dried intermediate was combined with $Pd_2(dba)_3$ (3 mg, 3.3 μmol), PPh_3 (3.5 mg, 13.5 μmol) and CuI (1.25 mg, 6.75 μmol) and 4-iodo pyridine (135 mg, 660 μmol) before further drying for 1 h *in vacuo*. Et_3N (5 ml) was added and the reaction freeze-pump-thaw degassed. The reaction was stirred at 40 °C until deemed to have gone to completion and purified by column chromatography to yield **2a.2H** as a dark glassy solid (52 mg, 62 %). λ_{max} (DMF)/nm (log ε) 430 (5.15), 630 (4.64), 712 (4.66). ^{1}H NMR (400 MHz, $CDCl_3$) δ_H 9.67 (d, J = 4.45 Hz, 2H), 9.57 (d, J = 4.45 Hz, 2H), 8.87 (d, J = 4.77 Hz, 2H), 8.82 (m, 4H), 7.87 (m, 4H), 7.80 (m, 4H), 7.69 (m, 4H), 6.78 (m, 2H), 4.38 (m, 4H), 3.99 (m, 4H), 3.82 (m, 4H), 3.73 (m, 4H), 3.64 (m, 4H), 3.50 (m, 4H), 3.32 (s, 6H), 1.25 (m, 25H), 0.92 (m, 9H), -1.80 (s, 2H) ^{13}C NMR (125 MHz, $CDCl_3$/1% pyridine-*d*5) δ_C 157.3, 150.0, 148.5, 142.5, 133.2, 132.0, 127.6, 125.3, 121.7, 121.0, 114.4, 111.5, 108.8, 104.7, 100.7, 97.7, 96.8, 93.8, 90.3, 71.8, 70.9, 70.6, 70.5, 69.8, 67.7, 58.9, 51.0, 31.8, 29.5, 29.3, 27.3, 27.1, 22.6, 14.1 *m/z* (MALDI-ToF) 1227.24 ($[M]^+$ 100%, $C_{77}H_{91}N_6O_8^+$ requires 1226.68).

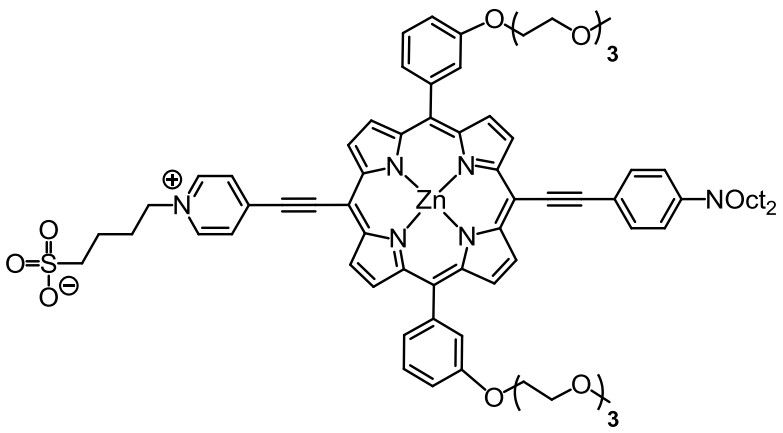

Porphyrin **2c.Zn**, was prepared as follows: $Zn(OAc)_2$ (16 mg, 87 μmol) in MeOH (0.5 mL) was added to porphyrin **2c.2H** (9 mg, 6.6 μmol) in $CHCl_3$ (5 mL) and stirred at 40 °C for 2 hours. The mixture was passed through a SEC column in THF and evaporated to dryness. The resulting solid was precipitated from toluene with petrol ether 40:60 and filtered to yield **2c.Zn** as a black dyestuff (6 mg, 64%). λ_{max} ($CHCl_3$/1% pyridine)/nm (log ε) 742 (4.97), 462 (4.87), ^{1}H NMR (400 MHz, $CDCl_3$) δ_H 9.76 (d, *J* = 4.41 Hz, 2H), 9.65 (d, *J* = 4.41 Hz, 2H), 9.23 (d, *J* = 6.47 Hz, 2H), 8.86 (d, *J* = 4.57 Hz, 2H), 8.79 – 8.75 (m, 4H), 7.87 (d, *J* = 7.78 Hz, 2H), 7.75 – 7.03 (m, 6H), 7.45 (d, *J* = 7.57 Hz, 2H), 6.85 (d, *J* = 8.65 Hz, 2H), 4.70 (t, *J* = 7.28 Hz, 2H), 4.36 (t, *J* = 4.37 Hz, 4H), 3.88 (t, *J* = 4.37 Hz, 4H), 3.68 – 3.65 (m, 4H), 3.59 – 3.56 (m, 4H), 3.53 – 3.50 (m, 4H), 3.41 – 3.38 (m, 4H), 3.19 (s, 6H), 2.61 (t, *J* = 7.88 Hz, 2H), 2.15 (quin, *J* = 7.88 Hz, 2H), 1.74 (quin, *J* = 7.88 Hz, 2H), 1.62 (m, 4H), 1.39 – 1.22 (m, 24H), 0.91 – 0.86 (m, 6H) ^{13}C NMR (125 MHz, $CDCl_3$) δ_C 156.9, 152.8, 150.5, 149.8, 149.5, 144.4, 142.9, 139.5, 135.8, 133.4, 133.1, 132.0, 131.1, 128.5, 127.8, 127.2, 123.6, 120.7, 114.1, 111.5, 71.3, 70.0,69.9, 69.6, 69.1, 67.5, 58.0, 50.3, 50.2, 31.3, 30.0, 28.9, 28.8, 26.8, 26.5, 22.1, 21.7, 13.9

2.10 References

1. K. Ataka and V. A. Pieribone, *Biophys. J.*, 2002, **82**, 509-516.
2. L. B. Cohen, B. M. Salzberg, H. V. Davila, W. N. Ross, D. Landowne, A. S. Waggoner and C. H. Wang, *J. Membr. Biol.*, 1974, **19**, 1-36.
3. R. D. Fields and B. Stevens-Graham, *Science*, 2002, **298**, 556-562.
4. A. Grinvald, L. Anglister, J. A. Freeman, R. Hildesheim and A. Manker, *Nature*, 1984, **308**, 848-850.
5. A. Grinvald and R. Hildesheim, *Nat. Rev. Neurosci.*, 2004, **5**, 874-885.
6. R. K. Gupta, B. M. Salzberg, A. Grinvald, L. B. Cohen, K. Kamino, S. Lesher, M. B. Boyle, A. S. Waggoner and C. H. Wang, *J. Membr. Biol.*, 1981, **58**, 123-137.
7. Y. Barad, H. Eisenberg, M. Horowitz and Y. Silberberg, *Appl. Phys. Lett.*, 1997, **70**, 922-924.
8. J.-x. Cheng, A. Volkmer, L. D. Book and X. S. Xie, *J. Phys. Chem. B*, 2001, **105**, 1277-1280.
9. A. C. Millard, P. J. Campagnola, W. Mohler, A. Lewis, L. M. Loew, G. Marriott and I. Parker, in *Methods Enzymol.*, Academic Press, 2003, vol. Volume 361, pp. 47-69.
10. J. Squier, M. Muller, G. Brakenhoff and K. R. Wilson, *Opt. Express*, 1998, **3**, 315-324.
11. S.-W. Chu, T.-M. Liu, C.-K. Sun, C.-Y. Lin and H.-J. Tsai, *Opt. Express*, 2003, **11**, 933-938.
12. S. Tang, T. B. Krasieva, Z. Chen, G. Tempea and B. J. Tromberg, *J. Biomed. Opt.*, 2006, **11**, 020501-020503.
13. O. Bouevitch, A. Lewis, I. Pinevsky, J. P. Wuskell and L. M. Loew, *Biophys. J.*, 1993, **65**, 672-679.
14. J. Jiang, K. B. Eisenthal and R. Yuste, *Biophys. J.*, 2007, **93**, L26-L28.
15. L. Moreaux, O. Sandre, S. Charpak, M. Blanchard-Desce and J. Mertz, *Biophys. J.*, 2001, **80**, 1568-1574.
16. Y. Wu, F. L. Yeh, F. Mao and E. R. Chapman, *Biophys. J.*, 2009, **97**, 101-109.
17. V. Alain, S. Rédoglia, M. Blanchard-Desce, S. Lebus, K. Lukaszuk, R. Wortmann, U. Gubler, C. Bosshard and P. Günter, *Chem. Phys.*, 1999, **245**, 51-71.
18. C. Barsu, R. Fortrie, K. Nowika, P. L. Baldeck, J.-C. Vial, A. Barsella, A. Fort, M. Hissler, Y. Bretonniere, O. Maury and C. Andraud, *Chem. Commun. (Cambridge, U. K.)*, 2006, 4744-4746.
19. L. M. Loew and L. L. Simpson, *Biophys. J.*, 1981, **34**, 353-365.
20. J. E. Reeve, H. A. Collins, K. D. Mey, M. M. Kohl, K. J. Thorley, O. Paulsen, K. Clays and H. L. Anderson, *J. Am. Chem. Soc.*, 2009, **131**, 2758-2759.
21. M. J. Therien, *Nature*, 2009, **458**, 716-717.
22. A. Rodríguez-Moreno, M. M. Kohl, J. E. Reeve, T. R. Eaton, H. A. Collins, H. L. Anderson and O. Paulsen, *J. Neurosci.*, 2011, **31**, 8564-8569.
23. V. Andresen, S. Alexander, W.-M. Heupel, M. Hirschberg, R. M. Hoffman and P. Friedl, *Curr. Opin. Biotechnol.*, 2009, **20**, 54-62.
24. P. J. Campagnola, H. A. Clark, W. A. Mohler, A. Lewis and L. M. Loew, *J. Biomed. Opt.*, 2001, **6**, 277-286.
25. D. A. Dombeck, M. Blanchard-Desce and W. W. Webb, *J. Neurosci.*, 2004, **24**, 999-1003.
26. D. A. Dombeck, L. Sacconi, M. Blanchard-Desce and W. W. Webb, *J. Neurophysiol.*, 2005, **94**, 3628-3636.
27. A. Lewis, A. Khatchatouriants, M. Treinin, Z. Chen, G. Peleg, N. Friedman, O. Bouevitch, Z. Rothman, L. Loew and M. Sheres, *Chem. Phys.*, 1999, **245**, 133-144.

28. A. C. Millard, L. Jin, J. P. Wuskell, D. M. Boudreau, A. Lewis and L. M. Loew, *J. Membr. Biol.*, 2005, **208**, 103-111.
29. B. A. Nemet, V. Nikolenko and R. Yuste, *J. Biomed. Opt.*, 2004, **9**, 873-881.
30. J. E. Reeve, H. L. Anderson and K. Clays, *Phys. Chem. Chem. Phys.*, 2010, **12**, 13484-13498.
31. B. A. Wilt, L. D. Burns, E. T. Wei Ho, K. K. Ghosh, E. A. Mukamel and M. J. Schnitzer, *Annu. Rev. Neurosci.*, 2009, **32**, 435-506.
32. W. R. Zipfel, R. M. Williams and W. W. Webb, *Nat Biotech*, 2003, **21**, 1369-1377.
33. W. J. Betz, F. Mao and G. S. Bewick, *J. Neurosci.*, 1992, **12**, 363-375.
34. W. J. Betz, F. Mao and C. B. Smith, *Curr. Opin. Neurobiol.*, 1996, **6**, 365-371.
35. K. Wostyn, K. Binnemans, K. Clays and A. Persoons, *Rev. Sci. Instrum.*, 2001, **72**, 3215-3220.
36. A. Grinvald, R. Hildesheim, I. C. Farber and L. Anglister, *Biophys. J.*, 1982, **39**, 301-308.
37. E. Fluhler, V. G. Burnham and L. M. Loew, *Biochemistry*, 1985, **24**, 5749-5755.
38. M. Kee, J. Wuskell, L. Loew, G. Augustine and Y. Sekino, *Brain Cell Biology*, 2008, **36**, 157-172.
39. S. Keinan, M. J. Therien, D. N. Beratan and W. Yang, *J. Phys. Chem. A*, 2008, **112**, 12203-12207.
40. S. M. LeCours, H.-W. Guan, S. G. DiMagno, C. H. Wang and M. J. Therien, *J. Am. Chem. Soc.*, 1996, **118**, 1497-1503.
41. S. Priyadarshy, M. J. Therien and D. N. Beratan, *J. Am. Chem. Soc.*, 1996, **118**, 1504-1510.
42. T.-G. Zhang, Y. Zhao, I. Asselberghs, A. Persoons, K. Clays and M. J. Therien, *J. Am. Chem. Soc.*, 2005, **127**, 9710-9720.
43. J. Y. Huang, A. Lewis and L. Loew, *Biophys. J.*, 1988, **53**, 665-670.
44. A. C. Millard, L. Jin, A. Lewis and L. M. Loew, *Opt. Lett.*, 2003, **28**, 1221-1223.
45. A. L. Obaid, L. M. Loew, J. P. Wuskell and B. M. Salzberg, *J. Neurosci. Methods*, 2004, **134**, 179-190.
46. T. Z. Teisseyre, A. C. Millard, P. Yan, J. P. Wuskell, M.-d. Wei, A. Lewis and L. M. Loew, *J. Biomed. Opt.*, 2007, **12**, 044001.
47. P. Yan, A. C. Millard, M. Wei and L. M. Loew, *J. Am. Chem. Soc.*, 2006, **128**, 11030-11031.
48. S. R. Marder, D. N. Beratan and L. T. Cheng, *Science*, 1991, **252**, 103-106.
49. S. R. Marder, L.-T. Cheng, B. G. Tiemann, A. C. Friedli, M. Blanchard-Desce, J. W. Perry and J. Skindhøj, *Science*, 1994, **263**, 511-514.
50. S. R. Marder, C. B. Gorman, B. G. Tiemann and L. T. Cheng, *J. Am. Chem. Soc.*, 1993, **115**, 3006-3007.
51. F. Meyers, S. R. Marder, B. M. Pierce and J. L. Bredas, *J. Am. Chem. Soc.*, 1994, **116**, 10703-10714.
52. H. T. Uyeda, Y. Zhao, K. Wostyn, I. Asselberghs, K. Clays, A. Persoons and M. J. Therien, *J. Am. Chem. Soc.*, 2002, **124**, 13806-13813.
53. L. Moreaux, T. Pons, V. Dambrin, M. Blanchard-Desce and J. Mertz, *Opt. Lett.*, 2003, **28**, 625-627.
54. L. Moreaux, O. Sandre, M. Blanchard-Desce and J. Mertz, *Opt. Lett.*, 2000, **25**, 320-322.
55. T. Pons, L. Moreaux, O. Mongin, M. Blanchard-Desce and J. Mertz, *J. Biomed. Opt.*, 2003, **8**, 428-431.
56. James E. Reeve, Alex D. Corbett, I. Boczarow, T. Wilson, H. Bayley and Harry L. Anderson, *Biophys. J.*, 2012, **103**, 907-917.
57. G. Gonella, H.-L. Dai, H. C. Fry, M. J. Therien, V. Krishnan, A. Tronin and J. K. Blasie, *J. Am. Chem. Soc.*, 2010, **132**, 9693-9700.

58. J. L. Oudar and D. S. Chemla, *The Journal of Chemical Physics*, 1977, **66**, 2664-2668.
59. J. L. Oudar and H. Le Person, *Opt. Commun.*, 1975, **15**, 258-262.
60. C. Barsu, R. Cheaib, S. Chambert, Y. Queneau, O. Maury, D. Cottet, H. Wege, J. Douady, Y. Bretonniere and C. Andraud, *Org. Biomol. Chem.*, 2009, **8**, 142-150.
61. K. De Mey, J. Perez-Moreno, J. E. Reeve, I. Lopez-Duarte, I. Boczarow, H. L. Anderson and K. Clays, *J. Phys. Chem. C*, 2012, **116**, 13781-13787.
62. G. De Santis, L. Fabbrizzi, M. Licchelli, C. Mangano and D. Sacchi, *Inorg. Chem.*, 1995, **34**, 3581-3582.
63. M. I. Demchuk, A. A. Ishchenko, V. P. Mikhailov and V. I. Avdeeva, *Chem. Phys. Lett.*, 1988, **144**, 99-103.
64. O. S. Wolfbeis and E. Urbano, *J. Heterocycl. Chem.*, 1982, **19**, 841-843.
65. K. Clays and A. Persoons, *Phys. Rev. Lett.*, 1991, **66**, 2980.
66. K. Clays and A. Persoons, *Rev. Sci. Instrum.*, 1992, **63**, 3285-3289.
67. G. Olbrechts, R. Strobbe, K. Clays and A. Persoons, *Rev. Sci. Instrum.*, 1998, **69**, 2233-2241.
68. T. Xu, S. P. Wu, I. Miloradovic, M. J. Therien and J. K. Blasie, *Nano Lett.*, 2006, **6**, 2387-2394.
69. G. Olbrechts, K. Wostyn, K. Clays and A. Persoons, *Opt. Lett.*, 1999, **24**, 403-405.
70. X. Hu, D. Xiao, S. Keinan, I. Asselberghs, M. J. Therien, K. Clays, W. Yang and D. N. Beratan, *J. Phys. Chem. C*, 2010, **114**, 2349-2359.
71. M. Balaz, H. A. Collins, E. Dahlstedt and H. L. Anderson, *Org. Biomol. Chem.*, 2009, **7**, 874-888.
72. M. K. Kuimova, H. A. Collins, M. Balaz, E. Dahlstedt, J. A. Levitt, N. Sergent, K. Suhling, M. Drobizhev, N. S. Makarov, A. Rebane, H. L. Anderson and D. Phillips, *Org. Biomol. Chem.*, 2009, **7**, 889-896.
73. A. C. Millard, M. Terasaki and L. M. Loew, *Biophys. J.*, 2005, **88**, L46-L48.
74. V. Krishnan, A. Tronin, J. Strzalka, H. C. Fry, M. J. Therien and J. K. Blasie, *J. Am. Chem. Soc.*, 2010, **132**, 11083-11092.
75. H. Nojima, T. Sasaki and I. Kimura, *Brain Res.*, 2000, **852**, 233-238.
76. C. Eggeling, J. Widengren, R. Rigler and C. A. M. Seidel, *Anal. Chem.*, 1998, **70**, 2651-2659.
77. R. A. Hoebe, C. H. Van Oven, T. W. J. Gadella, P. B. Dhonukshe, C. J. F. Van Noorden and E. M. M. Manders, *Imaging & Microscopy*, 2007, **9**, 32-34.
78. P. J. Campagnola and L. M. Loew, *Nat Biotech*, 2003, **21**, 1356-1360.
79. P. Pantazis, J. Maloney, D. Wu and S. E. Fraser, 2010, **107**, 14535-14540.
80. E. Dahlstedt, H. A. Collins, M. Balaz, M. K. Kuimova, M. Khurana, B. C. Wilson, D. Phillips and H. L. Anderson, *Org. Biomol. Chem.*, 2009, **7**, 897-904.
81. H. L. Anderson, *Tetrahedron Lett.*, 1992, **33**, 1101-1104.
82. J. M. McFarland and M. B. Francis, *J. Am. Chem. Soc.*, 2005, **127**, 13490-13491.

Chapter 3

Orientational Distribution of Dyes in Membranes

Summary

Numerous dyes are available or under development for probing the structural and functional properties of biological membranes. Exogenous chromophores adopt a range of orientations when bound to membranes and the orientation of these molecules has a drastic effect on their biophysical behaviour. Here, we present a method which employs optical anisotropy data from three polarisation imaging techniques to establish the distribution of orientations adopted by molecules in monolayers and bilayers. The resulting probability density functions, which contain the preferred molecular tilt μ and distribution breadth γ are more informative than an average tilt angle $<\varphi>$ which is found by previous studies.

We describe a methodology for the extraction of anisotropy data through a novel image processing technology that decreases the error in polarisation measurements by about a factor of four.[†] We use this technique to compare di-4-ANEPPS and di-8-ANEPPS, both dipolar dyes, using data from polarised 1-photon fluorescence, 2-photon fluorescence and second harmonic generation imaging. We find that di-8-ANEPPS has a lower tilt μ but the same distribution width, γ. We find the distribution of tilt angles taken by di-4-ANEPPS in two phospholipid membrane models: giant unilamellar vesicles and water-in-oil droplet monolayers. Both models result in similar distribution functions with average tilt angles of 52° and 47°, respectively.

[†]Part of the work in this chapter was published in: JE Reeve, AD Corbett, I Boczarow, T Wilson, H Bayley, HL Anderson, *Biophys. J.*, 2012, **103**, 907-917.

3.1 Introduction

Dyes are versatile reporters of structure and activity in biological membranes. However, the behaviour of dyes bound to membranes is influenced by their orientation.[1–5] The intramembrane tilt angle, φ, is the angle between the long axis of a molecule and the normal of the membrane plane (Figure 1A). In most cases, the long axis of the dye molecule can be assumed to be coincident with its transition dipole moment (TDM). Previously, studies which have quantified tilt angles have employed solid-state NMR,[6–8] electron paramagnetic resonance,[9, 10] polarisation coherent anti-Stokes Raman scattering,[11] infra-red dichroism,[12–15] polarisation anisotropy fluorescence[16–26] and second harmonic generation (SHG) microscopy.[11, 27–34] Experimental data from these investigations have been complemented by computational methods for modelling molecules in membranes.[8, 35–38] Further, the attachment of dyes onto larger substrates, such as proteins, has provided a method for investigating the tilt of membrane proteins.[33] Change in tilt angle can also be used to monitor biophysical processes such as membrane potential changes: Voltage-sensitive dyes such as RH421 rely on a reorientation mechanism for their 'slow' voltage-sensitive response as an applied electric field changes their alignment in the membrane.[39, 40]

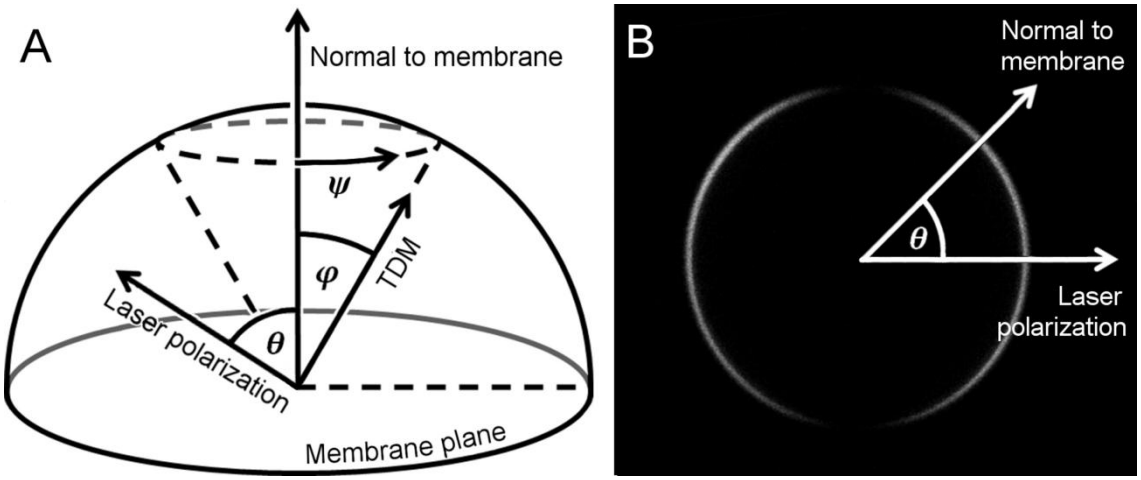

Figure 1 (A) The transition dipole moment (TDM) of each molecule is tilted at an angle φ from the membrane normal and an angle ψ around it. The intensity of fluorescence or SHG from the ensemble of dyes is dependent on the angle away from the laser polarisation, θ. (B) Variation of SHG from di-4-ANEPPS which varies periodically with θ around the equator of a model membrane (giant unilamellar vesicle). The shape of this angular intensity function, when fit to a model, allows extraction of trigonometric moments of the tilt distribution – $P_{tilt}(\varphi)$. The direction of laser excitation is co-linear with the direction of signal detection and perpendicular to the plane of the image in (B).

The most intuitive description of molecular alignment, the expected tilt angle $\langle\varphi\rangle$, may be found by substituting $f(\varphi)=\varphi$ into the following general expression:

$$\left\langle f(\varphi)\right\rangle = \int_0^{\pi} f(\varphi) P_{tilt}(\varphi) d\varphi \qquad \text{(Eq. 1)}$$

Where $P_{tilt}(\varphi)$ is the tilt angle probability density function (PDF) over all available orientations. Measurements of orientation-dependent phenomena typically rely on simplifications of the PDF, to find $\langle\varphi\rangle$ but do not reach a general solution for $P_{tilt}(\varphi)$ itself. This sheds little light on the nature of the system since identical $\langle\varphi\rangle$ values may arise from different PDFs, as illustrated in Figure 2. We introduce two new parameters, μ and γ, which, when included in the tilt PDF, allow a more complete description of the tilt distribution of any species in a biological membrane. The parameter μ describes the preferred, or lowest enthalpy, molecular state before the density of available states is considered, while γ is the range of states around μ that the dye is capable of adopting, i.e. the breadth of the distribution (see Figure 8). Furthermore,

comparison or unification of the physical techniques which extract dye orientation from experiment requires consensus on the form of the tilt PDF. By choosing a specific case, a uniaxial dye, and using a more accurate image processing methodology, we compare the tilt PDF of a molecule in two model phospholipid membranes through the application of three methods in parallel: polarised 1-photon fluorescence, 2-photon fluorescence and SHG imaging (Figure 1 *B*).

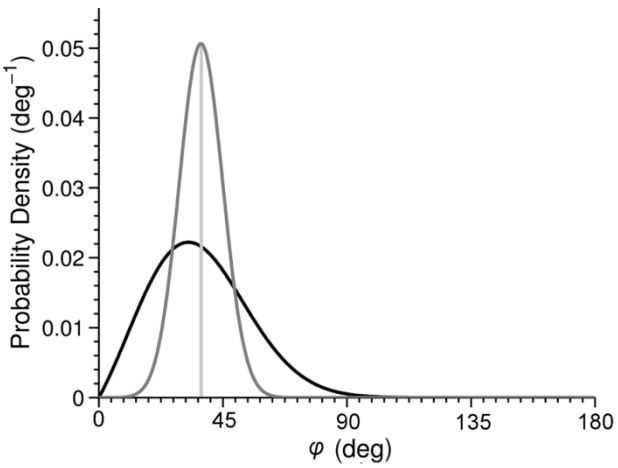

Figure 2 Two different probability density functions can produce identical <φ> values (*vertical line*). Therefore, measures of <φ> alone do not adequately describe the system. For examples, these two probability density functions differ in where the lowest energy molecular tilt (μ) lies—normal to the membrane (*black*) or tilted by 37° (*gray*).

3.2 Theory

3.2.1 Tilt Angle from Ratiometric Imaging

Dipolar chromophores are uniquely suited to optical investigation through the use of one- and two-photon linear dichroism, as well as polarisation-dependent SHG. For most dyes, the angle between the long molecular axis and optical transition dipole moment (TDM or dominant hyperpolarisability tensor element) is small. The fluorescence or SHG signal observed from any point in a dye-doped membrane is a function of the tilt distribution of chromophores in the

membrane, $P_{tilt}(\varphi)$, and the angle between the membrane normal and the polarisation of the excitation source, θ (Figure 1).[19, 23, 30, 31]

In general, linear dichroism is a consequence of the photoselection rule: Light absorbed by a molecule is proportional to the projection of its TDM vector onto the electric field vector of the excitation field. Application of the one- and two-photon photoselection rule requires that we assume dyes have a single, well-defined TDM at the wavelength of excitation.[41] We avoid effects resulting from polarisation of the emission by excluding polarisers from the collection channels and choosing an experimental set-up with $D_{\infty h}$ symmetry. We ensure the highest possible polarisation purity through inclusion of a 1000:1 polarising beamsplitter as the penultimate optic before the objective, and we use a relatively low *N.A.* lens (objective *N.A.* = 0.8, see Methods) to prevent the convergence of the beam from generating significant off-axis polarisation.

The direction of laser excitation is co-linear with the direction of signal detection, and the whole set-up is radially symmetric with respect to this principal axis (into the page, Figure 1B). We choose this arrangement so that in the far field, fluorescence anisotropy does not vary with angular displacement, θ: The geometric arrangement of the TDM, in the plane perpendicular to the beam axis, means that projection of the toroidal emission onto the detector is independent of θ.[41]

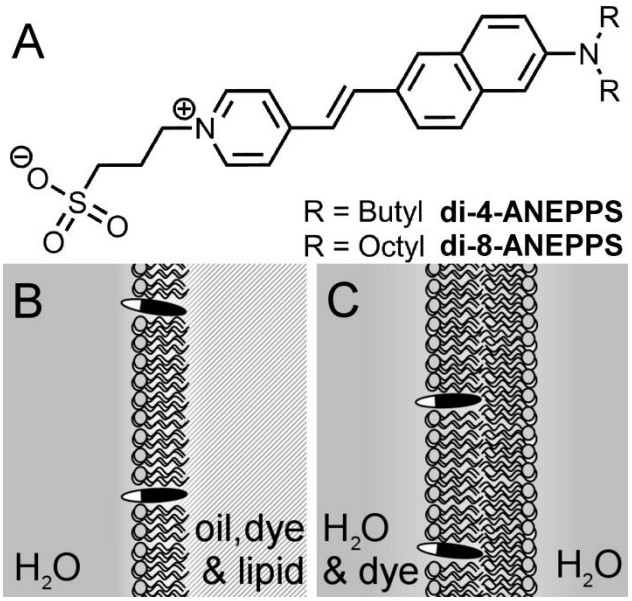

Figure 3 (A) The structure of di-4-ANEPPS and di-8-ANEPPS, the dyes used in this study and the membrane models used in this experiment: Phospholipid DPhPC (*lipid*) bilayers incorporating ANEPPS dyes (*black and white lozenges*) in (B) the water droplet model and (C) GUVs.

In the case of SHG images (where all output light is collected with condensing optics), we only consider the angular dependence of scattered second harmonic light from dyes possessing a single dominant hyperpolarisability vector, β_{zzz}. To satisfy these requirements, we use ANEPPS chromophores (Figure 3 A),[42] which are dipolar molecules with a single dominant TDM and β_{zzz} directed along the primary molecular axis.[30, 31] di-4-ANEPPS and di-8-ANEPPS are suitable for imaging in each of the modalities described here and have been shown to be useful voltage-sensitive plasma membrane reporters.[42]

A dilute solution of chromophores ensures that dye molecules act as individual radiators or scatterers within the membrane and we assume that in this regime, there is no aggregation and thus no effect of concentration on tilt angle.

3.2.2 Tilt Angle Intensity Functions

Absorption and subsequent fluorescence of polarised light is governed by the photoselection rule[19, 41]

$$I_{1PF}(\alpha) = I_0 \cos^2 \alpha \qquad \text{(Eq. 2)}$$

for an isolated dipolar fluorophore with its TDM oriented at an angle α to the polarisation of the excitation. The relationship between the tilt of the population of chromophores and polarisation of laser light can be found by starting with the molecular dipole for a uniaxial absorber

$$\vec{\mu} = \begin{bmatrix} 0 \\ 0 \\ |\mu| \end{bmatrix} \qquad \text{(Eq. 3)}$$

and performing a series of rotations, taking into account the tilt (φ), rotation around the normal at that tilt (ψ) and the rotation relative to the laboratory frame (θ), shown in Figure 1:

$$\vec{\mu}' = \begin{bmatrix} 1 & 0 & 0 \\ 0 & \cos\theta & -\sin\theta \\ 0 & \sin\theta & \cos\theta \end{bmatrix} \begin{bmatrix} \cos\psi & \sin\psi & 0 \\ -\sin\psi & \cos\psi & 0 \\ 0 & 0 & 1 \end{bmatrix} \begin{bmatrix} 1 & 0 & 0 \\ 0 & \cos\varphi & -\sin\varphi \\ 0 & \sin\varphi & \cos\varphi \end{bmatrix} \vec{\mu} \qquad \text{(Eq. 4)}$$

For a polarised electric field oscillating collinearly with the dipole,

$$\overrightarrow{E_{\square}} = \begin{bmatrix} 0 \\ 0 \\ E \end{bmatrix} \qquad \text{(Eq. 5)}$$

photoselection may be expressed as a dot product:

$$\cos\alpha = \frac{\vec{\mu}' \square \boldsymbol{E}}{|\vec{\mu}'||\boldsymbol{E}|} \qquad \text{(Eq. 6)}$$

Integration over the solid angle (ψ), rotation on its own axis (η), and the population of tilted dyes (φ) yields an expression for the angular dependence of emission for a distribution of dyes, where I_0 is emission at optimum alignment:

$$I_{1\mathrm{PF}}(\theta,\varphi) = I_0 \int_0^{2\pi} d\eta \int_0^{2\pi} d\psi \int_0^{\pi} d\varphi P_{tilt}(\varphi) \cos^2\alpha \qquad \text{(Eq. 7)}$$

After substituting and normalising,

$$I_{1\mathrm{PF}}(\theta,\varphi) = \frac{I_0}{4\pi^2} \int_0^{2\pi} d\eta \int_0^{2\pi} d\psi \int_0^{2\pi} d\varphi P_{tilt}(\varphi) \left(\cos\theta\cos\varphi - \sin\theta\cos\psi\sin\varphi\right)^2 \qquad \text{(Eq. 8)}$$

which simplifies to give an expression for the angular dependence of 1-photon fluoresence:

$$I_{1\mathrm{PF}}(\theta,\varphi) = I_0 \left(\cos^2\theta \left\langle \cos^2\varphi \right\rangle + \frac{1}{2}\sin^2\theta \left\langle \sin^2\varphi \right\rangle \right) \qquad \text{(Eq. 9)}$$

Therefore, through a similar approach to that of Corry *et al.*,[19] we find that the one-photon fluorescence (1PF) of an ensemble of dyes with a given $P_{tilt}(\varphi)$ distribution at an angle θ from the excitation polarisation depends on the expression:

$$I_{1\mathrm{PF}}(\theta,\varphi) \propto \left(\vartheta_{1PF} \cos^2\theta + \frac{1}{2}\sin^2\theta \right) \qquad \text{(Eq. 10)}$$

where the angular intensity function's shape is determined by the relative contributions of the $\cos^2\theta$ and $\frac{1}{2}\sin^2\theta$ terms. We call the ratio of these terms the 1PF order parameter, $\vartheta_{1PF} = \left\langle \cos^2\varphi \right\rangle / \left\langle \sin^2\varphi \right\rangle$ which in turn is a function of the tilt angle PDF (Eq. 1).

Two-photon linear dichroism depends on the square of the one-photon photoselection rule since the absorption of two photons requires two photoselection events. For two-photon excitation of a dipolar dye, we assume that absorption is dominated by a single tensor element, such that we may treat the molecule as having a single two-photon pseudo-TDM, directed along its molecular axis (23). Therefore, the two-photon selection rule[18, 19, 41]

$$I_{2\mathrm{PF}}(\alpha) = I_0' \cos^4\alpha \qquad \text{(Eq. 11)}$$

when taking the appropriate rotations yields the dependence

$$I_{2PF}(\theta,\varphi) = \frac{I_0}{4\pi^2}\int_0^{2\pi} d\eta \int_0^{2\pi} d\psi \int_0^{2\pi} d\varphi P_{tilt}(\varphi)\left(\cos\theta\cos\varphi - \sin\theta\cos\phi\sin\varphi\right)^4 \qquad \text{(Eq. 12)}$$

integrated,

$$I_{2PF}(\theta,\varphi) = I_0\left(\cos^4\theta\left\langle\cos^4\varphi\right\rangle + 3\sin^2\theta\cos^2\theta\left\langle\cos^2\varphi\sin^2\varphi\right\rangle + \frac{3}{8}\sin^4\theta\left\langle\sin^4\varphi\right\rangle\right) \qquad \text{(Eq. 13)}$$

and simplified yields the following expression for the angular dependence of two-photon fluorescence:

$$I_{2PF}(\theta,\varphi) \propto I_0^{'}\left(\vartheta_{2PF}\cos^4\theta + \frac{3}{16}\sin^2 2\theta + \frac{3}{8}\vartheta'_{2PF}\sin^4\theta\right) \qquad \text{(Eq. 14)}$$

Where the 2PF order parameters are defined $\vartheta_{2PF} = \left\langle\cos^4\varphi\right\rangle / \left\langle\sin^2 2\varphi\right\rangle$ and $\vartheta'_{2PF} = \left\langle\sin^4\varphi\right\rangle / \left\langle\sin^2 2\varphi\right\rangle$ and are trigonometric moments of a probability density function, (see later Eq. 18B and 18C respectively).

As with one- and two-photon fluorescence, the angular dependence of SHG is a consequence of photoselection. For SHG, since the interaction of light with the tilted chromophores is via coherent scattering rather than absorption, the mechanism of photoselection is different. Output SHG intensity is a function of the second order nonlinear susceptibility tensor, $\chi^{(2)}$ normal to the membrane, which is derived through the projection of molecular contributions to the hyperpolarisability onto the membrane frame.[31] Since SHG is a second order nonlinear phenomenon, we arrive at a tilt-angle dependent expression for $\chi^{(2)}$ by performing the appropriate rotations on β, the rank 3 tensor which describes the molecule's hyperpolarisability. We find that the induced second harmonic dipole moment $\mu^{(0)}_{2\omega,z}$ across the membrane has two major contributions:

$$\mu_{2\omega,z}^{(0)} = \tfrac{1}{2} E_\omega^2 \left(\beta_z \cos^2\theta + \beta_t \sin^2\theta \right) \quad \text{(Eq. 15)}$$

where $\beta_z = \langle \cos^3\varphi \rangle B_z$ and $\beta_t = \tfrac{1}{2}\langle \sin^2\varphi \cos\varphi \rangle B_z$, are the tilt angle dependent hyperpolarisabilities converted from contributions in the molecular frame B_z to the membrane frame and E_ω is the excitation field amplitude. Since total power radiated parallel, $P_{SHG}^{\parallel}$, scales as the square of induced polarisation, and by transforming to the laboratory frame, we arrive at the relation

$$P_{SHG}^{\parallel} \propto \mu_{2\omega,z}^{(0)2} \cos^2\theta \quad \text{(Eq. 16)}$$

thus leading us to an expression for the angular dependence of SHG parallel to the incident field: [29, 30]

$$I_{SHG}^{\parallel}(\theta,\varphi) \propto \left(\cos^3\theta + 3\vartheta_{SHG} \sin^2\theta \cos\theta \right)^2 \quad \text{(Eq. 17)}$$

With a SHG order parameter $\vartheta_{SHG} = \tfrac{1}{2}\langle \sin^2\varphi \cos\varphi \rangle / \langle \cos^3\varphi \rangle$. From this collection of models, if given experimental data for how intensity, *I*, varies with θ, we may extract the four order parameters:

$$\vartheta_{1PF} = \langle \cos^2\varphi \rangle / \langle \sin^2\varphi \rangle \quad \text{(Eq. 18A)}$$

$$\vartheta_{2PF} = \langle \cos^4\varphi \rangle / \langle \sin^2 2\varphi \rangle \quad \text{(Eq. 18B)}$$

$$\vartheta'_{2PF} = \langle \sin^4\varphi \rangle / \langle \sin^2 2\varphi \rangle \quad \text{(Eq. 18C)}$$

$$\vartheta_{SHG} = \tfrac{1}{2}\langle \sin^2\varphi \cos\varphi \rangle / \langle \cos^3\varphi \rangle \quad \text{(Eq. 18D)}$$

Previous studies have only extracted one of these order parameters and subsequently assumed the simplest possible distribution of tilt angles. For example, the assumption that all molecules lie at only one angle φ from the membrane normal (as in Figure 1) results in the simplification: $\langle f(\varphi) \rangle = f(\langle \varphi \rangle)$. Furthermore, although estimated values of $\langle \varphi \rangle$ may be compared between compounds, it is not particularly instructive without more information on the breadth of the

distribution or the preferred tilt of the molecule (Figure 2). More recent studies have taken tilt distribution into account—Benninger et al.[18] found $\langle \cos^2 \varphi \rangle$ and $\langle \cos^4 \varphi \rangle$ moments from 2PF images, but experimental imprecision left them unable to resolve a parameterised distribution function. In the study of a densely incorporated dye, Blasie and coworkers excluded particular distributions by combining SHG imaging with grazing-incidence X-Ray diffraction, but were left with a range of possible distributions due to experimental constraints.[34]

3.3 Methods

3.3.1 Experimental Models

The order parameters in Eq. 18, A–D which determine the variation of I with θ can be extracted from experimentally obtained images of membranes aligned over a range of angles relative to the excitation field. Laser scanning confocal microscopy images of spherical cell models give the signal intensity of a membrane over the full range of θ, which may then be fit to Eq. 18, A–D, to yield the relevant order parameter. We choose spherical cellular models, imaging at the equator such that the cross-sectional image is a circle or ellipse with periodically varying intensity around its circumference.

We have previously used a basic cellular model, which is constructed from droplets of water in oil encapsulated by a lipid monolayer (Figure 3B), providing a stable system that is easily imaged.[43] Here, we show that this model provides a robust, reproducible, high-throughput method of quantifying tilt angle with the minimum of specialist equipment. The drawbacks are that the oil-water phase boundary may cause lensing effects which can divert some emitted light

or distort the point-spread function required for 2PF and SHG modes. Further, oil may partition into the membrane, influencing the orientation of the embedded dye molecules.

The second model, giant unilamellar vesicles (GUVs, Figure 3C), is more biologically relevant but has the disadvantage of being less robust and prone to SHG fading over time as dyes undergo flip-flop.[32] GUVs are more mobile and deformable than water droplets and must be immobilised or else image distortion occurs during scanning microscopy. GUVs also require a more sophisticated fabrication, have a limited lifetime and are more difficult to produce in a quantity suitable for high-throughput imaging.

3.3.2 Image Processing

To find the tilt-angle dependent order parameters ϑ_{1PF}, ϑ_{2PF}, ϑ'_{2PF} and ϑ_{SHG} (Eq. 18, A–D) with a high degree of accuracy, we develop a novel image processing methodology (Figure 4, and Software Outline). Our algorithm treats the image as a surface and fits the data to a two-dimensional function. This polar fitting approach has the advantage of taking the entire weighted radial cross-sectional circumference into account, so that all pixels in the image contribute to the fit (as opposed to user-defined region-of-interest approaches, such as taking an oval profile,[1, 18, 25, 30] which are prone to human bias and sampling error). A successful fit produces a parameterised model which may be plotted as either a 2D intensity plot or 3D surface (Figure 5D, Figure 6, B and D) for comparison with the original image (Figure 6, A and C).

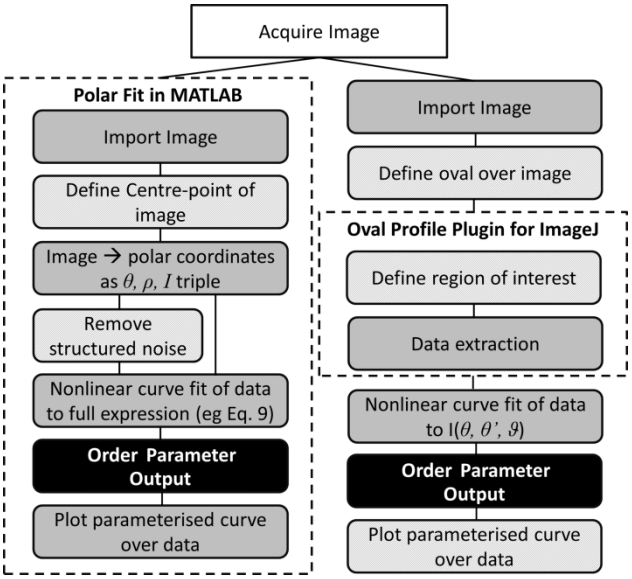

Figure 4 Flow chart for image processing with our polar fitting technique (*left*) and the oval profile technique (*right*), showing the reduction in the number of essential manual steps which may lead to error. Experimental steps (*white*), automatic (*dark gray*) and manual steps (*light gray*) result in the desired output (*black*). In each case the dashed box represents the software used to process the image – steps outside of the dashed box require manual processing.

Images were processed by a custom-made MATLAB® program.[44] Once the circle centre-point is either manually or semi-automatically defined, the software expresses the image in polar coordinates, whereupon each pixel is described by an angle from the excitation polarisation, $\boldsymbol{\theta}$, a radius from the center of the circle, $\boldsymbol{\rho}$ and an intensity, $\boldsymbol{I}$. This expression of the image in polar coordinates may then be fit to Eq. 19 (Figure 5D):

$$\boldsymbol{I} = aI\left(\boldsymbol{\theta},\theta',\vartheta\right)R\left(\boldsymbol{\rho},\rho',\sigma,\varepsilon,\boldsymbol{\theta},\theta''\right)+\nu_n \qquad \text{(Eq. 19)}$$

where bold terms are input data and others such as a, the amplitude of the signal, are fitting parameters. $I\left(\boldsymbol{\theta},\theta',\vartheta\right)$ is the angular intensity function around the circumference (see Tilt Angles from Ratiometric Imaging and Figure 5A), which depends on θ', the direction of polarisation relative to the image frame and ϑ the characteristic order parameter of the dye in the membrane. $R\left(\boldsymbol{\rho},\rho',\sigma,\varepsilon,\boldsymbol{\theta},\theta''\right)$ defines the radial form, a Gaussian of breadth σ centered at a distance ρ' from

the centre-point (Figure 5B) with eccentricity ε along a major axis θ'' from the laboratory frame. v_n is the background or shot noise. The full expressions are presented as Eq. 22–24.

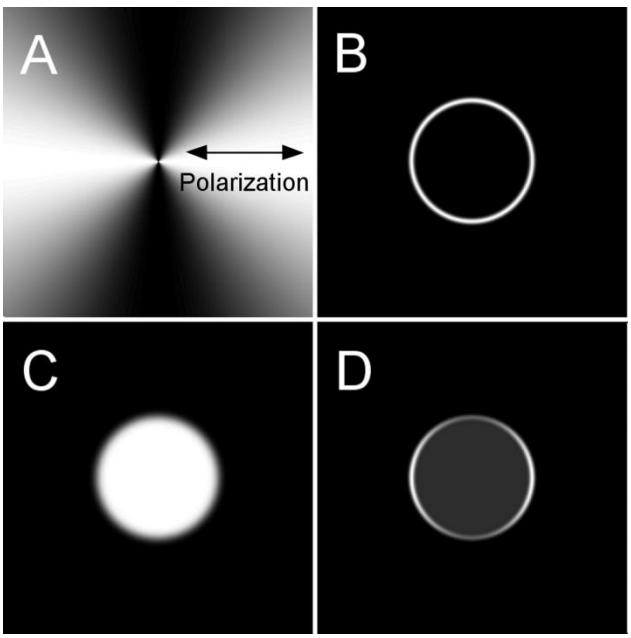

Figure 5 2-dimensional (A) angular function modelled with $\theta' = \pi/2$ (relative to polarisation, *double-headed arrow*), $\vartheta_{IPF} = \pi/2$, (B) radial function modelled with $\rho' = 100$ pixels, $\sigma = 10$ pixels, $\varepsilon = \theta'' = 0$ and (C) background function modelled with $\sigma' = 5$ pixels and $\varepsilon = \theta'' = 0$. Their combination results in equations 10 and 11 which are represented by function (D).

Unlike SHG images, where signal is only generated from ordered regions, 1PF and 2PF images suffered from both structured and isotropic background that required the inclusion of a further modifier (besides the additional order parameter ϑ' for 2PF images). In Eq. 20, b is a multiplier that determines the contribution of $E(\boldsymbol{\rho},\rho',\sigma',\varepsilon,\boldsymbol{\theta},\theta'')$, a radial error function with breadth determined by σ'.

$$\boldsymbol{I} = aI(\boldsymbol{\theta},\theta',\vartheta,\vartheta')R(\boldsymbol{\rho},\rho',\sigma,\varepsilon,\boldsymbol{\theta},\theta'') + bE(\boldsymbol{\rho},\rho',\sigma',\varepsilon,\boldsymbol{\theta},\theta'') + v_n \qquad \text{(Eq. 20)}$$

The models are parameterised using a nonlinear least squares minimisation, producing either 7 or 10 outputs, one of which is the order parameter. Re-insertion of these parameters into the model reconstructs the fit as an idealised image which may then be assessed for goodness of fit (Figure 5D and Figure 6, A and B).

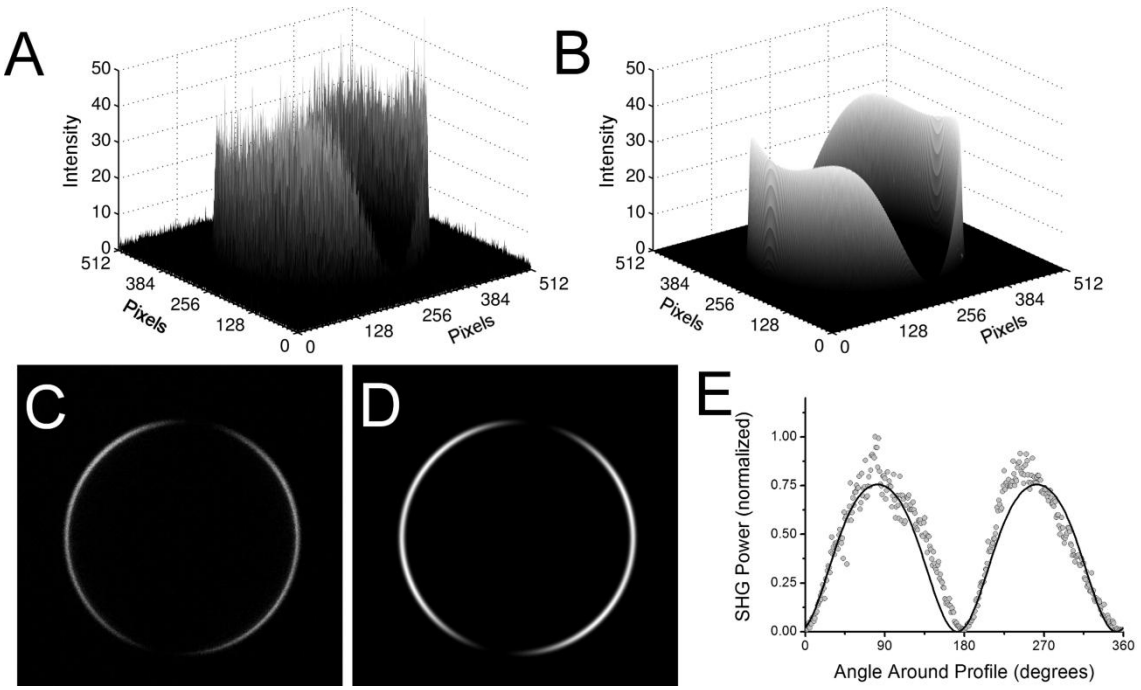

Figure 6 Analysis of a SHG image of di-4-ANEPPS in a monolayer of DPhPC on the surface of a water droplet in oil. The polar fitting technique renders the SHG image as a surface (A), with signal intensity plotted on the z-axis and pixel location on the x- and y-axis. The parameterised model (B) is also plotted for comparison. Similarly, the 2D SHG image (C) is plotted alongside the 2D parameterised model (D) for comparison, image dimensions: 300 × 300 μm. We also include a plot from analysis of the image by the oval profile method (E). This method considers only a subset of data points (*gray points*), which do not accurately represent the image and subsequently is prone to experience more error and a poorer fit (*black line*).

3.3.3 Polar fitting equations

The image data to be fit are delivered to the fitting algorithm as (θ,ρ,I) triples, where every pixel in the images is described by its angular displacement (θ) from the laboratory (image) frame, its distance (ρ) from the centre-point of the membrane model and its intensity value (I).

The general model

$$\boldsymbol{I} = aI\left(\boldsymbol{\theta},\theta',\vartheta\right)R\left(\boldsymbol{\rho},\rho',\sigma,\varepsilon,\boldsymbol{\theta},\theta''\right)+\nu_n \qquad \text{(Eq. 21)}$$

is parameterised to best reflect the data in MATLAB®[44] via a conjugate gradient minimisation (trust-region reflective), giving a value for the structure factor (ϑ) as an output. More specifically, we fit SHG images to the following model:

$$\boldsymbol{I} = a\left(\cos^3\left(\boldsymbol{\theta}+\theta'\right)+3\vartheta_{SHG}\sin^2\left(\boldsymbol{\theta}+\theta'\right)\cos\left(\boldsymbol{\theta}+\theta'\right)\right)^2\left(\exp\left(\frac{-\left(\boldsymbol{\rho}-\frac{\rho'}{1+\varepsilon\cos\left(\boldsymbol{\theta}+\theta''\right)}\right)^2}{2\sigma}\right)\right)+\nu_n \qquad \text{(Eq. 22)}$$

Where the blue factor defines the angular dependence of the SHG signal, the red factor describes a Gaussian at distance ρ from the center of the image with width σ and the pink term allows the circular Gaussian described by the red term to be modified to an ellipse of eccentricity ε, at an angle θ'' from the laboratory frame. Any overall background is accounted for by ν_n. We fit 1PF images to the model:

$$I = a\left(\vartheta_{1PF}\cos^2(\theta+\theta') + \frac{1}{2}\sin^2(\theta+\theta')\right)\exp\left(\frac{-\left(\rho - \frac{\rho'}{1+\varepsilon\cos(\theta+\theta'')}\right)^2}{2\sigma}\right) + b\,\mathrm{erfc}\left(\frac{-\left(\rho - \frac{\rho'}{1+\varepsilon\cos(\theta+\theta'')}\right)^2}{\sigma'}\right) + \nu, \quad \text{(Eq. 23)}$$

and 2PF images to the model:

$$I = a\left(\vartheta_{2PF}\cos^4(\theta+\theta') + \frac{3}{16}\sin^2(2(\theta+\theta')) + \frac{3}{8}\vartheta'_{2PF}\sin^4(\theta+\theta')\right)\exp\left(\frac{-\left(\rho - \frac{\rho'}{1+\varepsilon\cos(\theta+\theta'')}\right)^2}{2\sigma}\right) + b\,\mathrm{erfc}\left(\frac{-\left(\rho - \frac{\rho'}{1+\varepsilon\cos(\theta+\theta'')}\right)^2}{\sigma'}\right) + \nu_n \quad \text{(Eq. 24)}$$

Where the blue factor defines the angular dependence of the 1 or 2PF signal (see main text, equations 10 and 14), the red factor describes a Gaussian at distance ρ from the center of the image with width σ and the green term describes a filled circle of intensity b which accounts for differences in the signal background from inside and outside the model membrane. The pink terms allows the circular form described by the red and green terms to be modified to an ellipse of eccentricity ε, at an angle θ'' from the laboratory frame. Any overall background is accounted for by ν_n.

Materials used, fabrication of the membrane models and the microscopy set-up are described in the experimental section.

3.4 Results

3.4.1 Polar Fitting vs. Oval Profile

Our polar fitting approach to image analysis (Figure 6, B and C) confers a significantly greater accuracy compared to the standard oval profile approach (Figure 6D). We eliminate a degree of

the human error involved in ellipsoid definition and use significantly more data points (by fitting the Gaussian weighted profile of the circular lineform) resulting in a four-fold improvement in the reproducibility of the fit (Table 1).

Table 1 Order parameters for di-4-ANEPPS in GUVs found by three image processing methods and the error associated with each technique for both analysis of one image and for a batch of images (n = 7)

	One Image		Twelve Images	
	ϑ_{1PF}	± Error	ϑ_{1PF}	± Error
Oval Profile	0.729	0.019 (2.6%)	0.747	0.078 (10.4%)
Polar Manual	0.715	0.0027 (0.4%)	0.725	0.018 (2.5%)
Polar Semi-Automated	0.716	0.0013 (0.2%)	0.727	0.018 (2.5%)

Furthermore, the fitting approach is less influenced by noise overlapping the equator since we consider the image in its entirety (Figure 7). The oval profile method relies on data points extracted from beneath a user-defined oval placed over the region of interest. Our polar fitting 'manual' technique requires that the user specifies only the extremities of the oval.

The software uses this input to calculate the centre-point, and then fits an oval to the image. The semi-automated approach operates on a similar algorithm; however, the image is thresholded, then extremities of the oval are found automatically.

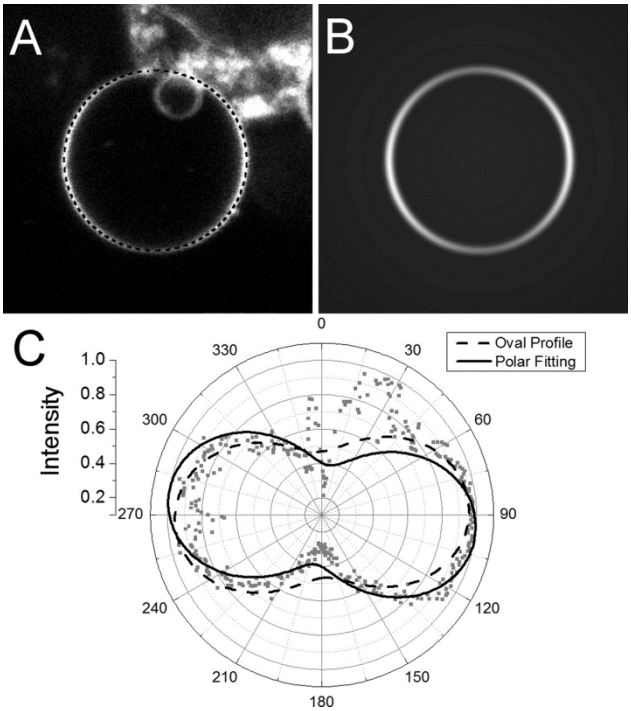

Figure 7 (A) One-photon fluorescence intensity around the equator of a bleb on the exterior of a cultured HeLa cell stained with di-4-ANEPPS and (B) a model image of a single bleb reconstructed from the original image after parameterisation. The result of this parameterisation and of a fit obtained through an oval profile (A, *black dotted line*) is shown in (C) a polar plot. Each fitting technique (*black lines*) generates an angular intensity fit that overlays the data (*gray points*). The overlap of the signal data with background fluorescence from the cell can be seen as an anomaly on the polar plot from 345 degrees to 60 degrees. The polar fitting (*solid line*) is less influenced by this anomaly than the oval profile (*dashed line*), resulting in a better fit.

3.4.2 Testing Polar Fitting

As a test of our protocol, inexperienced operators (n = 7) were asked to perform each of these three data extraction operations (oval profile, polar manual and polar semi-automated) on one image. The human error from oval profiling led to a six- to ten-times greater variance when finding order parameters compared to the polar fitting techniques. We found that in general, this difference arose from erroneous placement of the oval profile; an operation performed by eye and consequently subject to human error. Each of the inexperienced users was then asked to process a series of 12 similar images, again using each of the three processing techniques. The

oval profiling approach gave order parameters with four times the experimental imprecision of our techniques which returned order parameters with only 2.5% error (Table 1).

We demonstrate that our polar fitting approach is general and robust by processing an image superimposed with structured background noise (Figure 7A): blebs formed at the surface of an apoptotic cultured HeLa cell. A polar fitting analysis of the image yields a closer fit than the oval profile method and allows reconstruction an image of the bleb itself (Figure 7B). The polar fit generates a more accurate fit that is less influenced by the structured noise of the cell (Figure 7C).

3.4.3 Distributional Analysis

Describing the physical system which gives rise to functional behaviour and the average tilt, $\langle\varphi\rangle$, requires the tilt probability density function, $P_{tilt}(\varphi)$, of molecules in the membrane. The form of $P_{tilt}(\varphi)$ is a product of the molecule's preferred tilt and a statistical term which describes the number of available states (Figure 8). An amphiphilic molecule will be most stable when its lipophilic parts are embedded in the hydrocarbon core of the membrane and its hydrophilic parts are embedded in the polar region of the membrane. This tends to drive the molecule to orient normally with respect to the membrane plane (i.e. $\varphi = 0$). Our model assumes that the preferred tilt adopts a Gaussian distribution centered at a tilt μ from the normal, with a variance γ away from this tilt μ (Figure 8). The statistical $\sin\varphi$ term describes the change in the density of states with φ. The normalised product is our proposed PDF:

$$P_{tilt}(\varphi) = \frac{1}{N}\sin\varphi\exp\left(\frac{-(\varphi-\mu)^2}{2\gamma^2}\right) \qquad \text{(Eq. 25)}$$

Where N is a complex term depending on μ and γ which normalises the probability density function. Given this proposed probability function, we may solve Eq. 18, A–D as a system of nonlinear equations for the values of μ and γ (Figure 9 and 10). This overdetermined system may be expected to present a number of solutions; however either solving equations in pairs or solving the full set of four equations via a Levenberg–Marquardt minimisation both provide solutions consistent with the equations plotted in $\mu \times \gamma$ space (Figure 9). The combination of any two of the three microscopy modalities we employ is sufficient to estimate values of μ and γ, as demonstrated by our droplet monolayer model. In this case, 1PF images could not be obtained due to out-of-plane fluorescence, but a probability density function may still be found through the combination of SHG and 2PF (Table 2). Our solutions give values of μ and γ from which we obtain the full probability density function and then can calculate a value of $\langle\varphi\rangle$ for comparison with literature values.

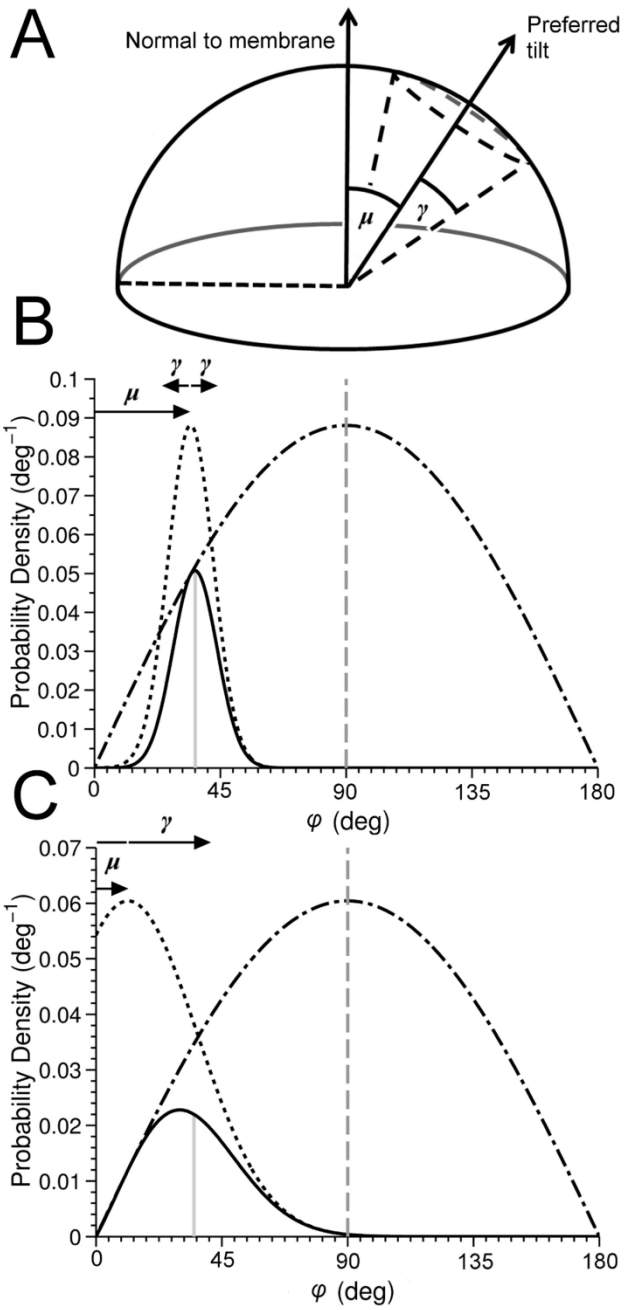

Figure 8 Two distinct tilt probability density functions (*solid curves*) showing <φ> (*vertical solid line*), and their contributing preferred tilt (*dotted curves*) and statistical (*dot-dashed curve*) terms, one having a large μ and a small γ (B), whereas the other has a small μ and large γ (C) and a representative cartoon (A) showing the physical interpretation of the quantities μ and γ which may be calculated for given experimentally extracted order parameters.

We solve nonlinear equations 18 A–D for the two parameters, μ and γ in our probability density function (Eq. 21). Since this system is overdetermined, we demonstrate that the solution to these equations found by a Levenberg–Marquardt minimisation algorithm (represented by the black disc in Figures 9 and 10) is a reasonable solution for each of the input equations, and that only one solution exists in the range $0^o < \mu < 90^o$ and $0^o < \gamma < 90^o$. For each equation 18 A–D, we plot the output of each equation as isosurfaces in $\mu \times \gamma$ space for GUVs, Figures 9 and 10, and their normalised linear combination, in logarithmic scale, Figure 9.

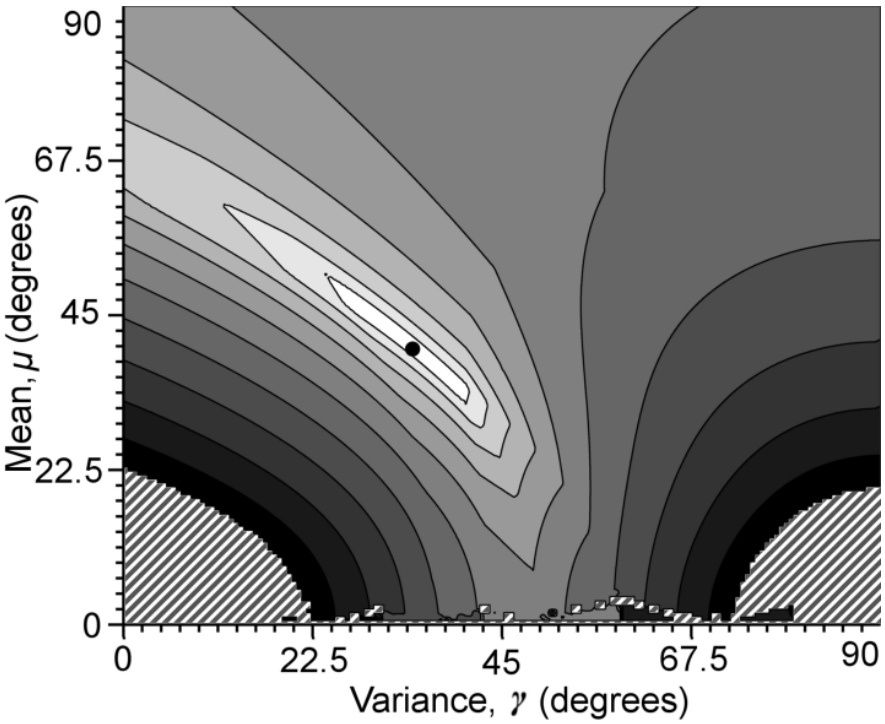

Figure 9 Isosurface of the normalised linear combination of solutions to equations 18 *A–D* for di-4-ANEPPS in GUVs. The surface is plotted on a logarithmic scale in $\mu \times \gamma$ space: lighter shades represent regions of lowest error. The hatched area represents regions of very high RMS error which have been removed from the plot for clarity. The black disc represents the solution presented in Table 1, found by a Levenberg–Marquardt minimisation algorithm.

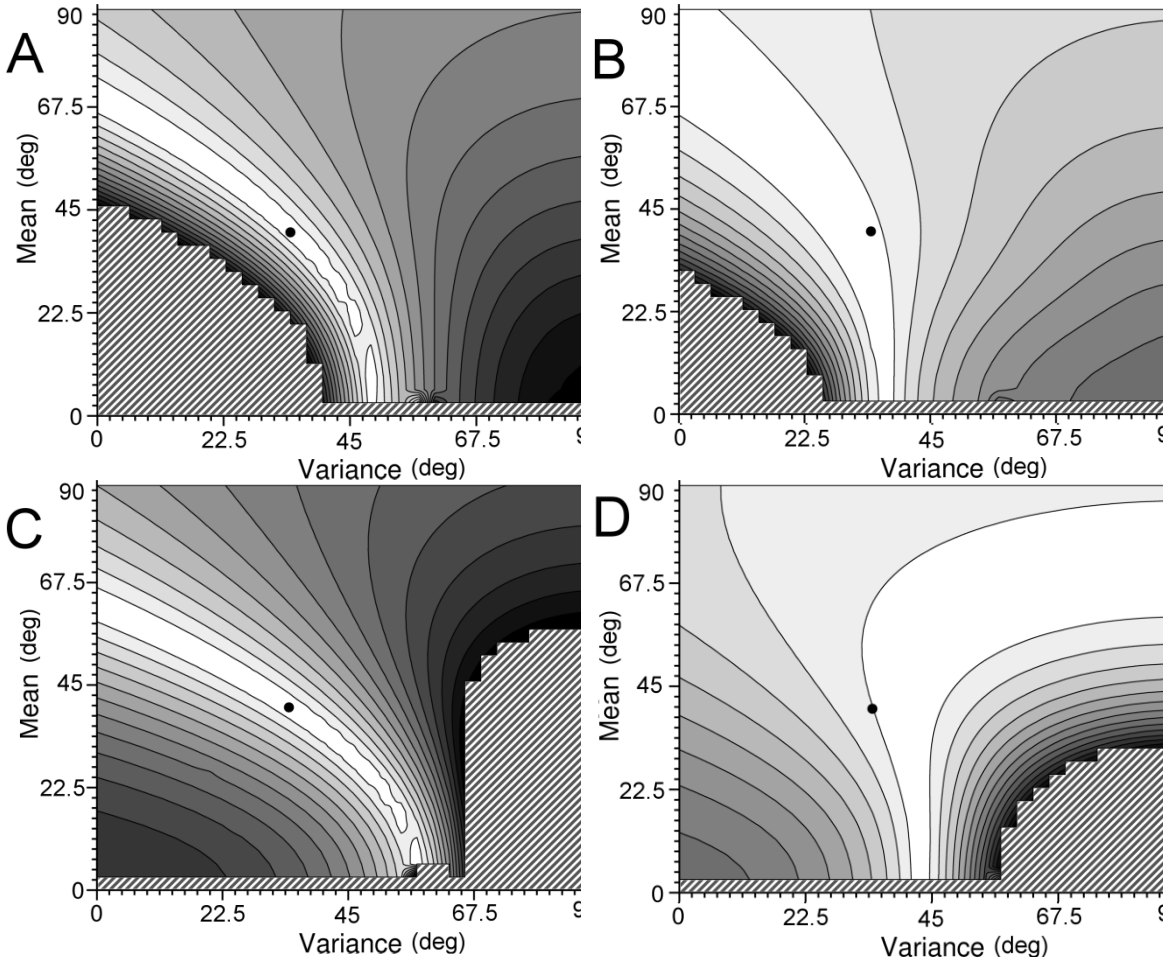

Figure 10 Isosurfaces of equation 18 *A–D*, in $\mu \times \gamma$ space, where lighter shades represent regions of lowest error. The hatched area represents regions of very high RMS error which have been removed from the plot for clarity. The black disc represents the solution presented in Table 1, found by a Levenberg–Marquardt minimisation algorithm.

3.4.4 Tilt angle of ANEPPS chromophores in membranes

Our multidimensional modelling approach yielded order parameters for ANEPPS chromophores in two models membrane systems over three microscopy modalities (Table 2). Images of both GUVs and water droplets in oil were acquired in 1PF, 2PF and SHG. Representative analyses are presented in Appendix 1. The results, which represent the collation of a number of images ($n > 6$), are summarised in Table 2.

Table 2 One-photon, two-photon and SHG order parameters and calculated biophysical parameters which describe the tilt angle probability density function of di-4-ANEPPS in two model membrane systems and di-8-ANEPPS in one.

		$\mathcal{D}_{1PF}$	$\mathcal{D}_{2PF}$	$\mathcal{D}'_{2PF}$	$\mathcal{D}_{SHG}$	μ	γ	$\langle\varphi\rangle$
di-4-ANEPPS	Droplets	–[a]	0.60 ± 0.033	0.45 ± 0.068	0.59 ± 0.024	35.8° ± 1.5°	31.2° ± 3.6°	47°
	GUVs	0.75 ± 0.056	0.45 ± 0.058	0.63 ± 0.059	0.44 ± 0.026	36.7° ± 6.6°	38.1° ± 4.7°	52°
di-8-ANEPPS	Droplets	–[a]	0.58 ± 0.052	0.23 ± 0.047	0.38 ± 0.040	21.8° ± 5.5°	31.4° ± 3.1°	38°

a) One-photon fluorescence data cannot obtained for the droplet model since background fluorescence is too intense.

After solving the order parameters for μ and γ, we can plot their probability density functions (Figure 11), which are good descriptions of the tilt of the ANEPPS chromophores in model systems. The parameters μ and γ give a better description of the distribution of orientations than $\langle\varphi\rangle$, however, we calculate $\langle\varphi\rangle$ from μ and γ to facilitate comparison with results from other research groups. For di-4-ANEPPS, we obtain an average expectation value $\langle\varphi\rangle$ over the two membrane systems of 49.5° ± 2.5°.

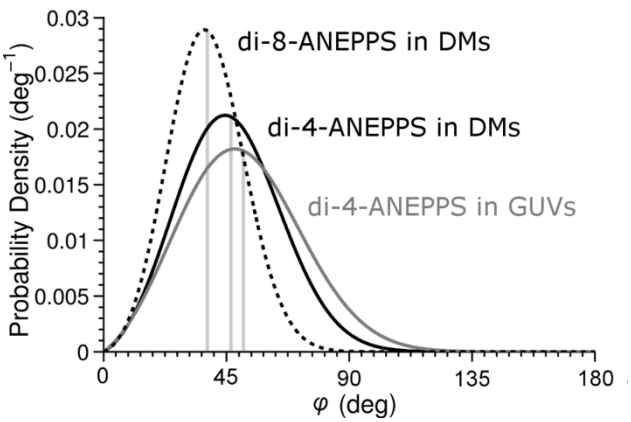

Figure 11 Probability density functions for di-4-ANEPPS (*solid lines*) and di-8-ANEPPS (*dashed line*) with accompanying expected tilt angles (*vertical lines*) for monolayers (*black*) and GUVs (*gray*).

A comparison with published studies of di-4-ANEPPS reveals that our values in model membranes are similar to those obtained from Langmuir-Blodgett films: 49° at a realistic bilayer pressure of 22 mN/m.[28] Our outcome of 38° for the analogous di-8-ANEPPS (Table 2) agrees with both studies of black lipid membrane bilayers, in which it adopts a tilt angle of 36° ± 3° and with an investigation of silicon supported POPC bilayers, in which it tilts to 38°.[32, 48] An earlier study of similar styryl dyes[49] found that longer alkyl chains encourage tilting in membranes, however computation by Hinner[35] on slightly different compounds reached the opposite conclusion, illustrating that the factors determining tilt distribution are not fully understood. We find that the mean tilt (μ) of di-8-ANEPPS is lower than that of di-4-ANEPPS (Table 2) but that both have similar distributional variance (γ) .From our values of μ and γ, we see that in both systems, di-4-ANEPPS has a preferred attitude relative to the membrane; the variety of positions that it can fill, however, is larger in GUVs than in lipid monolayers. Differences in the bilayer pressure or lipid phase may account for this difference; the droplet monolayer is more likely to be swollen by its exposure to dodecane (Figure 3B and 3C) which increases lateral pressure in the membrane area and reduces the range of available states.[38]

3.5 Discussion

We have demonstrated that the combined analysis of three types of optical image (1PF, 2PF and SHG) of the same dye-containing lipid membrane provides a level of insight into the angular distribution of the dye that cannot be obtained from a single imaging technique. Appropriate treatments of fluorescence and second harmonic generation photoselection yield a system of equations for signal strength with angular displacement from a polarised excitation. These equations may be expressed in terms of trigonometric moments of the distribution of tilt angles that a dipolar chromophore in a membrane may occupy.

Image analysis using the entire circular image in polar coordinates allows us to achieve a more accurate and reproducible fit than use of an oval profile. We have demonstrated the versatility and robustness of this method over a range of imaging modes and with significant background noise. The additional accuracy gained through use of this technique allows a better parameterisation of $P_{tilt}(\varphi)$, the probability density function, which describes the tilt of a population of molecules in the bilayer. The finding that tilt angle distribution varies little between GUVs and the droplet monolayer system confirms that the droplet monolayer system is representative of a biological membrane for imaging applications. This is a valuable finding for high-throughput imaging studies since the droplet monolayer system is simpler to construct and reliably image.[50]

Since model membranes are homogeneous on the length-scales of a multiphoton point-spread function (~1 μm), theoretical treatment of photoselection allows determination of molecular tilt. Heterogeneous cell membranes complicate this process, though tilt dependent SHG may still be observed in the presence of membrane structures such as invaginations.[51] While invaginations may obfuscate tilt-dependent fluorescence by causing deviation from the $D_{\infty h}$ symmetry, some groups have been able to resolve fluorescence anisotropy from cellular membranes.[23, 29] The ramifications of these findings extend over a range of imaging and biophysical techniques. Given the heterogeneity of cellular membranes, probing the local lipid environment is important for the study of cellular processes.[3] The differences in polarity and viscosity in different regions of a cellular membrane may have a significant effect on the tilt of an exogenous dye such as di-4-ANEPPS.[52] For example, understanding the orientational distribution of molecular rotors, which probe local intracellular and intramembrane viscosity could have a large impact on how viscosity measurements are interpreted.[53, 54] The frustrated rotation of such probes should be a function of both their tilt and position in the membrane; a known probability density function

can be inserted directly into a theoretical treatment (a singular expected tilt, $\langle\varphi\rangle$, cannot), the implications of which could be addressed by molecular dynamics simulations.

Further work could reveal mechanistic detail behind the electric field modulation of 'slow' voltage-sensitive dyes, estimating the distribution of dyes before and after the application of a field. Application of potential to a membrane could affect both the mean tilt of a dye in the membrane (μ), and the range of tilts away from that position (γ). For example, a dye with a low mean tilt may have a voltage-sensitive mechanism which relies on the reduction of γ, while sensitivity from a dye with a high mean tilt is more likely to be a consequence of alignment of the mean dipole with the field, reducing μ. Our approach resolves these mechanisms, whereas use of a single modality would be constrained to simply monitoring the change in structure factor upon application of a field. Improving our understanding of dipolar dyes through predictable tilt behaviour in membranes will lead us towards designing more effective voltage-sensitive dyes for the study of action potentials.[39, 40, 42]

3.6 Experimental

3.6.1 Software

The MATLAB software used in this publication and some sample membrane images are available at https://github.com/jereeve/BIOJ_Structure_Factor. The outline of the manual and processing steps is presented below. Since we employ a MATLAB®[44] GUI, some steps (in italics) are those that require user interaction with the GUI. For simplicity, we omit the code for semi-automated centerpoint definition, and the majority of the housekeeping code that keeps the GUI in order.

```
%% Initialisation
Initialise GUI
Set initialisise
ation status of graphical elements
%% Import Image
On user input: Import Image
      Open select-file
            On user input: Select File
                  Import dataset
            Check file is an image else error
            Find image dimensions
            If image is signed 64 bit integer
                  Convert to unsigned
            Convert dataset to double-precision
            Pass variables and dataset back to main window
      Plot dataset as image
      Plot dataset as surface
%% Manually-defined centerpoint
On user input: Manual Definition
      Open manual-definition
            User defines boundaries of ellipse
            Get user-defined boundaries of ellipse
            Calculate centerpoint from boundaries
            Plot boundary-lines and centerpoint lines for illustration
            Calculate initial value of radius parameter
            Construct architecture for theta, rho, I triple
            Insert dataset into theta, rho, I triple
%% Remove Structured Noise
On user input: Remove Structured Noise
      Open remove-structured-noise
            User defines segment containing noise
            Get user-defined segment
            Convert inputs to range of values from theta, rho, I
triple
            Remove values within range from theta, rho, I triple
%% Parameterise Model
On user input: Parameterise model
      Open parameterise-model
            User selects appropriate model
            User selects approximate image intensity
```

```
            Get user-estimation of intensity
            Get user-selection of model
            Non-linear least-squares minimisation of model to input
dataset (theta, rho, I triple), using either expected (e.g.
eccentricity ≈ 0) or estimated (e.g. radius and intensity) starting
values to produce parameters
            Insert parameters into model to generate parameterised-
model
            Plot parameterised-model as image and surface
            Export parameterised-model as new image
            Output parameters to excel spreadsheet
```

3.6.2 Materials

di-4-ANEPPS (3-(4-(2-(6-(dibutylamino)naphthalen-2-yl)vinyl)pyridin-1-ium-1-yl)propane-1-sulfonate) and di-8-ANEPPS (3-(4-(2-(6-(dioctylamino)naphthalen-2-yl)vinyl)pyridin-1-ium-1-yl)propane-1-sulfonate) were purchased from Biotium (Hayward, CA) and diphytanoyl phosphatidylcholine (DPhPC) was obtained as a lyophilised powder from Avanti Polar Lipids (Alabaster, AL). All other materials, including dodecane and indium-tin oxide coated glass slides were obtained from Sigma (St. Louis, MO).

3.6.3 Droplet Imaging

Droplets of buffer were introduced into a bath of lipid and dye in dodecane according to the following protocol:

Phosphate buffered saline (20 μL, 50 mM H_2NaPO_4, 50 mM NaCl, pH 7.0) was added to a solution of DPhPC (1.0 mg/mL) and ANNEPS dye (50 μM) in dodecane (1.0 mL) in a small vial and the mixture was shaken gently. Alternatively, DPhPC (0.5 mg/mL) and ANNEP dye (50 μM) was dissolved in phosphate-buffered saline (20 μL, 50 mM H_2NaPO_4, 50 mM NaCl, pH 7.0) then added to dodecane (1.0 mL) in a small vial and the mixture was shaken gently. The mixture was poured into a well with a silanised borosilicate coverslip (100 μm thickness)

forming the base. Droplets approximately 60 μm in diameter were allowed 10 minutes to equilibrate and imaged by scanning multiphoton microscopy.

3.6.4 Giant Unilamellar Vesicles

GUVs were prepared from DPhPC in 200 mM sucrose via an electroformation method.[45, 46] Each dye was added to obtain a concentration of 50 μM, then the mixture was immobilised in a silica glass immediately before imaging. Immobilisation was performed as recently described by Esquembre *et al*.[47] by formation of an aqueous silica sol through hydrolysis of tetramethylorthosilicate followed by gelation with pH 7.4 buffer. Once a suitable GUV was located, SHG and 2PF images were obtained in transmission and epifluorescence channels respectively.

3.6.5 Microscopy Setup

Imaging was conducted on a custom-built microscope based around an Olympus BX60M upright microscope adapted with standard Linos microbench components (Figure 15, courtesy of Dr. Alexander Corbett). The light source was a Ti:Sapphire laser (Tsunami, Spectra Physics) producing 100 fs pulses centered at 850 nm. An Olympus LUMPlanFL N 40X 0.8 NA lens was illuminated at the back aperture with a 90 mW beam after passing through a 1000:1 Newport polarising beamsplitter. After passing through an excitation filter the two-photon epi-fluorescence was filtered with a 550–650 nm bandpass filter (Semrock FF568-Di01-25x36) before being captured with a Hamamatsu H7422P series photon counting PMT. Use of a dichroic to filter emission may result in a polarisation bias of no more than 10% and we calculate that this should influence detected light intensity by only ±2%. SHG emission was condensed in the forward direction, passing through an excitation filter and a 422–432 nm notch filter (Semrock FF01-427/10-25) before reaching a Sens-Tech DM0016 photon counting PMT.

The alignment of the emission polariser in SHG imaging was determined using a non-linear frequency-doubling crystal.

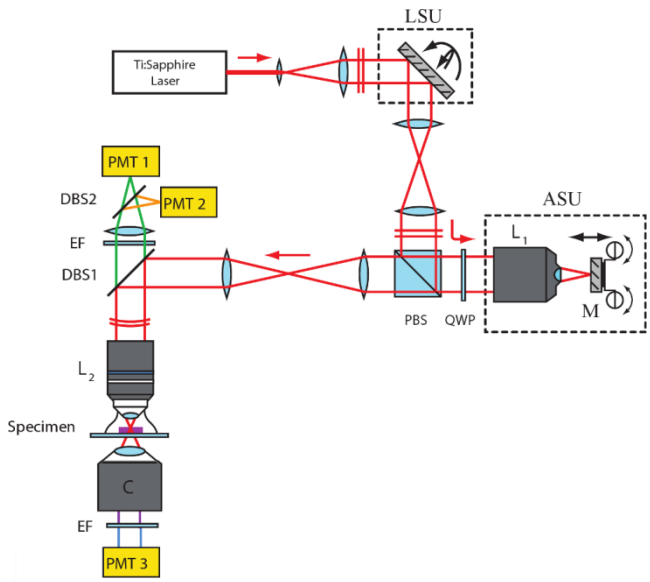

Figure 15 Schematic diagram of the bespoke Ti:Sapphire driven scanning confocal multiphoton microscope used in this Chapter. For reference, 'Specimin' relates to the image plane of Figure 1B.

Laser scanning was achieved with a pair of orthogonally mounted galvanometer mirrors (VM1000+, Cambridge Technology). Synchronous point scanning and data collection were orchestrated through LABVIEW software running on a reconfigurable FPGA card (NI PCI-7830R, both National Instruments).

3.7 References

1. S. M. Blackman, C. E. Cobb, A. H. Beth and D. W. Piston, *Biophys. J.*, 1996, **71**, 194-208
2. C. E. B. Brattwall, P. Lincoln and B. Nordén, *J. Am. Chem. Soc.* 2003, **125**, 14214-14215
3. P. A. Janmey and P. K. J. Kinnunen, *Trends Cell Biol.*, 2006, **16**, 538-546
4. A. K. Mitra, H. Célia, G. Ren, J. G. Luz, I. A. Wilson and L. Teyton, *Curr. Biol.*, 2004, **14**, 718-724
5. M. S. Turner and P. Sens, *Phys. Rev. Lett.*, 2004, **93**, 118103
6. G. A. Cook and S. J. Opella, *Biochim. Biophys. Acta*, 2010, **1808**, 1448-1453
7. F. Tian, Z. Song and T. A. Cross, *J. Magn. Reson.*, 1998, **135**, 227-231
8. M. B. Ulmschneider, M. S. P. Sansom and A. Di Nola, *Biophys. J.*, 2006, **90**, 1650-1660
9. P. G. Fajer, *Proc. Natl. Acad. Sci. USA.*, 1994, **91**, 937-941
10. J. J. Inbaraj, M. Laryukhin and G. A. Lorigan, *J. Am. Chem. Soc.*, 2007, **129**, 7710-7711
11. C. P. Pfeffer, B. R. Olsen, F. Ganikhanov and F. Légaré, *Biomed. Opt. Express*., 2011, **2**, 1366-1376
12. M. D. Bazzi and R. W. Woody, *Biophys. J.*, 1985, **48**, 957-966
13. A. Kukol, P. D. Adams, L. M. Rice, A. T. Brunger and I. T. Arkin, *J. Mol. Biol.*, 1999, **286**, 951-962
14. M. Lundeen, B. Chance and L. Powers, *Biophys. J.*, 1987, **51**, 693-695
15. A. A. Sigarev, J. K. Vij, A. W. Hall, S. Cowling and J. W. Goodby, *Ferroelectrics*, 2006, **343**, 167-175
16. R. A. Badley, W. G. Martin and H. Schneider, *Biochemistry*, 1973, **12**, 268-275
17. R. A. Badley, H. Schneider and W. G. Martin, *Biochem. Biophys. Res. Commun.*, 1971, **45**, 174-183
18. R. K. P. Benninger, B. Önfelt, M. A. A. Neil, D. M. Davis and P. M. W. French, *Biophys. J.*, 2005, **88**, 609-622
19. B. Corry, D. Jayatilaka, B. Martinac and P. Rigby, *Biophys. J.*, 2006, **91**, 1032-1045
20. T. E. Fisher, P. E. Marszalek and J. M. Fernandez, *Nat. Struct. Mol. Biol.*, 2000, **7**, 719-724
21. U. A. Heide, B. Orbons, H. C. Gerritsen and Y. K. Levine, *Eur. Biophys. J.*, 1992, **21**, 263-272
22. U. A. Heide, O. E. Rem, H. C. Gerritsen, E. L. Beer, P. Schiereck, I. P. Trayer and Y. K. Levine, *Eur. Biophys. J.*, 1994, **23**, 369-378
23. J. Lazar, A. Bondar, S. Timr and S. J. Firestein, *Nat. Methods*., 2011, **8**, 684-690
24. P. W. Livanec, H. A. Huckabay and R. C. Dunn, *J. Phys. Chem. B*., 2009, **113**, 10240-10248
25. J. V. Rocheleau, M. Edidin and D. W. Piston, *Biophys. J.*, 2003, **84**, 4078-4086
26. S. E. Sund, J. A. Swanson and D. Axelrod, *Biophys. J.*, 1999, **77**, 2266-2283
27. C.-L. Hsieh, Y. Pu, R. Grange and D. Psaltis, *Opt. Express*, 2010, **18**, 11917-11932
28. J. Y. Huang, A. Lewis and L. Loew, *Biophys. J.*, 1988, **53**, 665-670
29. J. Jiang, K. B. Eisenthal and R. Yuste, *Biophys. J.*, 2007, **93**, L26-L28
30. L. Moreaux, T. Pons, V. Dambrin, M. Blanchard-Desce and J. Mertz, *Opt. Lett.*, 2003, **28**, 625-627
31. L. Moreaux, O. Sandre and J. Mertz, *J. Opt. Soc. Am. B.*, 2000, **17**, 1685-1694

32. R. S. Ries, H. Choi, R. Blunck, F. Bezanilla and J. R. Heath, *J. Phys. Chem. B.*, 2004, **108**, 16040-16049
33. J. S. Salafsky, *Phys. Chem. Chem. Phys.*, 2007, **9**, 5704-5711
34. G. Gonella, H.-L. Dai, H. C. Fry, M. J. Therien, V. Krishnan, A. Tronin and J. K. Blasie, *J. Am. Chem. Soc.*, 2010, **132**, 9693-9700
35. , M. J. Hinner, S.-J. Marrink and A. H. de Vries, *J. Phys. Chem. B.*, 2009, **113**, 15807-15819
36. A. Kyrychenko, *Chem. Phys. Lett.*, 2010, **485**, 95-99
37. T. L. Mazely and I. W. M. Hetherington, *J. Chem. Phys.*, 1987, **86**, 3640-3647
38. K. C. Song, P. W. Livanec, J. B. Klauda, K. Kuczera, R. C. Dunn and W. Im, *J. Phys. Chem. B.*, 2011, **115**, 6157-6165
39. R. J. Clarke, A. Zouni and J. F. Holzwarth, *Biophys. J.*, 1995, **68**, 1406-1415
40. T. Sugihara, H. Haga and S. Yamamoto, *Appl. Phys. Lett.*, 1996, **68**, 144-146
41. J. R. Lakowicz, Principles of Fluorescence Spectroscopy, 1999, Springer, New York
42. L. Loew, L. Cohen, J. Dix, E. Fluhler, V. Montana, G. Salama and W. Jian-young, *J. Membr. Biol.*, 1992, **130**, 1-10
43. M. A. Holden, D. Needham and H. Bayley, *J. Am. Chem. Soc.*, 2007, **129**, 8650-8655
44. MATLAB (The MathWorks Inc, Natick, Massachusetts)
45. M. I. Angelova and D. S. Dimitrov, *Faraday Discuss*, 1986, **81**, 303-311
46. T. Mach, C. Chimerel, J. Fritz, N. Fertig, M. Winterhalter and C. Fütterer, *Anal. Bioanal. Chem.*, 2008, **390**, 841-846
47. R. Esquembre, S. N. Pinto, J. A. Poveda, M. Prieto and C. R. Mateo, *Soft Matter*, 2012, **8**, 408-417
48. A. Lambacher and P. Fromherz, *J. Phys. Chem. B.*, 2000, **105**, 343-346
49. L. M. Loew and L. L. Simpson, *Biophys. J.*, 1981, **34**, 353-365
50. N. F. Morales-Penningston, J. Wu, E. R. Farkas, S. L. Goh, T. M. Konyakhina, J. Y. Zheng, W. W. Webb and G. W. Feigenson, *Biochim. Biophys. Acta.*, 2010, **1798**, 1324-1332
51. A. C. Millard, Terasaki, M. and L. Loew, *Biophys. J.*, 2005, **88**, L46-L48
52. P. L. Yeagle, The Structure of Biological Membranes, 2004, CRC Press, Boca Raton, FL
53. J. A. Levitt, M. K. Kuimova, G. Yahioglu, P.-H. Chung, K. Suhling and D. Phillips, *J. Phys. Chem. C.*, 2009, **113**, 11634-11642
54. M. E. Nipper, M. Dakanali, E. Theodorakis and M. A. Haidekker, *Biochimie*, 2011, **93**, 988-994

3.8 Appendix I

Images & Analysis

In each case, these images represent: (A) The angular part of the model (black line) plotted over data from within one standard deviation from the center of the radius (gray circles). (B) A surface plot of a representative image. (C) The parameterised model image. (D) The image and (E) a parameterised image.

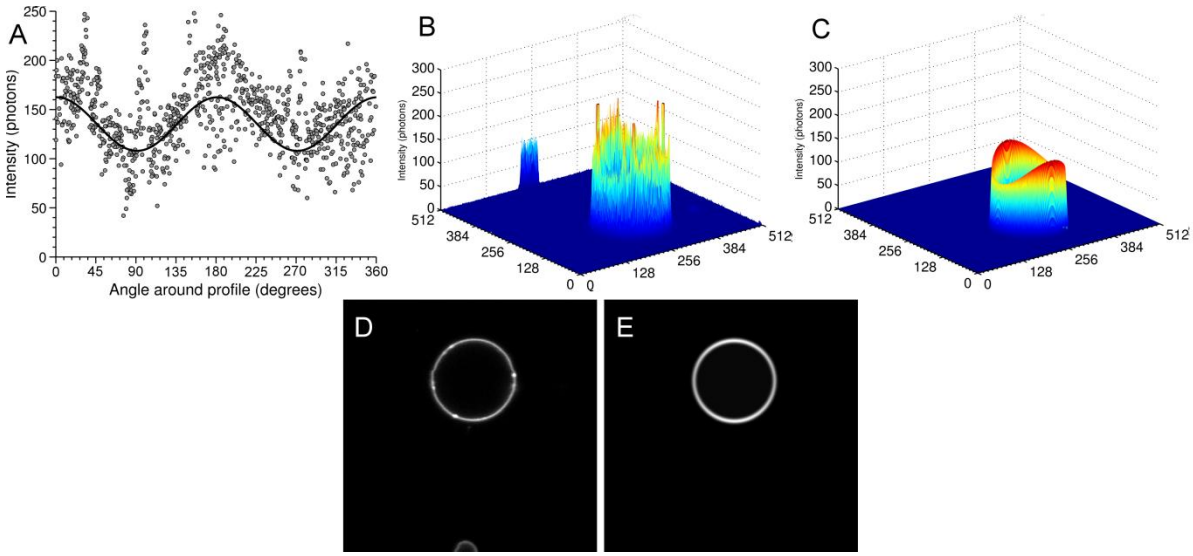

FIGURE A1 Analysis of di-4-ANEPPS in a GUV imaged by 1-photon microscopy showing (A) angular dependence on tilt angle, (B) the image plotted as a surface, (C) the parameterised model plotted as a surface with the photon counts recorded on the z-axis, (D) the image plotted as a linear grayscale intensity map and (E) the parameterised model plotted as a linear grayscale intensity map, image dimensions: 33.6 × 33.6 μm.

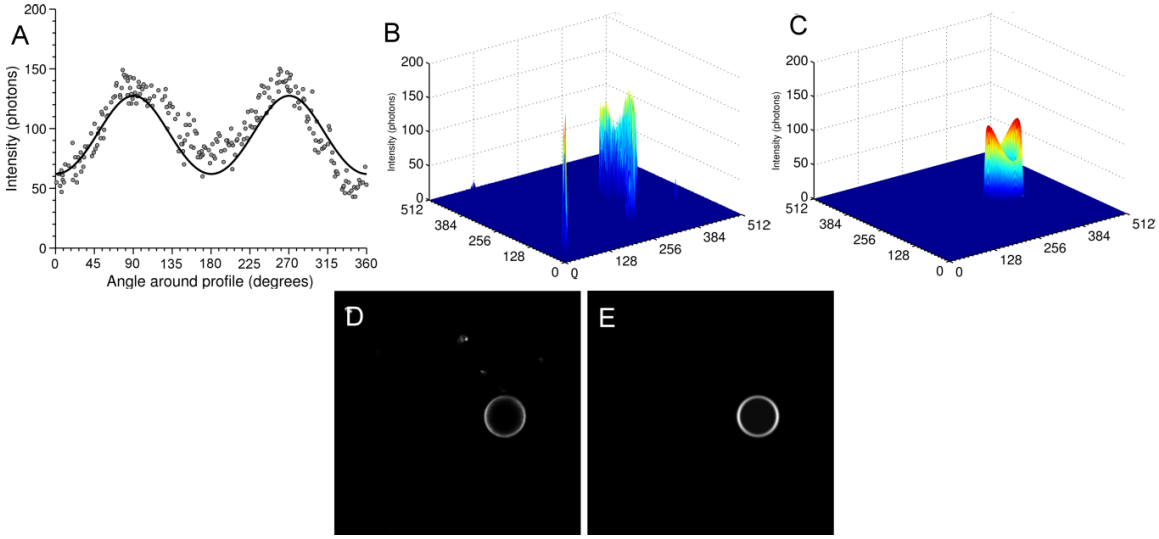

FIGURE A2 Analysis of di-4-ANEPPS in a GUV imaged by 2-photon microscopy showing (A) angular dependence on tilt angle, (B) the image plotted as a surface, (C) the parameterised model plotted as a surface with the photon counts recorded on the *z*-axis, (D) the image plotted as a linear grayscale intensity map and (E) the parameterised model plotted as a linear grayscale intensity map, image dimensions: 50 × 50 μm.

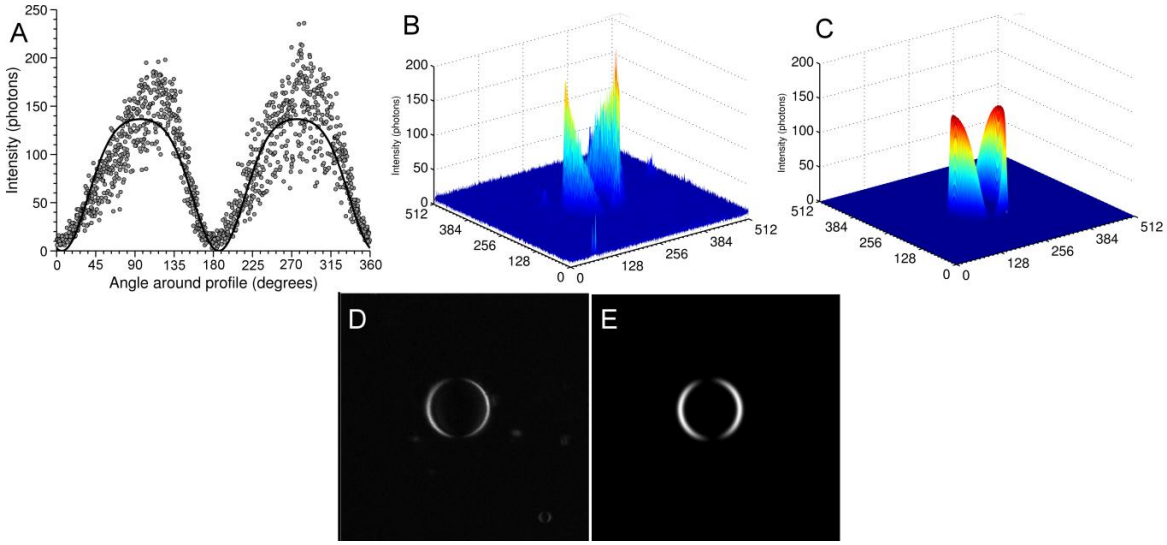

FIGURE A3 Analysis of di-4-ANEPPS in a GUV imaged by SHG microscopy showing (A) angular dependence on tilt angle, (B) the image plotted as a surface, (C) the parameterised model plotted as a surface with the photon counts recorded on the *z*-axis, (D) the image plotted as a linear grayscale intensity map and (E) the parameterised model plotted as a linear grayscale intensity map, image dimensions: 50 × 50 μm.

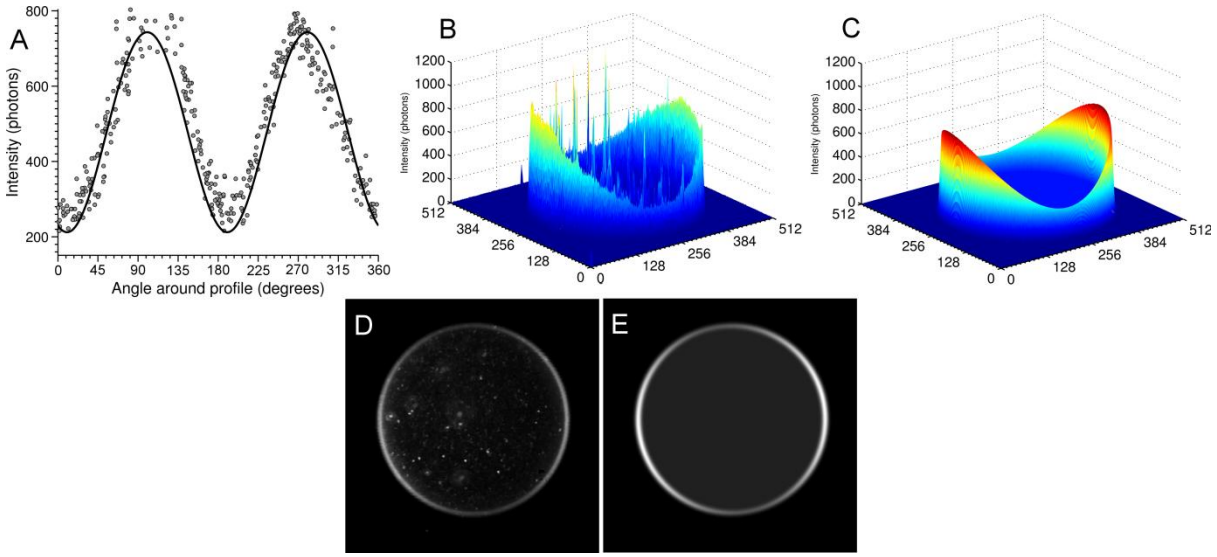

FIGURE A4 Analysis of di-4-ANEPPS in a droplet monolayer imaged by 2-photon microscopy showing (A) angular dependence on tilt angle, (B) the image plotted as a surface, (C) the parameterised model plotted as a surface with the photon counts recorded on the *z*-axis, (D) the image plotted as a linear grayscale intensity map and (E) the parameterised model plotted as a linear grayscale intensity map, image dimensions: 300 × 300 μm.

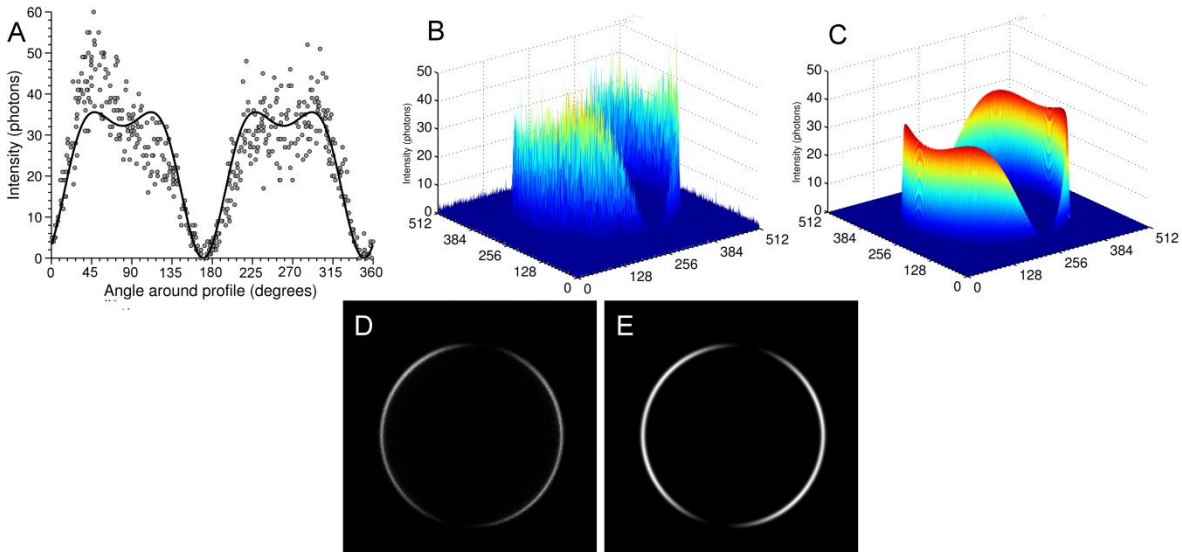

FIGURE A5 Analysis of di-4-ANEPPS in a droplet monolayer imaged by SHG microscopy showing (A) angular dependence on tilt angle, (B) the image plotted as a surface, (C) the parameterised model plotted as a surface with the photon counts recorded on the *z*-axis, (D) the image plotted as a linear grayscale intensity map and (E) the parameterised model plotted as a linear grayscale intensity map, image dimensions: 300 × 300 μm.

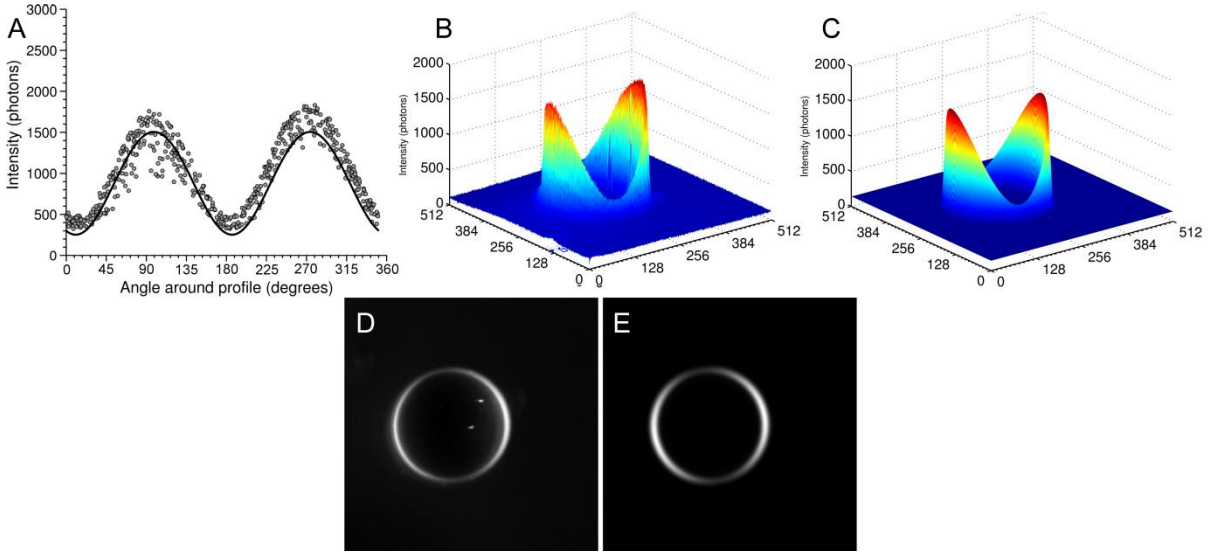

FIGURE A6 Analysis of di-8-ANEPPS in a droplet monolayer imaged by 2-photon microscopy showing (A) angular dependence on tilt angle, (B) the image plotted as a surface, (C) the parameterised model plotted as a surface with the photon counts recorded on the *z*-axis, (D) the image plotted as a linear grayscale intensity map and (E) the parameterised model plotted as a linear grayscale intensity map, image dimensions: 300 × 300 μm.

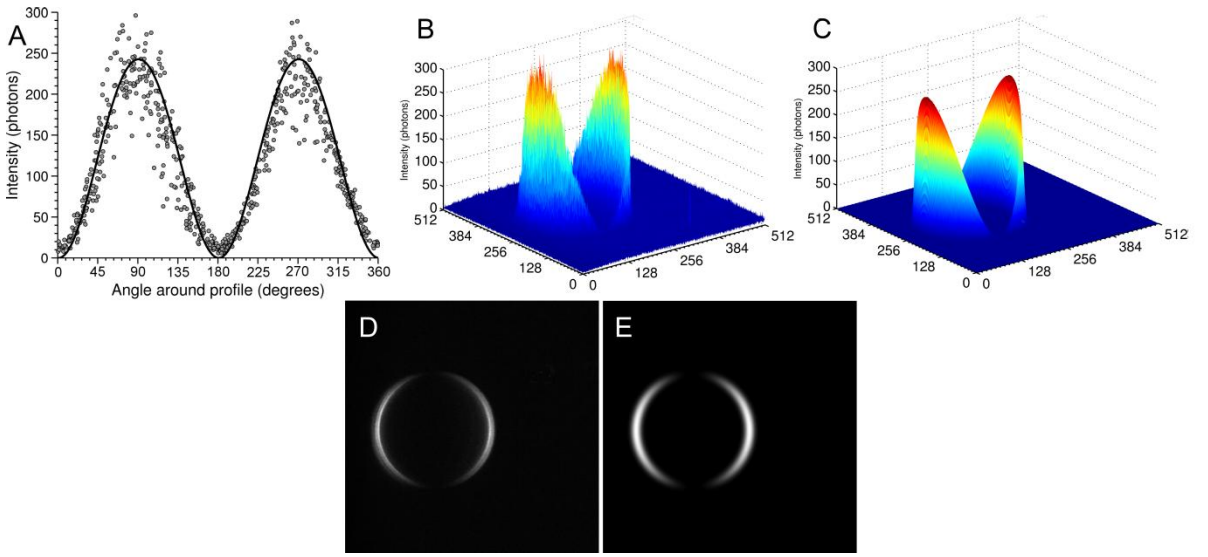

FIGURE A7 Analysis of di-8-ANEPPS in a droplet monolayer imaged by SHG microscopy showing (A) angular dependence on tilt angle, (B) the image plotted as a surface, (C) the parameterised model plotted as a surface with the photon counts recorded on the *z*-axis, (D) the image plotted as a linear grayscale intensity map and (E) the parameterised model plotted as a linear grayscale intensity map, image dimensions: 300 × 300 μm.

Chapter 4

cis-Donor *cis*-Acceptor Tetraethynyl Porphyrins

Summary

We design and synthesise a family of *cis*-donor *cis*-acceptor tetraethynyl porphyrins with the aim of maximising β through the strengthening of off-axis components. Synthesis of tetraethynyl porphyrins is non-trivial and typically requires a statistical step with considerable loss of material. We employ an iterative recycling approach to optimise this statistical hurdle, which allows production of *cis*-tetraethynyl porphyrins in gram-scale syntheses.

The linear optical properties of these dyes are fully characterised; the *cis*-geometry allows the attachment of two donors and two acceptors which cause a substantial red-shift. Furthermore, these molecular architectures are expected to be highly polarisable along the *x*-axis as well as the *z*-axis, specifically enhancing the contribution of the β_{zxx} component. We measure the hyperpolarisability of four *cis*-tetraethynyl porphyrin derivatives by hyper-Raleigh scattering, and demonstrate that they are capable of producing both second harmonic generation and two-photon fluorescence from membranes.

4.1 Introduction

4.1.1 *cis*-Porphyrins

Conventional wisdom (and indeed the guiding influence behind the dipolar porphyrins that I present in Chapter 2) dictates that the highest first order NLO properties are obtained by taking a highly polarisable bridge and placing a donor and acceptor at opposing ends.[1-3] This approach has led to a wide variety of donor-acceptor compounds with well characterised NLO responses. Push-pull type styryl dyes and their derivatives have been well characterised, and none supersede the apparent limit described by Kuzyk.[4] Therefore, it is likely that substitutions of the bridge, donor or acceptor as a method of optimising β appear not to give the paradigm-shifting advances in NLO properties that biological imaging needs. Drastic deviations from this push-pull architecture have been theoretically and synthetically investigated, covering porphyrin dimers,[5-7] TICToid chromophores,[8, 9] octupolar compounds,[10-13] metal complexes[14-16] and other compounds with significant off-axis contributions.[17, 18] In this chapter, I discuss an approach which employs a new molecular architecture for the optimisation of molecular beta, through the addition of significant off-axis tensor contributions: A *cis*-donor *cis*-acceptor tetraethynyl porphyrin (Figure 1).

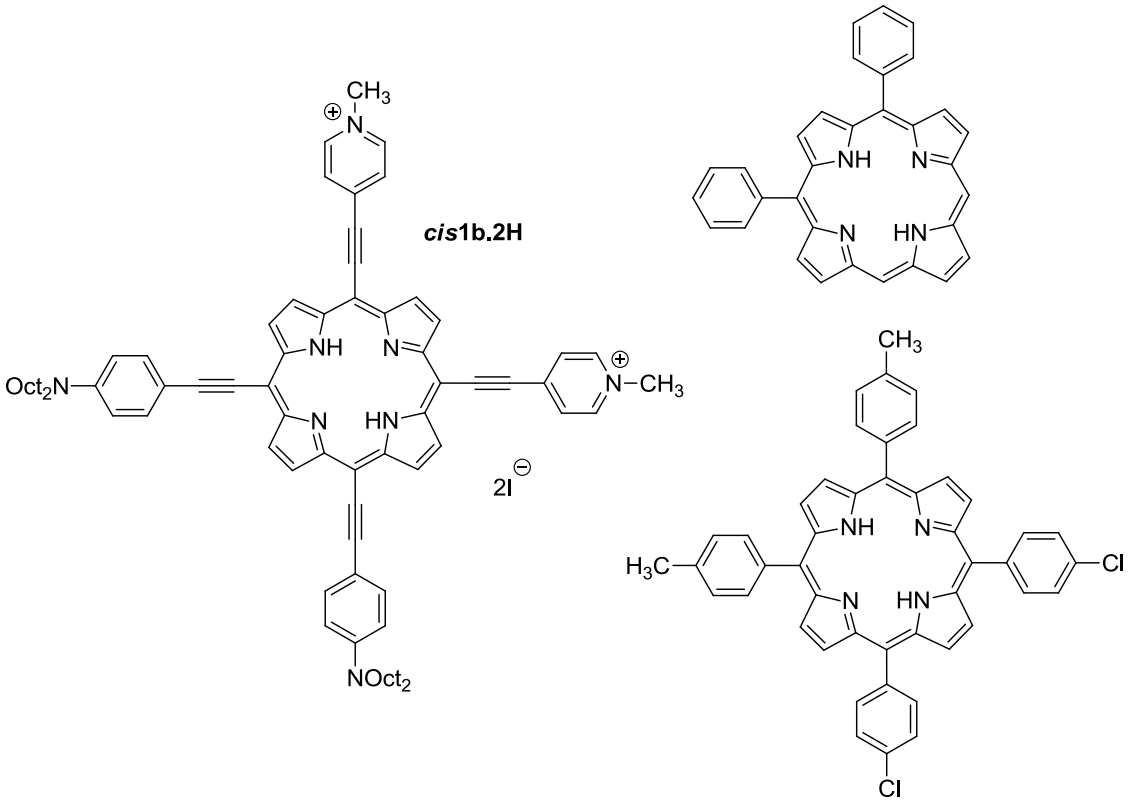

Figure 1 The model cis-donor cis-acceptor tetraethynyl porphyrin synthesised in this chapter (***cis*1b.2H**) and two cis-porphyrins previously synthesised: 5,10-diphenyl porphyrin (*top right*) by Hatscher et al.[19] and 5,10-di(*p*-methyl)phenyl 15,20-(*p*-chloro)phenyl porphyrin (*bottom right*) by Heo et al.[20]

cis-Porphyrins are an often neglected molecular motif due to the difficulty of synthesis of the 5,10-meso substitution pattern which is generally only achieved in low yield.[19, 21] However, this architecture presents unique opportunities for the creation of novel structures, exploiting a scaffold with 90° angles. This geometric orthogonality is not trivial in organic chemistry which relies on the arsenal of sp, sp^2 and sp^3 hydrocarbon hybrids with their characteristic angles of 180°, 120° and 109.5° respectively.

The first hyperpolarisability of a molecule is expressed as a rank three tensor, which describes all of the possible interactions between the vector describing the induced dipole moment and the two electric fields to which the molecule is subjected.[22, 23] Since we make this description in three dimensional Cartesian space, the hyperpolarisability and electric

field vectors have components along each of the three Cartesian axes; *x*, *y* and *z*. Molecular hyperpolarisability, which we term β, is composed of 27 terms, β_{ijk} where indices *i*, *j* and *k* take a value for each Cartesian axis (i.e. β_{zzz}, β_{zzx}, β_{zzy}, β_{zxz}, β_{zxx}, β_{zxy} etc.). The resulting description of β is a 3 x 3 x 3 array – the rank-three tensor schematically depicted in Figure 2. The total magnitude of β may be expressed in a number of ways, but for the sake of this chapter, I refer to either individual terms or β_{HRS} which is the magnitude of the β_{zzz} and β_{zxx} terms which is expressed $\beta_{HRS} = \sqrt{\langle\beta_{zzz}^2\rangle + \langle\beta_{zxx}^2\rangle}$.

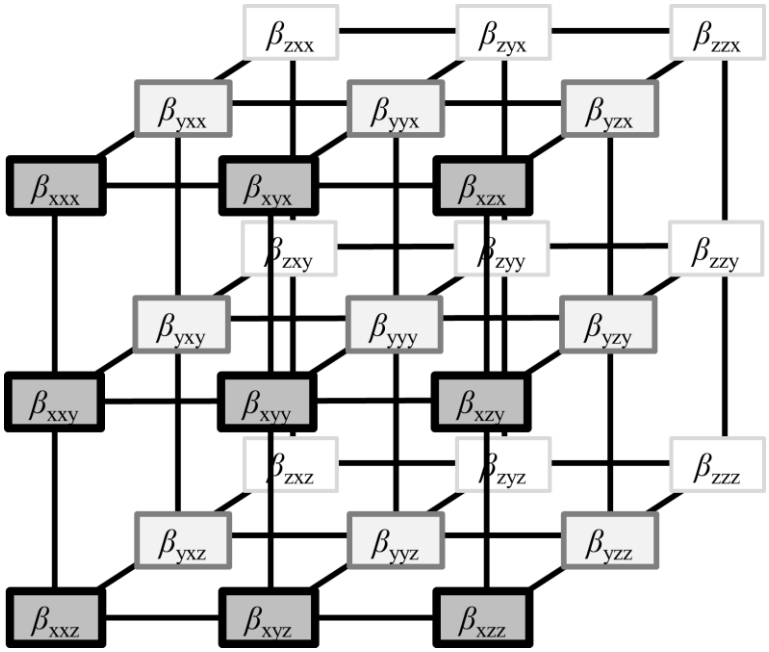

Figure 2 The 3 × 3 × 3 array which is the rank-3 tensor that describes the first hyperpolarisability, β. Each contributing element, β_{ijk}, represents the unique relationship between the hyperpolarisability along an axis, *i*, and the polarisation of the electric field along axes *j*,*k*.

The most important tensor component when designing a probe of membrane potential is β_{zzz} since it describes the hyperpolarisability associated with the molecular axis (where the electron cloud is most deformable) interacting with two electric fields directed along this same axis (read: two photons). Alignment of a dipolar probe normal to a membrane directs its molecular *z*-axis with the direction of an imposed electric field gradient of a

transmembrane potential. Therefore, β_{zzz} is the most suitable tensor component for probing transmembrane potential. Dipolar amphiphilic chromophores natuarally focus on obtaining a high β_{zzz}, often at the expense of other tensor contributions.[24-26] However, since the alignment of dyes with the membrane is not perfect (see Chapter 3), significant contributions to the bulk hyperpolarisability across the membrane may originate from off-axis contributions. If it is possible for us to increase the β_{zxx} contribution without detriment to the β_{zzz} contribution, significant off-axis contributions could lead to a substantial molecular β and therefore even stronger SHG.[17, 27]

cis-Donor *cis*-acceptor chromophores have been shown to have large off-axis tensor components,[17, 27, 28] inferring that they possess electron density which is polarisable away from the primary molecular charge-transfer axis. It is this property that we aim to harness through the synthesis and testing of our *cis*-donor *cis*-acceptor tetraethynyl porphyrins.

4.1.2 Optical and supermolecular properties of cis compounds

The unique geometry of *cis*-5,10-porphyrins has drawn attention from groups which are interested in the electronic and optical properties of molecules with distinctive chromophores. Unlike *trans*- or other symmetrically substituted porphyrins, *cis*-porphyrins may possess strong amphiphilic character due to their C_{2v} symmetry. Bujdák and cowokers[29] explored the possibility of elaborating a porphyrin with pyridinium acceptors in a 5,10-configuration. They infer from linear optical investigation of *cis*- and *trans*-pyridinium porphyrins adsorbed onto a charged clay surface that *cis*-geometries bind more strongly which they attribute to its amphiphilicity. Further fluorescence studies also find that *cis*-porphyrins enjoy superior solubility profiles, the constraints of their molecular geometry permits only the formation of J-dimers, whereas its trans- analogue was found to form larger J-aggregates in aqueous solution.[29]

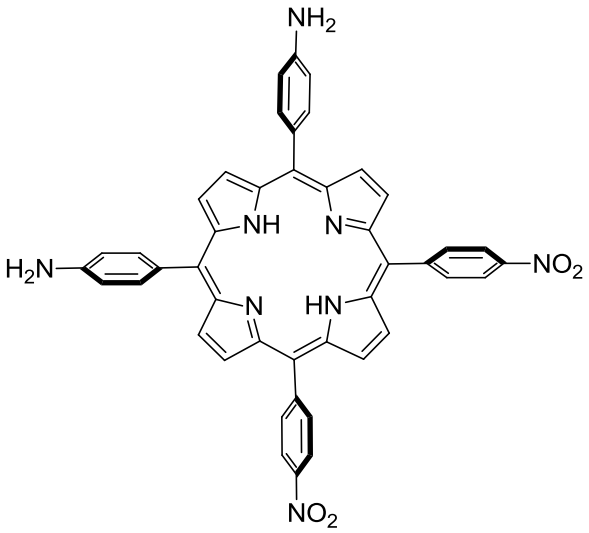

Figure 3 A previously synthesised cis-donor cis-acceptor porphyrin. Steric interaction between phenyl-H and porphyrinic β-H causes an out-of-plane twist in the case of each donor and acceptor. Despite posessing potent electron donating and accepting capabilities respectively, the lack of orbital overlap and subsequent low oscillator strength attenuates the nonlinear optical properties of this molecule.[30]

In 1992, Suslick et al.[30] attempted to synthesise a *cis*-donor *cis*-acceptor porphyrin by the statistical reduction of 5,10,15,20-tetrakis-(*p*-nitrophenyl)porphyrin (Figure 3). Their rationale was that with additional donors and acceptors, a large porphyrinic π-system should display substantial first hyperpolarisabilities. However, upon investigation with electric-field induced second harmonic generation (EFISHG), they found that their molecules underperformed compared to simple styryl chromophores. We attribute this to the 60° twist between the porphyrin plane and the donors or acceptors (Figure 3). Since 1992, many groups[16, 31-33] have observed that the inclusion of conjugated ethynyl linkers between the porphyrin ring and electron donors or acceptors permits substantially more of the charge-transfer band to be associated with porphyrinic orbitals, increasing the oscillator strength and consequently the molecular first hyperpolarisability. I exploit this evolution in molecular design to produce the first porphyrin SHG dyes in Chapter 2 of this thesis. Suslick *et al.*[30] also encounter difficulties in measuring β: EFISHG only accurately measures the projection of the hyperpolarisability tensor onto the molecular dipole (which

runs up the C_2 axis of the molecule), effectively ignoring the off-axis contributions to β (of which β_{zxx} will be the largest). HRS is capable of measuring one off-axis component (β_{zxx}) through the extraction of a depolarisation ratio.

4.1.3 Synthesis of *cis*-5,10-porphyrins

The synthetic challenge provided by *cis*-porphyrins has been undertaken by a number of groups. Corner (5,10)-porphyrins, have been synthesised by the '3+1' condensation of pyrrole with tripyrrane in the presence of the required aldehyde (Scheme 1).[21, 34-36]

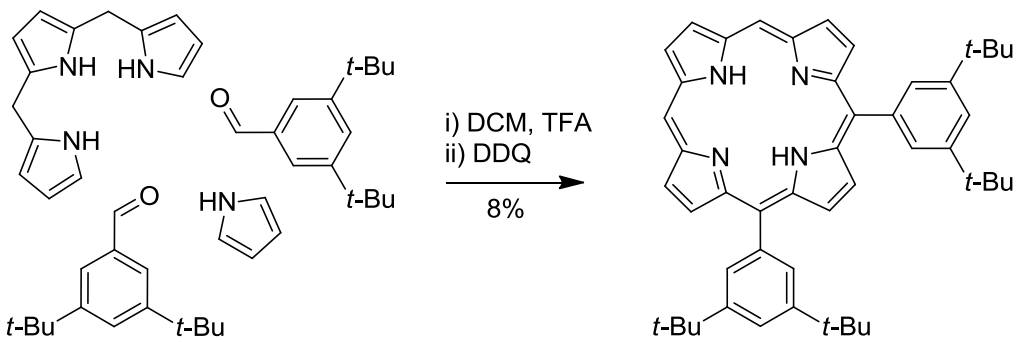

Scheme 1 The '3+1' technique first coined by Boudif *et al*.[34] in 1994 is applied to produce *cis*-meso functionalised porphyrin, a key intermediate in the synthesis of corner azo-linked corner porphyrins by Basic et al. in 2010. Despite the natural approach which avoids a statistical step, the proceedure is low yielding and requires the synthesis of tripyrrane, a sensitive intermediate.

Though this route does navigate around the need for a statistical step, they acknowledge the difficulty of the synthesis required for the porphyrin precursors and favour the more easily synthesised 5,15 analogues where possible and suitable.[21] Furthermore, this approach is limited to condensations with aldehydes that give good yields in the typically sensitive and unpredictable porphyrin condensation reaction. Synthetic access to the key *cis*-motif has also been investigated through an involved synthesis by Brukner which requires condensation of a diacyldipyrromethane intermediate.[37] Lindsey also suggests an approach from dipyrromethane-dicarbinols.[38] The synthetic and supramolecular interest in 5,10-

porphyrins was consolidated by Senge in 2003 with introduction of his addition-oxidation organolithium mechanism which can selectively derivatise a fourfold symmetric porphyrin to the elusive *cis*-form (Scheme 2).[19] The downside of this approach is the limitation placed on the *meso*-substituent, which may only be introduced in the form of an organolithium reagent.

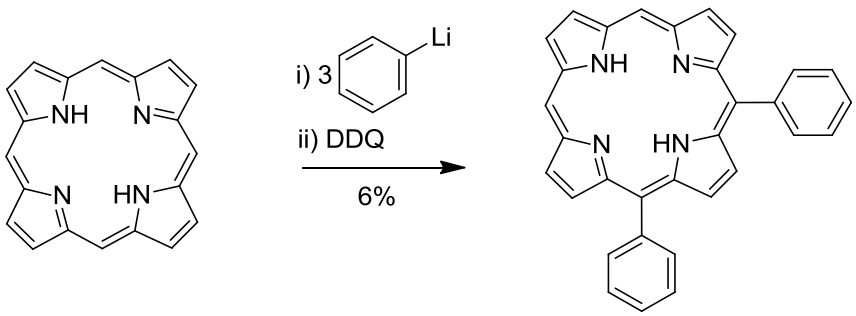

Scheme 2 The approach by Senge and coworkers[19] posesses good yields and high selectivity but only works for organolithium reagents, which may not always be prepared for all possible substituents. Furthermore, some organolithium reagents give poor yield or selectivity, with some, such as the more bulky isopentyl lithium actively preferring the trans 5,15 configuration.

Apart from these 'rational' syntheses, it is also possible to approach *cis*-porphyrins from a statistical viewpoint.[30, 39] This route is considerably quicker, but results in lower yields and can require a non-trivial purification step. Most importantly, statistical formation of *cis*-compounds allows much more versatile substitution (Senge notes that his rational routes are highly substrate-specific[19]), for example, a statistical scheme could use a traditional fourfold porphyrin condensation followed by a statistical derivitisation which simply employs two equivalents of the necessary reagent (for a doubly-derivatised porphyrin). The outcome would be a statistical mixture of A_4, A_3, *trans*-A_2, *cis*-A_2, A_1 and A_0, where A is the required functionality (e.g. our case, outlined below in Scheme 3 where A represents deprotection of a silyl protecting group) obtained in a 1:4:2:4:4:1 ratio.

4.2 Synthesis

The synthetic challenge associated with a statistical approach to *cis*-donor *cis*-acceptor tetraethynyl porphyrins is formation of the key desymmetrised intermediate. We choose this statistical route since the ethynyl substitution we require is incompatible with Senge's organolithium reaction or a non-statistical condensation.[19,21,34,35] Starting from silyl-protected tetraethynyl porphyrin, a scheme of sequential deprotections and Sonogashira couplings gives access to the desired substitution pattern. As such, the key desymmetrised intermediate is the *cis*-substituted porphyrin, from which the remainder of synthetic scheme is relatively trivial. The following section details the three statistical approaches to this key intermediate, from which the final, amphiphilic *cis*-donor *cis*-acceptor tetraethynyl porphyrins may be synthesised.

4.2.1 First Approach

The feasibility of a statistical approach was assessed by an initial study: statistical deprotection of a trihexylsilyl protected tetraethynyl porphyrin (Scheme 3). Anticipating that the main practical challenge would be purification of *cis*-deprotected from *trans*-deprotected porphyrin, this step was carried out on a relatively small scale.

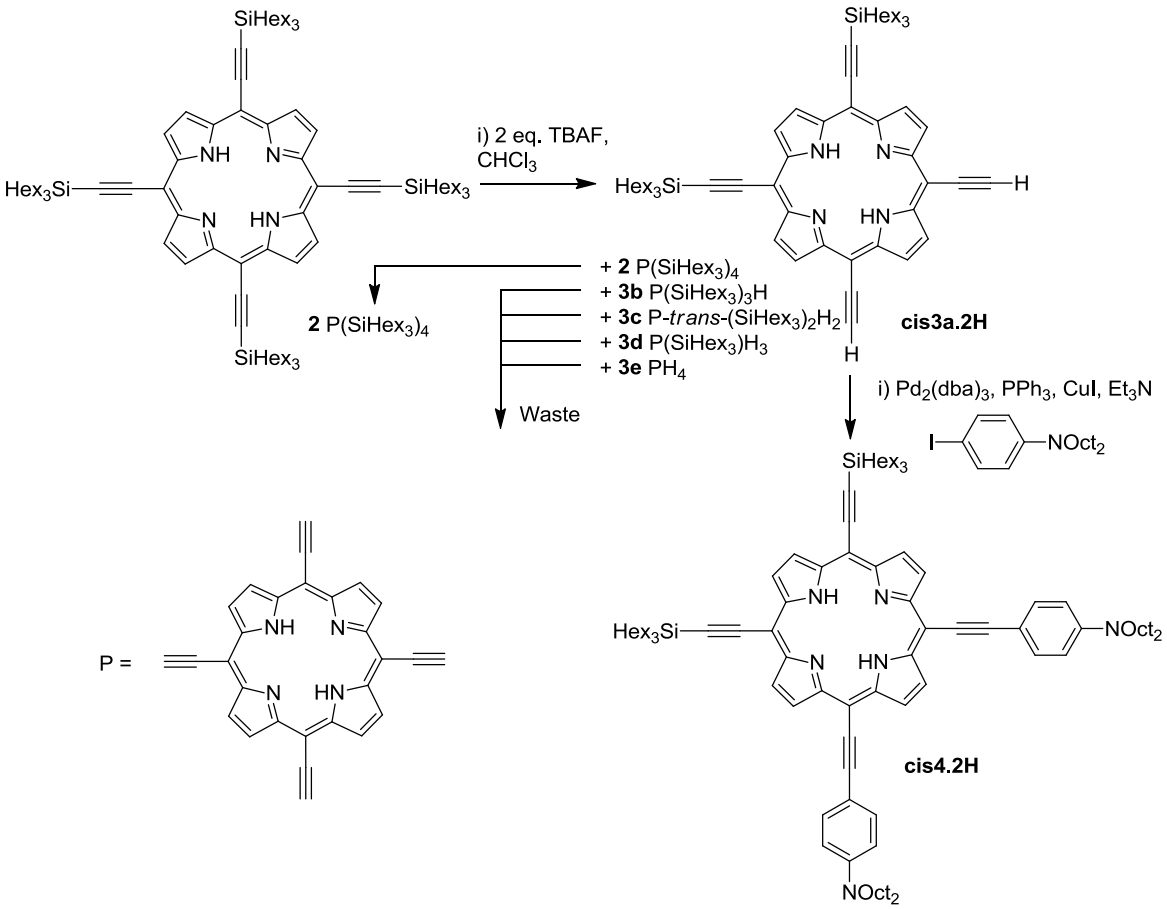

Scheme 3 Statistical deprotection of trihexylsilyl tetraethynyl porphyrin yields a statistical but seperable mixture of isomers, listed upon deprotection with TBAF. Decomposition of the product, even in the absence of oxygen, decreases the utility of this approach.

Purification proved possible with a slow gradient of CH_2Cl_2 in petrol ether, but more importantly we found that that deprotected material was highly succeptible to decomposition, forming insoluble precipitate even when stored for as little at 10 minutes in an inert atmosphere. I hypothesise that the source of this instability was the likelihood of the terminal porphyrinic acetylenes to undergo oxidative coupling, due to the insolubility of the resulting matter, which is most likely longer oligomers of the deprotected compound. MALDI spectroscopy showed the presence of low-order oligomers, suggesting that this was, indeed the case.[40, 41] Given the instability of the desymmetrised material and the low yield available through the statistical deprotection, this approach was abandoned.

4.2.2 Second Approach

Since terminal acetylene substituted porphyrins proved unstable when isolated, we investigated an approach that allows the use of in-situ deprotection and coupling, avoiding oligomerisation by effectively maintaining a very low concentration of deprotected terminal acetylenes. Taking advantage of the orthogonal deprotection conditions of trimethylsilyl acetylenes (TMS) and tri-isopropylsilyl (TIPS) acetylenes, we were able to perform a selective *cis*-deprotection and coupling *in situ* (Scheme 5). The difficulty in this approach is the synthesis of a *cis*-TMS *cis*-TIPS tetraethynyl porphyrin, which we synthesise through a statistical condensation from a mixture of the appropriate aldehydes and pyrrole. This compound may be isolated by column chromatography and the subsequent selective deprotection and *in situ* coupling is fast and high yielding.

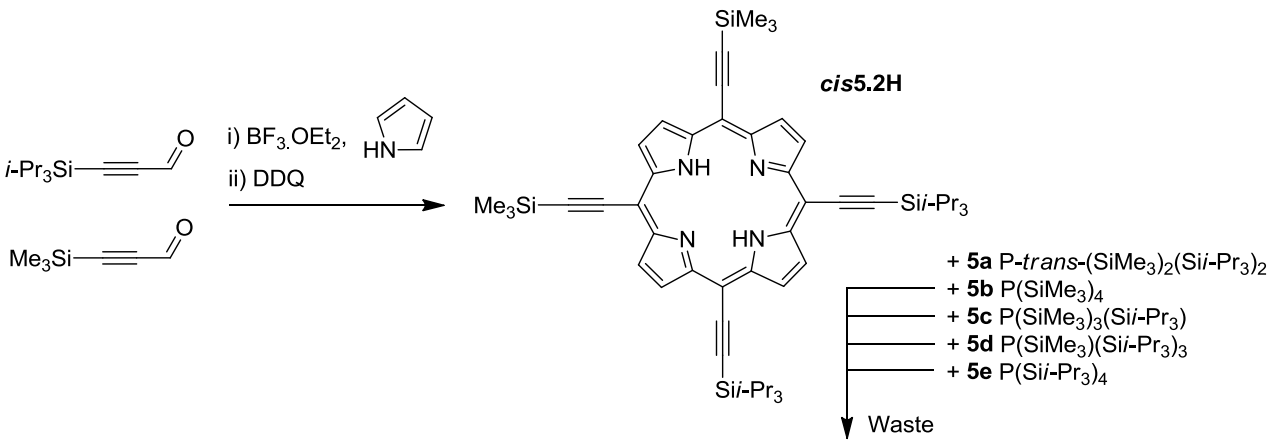

Scheme 4 Statistical acid-catalysed condensation yields a mixture of isomers which is easy to purify by column chromatography.

The purification step after the statistical condensation (Scheme 4) required for this approach presents a synthetic challenge, suffering from poor reproducibility and scalability. Adjusting the ratios of the appropriate TMS and TIPS protected acetylene aldehydes did not give predictable ratios of the *cis*-TMS *cis*-TIPS tetraethynyl porphyrin which made

optimisation of the reaction difficult. To counter this, high-dilution conditions were invoked, but these proved unfeasible on a large scale, leading us to consider a third approach.

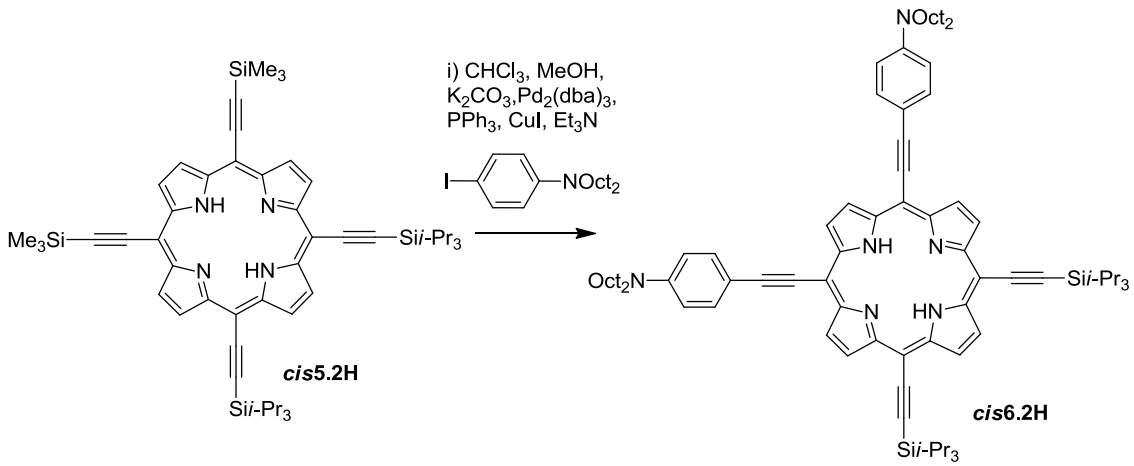

Scheme 5 In-situ deprotection of the trimethyl silyl protected acetylenes and immediate coupling with dioctyl aniline gives the key, stable desymmetrised product in one step.

During this synthesis, we were required to store *cis*-H *cis*-TIPS acetylene porphyrin–the THS analogue of which proved to be instable in Approach 1. We found that this compound was considerably more stable and would tolerate storage overnight at -20 °C in an inert atmosphere.

4.2.3 Third Approach

Encouraged by the finding of Approach 2 that *cis*-H *cis*-TIPS acetylene porphyrin is relatively stable, we attempted to replicate Approach 1 with TIPS protected instead of THS protected acetylenes. Furthermore, since the instability came from the high effective concentration of free-acetylenes, we adopt an approach which limits their exposure through both under-deprotection (i.e. the optimum ratio of the *cis*-product to starting material was not obtained in an effort to reduce the quantity of over-deprotected material which went to

waste, Scheme 6) and an immediate Sonogashira coupling without further deprotection. The under-deprotected material is then recycled back into the scheme and deprotected and coupled again, obtaining more *cis*-deprotected products in an iterative, cycling regime until the quantity of material recovered from the coupling is too small to warrant another pass (Scheme 6).

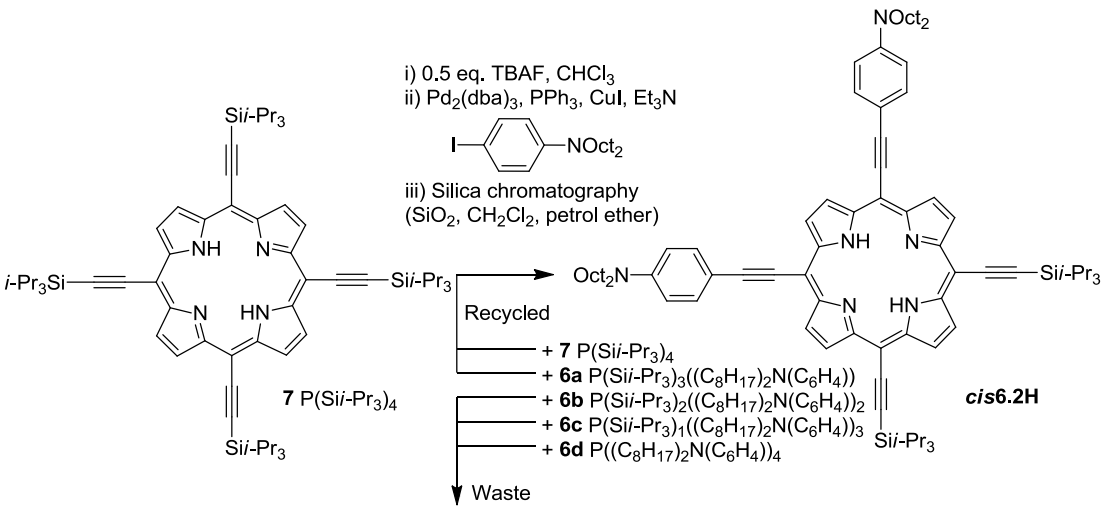

Scheme 6 The iterative recycling scheme that lead to a gram-scale statistical synthesis. The quantity of TBAF was kept low to ensure the production of the waste isomers was at a minimum and the cycle was iterated until no starting material remained.

4.2.4 Attachment of Acceptor Groups

Since TIPS tetraethynyl porphyrin can be synthesised at higher concentrations than the corresponding TMS derivative, these reactions may be scaled up and high enough yields obtained for the material to be carried on to the next step – the second deprotection and coupling to the pyridine acceptor. These steps are trivial, and proceeded in good yield, providing 25 mg (75%) of free-base and 21 mg (48%) of zinc-complexed *cis*-donor *cis*-acceptor tetraethynyl porphyrins.

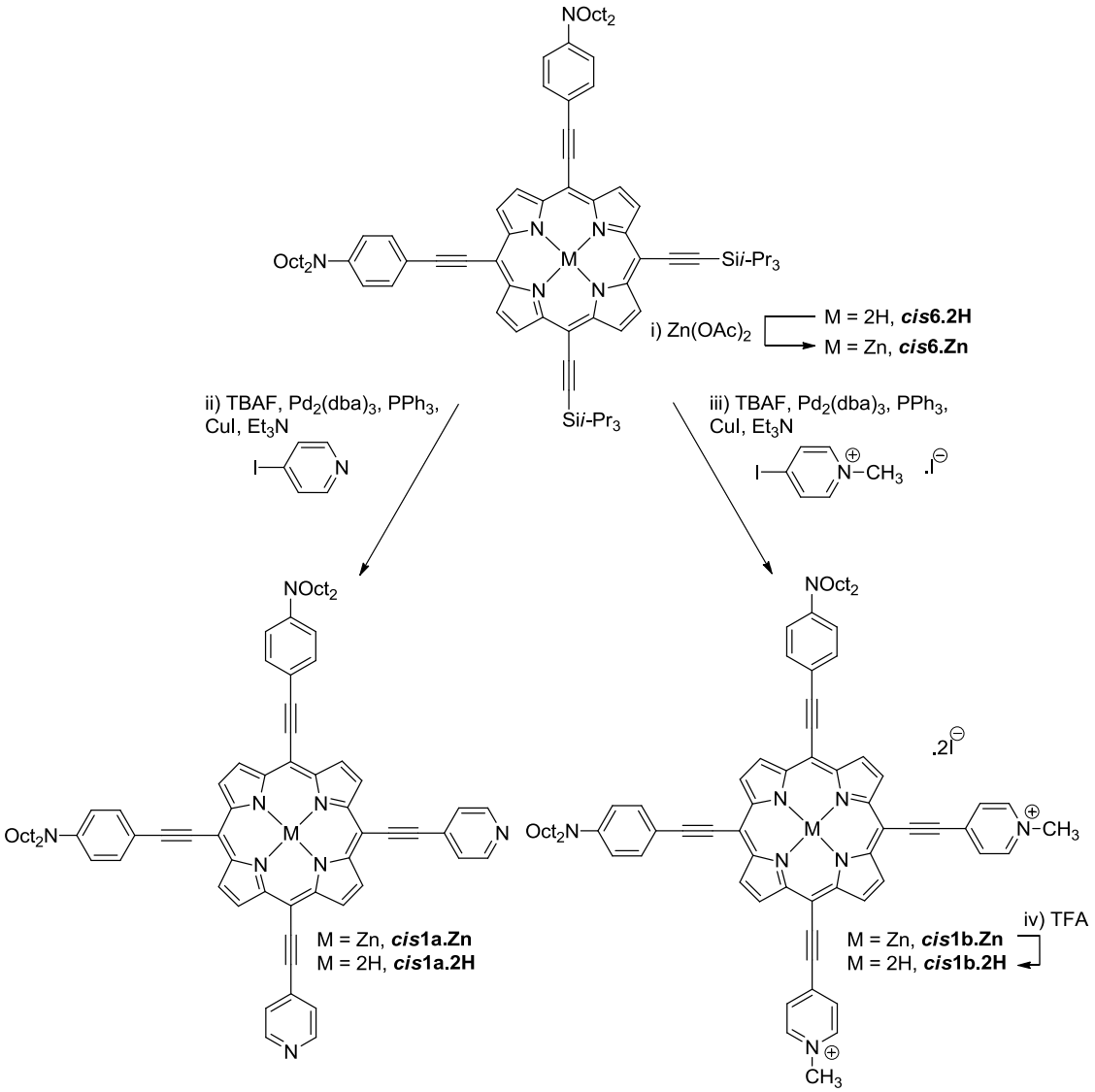

Scheme 7 Synthesis of the final family of four cis-donor cis-acceptor tetraethynyl porphyrin compounds from key intermediate 5.2H.

Methylation of the zinc complex ***cis*1a.Zn** was not possible since self-coordination of the zinc centre by pyridines reduced their nucleophilicity. An alternative route, the coupling performed instead with pre-methylated 4-iodo methylpyridinium iodide proceeded in 90% yield. Methylation of the free-base final product also proved troublesome due to poor solubility of the mono-methylated species (as confirmed by MALDI), which precipitated immediately on methylation with MeI, MeOTf or $Me_3O.BF_4$. Access to the free-base final

product ***cis*1b.2H** was eventually obtained through demetallation of the zinc complex ***cis*1b.Zn** with TFA in 85% yield (Scheme 7). Each of the target porphyrins was characterised by ^{1}H and ^{13}C NMR, MALDI mass spec, HRMS (ESI+), extinction coefficients were found when the compound was soluble, and some compounds were confirmed by elemental analysis.

4.3 Optical Properties

4.3.1 Linear Optical Trends

Given our synthetic access to key intermediate *cis*-donor *cis*-TIPS tetraethynyl porphyrin that we were granted through the use of our iterative recycling synthesis, we chose to construct a small library of *cis*-donor *cis*-acceptor tetraethynyl porphyrins and compare their linear and nonlinear optical properties. Full optical characterisation of potential NLO probes is important since the majority of their applications involve their interaction with light, thus better understanding these interactions can guide and enhance the development of future probes. Furthermore, the optical properties report the electronic structure of the underlying chromophore, so optical investigation will allow us to tease out the relationship between electronic structure and NLO properties.

While strong NLO properties are a key step towards in the optimisation of a structure for SHG imaging, to a large extent the linear optical properties can also have a predictive and interpretive role in understanding our findings. Information on the electronic structure present in absorption spectra may be used in Oudar and Chemla's model for predicting static beta, in the limit of a static electric field. (Equation 1).[42, 43] The molecular hyperpolarisability, β, when approximated to the two-level model (where one CT transition accounts for the majority of the hyperpolarisability) is related to the change in dipole

moment between the ground and excited state, $(\mu_{ee} - \mu_{gg})$, the transition dipole moment, μ_{ge}^2 and the energy gap between the two states, E_{ge}^2.

$$\beta \propto \frac{(\mu_{ee} - \mu_{gg})\mu_{ge}^2}{E_{ge}^2} \quad \text{(Eq. 1)}$$

Absorption spectra hold information on two of these terms, firstly the oscillator strength, which governs the strength of a transition and secondly the energy gap between ground and CT states, which is related to its wavelength.[1, 2] Additionally, the development of the Thomas-Kuhn-sum-rules, which rely on these two parameters, now allows for the accurate prediction of beta spectra over the entire optical spectrum.[44, 45] The predictive power of linear optical properties is only as good as the simplified models upon which they are based: in the static limit, the simplified model (Equation 1) does not take into account important factors such as resonance enhancement, aggregation or solvent effects. All UV/Vis spectra were recorded on a Perkin Elmer Lambda 20 UV-Vis spectrometer in DMF at 25 °C and are reported relative to a DMF blank.

4.3.2 Optical properties of *cis*-porphyrins and dipolar porphyrins

The absorption spectra of our *cis*-donor *cis*-acceptor tetraethynyl porphyrins show significant red-shifting in relation to their dipolar analogues (Figure 3), for both free-base and zinc derivatives. This trend would typically indicate that the *cis*-compounds have a lower HOMO-LUMO gap, whilst the oscillator strengths seem to remain approximately the same–an encouraging result which should lead to superior NLO properties.

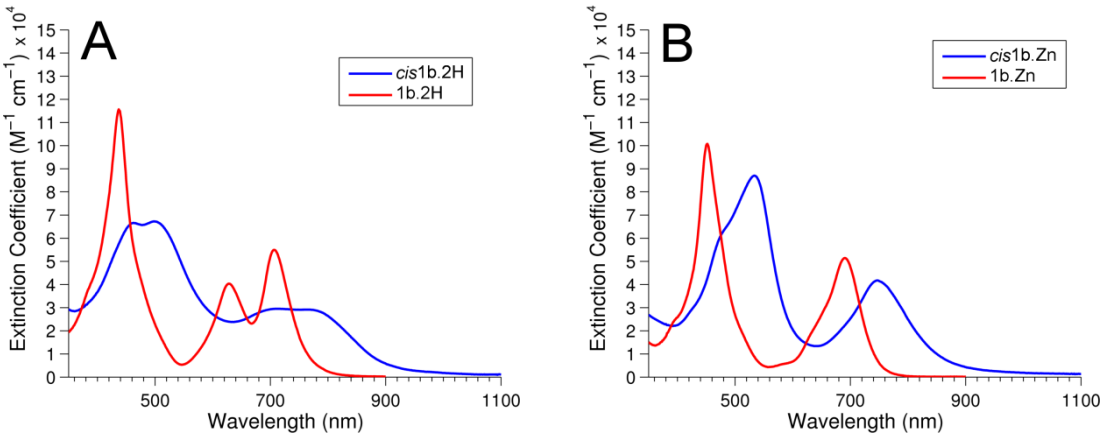

Figure 3 (A) Comparison of **1b.2H** (red) with ***cis*1b.2H** (blue) in DMF and (B) comparison of **1b.Zn** (red) with ***cis*1b.Zn** (blue) in DMF (1% py).

However, the significant broadening of the bands suggests that aggregation is also occurring in solution, and may be the source of the red-shift.[46] The inclusion of the zinc complex in this series should resolve this uncertainty–addition of a small quantity of pyridine triggers complete disaggregation as the zinc complex takes on a 5-coordinate geometry incompatible with an aggregated superstructure. This effect is apparent when we compare ***cis*1b.2H** with ***cis*1b.Zn** in the presence of pyridine. The band-broadening which deforms the spectrum of ***cis*1b.2H** is significantly reduced in the spectrum of ***cis*1b.Zn** (Figure 4B). Given the redshift of ***cis*1b.Zn** relative to dipolar **1b.Zn** in the absence of aggregation (Figure 3), we may surmise that *cis*-donor *cis*-acceptor compounds do have a smaller HOMO-LUMO gap, but we must also be acutely aware that they are prone to aggregation which may limit their usefulness.

4.3.3 Optical properties of free-base and zinc porphyrins

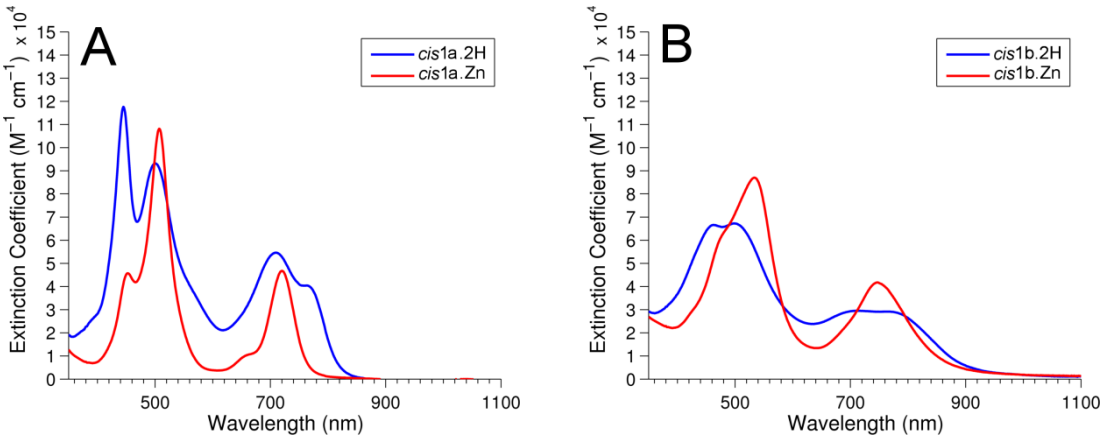

Figure 4 (A) Comparison of ***cis*1a.2H** (blue) in DMF with ***cis*1a.Zn** (red) in DMF (1% py) and (B) comparison of charged ***cis*1b.2H** (blue) in DMF with ***cis*1b.Zn** (red) in DMF (1% py).

Inclusion of a zinc complex in our library of compounds was motivated by the need for favourable solubility characteristics, despite our previous findings that the coordination of metals, and particularly zinc, causes attenuation of NLO properties. This is amply confirmed by the comparison of ***cis*1a.2H** and ***cis*1a.Zn** (Figure 4A), which we can be confident are not convolved by aggregation. We observe the lowest energy band of the free-base is shifted to the red by 50 nm in comparison with the zinc complex.

Undoubtedly the clearest trend within this family of compounds is the effect of moving from a weaker to a stronger electron acceptor by alkylation of the pyridine acceptors. Methyl pyridinium acceptors posess significantly lower electron density which adds to the charge-transfer character of the absorption band. In both the free-base and zinc complexs, we witness a dramatic redshift upon methylation (Figure 4), characteristic of a smaller HOMO-LUMO gap.

As previously discussed, the marked broadening of bands is attributable to substantial aggregation, particularly of ***cis*1b.2H**. Cationic porphyrins are well known to aggregate in a number of solvents, even in DMF which usually solvates cationic porphyrins relatively well (as a highly polar, relatively non-viscous solvent).[47, 48] While the aggregation of such porphyrins has previously been used to tune optical properties,[49, 50] accurate hyper-Rayleigh scattering (HRS) studies and SHG imaging in membranes both rely on the dyes acting as individual scatterers.

4.3.4 NLO properties

Quantification of molecular β via HRS is possible when a highly-dilute solution of a given chromophore is exposed to high-intensity laser light, a theoretical discussion of which may be found in Chapter 1, and a practical discussion of which may be found in Chapter 2.

Table 1 Hyper-Rayleigh scattering results for the *cis*-donor *cis*-acceptor tetraethynyl porphyrins described in the chapter with the molecular hyperpolarisability of dipolar dye **1b.2H** for comparison.

Porphyrin Dye	$\beta_{HRS,\ 1300}$	$\beta_{zzz,\ 1300}$
1b.2H	320 ± 10	760 ± 30
***cis*1a.2H**	174.4 ± 13.6	421.1 ± 32.9
***cis*1a.Zn**	128.3 ± 4.3	309.9 ± 10.5
***cis*1b.2H**	154.9 ± 4.6	374.0 ± 11.2
***cis*1b.Zn**	136.0 ± 7.6	328.4 ± 18.4

We see from Table 1 that despite the significant redshift exemplified in Figure 3, the *cis*-donor *cis*-acceptor porphyrins possess a weaker NLO response than their dipolar analogues. The following section will explore this inconsistency trends to rationalise some of the key trends within this family of NLO chromophores.

The first hyperpolarisability of each of the *cis*-donor *cis*-acceptor tetraethynyl porphyrins was measured in DMF at 1300 nm. Experiments at this wavelength rather than the 840 nm of the dipolar compounds are a consequence of the difficulty in obtaining high-quality data– since the molecule's absorption tails up to 1000 nm, Ti:Sapphire and pulsed 1064 nm Nd:YAG lasers could not be used (as the signal would be dominated by linear absorption). DMF and DMF with 1% pyridine was used to solvate the free-base and zinc complexes respectively, to encourage as much disaggregation as possible, but despite these measures, considerable aggregation was still observed for ***cis*1b.2H**.

These structural and electronic arguments do not explain why our *cis*-compounds have NLO properties *weaker* than their dipolar equivalents. Most likely, the two mechanisms which reduce measured hyperpolarisability in this case are aggregation and wavelength-dependence. Firstly, we have discussed the tendency of cationic porphyrins to aggregate or precipitate; if each substrate is not fully solvated when HRS is undertaken, the effective concentration of scatterers is drastically reduced, as head-to-tail dimers will be electrostatically favoured, which results in a low β_{HRS}. Secondly, the resonance enhancement of $\beta_{HRS,\,\lambda}$ at wavelength, λ, is highly chromophore dependent, and it may be that **1b.2H** is simply on-resonance at 1300 nm and ***cis*1b.2H** is off resonance. Extraction of wavelength-dependent β spectra of each compound could reveal the general wavelength ranges of resonance enhancements.

Despite these assertions, we are still able to use the trends within this family of data to make some important observations. The trend observed in Chapter 1 where we demonstrate that free-base porphyrins have stronger NLO properties than Zinc complexes is conserved, attributable to a lower HOMO-LUMO gap in the free-base which is widened upon complexation of zinc.

Previous studies have shown that in general, pyridine *N*-alkylation increases acceptor strength and subsequently the first hyperpolarisability. Given the results for this family of porphyrins, we find that charge-induced aggregation upon alkylation surpasses increase in acceptor strength. Dissapointingly, the weakness of the β_{HRS} observed meant that depolarisation ratios and therefore the off-axis contributions to β_{HRS} (specifically β_{zxx}) could not be quantified (as the data was too noisy). While we still expect β_{zzz} to be larger than β_{zxx} for these chromophores, not knowing β_{zxx} is a profound disadvantage when measuring molecular tilt, which will be covered in the next section.

4.4 Imaging in Membranes

Our previous work which determined the distribution of tilt angles from (amongst other techniques) SHG polarisation anisotropy relied heavily on the assumption that the dipolar molecule in question possessed a single dominant β_{zzz} tensor component.[51-53] The different contributions of β_{zzz} to the membrane bulk hyperpolarisability $\chi^{(2)}$ at different tilts gives the angular intensity function from which we may derive an expression for molecular tilt.

The *cis*-donor *cis*-acceptor tetraethynyl porphyrins which we have synthesised and investigated optically in this chapter deviate substantially from this model and will not conform by having single, dominant β_{zzz} tensor components. The 2nd component that we now need to consider is the β_{zxx} contribution to β, which may be understood physically as the interaction of the molecular hyperpolarisability along the molecular *z*-axis with two photons polarised in the *x*-direction (where the photon comes from *y*). This geometry will be present in biological samples, and especially in the droplet monolayer system used in Chapter 3.[53]

We may account for this off-axis contribution to $\chi^{(2)}$ by including β_{zxx} terms from the tensor rotations we perform to find the angular dependence of SHG (which we previously ignored in our previous treatment, found in Chapter 3).[52] The inclusion of these terms gives a more complex angular dependent behaviour:

$$I_{SHG}^{\parallel}(\theta,\varphi) \propto \cos^2\theta \left((2 + r\vartheta_{SHG})\cos^2\theta + \frac{1}{2}\left(r + \vartheta_{SHG}(3-r)\right)\sin^2\theta\right)^2 \qquad \text{(Eq. 2)}$$

Where θ is the angle between the ensemble of dyes and the laser light, υ_{SHG} is the angular structure factor and r is a depolarisation ratio $r = \frac{\beta_{zxx}}{\beta_{zzz}}$. This modified angular intensity function, now contains two unknown parameters, υ_{SHG}, the structure factor which reports on the tilt of the dye and r, the relative contributions of β_{zzz} and β_{zxx}. In the limit of small β_{zxx}, Equation 2 collapses to the angular intensity function for β_{zzz} alone. As β_{zxx} has a larger contribution, it will affect the form of the angular intensity function, regardless of the degree of tilt of the molecule. It is important to note that for dyes with a high average tilts, β_{zxx} makes more significant contributions to the transmembrane bulk hyperpolarisability, $\chi^{(2)}$, than for small tilts, causing a greater deviation from the expected behaviour (Figure 5).

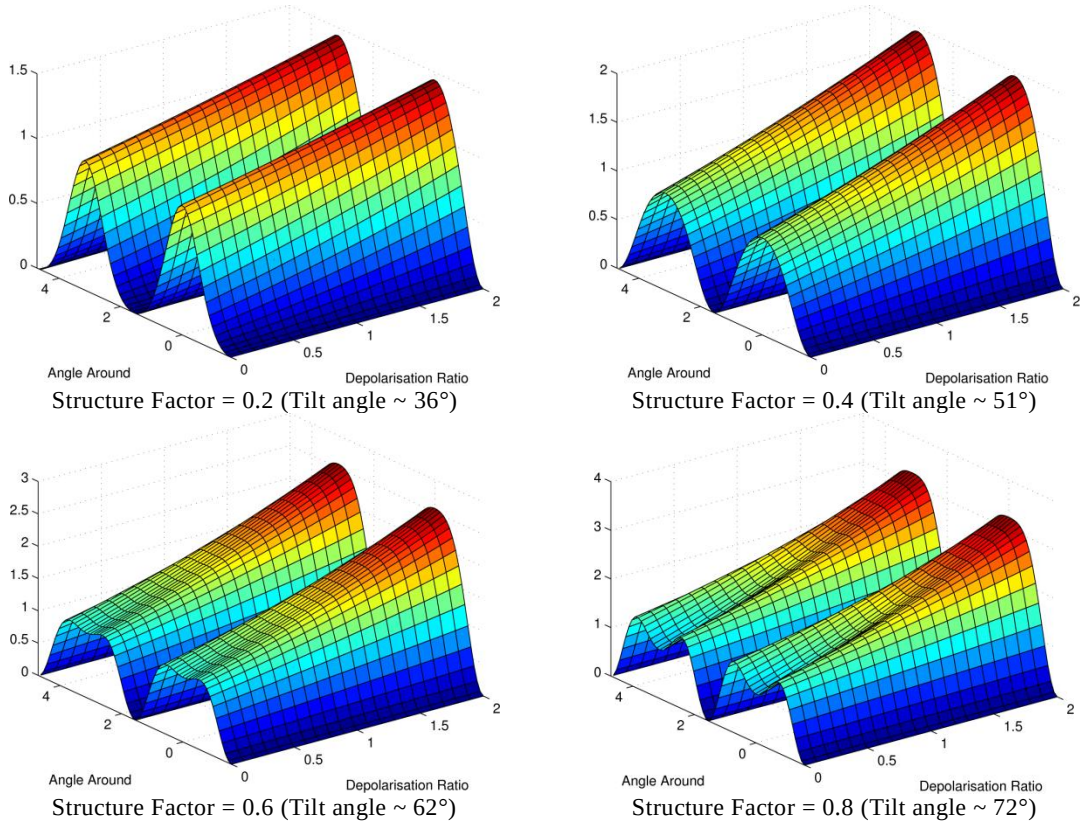

Figure 5 Plots of angular intensity functions for increasingly tilted dyes in membranes, representing structure factors of 0.2, 0.4, 0.6 and 0.8. Dyes with greater tilts (and higher structure factors) naturally allow for greater contributions of β_{zxx} to the transmembrane hyperpolarisability, $\chi^{(2)}$. Large depolarisation ratios have a greater influence on the shape of the angular intensity function than small depolarisation ratios. In all cases, if we increase the depolarisation ratio up to 2, so that β_{zxx} becomes the domination transmembrane component, angular intensity functions become nearly indistinguishable, only really acting to increase the overall intensity.

Therefore, when a dye contains significant off-axis tensor contributions to β, we must first find r from alternative methods before attempting to extract structure factors, otherwise a range of combinations of r and υ_{SHG} will still give satisfactory outcomes for the angular distribution function observed. Since we were unable to measure r by HRS, we are limited to finding combination of values of r and υ_{SHG} from SHG imaging. We were able to obtain weak SHG and 2PF images from ***cis*1b.Zn** (Figure 6) in the droplet monolayer model membrane system. While the SHG from these images is not as strong as for our dipolar dyes they still contain tilt-angle information.

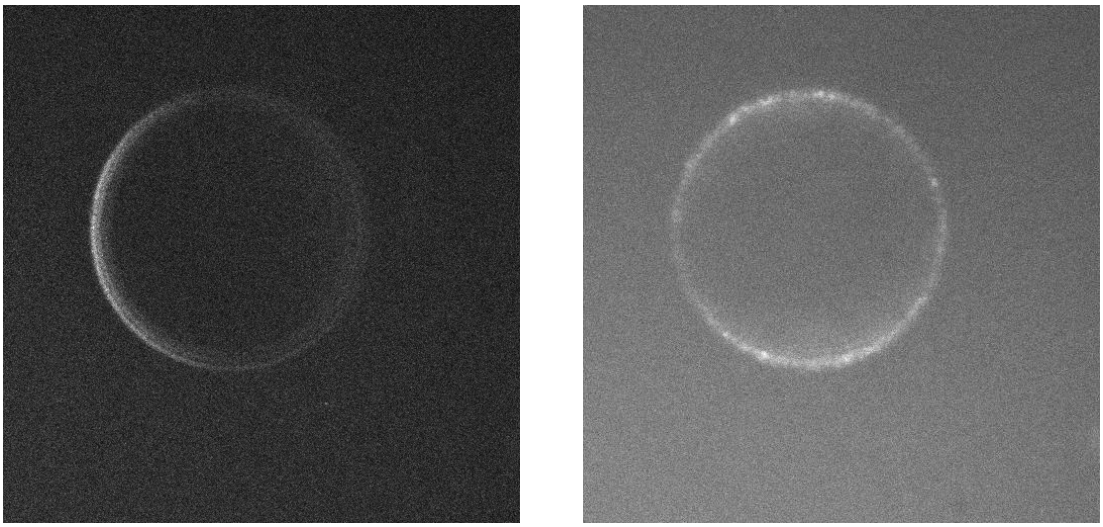

Figure 6 SHG (left) and 2PF (right) images of ***cis*1b.Zn** in droplet monolayer DPhPC model membranes. Each image is 300 μm × 300 μm.

As we do not know r or υ_{SHG} in Equation 2, we input a range of values for each and see which combinations give the best fits to the angular intensity data. If we take every combination of r and υ_{SHG}, then we can plot them as an isosurface in $r \times \upsilon_{SHG}$ space (Figure 7).

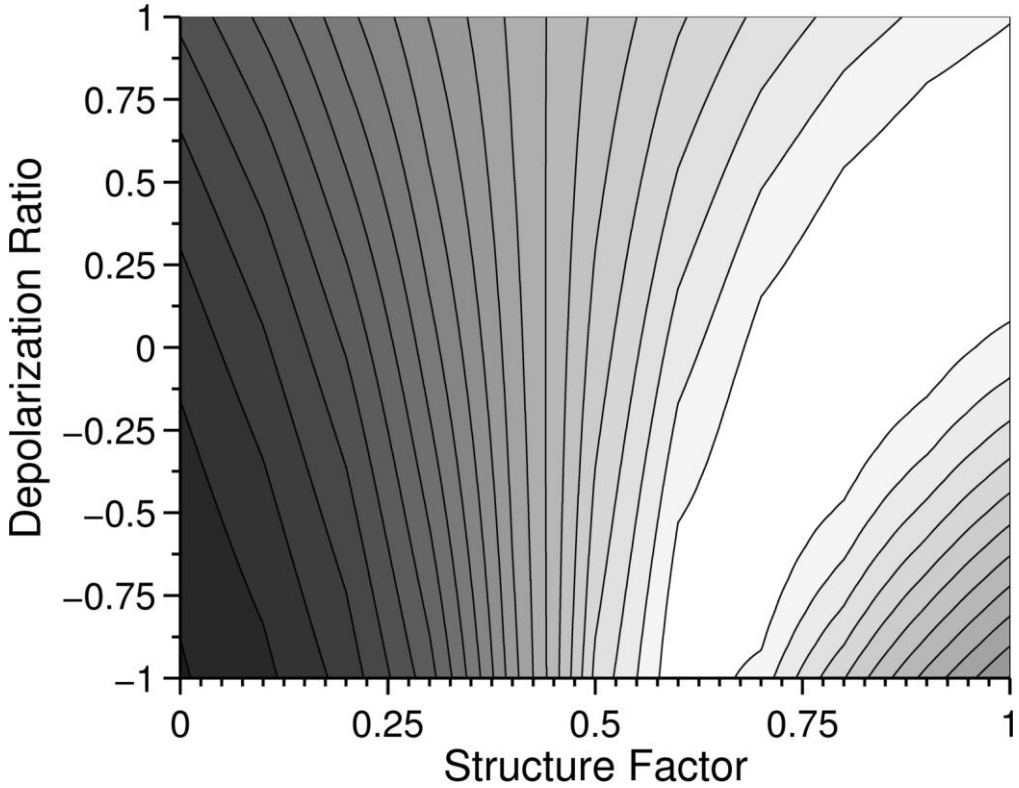

Figure 7 Isosurface in $r \times \upsilon_{SHG}$ space, illustrating the region of structure factors and depolarisation ratios which are likely. From the surface, we see a valley running through the potential surface, indicative of many pairs of r and υ_{SHG}, each of would give a satisfactory fit to the angular distribution function.

The overall shape of the landscape in Figure 7 may be broadly interpreted as follows: The greater the depolarisation ratio of the dye, the more tilted it must also be to give the kind of angular distribution function present in Figure 6. We may assume that that a) the depolarisation ratio lies in the range -1 to 1 (β_{zxx} cannot be larger than β_{zzz}, for this type of chromophore) and b) the structure factor must be less than 1 (since dyes may only be tilted from 0° – 90°, which defines the structure factor range 0 – 1). This allows us to place broad constraints on the depolarisation ratio and structure factor for this *cis*-donor *cis*-acceptor tetraethynyl porphyrin (Table 1).

Table 1 Constraints placed on the structure factor and depolarisation ratio of **cis1b.Zn** in a surface monolayer of DPhPC at the interface of a water droplet in dodecane by the potential surface shown in Figure 7.

	Structure Factor, υ_{SHG}	Expected tilt, $\langle\varphi\rangle$	Depolarisation Ratio (r)	$\beta_{zxx,\ 1300}$
Minimum	0.62	63.7°	-1	-328.4 ± 18.4
Maximum	1.00	90°	0.88	289.0 ± 15.8

This ability to place maximum and minimum bounds on these parameters, whilst not as instructive as finding the actual solution, does allow us to draw some interesting conclusions.[54] For example, the dye is heavily tilted in the membrane, lying at least 63.7° away from the normal: Despite its amphiphilic character, such a high structure factor tells us that this dye does not penetrate deeply into membranes (well-incorporated chromophores tend to have less orientational freedom and hence exhibit lower structure factors).

Two-photon polarisation anisotropy is not as well understood as linear dichroism or SHG polarisation anisotropy. Our 2PF anisotropy experiments rely on an assumption that the two-photon absorptivity tensor, $\hat{T}_{ij}$,[55] may be approximated to a pseudo-TDM which is collinear with the molecular axis (i.e. $\hat{T}_{zz}$ is the major tensor component). The *cis*-molecular architecture will have tensor components with significant off-axis contributions (e.g. $\hat{T}_{xz}$) thus decreasing the validity of the assumption $\hat{T}_{ij} = \hat{T}_{zz}$, and therefore, 2PF absorption may no longer be treated as a special case of linear dichroism (through the approach used in Chapter 3).[55-57]

A significantly more involved derivation of two-photon absorption anisotropy through a sum-over-states approach is required to interpret these 2PF images.[58] Given that we do not know $\hat{T}_{ij}$ for our cis-porphyrins, completing this derivation would not be fruitful and

therefore we consider it outside the scope of this chapter. In the absence of high quality images and subsequently trigonometric moments of the tilt angle probability density function, we remain unable to fully resolve the distribution of tilts–the like of which is found for di-4-ANEPPS and di-8-ANEPPS in Chapter 3. Nevertheless, we demonstrate that these dyes are capable of generating SHG light through the images obtained in Figure 7.

4.5 Conclusions

This chapter describes the synthesis and optical investigation of a new class of donor-acceptor chromophores, designed to take advantage of off-axis contributions to enhance nonlinear optical properties. The attachment of additional donors and acceptors to give a *cis*-substituted chromophore was performed by means of a statistical, recycling deprotection and coupling approach. The increased donor-acceptor character, when added to an already highly-polarisable π-system causes a large redshift, with the porphyrin Q-band tailing up to 1000 nm. Despite this redshift and the strong nonlinear properties that it confers, we were unable to resolve the expected high β_{HRS} as a consequence of either poor solubility or lack of resonance enhancement at 1300 nm (the only laser line available which avoided one-photon absorption).

The redshifted one-photon absorption and poor solubility of these compounds render them unsuitable for NLO biological imaging, since we cannot take advantage of SHG or 2PF in the biological transparency window. Nevertheless, we attempt to investigate the tilt angle and second harmonic generation of ***cis*1b.Zn** by imaging the dye incorporated within droplet monolayer model membranes. Since two-photon absorption does not have the same symmetry criteria as SHG, we may no longer ignore off-axis tensor components. Current

two-photon absorption anisotropy measurements rely on the assumption that an axial *z*-contribution dominates the two-photon absorptivity tensor. The addition of off-axis contributions to this tensor leads to an angular intensity function which is not well understood.

4.6 Experimental

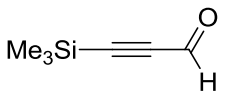

3-(Trimethylsilyl)propiolaldehyde was synthesised according to a literature procedure.[59] 3-(Trimethylsilyl)prop-2-yn-1-ol (500 mg, 3.9 mmol) was added to a suspension of 2-iodoxybenzoic acid (1.31 g, 4.7 mmol) in THF (4 mL). The mixture was brought to reflux and stirred for 4 hours under N_2 before it was allowed to cool to RT. The resulting solid was filtered off under vacuum and washed with ice cold diethyl ether (4 × 25 mL). The volume of the combined filtrates was reduced under vacuum and distilled (52 °C, 50 mbar) to obtain a transparent oil (477 mg, 97%). ^{1}H NMR (400 MHz, $CDCl_3$) δ_H 9.18 (s, 1H), 2.17 (s, 9H), ^{13}C NMR (50 MHz, CDCl3) δ_C 184, 109, 107, 5.11

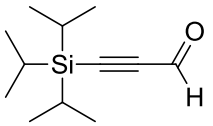

3-(Triisopropylsilyl)propiolaldehyde was synthesised according to a literature procedure.[60] *n*-Butyllithium (17.6 mL, 28.4 mmol, 1.6 M in hexanes) was added dropwise to a degassed solution of ethynyltriisopropylsilane (6 mL, 27 mmol) in dry THF (60 mL) at 0 °C. The mixture was stirred at 0 °C for 20 mins, allowed to warm to RT and stirred for a further 20 mins. The reaction was cooled to 0 °C again and *N*,*N*-dimethylformamide (1.96 ml, 28.4 mmol) was added in one portion. The reaction was heated to reflux for one hour then allowed to cool to RT. The reaction mixture was poured onto $H_2SO_{4(aq)}$ (5% by volume) at 0 °C. The resulting mixture was neutralised with a saturated solution of $NaHCO_3$ and extracted with $CHCl_3$. The organic layer was dried over $MgSO_4$ and the volume reduced in vacuo. The aldehyde was purified from the free acetylene by vacuum distillation (120 °C, 10 mbar) which gave a transparent oil (4.8 g, 85%). ^{1}H NMR (400 MHz, $CDCl_3$) δ_H 9.21 (s, 1H), 1.12 (s, 21H), ^{13}C NMR (50 MHz, $CDCl_3$) δ_C 176.90, 104.87, 101.01, 18.78, 11.32

Method #1

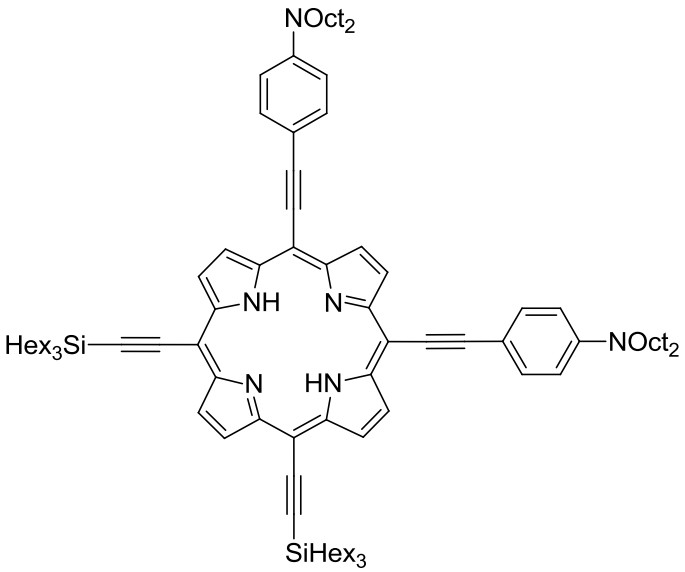

5,10-(4-(*N*,*N*-Dioctylamino)phenyl)ethynyl 15,20-(trihexylsilyl)ethynyl porphyrin ***cis*4.2H** was prepared by statistical deprotection according to a literature procedure.[33] 5,10,15,20-Trihexylsilyl ethynyl porphyrin **2** was obtained from a previous synthesis by Dr. Wouter Maes. The porphyrin (330 mg, 237 μmol) was stirred in $CHCl_3$ (500 mL) and TBAF (200 μL, 1.0 M in THF) was slowly added by syringe whilst monitoring the reaction by TLC (petrol ether:$CHCl_3$ 10:1). Once any tetra-deprotected product could be detected by TLC, the reaction was quenched by pouring onto a short silica plug. The solvent was removed in vacuo and the *cis*-deprotected product ***cis*3a.2H** was purified by column chromatography. The combined *cis*-deprotected fractions were dried *in vacuo* with $Pd_2(dba)_3$ (10 mg), PPh_3 (11 mg), CuI (1.5 mg) and dioctyl aniline (314 mg, 711 μmol). Et_3N (200 mL) was added and the mixture immediately freeze-thaw degassed. After all starting material had been consumed (about 15 minutes, monitoring by TLC) the reaction was allowed to stir for a further 30 minutes. The volume of mixture was then reduced *in vacuo* and the crude mixture columned on silica. Significant amounts of the *cis*-deprotected porphyrin had polymerised

and remained trapped at the top of the column. The combined fractions were dried to yield ***cis*4.2H** as a brown solid (7 mg, 2%). ^{1}H NMR (400 MHz, $CDCl_3$) δ_H 9.58 (m, 4H), 9.47 (m, 4H), 7.89 (d, 4H, *J* = 8.61 Hz), 7.80 (d, 4H, *J* = 8.61 Hz), 3.41 (t, 8H, *J* = 7.97 Hz), 1.8-0.8 (m, alkyl region), -1.13 (br. s, 2H) R_f = 0.74 (petrol ether:$CHCl_3$ 1:2), *m/z* (MALDI+) 1602.09 ($[M]^+$ 100%, $C_{108}H_{164}N_6Si_2^+$ requires 1602.26).

Method #2

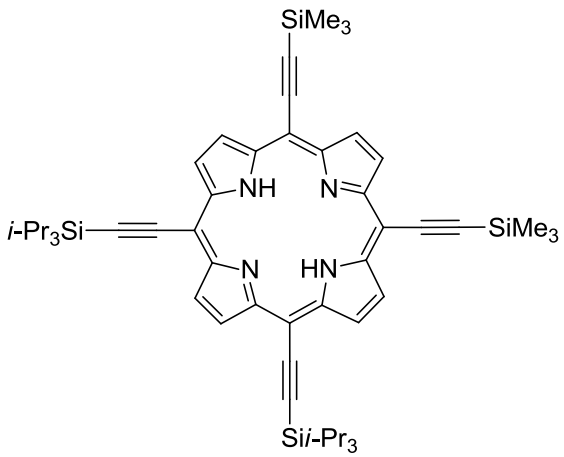

5,10-((Trimethylsilyl)ethynyl) 15,20-((triisopropylsilyl)ethynyl porphyrin ***cis*5.2H** was synthesised according to a literature procedure.[61] A solution of 3-(triisopropylsilyl)propiolaldehyde, (1.00 g, 4.75 mmol), 3-(trimethylsilyl)propiolaldehyde, (0.6 g, 4.75 mmol) and pyrrole (665 μL, 9.5 mmol) in CH_2Cl_2 (950 mL) was degassed through three freeze pump thaw cycles. $BF_3.OEt_2$ (152 μL, 1.235 mmol) was added dropwise and the mixture stirred under N_2 for one h. DDQ (2.16 g, 9.5 mmol) was added and the resulting mixture was allowed to stir for a further 15 mins. The volume of CH_2Cl_2 was reduced *in vacuo* and the mixture was passed through two short SiO_2 plugs in CH_2Cl_2 to remove tarry residues. The statistical mixture was purified by

column chromatography on SiO_2 (CH_2Cl_2:petrol ether 5:95 → 8:92). Both *cis* and *trans* isomers were collected together in one fraction and evaporated to dryness (68 mg, 3.3%). Due to inseperability of *cis*- and *trans*-isomers, the mixture was treated as intermediate and taken directly through to the next step.

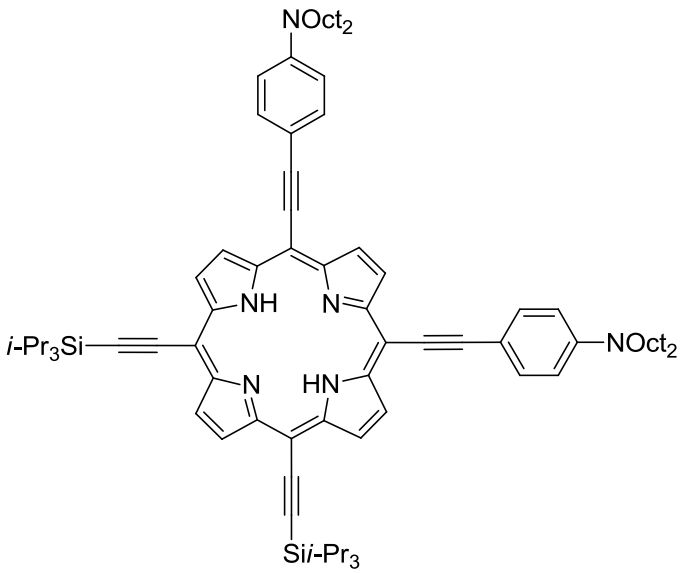

5,10-(4-(*N*,*N*-Dioctylamino)phenyl)ethynyl 15,20-(triisopropylsilyl)ethynyl porphyrin ***cis*6.2H** was synthesised according to an adapted literature procedure.[33] 5,10-((Trimethylsilyl)ethynyl) 15,20-((triisopropylsilyl)ethynyl porphyrin ***cis*5.2H** and **5a.2H** (combined cis and trans isomers, 54 mg, 62 μmol), $Pd_2(dba)_3$ (5 mg, 5.5 μmol), PPh_3 (6 mg, 22.9 μmol) and CuI (1 mg, 5.5 μmol) were dried *in vacuo* for 15 minutes. Triethylamine (3 mL) and 4-iodo-*N*,*N*-dioctylaniline (164 mg, 372 μmol) were added and the mixture freeze-pump-thaw degassed. A saturated solution of K_2CO_3 in degassed MeOH (100 μL) was added to the mixture which was stirred at 40 °C for 16 h. The reaction mixture was passed through a SiO_2 plug in CH_2Cl_2, then the *cis* isomer was purified by column chromatography on SiO_2 (CH_2Cl_2:petrol ether 1:9 → 2:8). The combined fractions containing the *cis* isomer were evaporated to yield the product ***cis*6.2H** as a purple glass

(31 mg, 34%). λ_{max} ($CHCl_3$)/nm (logε) 438 (4.94) 488 (5.11) 672 (4.74) 752 (4.36), ^{1}H NMR (250 MHz, $CDCl_3$) δ_H 9.65–9.3 (m, 8H), 7.91 (d, J = 8.31 Hz, 4H), 6.83 (d, J = 8.31 Hz, 4H), 3.34 (t, J = 7.5 Hz, 8H), 1.73 (m, 8H), 1.58–1.33 (m, 82H), 1.00–0.93 (m, 12H), -1.16 (br. s., 2H) ^{13}C NMR (125 MHz, $CDCl_3$) δ_C 148.50, 133.23, 133.18, 111.49, 108.93, 108.08, 105.06, 101.46, 100.40, 99.31, 89.90, 51.08, 31.85, 29.68, 29.52, 29.35, 27.30, 27.19, 22.67, 22.53, 19.11, 18.79, 18.50, 14.12, 12.32, 12.07, 11.85

Method #3

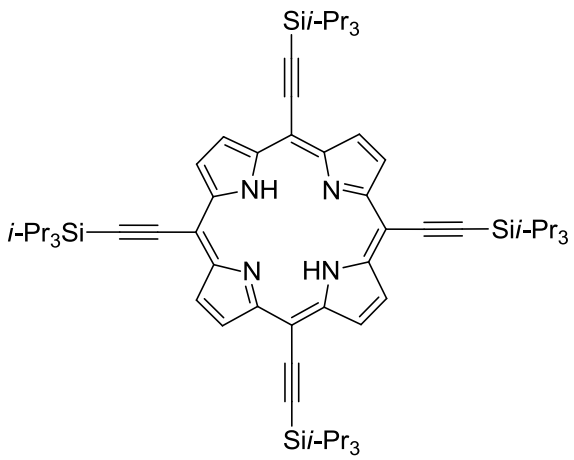

5,10,15,20-(Triisopropylsilyl)ethynyl porphyrin **7** was synthesised according to a literature procedure.[61] A solution of 3-(triisopropylsilyl)propiolaldehyde, (2.00 g, 9.5 mmol) and pyrrole (665 µL, 9.5 mmol) in CH_2Cl_2 (950 mL) was degassed through three freeze pump thaw cycles. $BF_3.OEt_2$ (152 µL, 1.235 mmol) was added dropwise and the mixture stirred under N_2 for one hour. DDQ (2.16 g, 9.5 mmol) was added and the resulting mixture was allowed to stir for a further 15 mins. The volume of CH_2Cl_2 was reduced *in vacuo* and the mixture was passed through two short SiO_2 plugs in CH_2Cl_2 to remove tarry residues. The statistical mixture was purified by column chromatography on SiO_2 (CH_2Cl_2:petrol ether 5:95 → 8:92) and evaporated to dryness (0.88 g, 36%). ^{1}H NMR (400 MHz, $CDCl_3$) δ_H 9.57 (s, 8H), 1.47 (s, 84H), -1.73 (br. s, 2H),

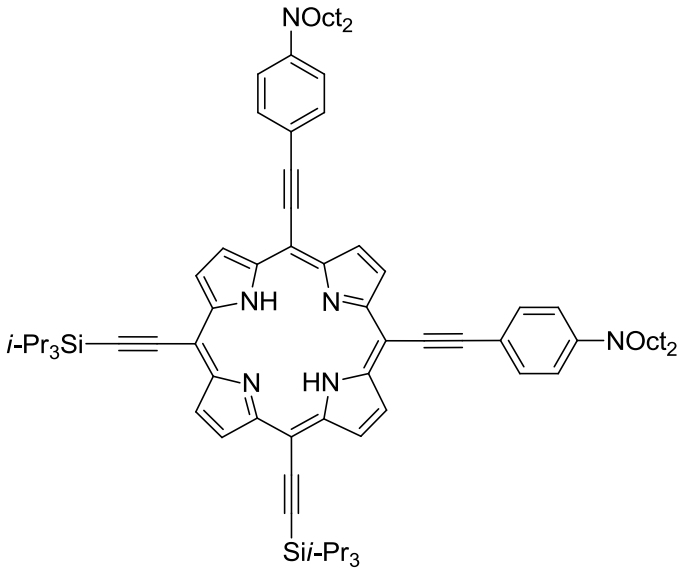

5,10-(4-(*N*,*N*-Dioctylamino)phenyl)ethynyl 15,20-(triisopropylsilyl)ethynyl porphyrin ***cis*6.2H** was synthesised according to a literature procedure.[33] 5,10-((Trimethylsilyl)ethynyl) 15,20-((triisopropylsilyl)ethynyl porphyrin **7** (3.7 g, 3.6 mmol) was stirred in $CHCl_3$ (500 mL) and tetrabutylammonium fluoride (up to 200 μL, 1.0 M in THF) was slowly added by syringe whilst monitoring the reaction by TLC (petrol ether:$CHCl_3$ 10:1). Once *bis*-deprotected product could be detected by TLC, the reaction was quenched by pouring onto a short silica plug. The solvent was removed in vacuo and the *cis*-deprotected product was subjected to a Sonogashira coupling by adding $Pd_2(dba)_3$ (300 mg, 327 μmol), PPh_3 (360 mg, 1.37 mmol) and CuI (60 mg, 315 μmol) and drying *in vacuo* for 15 minutes. Diisopropylamine (50 mL), toluene (50 mL) and 4-iodo-*N*,*N*-dioctylaniline (3.18 g, 7.16 mmol) were added and the mixture freeze-pump-thaw degassed. The mixture which was stirred at 40 °C for 4 h then passed through a SiO_2 plug in CH_2Cl_2. The *cis*-isomer was purified by column chromatography on SiO_2 (CH_2Cl_2:petrol ether 1:9 → 2:8), the trans isomer was discarded and *mono*- and *non*-substituted porphyrin were resubjected to deprotection conditions. Combined *cis*-isomer fractions were evaporated to yield the product ***cis*6.2H** as a purple glass (544 mg, 11%). λ_{max} ($CHCl_3$)/nm (logε) 438

(4.94) 488 (5.11) 672 (4.74) 752 (4.36), ^{1}H NMR (250 MHz, $CDCl_3$) δ_H 9.65–9.3 (m, 8H), 7.91 (d, J = 8.31 Hz, 4H), 6.83 (d, J = 8.31 Hz, 4H), 3.34 (t, J = 7.5 Hz, 8H), 1.73 (m, 8H), 1.58–1.33 (m, 82H), 1.00–0.93 (m, 12H), -1.16 (br. s., 2H) ^{13}C NMR (125 MHz, $CDCl_3$) δ_C 148.50, 133.23, 133.18, 111.49, 108.93, 108.08, 105.06, 101.46, 100.40, 99.31, 89.90, 51.08, 31.85, 29.68, 29.52, 29.35, 27.30, 27.19, 22.67, 22.53, 19.11, 18.79, 18.50, 14.12, 12.32, 12.07, 11.85

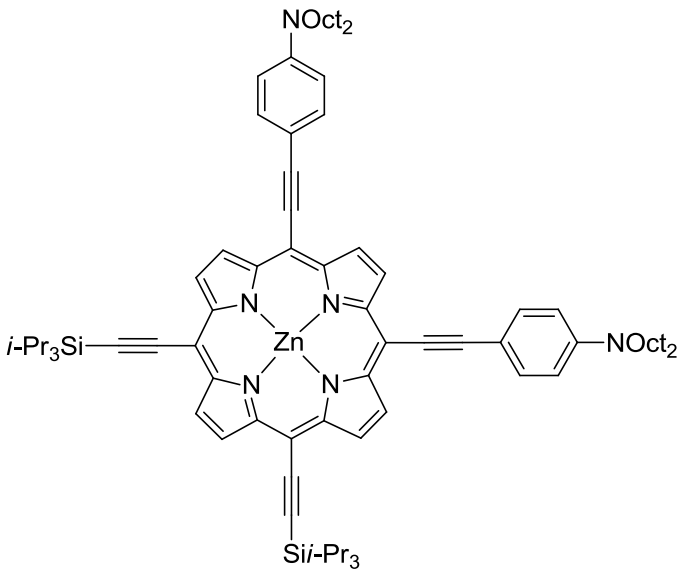

5,10-(4-(*N*,*N*-Dioctylamino)phenyl)ethynyl 15,20-(triisopropylsilyl)ethynyl porphyrin, Zn (II) complex ***cis*6.Zn** was synthesised from the corresponding free-base equivalent ***cis*6.2H**. $Zn(OAc)_2$ (55.5 mg, 300 μmol) in MeOH (0.5 mL) was added to a solution of 5,10-(4-(*N*,*N*-dioctylamino)phenyl)ethynyl 15,20-(triisopropylsilyl)ethynyl porphyrin (51 mg, 37.7 μmol) in $CHCl_3$ (10 mL) and the mixture stirred at 40 °C for 30 minutes. The mixture was evaporated to dryness then passed through a SiO_2 plug in CH_2Cl_2 to remove excess Zinc residues. The coloured fraction was evaporated to dryness to obtain the product ***cis*6.Zn** as a purple glass (49 mg, 92%). ^{1}H NMR (400 MHz, $CDCl_3$) δ_H 9.65–9.60 (m, 4H), 9.57–9.55 (m, 4H), 7.85 (d, J = 8.52 Hz, 4H), 6.76 (d, J = 8.63 Hz, 4H), 3.36 (t, J = 7.61 Hz, 8H), 1.72–1.61 (m, 8H), 1.48–1.21 (m, 82H), 0.93–0.88 (m, 12H).

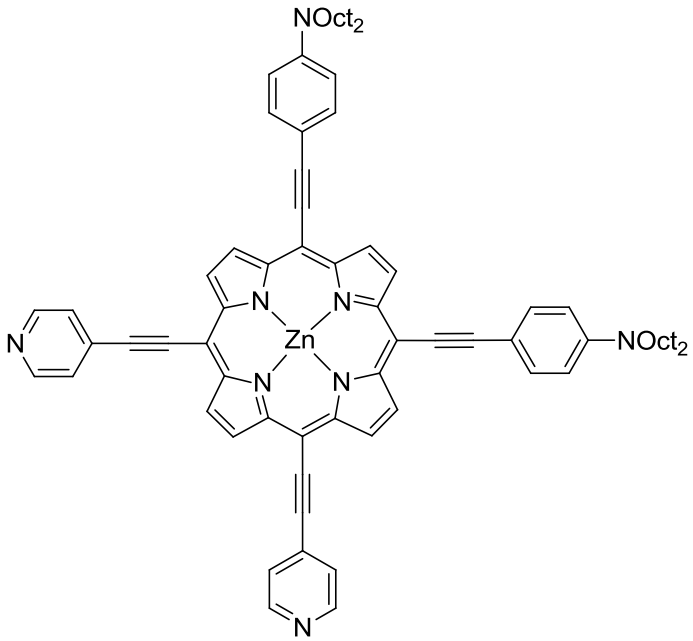

5,10-(4-(*N*,*N*-Dioctylamino)phenyl)ethynyl 15,20-(4-pyridyl)ethynyl porphyrin, Zn (II) complex ***cis*1a.Zn** was synthesised according to a literature proceedure.[33] 5,10-(4-(*N*,*N*-Dioctylamino)phenyl)ethynyl 15,20-(triisopropylsilyl)ethynyl porphyrin, Zn (II) complex ***cis*6.Zn** (49 mg, 34.7 μmol), $Pd_2(dba)_3$ (8 mg, 8.8 μmol), PPh_3 (9.6 mg, 36.6 μmol) and CuI (1.6 mg, 8.8 μmol) were dried in vacuo for 15 minutes. Toluene (8 mL), diisopropylamine (4 mL) and 4-iodopyridine (160 mg, 780 μmol) were added and the mixture freeze-pump-thaw degassed, and then stirred at 40 °C. Tetrabutylammonium fluoride (1.0 M in THF, 100 μL, 160 μmol, 4 equiv.) was added dropwise over 6 h to maintain a low concentration of free acetylene. The reaction was allowed to run for a further 2 hours at 40 °C and 16 hours at room temperature. The mixture was passed through a SiO_2 plug in CH_2Cl_2:pyridine 95:5 and evaporated to dryness. The compound was purified by column chromatography on SiO_2 (CH_2Cl_2:triethylamine 95:5) and precipitated from CH_2Cl_2 with petrol ether 40-60 to yield ***cis*1a.Zn** as a reddish dyestuff (21 mg, 48%). λ_{max} ($CHCl_3$, 1% pyridine)/nm (logε) 457 (4.63) 507 (5.10) 716 (4.65), ^{1}H NMR (500 MHz, $CDCl_3$) δ_H 9.45 (s, 2H), 9.42 (d, J = 4.29 Hz, 2H), 9.18 (d, J = 4.55 Hz, 2H), 9.04 (s, 2H),

8.65 (d, *J* = 4.29 Hz, 4H), 7.88 (d, *J* = 8.84 Hz, 4H), 7.75 (d, *J* = 5.36 Hz, 4H), 6.08 (d, *J* = 8.84 Hz, 4H), 3.41 (t, *J* = 7.77 Hz, 8H), 1.75–1.68 (m, 8H), 1.46–1.31 (m, 40H), 0.96–0.91 (m, 12H) ^{13}C NMR (125 MHz, $CDCl_3$) δ_C 151.40, 151.22, 151.02, 150.95, 149.79, 148.34, 133.18, 132.43, 128.90, 125.31, 111.50, 109.40, 105.87, 99.32, 99.09, 87.82, 82.88, 80.88, 51.09, 31.56, 29.55, 29.37, 27.35, 27.22, 24.10, 22.68, 19.70, 14.12, 13.64 CHN% Anal. calcd. for $C_{82}H_{92}N_8Zn$: C 78.47 H 7.39 N 8.93 found: C 78.59 H 7.49 N 8.87

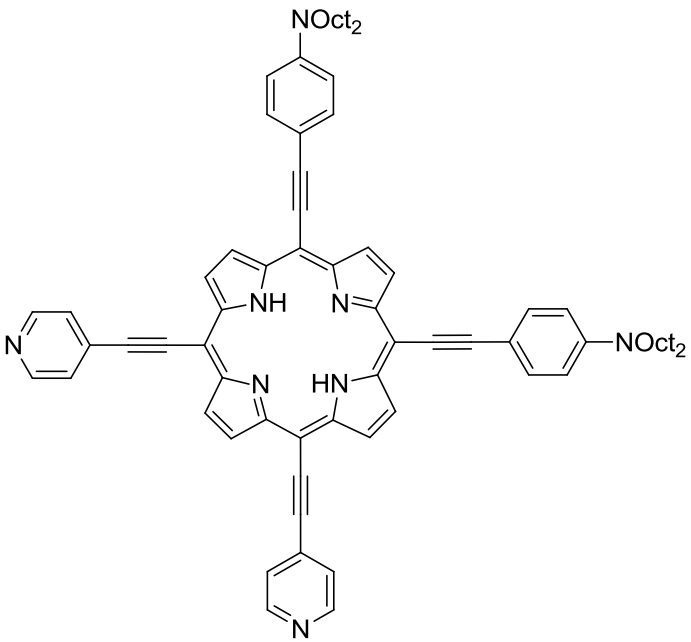

5,10-(4-(*N*,*N*-Dioctylamino)phenyl)ethynyl 15,20-(4-pyridyl)ethynyl porphyrin ***cis*1a.2H**, was synthesised according to a literature procedure.[33] 5,10-(4-(*N*,*N*-Dioctylamino)phenyl)ethynyl 15,20-(4-pyridyl)ethynyl porphyrin, Zn (II) complex ***cis*1a.Zn** (35 mg, 27.9 μmol) was stirred in CH_2Cl_2 (3.6 mL) and trifluoroacetic acid (0.366 mL, 4.7 mmol) was added dropwise. The mixture was stirred for 1 h, all porphyrin was observed to have precipitated, with no colour left in the solvent. The resulting mixture was washed with water (5 × 20 mL) until filtrate was neutral. The organic fraction was concentrated to dryness and precipitated from CH_2Cl_2 with

MeOH. (25 mg, 75%). λ_{max} ($CHCl_3$)/nm (logε) 445 (5.05) 498 (5.03) 692 (4.73), ^{1}H NMR (400 MHz, $CDCl_3$) δ_H 9.10–8.90 (m, 4H), 8.90–8.65 (m, 6H), 8.59–8.43 (m, 2H), 7.85 (d, *J* = 7.92 Hz, 4H), 7.69 (s, 4H), 6.80 (d, *J* = 7.92 Hz, 4H), 3.44 (t, *J* = 7.22 Hz, 8H), 1.81–1.71 (m, 8H), 1.51–1.36 (m, 40H), 1.02–0.95 (m, 12H) -3.81 (br. s, 2H) CHN% Anal. calcd. for $C_{82}H_{94}N_8$: C 82.65 H 7.95 N 9.4 found: C 82.55 H 7.84 N 9.61

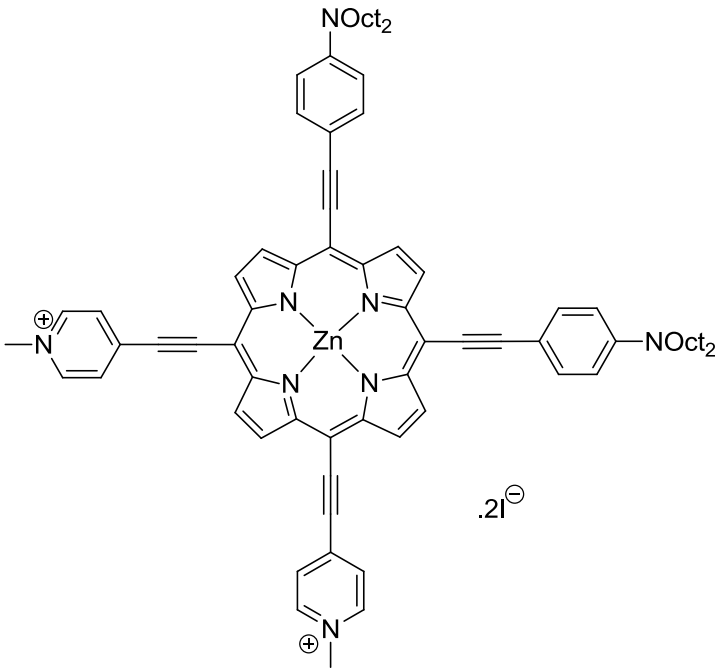

5,10-(4-(*N*,*N*-Dioctylamino)phenyl)ethynyl 15,20-(4-methylpyridinium)ethynyl porphyrin, Zn (II) complex ***cis*1b.Zn** was synthesised according to a literature proceedure.[33] 5,10-(4-(*N*,*N*-Dioctylamino)phenyl)ethynyl 15,20-(triisopropylsilyl)ethynyl porphyrin, Zn (II) complex ***cis*6.Zn** (25 mg, 17.7 μmol), $Pd_2(dba)_3$ (5 mg, 5.5 μmol), PPh_3 (6mg, 22.0 μmol) and CuI (1 mg,5.5 μmol) were dried in vacuo for 15 minutes. Toluene (8 mL), diisopropylamine (4 mL) and *N*-methyl 4-iodopyridinium iodide (31 mg, 88.5 μmol) were added and the mixture freeze pump-thaw degassed, and then stirred at 40 °C. Tetrabutylammoniumfluoride (1.0 M in THF, 50 μL, 80 μmol, 2.25 eq) was added in one portion. The reaction was allowed to run for 30

minutes at 40 °C. The mixture was washed with saturated ammonium chloride solution (3 × 60 mL) and water (2 × 60 mL). The mixture was evaporated to dryness and the mixture was passed through a SEC column in $CHCl_3$:pyridine 95:5 and the dark purple band was collected. The combined fractions were evaporated to dryness and precipitated from toluene with petrol ether 40:60 then filtered on a 0.2 μm membrane to yield the product ***cis*1b.Zn** as a dark greenish solid. (22 mg, 90%). λ_{max} (DMF)/nm (logε) 523 (4.72) 740 (4.35), 1H NMR (400 MHz, $CDCl_3$) δ_H 9.57 – 9.47 (m, 8H), 9.19 (d, *J* = 6.36 Hz, 4H), 8.72 (d, *J* = 5.50 Hz, 4H), 7.86 (d, *J* = 8.41 Hz, 4H), 6.84 (d, *J* = 7.91 Hz, 4H), 4.46 (s, 6H), 1.77 – 0.73 (m, 68H). m/z (MALDI+) 1283.70 ($[M+H]^+$, 100%, $C_{84}H_{99}N_8Zn^+$ requires 1183.72).

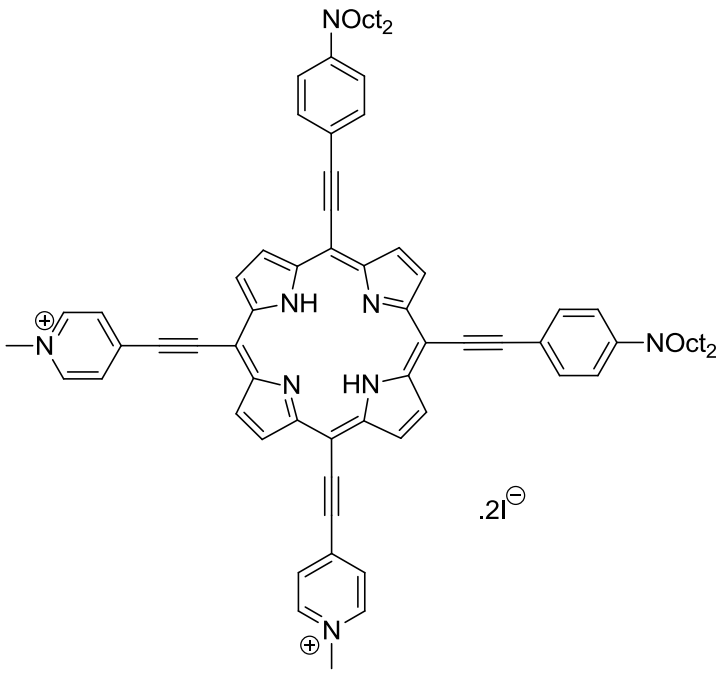

5,10-(4-(*N*,*N*-Dioctylamino)phenyl)ethynyl 15,20-(4-methylpyridinium)ethynyl porphyrin ***cis*1b.2H** was synthesised according to a literature procedure.[33] 5,10-(4-(*N*,*N*-Dioctylamino)phenyl)ethynyl 15,20-(4-methylpyridinium)ethynyl porphyrin, Zn (II) complex ***cis*1b.Zn** (5 mg, 3.7 μmol) was dissolved in $CHCl_3$ (5 mL) and trifluoroacetic acid

(50 μL) and stirred for 2 h. The mixture was then washed with saturated ammonium chloride solution (2 x 10 mL) and water (2 x 10 mL). The organic layer was evaporated to dryness and then dried *in vacuo* overnight to remove trace water to yield ***cis*1b.2H** as a purple-brown dyestuff (4 mg, 85%). m/z (MALDI+) 1221.81 ($[M+H]_+$, 100%, $C_{84}H_{101}N_8^+$ requires 1121.81). Characterised by MALDI only. NMR in all available solvents too poorly resolved.

4.7 References

1. S. R. Marder, D. N. Beratan and L. T. Cheng, *Science*, 1991, **252**, 103-106.
2. S. R. Marder, L.-T. Cheng, B. G. Tiemann, A. C. Friedli, M. Blanchard-Desce, J. W. Perry and J. Skindhøj, *Science*, 1994, **263**, 511-514.
3. B. Paci, C. Schmidt, C. Fiorini, J.-M. Nunzi, C. Arbez-Gindre and C. G. Screttas, *J. Chem. Phys.*, 1999, **111**, 7486-7492.
4. M. G. Kuzyk, *Phys. Rev. Lett.*, 2000, **85**, 1218.
5. M. Drobizhev, Y. Stepanenko, Y. Dzenis, A. Karotki, A. Rebane, P. N. Taylor and H. L. Anderson, *J. Am. Chem. Soc.*, 2004, **126**, 15352-15353.
6. N. Jiang, G. r. Zuber, S. Keinan, A. Nayak, W. Yang, M. J. Therien and D. N. Beratan, *J. Phys. Chem. C*, 2012, **116**, 9724-9733.
7. S. Priyadarshy, M. J. Therien and D. N. Beratan, *J. Am. Chem. Soc.*, 1996, **118**, 1504-1510.
8. E. C. Brown, T. J. Marks and M. A. Ratner, *J. Phys. Chem. B*, 2007, **112**, 44-50.
9. H. Kang, A. Facchetti, P. Zhu, H. Jiang, Y. Yang, E. Cariati, S. Righetto, R. Ugo, C. Zuccaccia, A. Macchioni, C. L. Stern, Z. Liu, S.-T. Ho and T. J. Marks, *Angew. Chem., Int. Ed.*, 2005, **44**, 7922-7925.
10. C. Andraud, T. Zabulon, A. Collet and J. Zyss, *Chem. Phys.*, 1999, **245**, 243-261.
11. B. R. Cho, Y. H. Kim, K. W. Son, C. Khalil, Y. H. Kim and S.-J. Jeon, *Bull. Korean Chem. Soc.*, 2002, **23**, 1253 - 1256.
12. B. R. Cho, S. B. Park, S. J. Lee, K. H. Son, S. H. Lee, M.-J. Lee, J. Yoo, Y. K. Lee, G. J. Lee, T. I. Kang, M. Cho and S.-J. Jeon, *J. Am. Chem. Soc.*, 2001, **123**, 6421-6422.
13. H. M. Kim and B. R. Cho, *Chem. Commun. (Cambridge, U. K.)*, 2009, 153-164.
14. G. Gonella, H.-L. Dai, H. C. Fry, M. J. Therien, V. Krishnan, A. Tronin and J. K. Blasie, *J. Am. Chem. Soc.*, 2010, **132**, 9693-9700.
15. T. Xu, S. P. Wu, I. Miloradovic, M. J. Therien and J. K. Blasie, *Nano Lett.*, 2006, **6**, 2387-2394.
16. T.-G. Zhang, Y. Zhao, I. Asselberghs, A. Persoons, K. Clays and M. J. Therien, *J. Am. Chem. Soc.*, 2005, **127**, 9710-9720.
17. H. S. Nalwa, T. Watanabe and S. Miyata, *Opt. Mat.*, 1993, **2**, 73-81.
18. P. Yan, A. C. Millard, M. Wei and L. M. Loew, *J. Am. Chem. Soc.*, 2006, **128**, 11030-11031.
19. S. Hatscher and M. O. Senge, *Tetrahedron Lett.*, 2003, **44**, 157-160.
20. P.-Y. Heo and L. Chang-Hee, *Bull. Korean Chem. Soc.*, 1996, **17**, 515-520.
21. B. Basic, J. C. McMurtrie and D. P. Arnold, *J. Porphyrins Phthalocyanines*, 2010, **14**, 481-493.
22. R. M. Metzger, *The Physical Chemist's Toolbox*, 2nd Edition edn., Wiley, New York, 2012.
23. T. Verbiest, K. Clays, C. Samyn, J. Wolff, D. Reinhoudt and A. Persoons, *J. Am. Chem. Soc.*, 1994, **116**, 9320-9323.
24. S. F. Hubbard, R. G. Petschek and K. D. Singer, *Opt. Lett.*, 1996, **21**, 1774-1776.
25. J. E. Reeve, H. L. Anderson and K. Clays, *Phys. Chem. Chem. Phys.*, 2010, **12**, 13484-13498.
26. M. Tomonari and N. Ookubo, *Chem. Phys. Lett.*, 2003, **376**, 504-514.
27. B. J. Coe, S. P. Foxon, E. C. Harper, M. Helliwell, J. Raftery, C. A. Swanson, B. S. Brunschwig, K. Clays, E. Franz, J. Gariì?n, J. s. Orduna, P. N. Horton and M. B. Hursthouse, *J. Am. Chem. Soc.*, 2010, **132**, 1706-1723.
28. R. d. Wortmann, S. Lebus-Henn, H. Reis and M. G. Papadopoulos, *THEOCHEM*, 2003, **633**, 217-226.

29. A. Čeklovský , S. Takagi and J. Bujdák, *J. Colloid Interface Sci.*, 2011, **360**, 26-30.
30. K. S. Suslick, C. T. Chen, G. R. Meredith and L. T. Cheng, *J. Am. Chem. Soc.*, 1992, **114**, 6928-6930.
31. C. Barsu, R. Cheaib, S. Chambert, Y. Queneau, O. Maury, D. Cottet, H. Wege, J. Douady, Y. Bretonniere and C. Andraud, *Org. Biomol. Chem.*, 2009, **8**, 142-150.
32. S. M. LeCours, H.-W. Guan, S. G. DiMagno, C. H. Wang and M. J. Therien, *J. Am. Chem. Soc.*, 1996, **118**, 1497-1503.
33. J. E. Reeve, H. A. Collins, K. D. Mey, M. M. Kohl, K. J. Thorley, O. Paulsen, K. Clays and H. L. Anderson, *J. Am. Chem. Soc.*, 2009, **131**, 2758-2759.
34. A. Boudif and M. Momenteau, *J. Chem. Soc., Chem. Commun.*, 1994, 2069-2070.
35. T. D. Lash, *Chem.--Eur. J.*, 1996, **2**, 1197-1200.
36. K.-i. Sugiura, Y. Fujimoto and Y. Sakata, *Chem. Commun. (Cambridge, U. K.)*, 2000, 1105-1106.
37. R. P. Briñas and C. Brückner, *Tetrahedron*, 2002, **58**, 4375-4381.
38. C.-H. Lee, F. Li, K. Iwamoto, J. Dadok, A. A. Bothner-By and J. S. Lindsey, *Tetrahedron*, 1995, **51**, 11645-11672.
39. D. K. Dogutan, M. Ptaszek and J. S. Lindsey, *J. Org. Chem.*, 2008, **73**, 6187-6201.
40. M. Balaz, H. A. Collins, E. Dahlstedt and H. L. Anderson, *Org. Biomol. Chem.*, 2009, **7**, 874-888.
41. R. W. Wagner, T. E. Johnson, F. Li and J. S. Lindsey, *J. Org. Chem.*, 1995, **60**, 5266-5273.
42. J. L. Oudar and D. S. Chemla, *J. Chem. Phys.*, 1977, **66**, 2664-2668.
43. J. L. Oudar and H. Le Person, *Opt. Commun.*, 1975, **15**, 258-262.
44. K. De Mey, J. Perez-Moreno, J. E. Reeve, I. Lopez-Duarte, I. Boczarow, H. L. Anderson and K. Clays, *J. Phys. Chem. C*, 2012, **116**, 13781-13787.
45. X. Hu, D. Xiao, S. Keinan, I. Asselberghs, M. J. Therien, K. Clays, W. Yang and D. N. Beratan, *J. Phys. Chem. C*, 2010, **114**, 2349-2359.
46. N. C. Maiti, S. Mazumdar and N. Periasamy, *J. Phys. Chem. B*, 1998, **102**, 1528-1538.
47. K.-P. S. Dancil, L. F. Hilario, R. G. Khoury, K. U. Mai, C. K. Nguyen, K. S. Weddle and A. M. Shachter, *J. Heterocycl. Chem.*, 1997, **34**, 749-755.
48. K. Šiškova, B. Vlčková and P. Mojzeš, *J. Mol. Struct.*, 2005, **744-747**, 265-272.
49. S. Biswas, H.-Y. Ahn, M. V. Bondar and K. D. Belfield, *Langmuir*, 2012, **28**, 1515-1522.
50. K. Fujiwara, S. Wada, H. Monjushiro and H. Watarai, *Langmuir*, 2006, **22**, 2482-2486.
51. L. Moreaux, T. Pons, V. Dambrin, M. Blanchard-Desce and J. Mertz, *Opt. Lett.*, 2003, **28**, 625-627.
52. L. Moreaux, O. Sandre and J. Mertz, *J. Opt. Soc. Am. B*, 2000, **17**, 1685-1694.
53. James E. Reeve, Alex D. Corbett, I. Boczarow, T. Wilson, H. Bayley and Harry L. Anderson, *Biophys. J.*, 2012, **103**, 907-917.
54. B. Corry, D. Jayatilaka, B. Martinac and P. Rigby, *Biophys. J.*, 2006, **91**, 1032-1045.
55. J. R. Lakowicz, *Principles of Fluorescence Spectroscopy*, Springer, New York, 1999.
56. P. R. Callis, *J. Chem. Phys.*, 1993, **99**, 27-37.
57. T. Matsusue, H. Bando, S. Fujita and Y. Takayama, *physica status solidi (c)*, 2010, **8**, 387-389.
58. C. Wan and C. K. Johnson, *Chem. Phys.*, 1994, **179**, 513-531.
59. I. A. Novokshonova, V. V. Novokshonov and A. S. Medvedeva, *Synthesis*, 2008, **2008**, 3797-3800.
60. C. J. Wilson, University of Oxford, 2006.
61. H. L. Anderson, *Tetrahedron Lett.*, 1992, **33**, 1101-1104.

Chapter 5

Porphyrins as Transmembrane-Potential Sensitive Probes

Summary

The ultimate goal of our new class of SHG chromophores is the optical monitoring of transmembrane potential. To quantify the suitability of our family of porphyrinic SHG dyes for voltage-sensitive imaging *in vivo*, we first benchmark their optical response in a model membrane. The two key metrics are the magnitude of response, as a proportion of the total signal, termed $\Delta S/S$, and the speed of the response, for which we report the half-life, $t_{1/2}$, in response to a step-change in applied potential.

Firstly, we discuss how we arrive at a suitable model for cellular membranes, the hemispherical lipid bilayer, and describe how a potential may be applied in synchrony with SHG line scanning across the bilayer membrane. We then use this model system to benchmark our porphyrin dyes, and in particular model dye **1b.2H**, against three commercially available voltage-sensitive SHG probes: di-4-ANEPPS, FM4-64 and RH237. We find that our dye is more than four times more sensitive to transmembrane potential than the best commercially available probe and responds nearly an order of magnitude more quickly. Outperforming commercially available probes in both of these key metrics, we find that our porphyrinic chromophore possesses the scope to revolutionize voltage-sensitive imaging.

5.1 Introduction

Transmembrane potentials established at synaptic interfaces are the signals which trigger the symphony of action potentials (APs) which drive the brain's neurological circuitry. The effort to measure and detect these electrical spikes with accurate spatiotemporal resolution has bridged microscopy,[1-3] neurophysiology,[4-6] feature detection,[2, 7, 8] molecular design,[9-11] nanotechnology[12, 13] and photophysics.[3, 9, 14] Cellular APs have been resolved spatially in real time through a number of techniques.[6, 12, 15] However, postsynaptic potentials (PSPs) which trigger APs are frequently too small to be satisfactorily resolved optically with accurate spatial and temporal resolution. APs and PSPs may be resolved once a number of traces have been averaged, but trial-by-trial recording of single or multiple cellular potentials has not been achieved.

Each of the techniques developed for probing neuronal communication between cells *in vivo* lack concurrent spatial and temporal resolution. Patch-clamping of individual neurons gives a precise electrophysiological readout of cellular synaptic potentials, but due to its invasive nature, patching any more than triplets or quadruplets of neurons remains a significant challenge.[16] Neuronal networks have been broadly mapped by calcium dyes which fluoresce more brightly following an AP due to elevated levels of Ca^{2+}. However, calcium flux is a downstream consequence of transmembrane potentials, and as such has onset dynamics of hundreds of milliseconds and offset dynamics lasting several seconds.[15, 17, 18]

Voltage-sensitive dyes (VSDs) identify APs via an ultrafast electric field induced hypso- or bathochromic shift.[10] Since VSDs respond to transmembrane potential, the trigger for synaptic transmission, they may be used to detect PSPs in microcultures.[19, 20] It has been

problematic to transfer successful fluorescence recording of transmembrane potentials *in vitro* to single cell recording *ex vivo* due to the lack of voltage-sensitivity and depth penetration. The structure and behaviour of the membrane may also be influenced by incorporation of the dyes.

Nonlinear optical (NLO) techniques such as second harmonic generation (SHG) and two-photon fluorescence (2PF) also respond to voltage via an electrochromic mechanism and are powerful tools for imaging voltage sensitive dyes deep inside tissue.[21-24] Voltage-sensitive SHG from conventional probes is typically averaged over multiple acquisitions to accurately resolve APs due to poor signal-to-noise, an undesirable limitation when recording APs in real time.[3-5] The speed of response is a matter of some dispute, with some claiming an electro-optical mechanism[22] and others excluding it.[14]

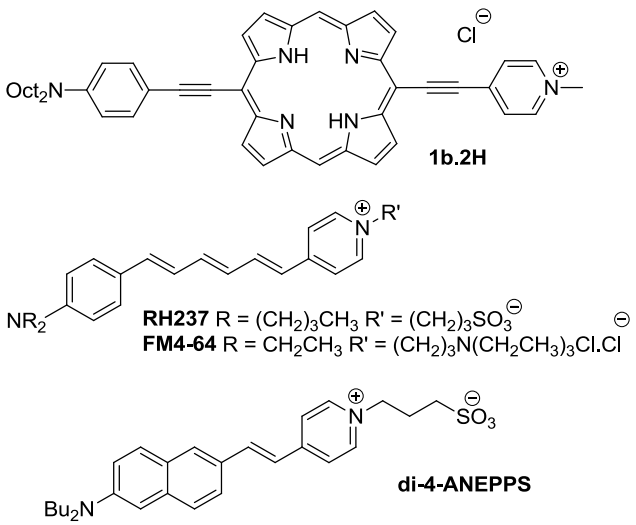

Figure 1 Structures of dyes examined in this chapter.

Our previous report[25] finds that porphyrin-based SHG probes possess considerably higher molecular first hyperpolarizabilities than comparable styryl dyes (Table 1), a property bestowed by their extremely polarizable π-delocalized bridge. The sensitivity of a probe to transmembrane potential, β_{eff}, is the sum of field independent and dependent terms

$$\beta_{eff,\lambda} = \beta_\lambda + \gamma_\lambda E \qquad \text{(Eq. 1)}$$

where β_λ is the resonance-enhanced first hyperpolarizability at wavelength λ, and γ_λ is the field dependent second hyperpolarisability which scales the molecular response to applied electric field, *E*. Consequently, each probe has a potential sensitivity ($\gamma_\lambda E/\beta_\lambda$ which is wavelength dependent and which may be found both experimentally[14] or through calculation of β_λ and γ_λ through a sum-over-states model. Porphyrin **1b.2H** displays a strong sensitivity maximum in the biological transparency window. In this chapter we show that it is more responsive to potential than conventional styryl dyes. I survey a variety of methods for construction of model membranes which simulate plasma membranes but which avoid complications of biological imaging. Method development involved selecting a suitable model membrane and devising a rigorous method of both applying a potential and monitoring its effect on SHG with fast temporal resolution. I find that HLBs offer the most stable and reproducible solution, and go on to develop a method on this basis.

We benchmark the SHG voltage sensitivity ($\Delta S/S$) and response time (decay half-life, $t_{1/2}$) of recently published amphiphilic donor-acceptor porphyrin chromophore **1b.2H**[25] against three well characterised membrane probes, RH237, di-4-ANEPPS and FM4-64 (Figure 1).[5, 14, 26-32] We record voltage-modulated SHG from a model membrane, DPhPC hemispherical lipid bilayers (HLBs)[33] which allow for high-fidelity SHG recording with a minimum of extraneous variables; ideal for benchmarking different dyes.[10, 34] In this chapter, we present a probe which possesses sufficient sensitivity to transmembrane potential via SHG that it could be used to detect PSPs from in-tact neuronal networks in real time.

5.2 Method Development

The physical process which creates frequency-doubled light places a natural constraint on the imaging geometries which can be used to perform SHG imaging. Incoming light, directed along the lab Y axis and polarized with its electric field in the YZ plane will have its optimum interaction with dyes (or rather their β_{zzz} tensor components) aligned collinear with the lab Z axis. Deviations from this geometry, especially those in the polar angle (i.e. tilts away from the XZ plane, Figure 2) will cause drastic signal attenuation. Rotations of the dye around the Y axis will cause the gentle drop-off in intensity that we see in Chapter 3, however tilting the dye out of the XZ plane causes the generated second harmonic light to miss the condensing optics (Figure 2B).

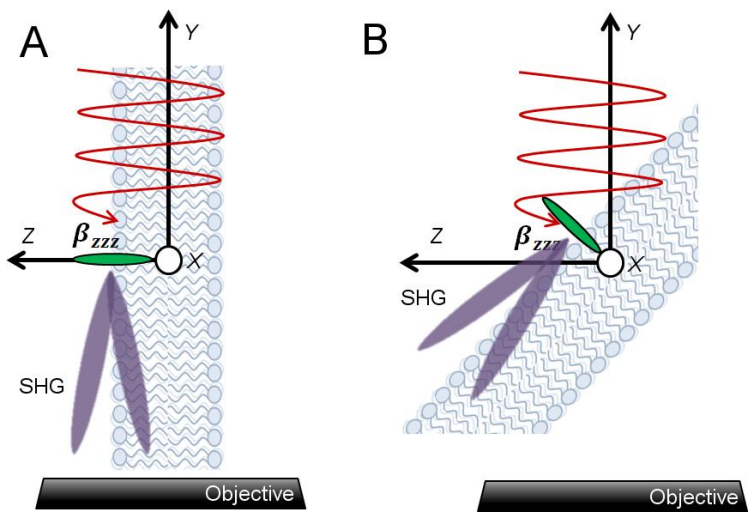

Figure 2 (A) The imaging geometry which can be used to give maximum SHG signal: the β_{zzz} hyperpolarizability component (green lozenge) lies within both the YZ and XZ planes, giving maximum SHG from SHG both dichroism and emission anisotropy respectively. When the dye no longer lies within the XZ plane, (B), the projection of the β_{zzz} component onto the electric field of the driving field (red wave) is reduced and the anisotropic emission (purple lobes) is directed away from the condensing optics (marked 'Objective').

A model membrane in this imaging geometry is challenging to fabricate, since a stationary synthetic bilayer requires a solid support. Many of the simpler apparatus for solid-supported bilayers are unsuitable for these SHG imaging experiments. For example, Teflon-supported bilayer lipid membranes, where a small bilayer is constructed inside a small hole in a Teflon film, could not be imaged, as the Teflon itself would block the incoming laser light. To support a bilayer in the geometry described in Fig. 2A, the support must be optically transparent, or should not obstruct the point of excitation. This leads to two membrane models which I describe in the following sections: droplet interface bilayers (DIBs) and hemispherical lipid bilayers (HLBs).

5.2.1 Droplet Interface Bilayers

Two droplet monolayers, when brought into contact have the tendency to exclude their solvation layers and form a metastable bilayer at their interface. This bilayer has been shown to be a good biomimic, and easily incorporates a number of transmembrane proteins.[35, 36] Since droplet interface bilayers (DIBs) may be constructed from oil and buffer, they are optically transparent, and the issue of imaging geometry may be resolved by scanning at the lateral equator of the droplet (i.e. the widest part of the droplet in the ZX plane). The 'lipid-in' technique, developed by Hwang et al. in 2008 (Figure 3)[37] provides a route to the membrane asymmetry that is the final requirement for an SHG image.

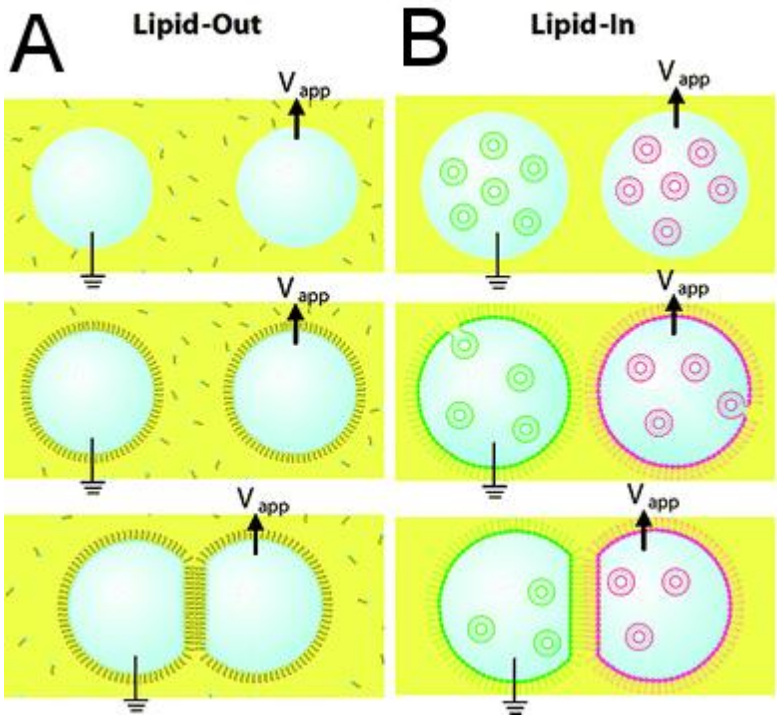

Figure 3 (A) The construction of DIBs using the lipid-out approach: lipid in an oil bath forms a monolayer at the oil-water interface which excludes oil and forms a bilayer when the two droplets are brought together. (B) The construction of asymmetric DIBs using the lipid-in approach: the water droplets contains DPhPC micelles (green) or DPhPC micelles with an SHG dye (red) which over time forms a droplet monolayer at the phase boundary. When these two droplets are brought into contact, an asymmetric lipid bilayer can be formed, in a geometry suitable for SHG imaging. Adapted with permission from Hwang el al., *J.A.C.S*, **2008**, 130, 5878. Copyright, 2008, American Chemical Society.

The challenge faced when constructing droplet interface bilayers on a microscope stage is the manipulation of the droplets into position for imaging. Whenever this technique was previously used, the droplets are held, from above, on Ag/AgCl electrodes coated with a thin layer of agarose hydrogel. This ensures that the droplet does not fall off of the electrode, and that the electrode does not become coated with an insulating layer of lipid. Since SHG requires detection in the forward direction for maximum contrast, there is little space between the two objectives for micromanipulators which are typically employed to bring the droplets together. To address this problem, I constructed a ‘chip’, a small acrylic

device which was capable of manipulating the droplets, and bringing them together whilst still fitting between the two objectives.

Two generations of 'chips' (Figure 4) were designed in SolidWorks and machined on a computer numerical control machine tool out of clear acrylic. A 100 μm thick borosilicate coverslip was silanised after oxygen plasma treatment and glued firmly to the base with epoxy resin. Each device was capable of holding a reservoir of oil for long periods of time, and contained two electrodes (upon which the droplets were mounted) which may be maneuvered along the long axis of the chip. The design contained a thin, optically transparent base so that it can be used on microscopes with short working distances.

Droplet interface bilayers were fabricated by filling the bath with oil, then introducing 100 nL droplets of buffer containing DPhPC (0.5 mg/mL) or DPhPC (0.5 mg/mL) with an SHG dye (10 μM) onto the agarose-coated Ag/AgCl electrodes (pictured, Figure 4, *left*). After bathing the droplets for 5–10 minutes to allow a full monolayer to form, the two platforms were manipulated together on the microscope stage so that the droplets came into contact. Within 30 seconds, a bilayer would spontaneously form between the two droplet monolayers, giving the DIB which can be imaged via multiphoton microscopy (MPM).

Bilayer quality and dimensions were monitored by the application of 16.67 Hz, 15 mV (peak-to-peak) triangle waves which return a current trace with a characteristic square-wave form, representing the capacitance of the bilayer. Once a high-quality bilayer is established, it can be imaged, and a potential applied in order to measure voltage-sensitive SHG.

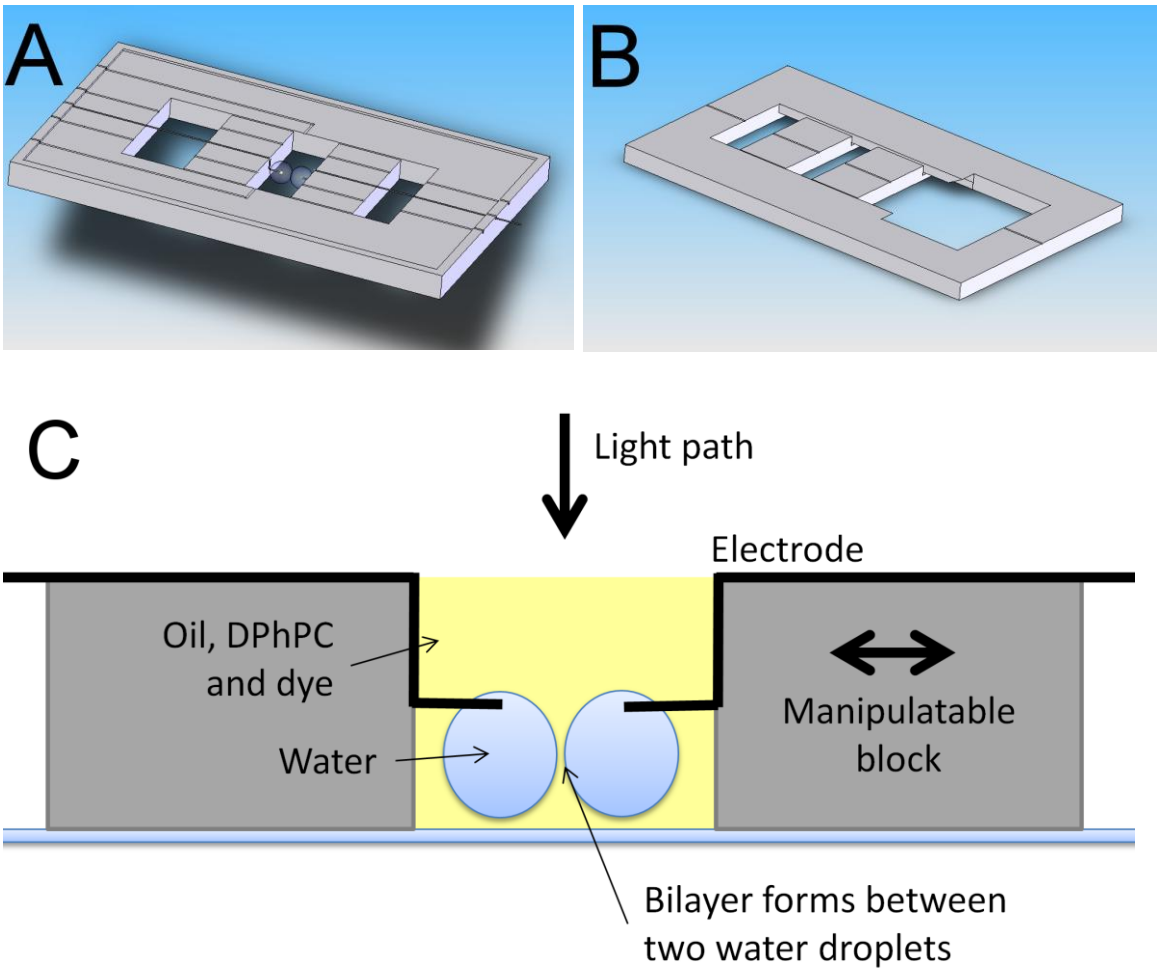

Figure 4 3-dimensional SolidWorks renders of the (A) first generation chip with a droplet interface bilayer mounted and (B) second generation chip which were both used for the fabrication of droplet interface bilayers on MPM stages. Both generations of chip contain the arrangement depicted in (C), an oil reservoir, inside which two sliding platforms were introduced and could be manipulated along their axis of freedom by means of a stiffened steel wire attached to the platform with epoxy resin. The second generation (B) incorporated a lip to keep the platforms anchored in the oil bath and introduced channels for the oil to flow around the platforms as they were moved. The redundant channels designed into the first generation were removed and the size of the oil bath was increased to counteract seepage and evaporation. Agarose-coated Ag/AgCl 100 µm electrodes were attached to the platform in both cases and lead out of the designated channels to an AxoPatch 200B amplifier.

Despite considerable effort and development, this approach could not be employed to measure transmembrane potential. At this point, the only accessible MPM had a drastically reduced field of view due to misaligned optics. Furthermore, four fatal flaws in the DIB system came to light once I began MPM imaging. Figure 5 shows representative images of the DIB system fabricated on a chip contained within a MPM stage and the first flaw: Whenever the DIB was anchored on an agarose electrode; the droplet monolayer seemed to be disrupted to the point that no SHG was produced (contrast with Figure 6).

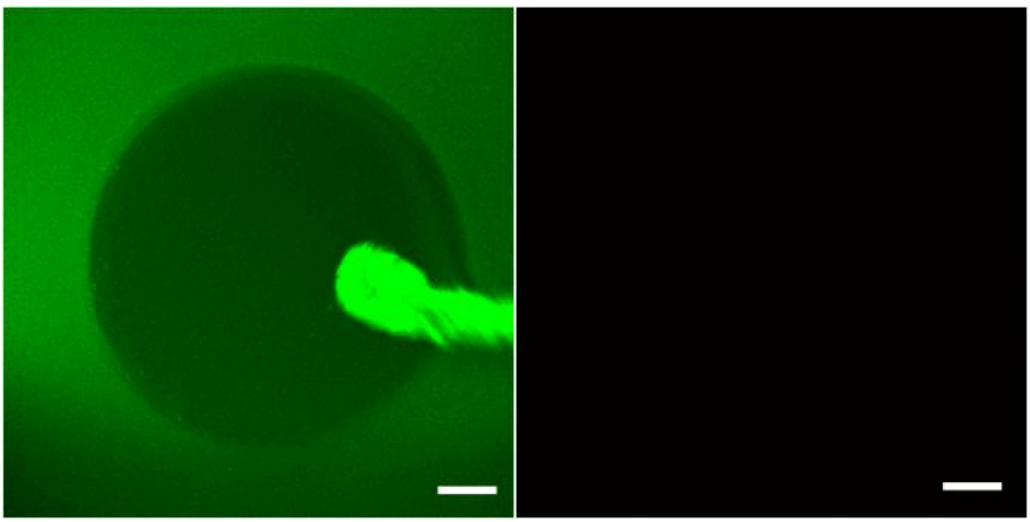

Figure 5 2PF (green, left) and SHG (red, right) from a droplet monolayer stained with RH237 when mounted on an agarose-coated Ag/AgCl electrode. Disruption of the monolayer by inclusion of the electrode seemed to prevent the evolution of SHG light under MPM imaging conditions. Contrast with Figure 6.

Secondly, with the high *N.A.* objectives required for NLO imaging, lensing of the incoming light beam by the oil-water interface was causing significant aberration of the focal spot (Figure 6A). This disrupted SHG imaging to the point that the droplet interface bilayer could not be successfully resolved (Figure 6B).

Thirdly, when we attempted to image DIBs, since the two droplets were not identical, the bilayer would often form in an arbitrary plane, rather than being constrained to the XY plane we require (Figure 2). This additional complication reduced the utility of the technique.

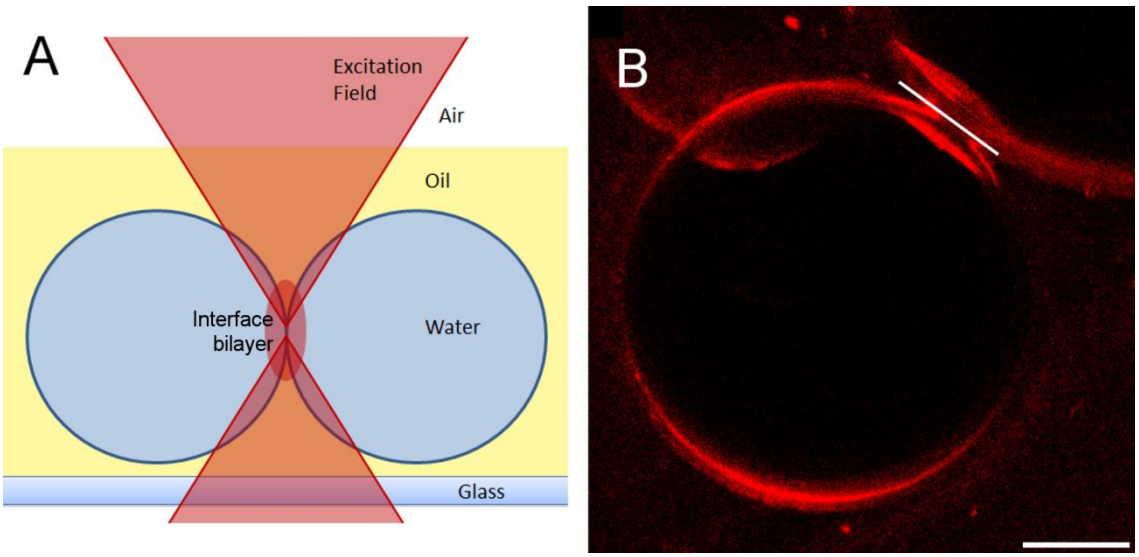

Figure 6 (A) Schematic of DIB system demonstrating aberration of the focal spot due to refractive lensing of the excitation field. (B) SHG (red) from a free-standing DIB stained with **1c.Cu** illustrating how aberration prevented resolution of the interface bilayer. The white line between two droplets indicates the plane that contains the bilayer. Scale bar 100 μm.

Finally, and most critically, DIBs were not sufficiently robust to withstand MPM imaging. The energy contained within the 100 femtosecond pulses of the IR laser, even at low average powers was sufficient to cause two droplets, connected by a DIB, to fuse into one larger droplet. I postulated that linear absorption of the 800 nm IR beam was sufficient to drill small pores in the membrane (optoporation), which can rapidly grow, causing membrane rupture. Even unsupported (i.e. no electrode attached) DIBs, could not withstand a single imaging pass, which made the system wholly unsuitable for time-resolved voltage-sensitive imaging. Failure of the DIB method to provide a suitable imaging platform led me to investigate another technique which possesses a more appropriate imaging geometry.

5.2.2 Hemispherical Lipid Bilayers

HLBs are micro-scale lipid bilayer membranes formed at the tip of a pipette. Most of the problems with DIBs stemmed from the intricate nature of bringing two nanolitre droplets against one another. By moving to hemispherical lipid bilayers (HLBs), we are granted a much more stable system, with greater biological relevance. This section will briefly cover the development of the technique, but a detailed procedure is provided in the Methods section.

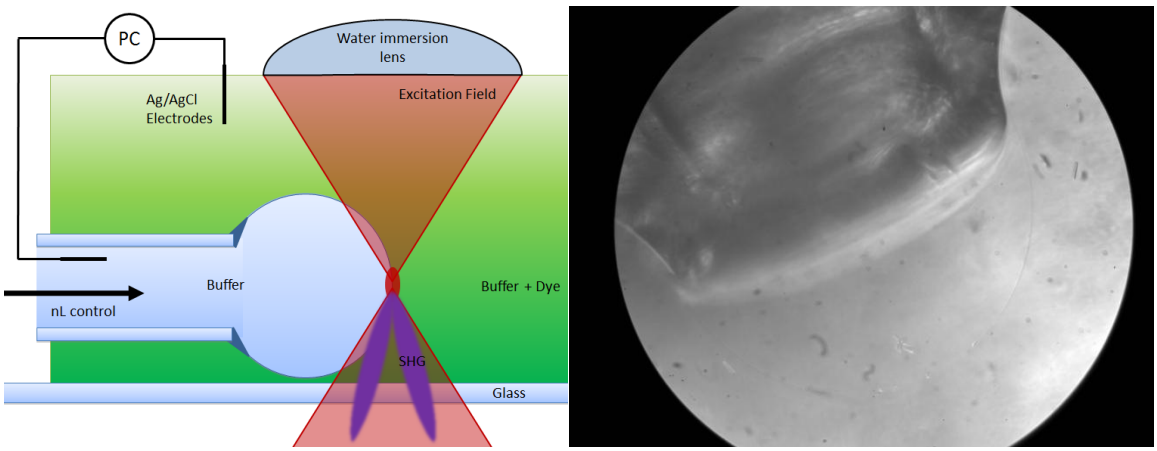

Figure 7 (*left*) Schematic diagram of the equipment used to image voltage-sensitive SHG via fabrication of HLBs and (*right*) an HLB at the tip of a pipette tip under wide-field illumination. Oil-in-lipid within the pipette can be blown into a hemispherical lipid bilayer by means of a pressure differential. The dye can be introduced asymmetrically, both sides of the bilayer can be placed in electrical contact and routed to a PC via a patch-clamp amplifier and importantly, a portion of the bilayer is in the appropriate geometry for imaging without obfuscating the image with any sources of optical aberration.

Hemispherical lipid bilayers (or "tip-dip bilayers") may be formed between two buffer solutions at the tip of an oil-and-lipid coated pipette upon the application of a positive pressure differential. The effect of blowing the oil and lipid mixture out of the pipette tip into a bath forms a 'bubble' of lipid bilayer attached to the pipette tip by oil reservoirs. Dye introduced to the buffer bath allows the asymmetric incorporation of SHG chromophores

needed for SHG imaging, and an electric field may be applied via electrodes placed in the bath and inside the pipette (Figure 7). Importantly, a region of the bilayer exists (the part at the focus of the excitation field, Figure 7) which is in the correct geometry for the imaging we set out in Figure 2. Proof-of-principle experiments utilized a screw-driven 10 μL syringe (Figure 8) to provide fine control for the pressure differential. After development of suitable lipid and buffer compositions, stable HLBs could be formed consistently on a wide-field light microscope.

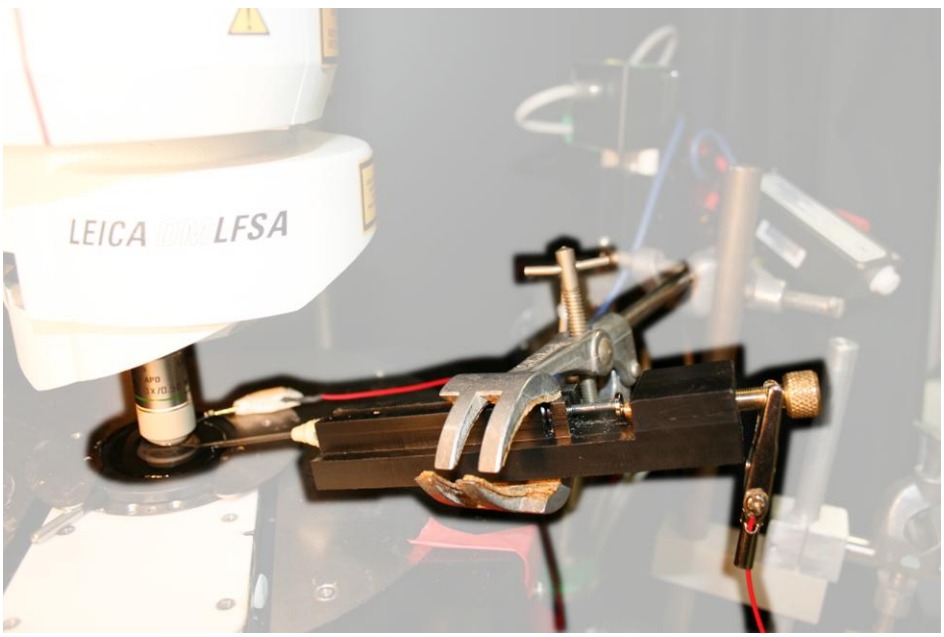

Figure 8 First generation HLB apparatus: A HLB is blown beneath the objective lens (left hand side) at the tip of a glass capillary connected to a screw-driven 10 μL syringe. Electrical contact is made via the plunger of the syringe and an Ag/AgCl bath electrode. This image also illustrates the constraints placed on the imaging setup: note the lack of space above the objective.

Initial imaging on a Leica microscope (see Methods, Chapter 2) gave poor SHG when dye was introduced from the pipette side (Figure 9A). However adding the dye to the bath instead (Figure 9B) gave much stronger images, since the asymmetry of the dye in the bilayer was no longer destroyed by diffusion into the oil reservoirs before the bilayers were blown.

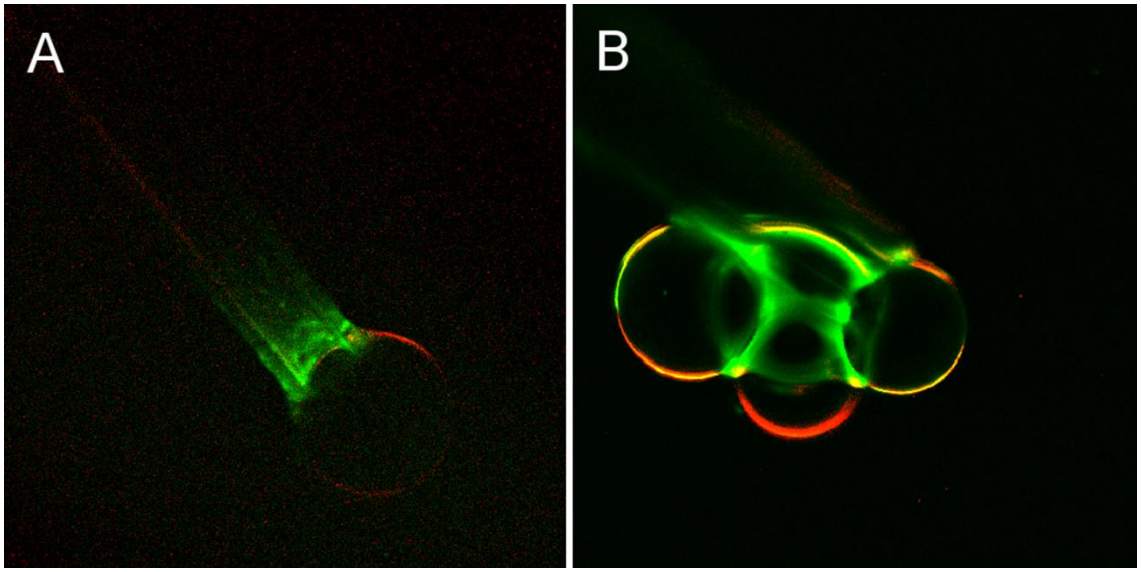

Figure 9 (A) SHG (*red*) and TPF (*green*) overlay from a RH237-stained HLB blown at the surface of a silanised glass pipette when dye is introduced via the pipette. Note the adsorption of dye onto the inner surface of the pipette and the markedly weaker SHG. (B) SHG (*red*) and TPF (*green*) overlay from a RH237-stained HLB (which has slipped off the tip to form a 4-bubble 'foam'). In contrast, note the relative strength of the SHG and lack of signal from the pipette. Scale bar 60 μm.

A second generation HLB-fabrication setup was developed to allow for finer control of the pressure differential via a Bourdon tube and more precise electrophysiological monitoring via a digitizer and patch-clamp amplifier. This set-up was built on a custom-made microscope in the Wilson lab (Department of Engineering, University of Oxford). The final arrangement is described in the methods section, below. At this point, an important collaboration was established with Professor Tony Wilson, Department of Engineering, University of Oxford and his group: Dr. Edward Botcherby, Dr. Christopher Smith and Dr. Alex Corbett. With their expertise, we were able to establish a line-scanning microscopy experiment which allowed us to measure voltage-sensitive SHG from HLBs. This collaboration resulted in a line-scanning acquisition synchronized with transmembrane potential applied via the microscope control-box. We also made modifications to the software to allow variable voltage trains to be applied (red trace, Figure 10).

5.3 Methods

Imaging was conducted on a custom-built microscope based around an Olympus BX60M upright microscope adapted with standard Linos microbench components. The light source was a Ti:Sapphire laser (Tsunami, Spectra Physics) producing 100 fs pulses centered at 850 nm. An Olympus LUMPlanFL N 40X 0.8 NA lens was illuminated at the back aperture with a 90 mW beam to maximize image contrast. After passing through an excitation filter, the two-photon epi-fluorescence was filtered again with a 550–650 nm bandpass filter (Semrock FF568-Di01-25x36) before being captured with a Hamamatsu H7422P series photon counting PMT. SHG was condensed in the forward direction, passing through an excitation filter and a 422–432 nm notch filter (Semrock FF01-427/10-25) before reaching a Sens-Tech DM0016 photon counting PMT.

Laser scanning was achieved with a pair of orthogonally mounted galvanometer mirrors (VM1000+, Cambridge Technology). Synchronous point scanning, data collection and voltage commands were orchestrated through LABVIEW software running on a reconfigurable FPGA card (NI PCI-7830R, both National Instruments).

Applied voltage commands, resultant current and scanning commands sent to the x-galvanometer mirrors were monitored via an AxoPatch 200B (Axon Instruments) following digitization by a Digiclamp 1322A digitizer, and collected online using the pClamp 9.2 acquisition and analysis program (Axon Instruments).

HLBs were formed at the mouth of a PTFE-tipped glass capillary. After filling with pH 7.4, 50 mM NaCl, 50 mM phosphate buffer the capillary was dipped into a solution of DPhPC (30 mM) and oxidised cholesterol (5 mM) in dodecane. A stock solution of each dye (5

mM) in DMSO was added to a buffer bath up to a final concentration of 5 μM. The oil-coated tip was then introduced into the bath and a HLB was blown by establishing a positive pressure differential via either a 10 μL Hamilton Gastight syringe or a custom-made Bourdon tube. HLBs were examined both visually (through decay in interface scattering under wide-field illumination) and electronically (confirming a GΩ seal and capacitance > 200 pF) to establish that a bilayer had formed.

A line between 15 and 250 pixels long was defined across the membrane and was scanned repeatedly in a return path mode with a pixel dwell time of 10 μs (giving sampling at between 3.3 kHz and 200 Hz respectively). The resulting $x \times t$ image shows the evolution of the bilayer with time and varying with a pre-determined voltage waveform (Figure 10).

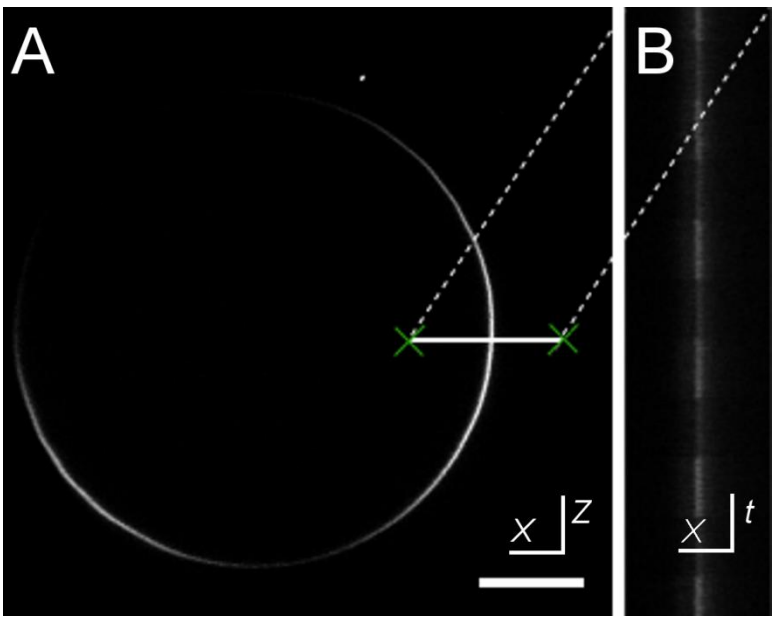

Figure 10 (B) Voltage-synchronized line-scan from (A) a hemispherical lipid bilayer stained with porphyrin SHG dye **1b.2H**. A path *x* pixels long is defined across the most intense part of the hemispherical lipid bilayer (between the two green crosses) and scanned *t* times whilst the desired voltage train is applied. Individual lines are concatenated to give (B) an $x \times t$ image which represents the entire acquisition. SHG intensity data may then be extracted from this image and compared to the applied voltage recorded via a patch-clamp amplifier. Scale bar 50 μm.

Data were extracted from $x \times t$ images by selecting the bilayer as a region of interest then averaging the pixel intensity (in counts) row-wise. Images containing significant movement of the HLB and images with baseline RMS error greater than 10% of total signal were excluded. Sensitivities were obtained by averaging the last 30% of datapoints from each square wave 'window', and plotting this against the potential applied for that window ($n > 6$ for each dye). Kinetic plots were obtained by summing consecutive periods from an applied 100 mV square wave ($n > 12$). Transmembrane potentials were estimated using recorded current injection data by modelling the bilayer charging dynamics through a first-order expression for the potential across a capacitor. The SHG kinetic response to potential was fit to first order kinetics for **1b.2H** and FM4-64, dyes RH237 and di-4-ANEPPS gave more complex behavior.

5.4 Results

The sensitivity of **1b.2H** and three commercially available styryl dyes to transmembrane potential was measured by SHG microscopy (Table 1). Application of a square wave train containing varying potential amplitudes was applied across the bilayer during a continuous line-scan (Figure 11). This allowed us to find the SHG modulation at a range of voltages inside the same acquisition. By applying the potential in wide enough time windows, we give the system enough time to respond optically to the applied potential. Simple visual inspection confirms that **1b.2H** is a superior reporter of membrane potential than any other probe. However, I extract response data computationally and establish a variety of kinetic and magnitude metrics to obtain a quantitative comparison of these probes.

di-4-ANEPPS and RH237 produce inferior responses (Figure 12), primarily due to their complex dynamic response and so are inferior benchmarks. Whilst I still include the traces, for the sake of completeness, for clarity and interest, most comparisons are made to FM4-64.

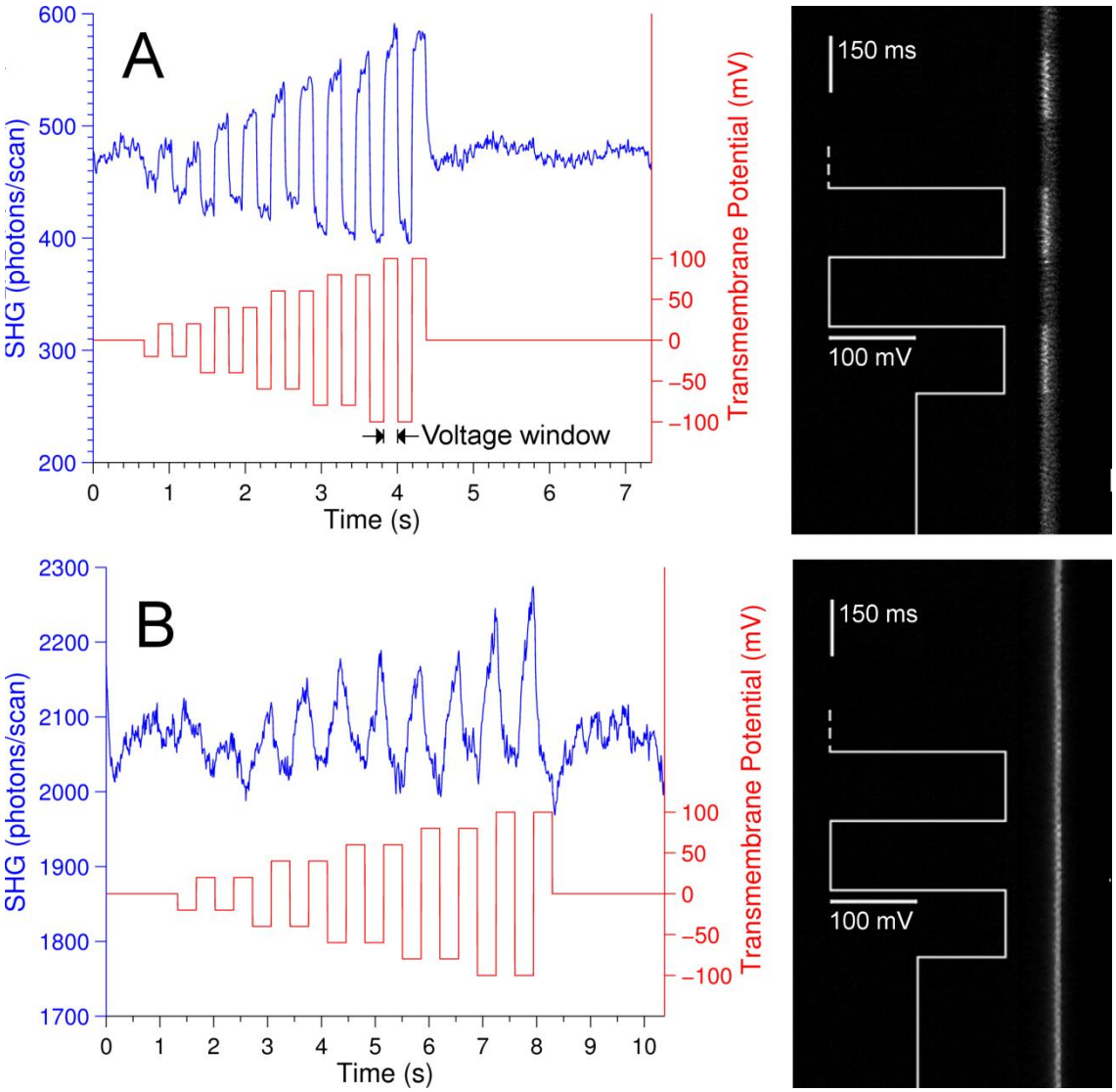

Figure 11 SHG power over time (blue trace) in the presence of an applied electric field (red trace), left, and the applied potential overlaid on a linescan image showing the modulation in SHG intensity with time, right, for **1b.2H** (A) and FM4-64 (B). Traces for di-4-ANEPPS and RH237 may be found in the supporting information.

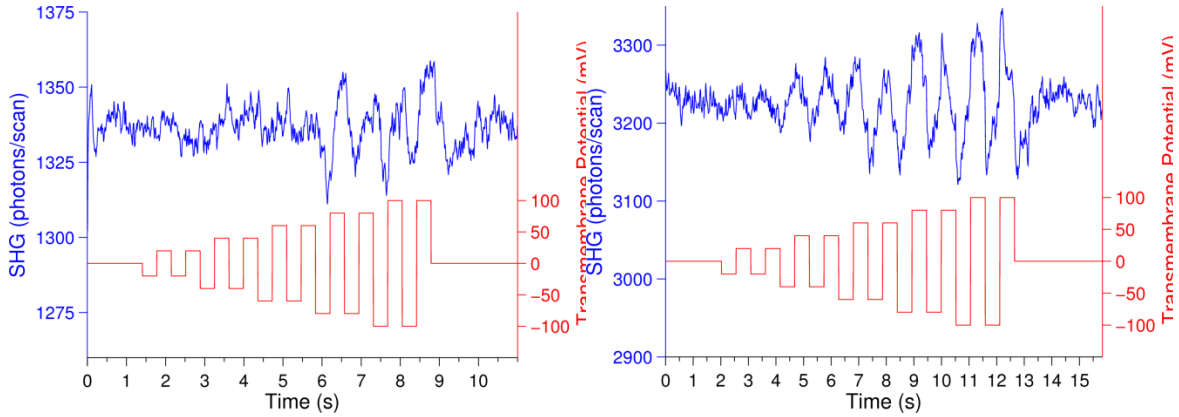

Figure 12 Magnitude of SHG response (blue trace) to applied voltage (red trace) for RH237 (left) and di-4-ANEPPS (right) in DPhPC bilayers.

The magnitude of the change in response to potential was extracted from the final 30% of points collected in each voltage 'window' (Figure 1A, marked) to ensure that for kinetically slow dyes, a representative measure of their response was used. Porphyrin chromophore **1b.2H** possesses SHG sensitivity to transmembrane potential of 20% / 100 mV, outperforming FM4-64, currently the best benchmark dye[4] by more than a factor of four (Figure 13).

The recorded response of RH237 and di-4-ANEPPS to transmembrane potential is smaller than reported in previous studies.[14, 29] Since we sample from the end of each time window, the maximum value may not have been reached before the polarity is switched. However, since we are examining their fast (<1 ms) response, the magnitude changes over the shorter timescales used remain an important metric.

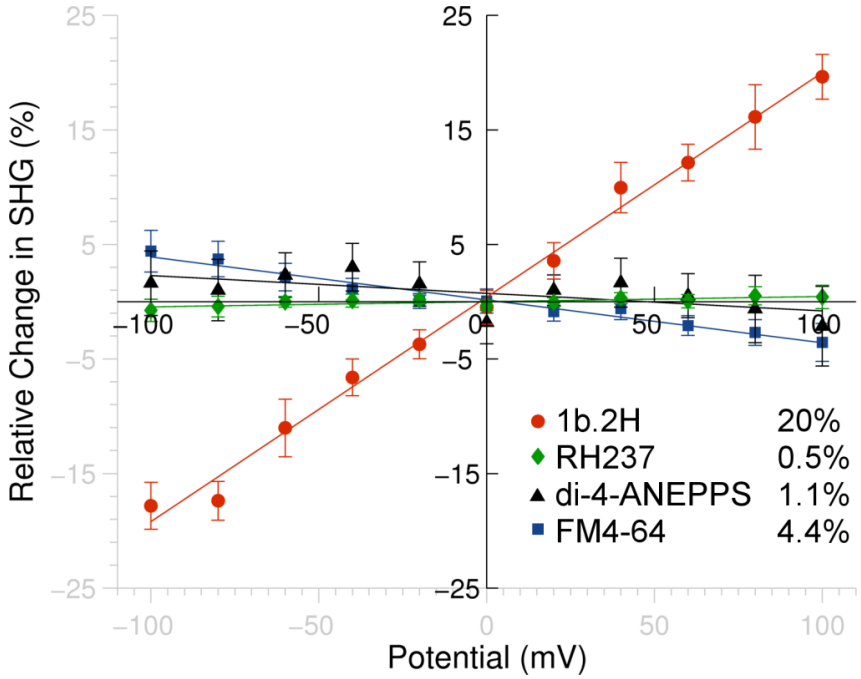

Figure 13 Relative change in SHG with respect to potential is far greater for **1b.2H** (red circles) than any commercially available dye; RH237 (green diamonds), di-4-ANEPPS (black triangles) or FM4-64 (blue squares).

Increasing sampling frequency to greater than 1 kHz allows resolution of each dye's characteristic response time (Table 1). A square wave of ±100 mV was applied to the membrane and successive periods were summed to yield the kinetic traces of Figure 14. We find **1b.2H** responds to the application of a field with a half-life of $t_{1/2}$ = 7.3 ms, an order of magnitude faster than FM4-64 which undergoes its modulation with a half-life of $t_{1/2}$ = 80 ms (Figure 14). The kinetic responses of di-4-ANEPPS and RH237 are more complex than **1b.2H** and FM4-64. di-4-ANEPPS has a fast response with half-life $t_{1/2}$ = 63 ms, similar to that found by Millard *et al.* ($t_{1/2}$ = 49 ms)[14] but this is convolved with a slow decay at a rate of 3.1% / sec (Figure 15). The response of RH237 is more complex, rising to its positive extreme upon application of a positive potential ($t_{1/2}$ = 70 ms), but displaying a biexponential response upon application of a negative transmembrane potential (Figure 15).

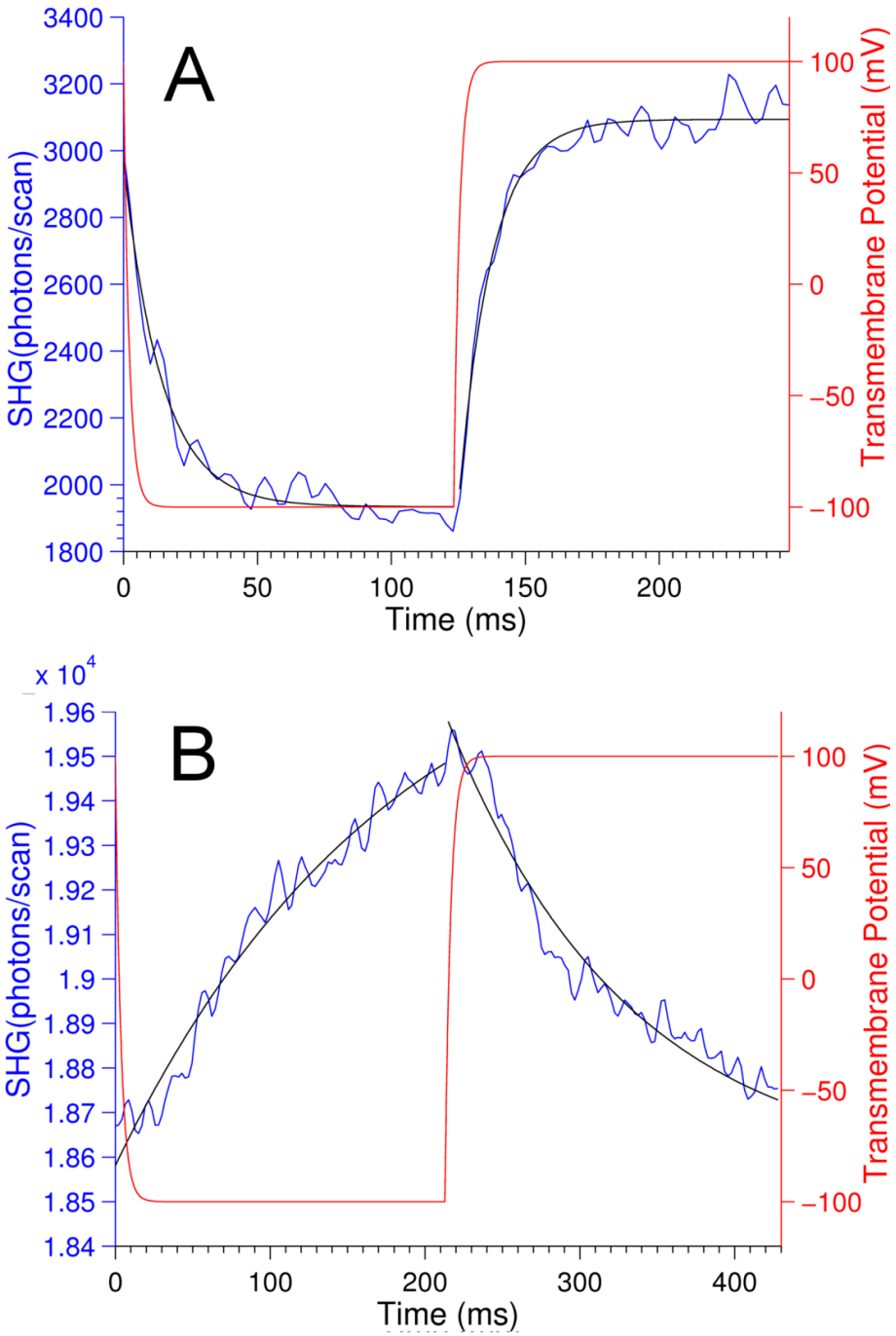

Figure 14 Change in SHG (*blue trace*) when an alternating transmembane potential of ±100 mV (*red trace, calculated*) was applied to **1b.2H** (A) and FM4-64 (B). A first order fit of the rise and decay times (*black line*) shows that **1b.2H** is more than an order of magnitude faster than FM4-64.

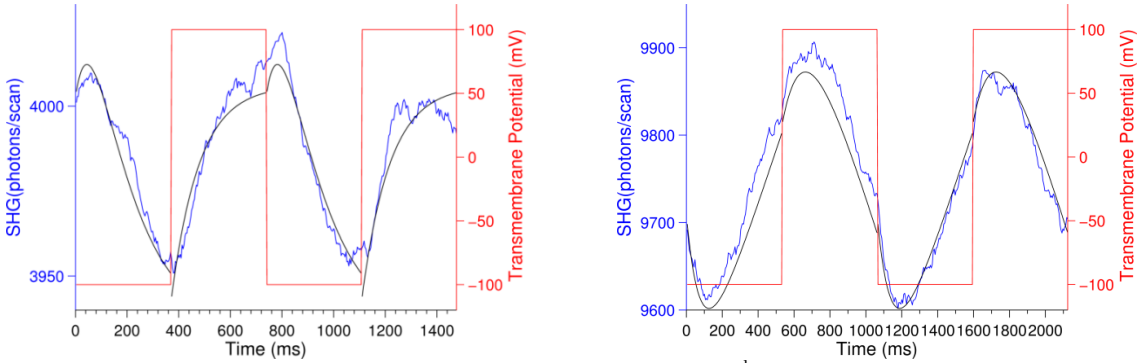

Figure 15 Kinetics of SHG response (*intensity data, blue* trace; 2nd order model, black line) to applied voltage (*red trace, calculated*) for RH237 (*left*) and di-4-ANEPPS (*right*) in DPhPC bilayers. Traces are displayed over two periods, to demonstrate the reproducibility of the kinetics.

A measure of how accurately the SHG signal, *s*, reports the voltage waveform, *v*, may be found by taking their normalized cross correlation, $\bar{R}_{v,s}$ (Figure 16). This measure calculates the similarity between traces when overlaid (Number of Lags = 2000), then when the two traces are shifted relative to each other in both the positive and negative directions. Not only does this grant a measure of how well the SHG reports on the applied potential, but also confirms that the two traces are perfectly in phase when we observe the maximum as a spike at lags = 2000.

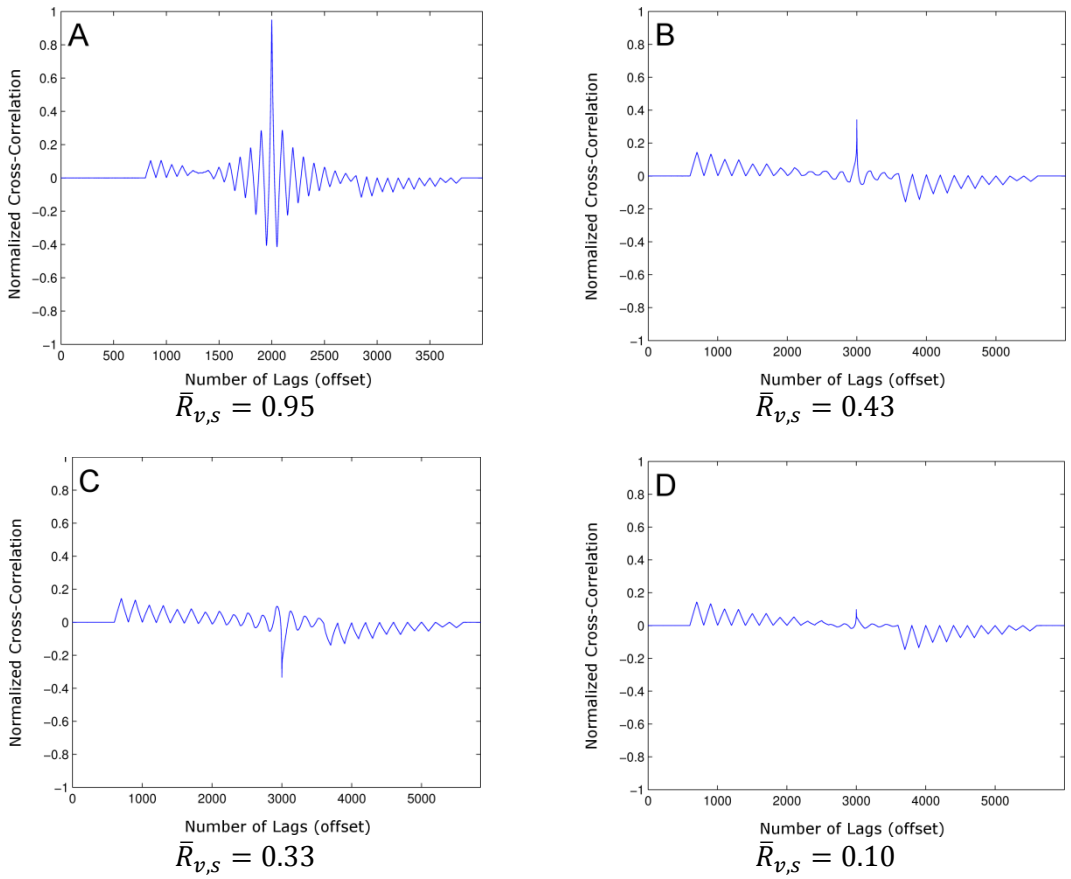

Figure 16 The similarity of SHG traces to their parent voltage waveform can be found by taking the normalized cross-correlation. This figure shows the normalized cross-correlation of SHG and voltage waveform for (A) **1b.2H**, (B) di-4-ANEPPS, (C) FM4-64 and (D) RH237.

We find that **1b.2H** displays near perfect covariance, having a normalized maximum of $\bar{R}_{v,s} = 0.95$ (Table 1). The normalized maximum correlation for the styryl type chromophores are significantly less, the highest only $\bar{R}_{v,s} = 0.46$ for di-4-ANEPPS.

Table 1 Performance of voltage sensitive SHG probes investigated in this article.

Dye	β_{zzz} / esu × 10^{-30} (λ / nm)	$\Delta S/S$ (% / 100 mV)	$\bar{R}_{v,s}{}^{a}$	$t_{1/2}$ (ms)
1b.2H	2300 (800) 5800 (840)	20	0.95	7.3
FM4-64	1085 (800)	-4.4	0.33	80
RH237	1085 (800)	0.5	0.10	47
di-4-ANEPPS	– [b]	-1.1	0.46	63

a) Normalized cross-correlation, a measure of how well the dye reports on the applied transmembrane potential (Figures 16). b) No data are available for the resonance-enhanced first hyperpolarisability of di-4-ANEPPS.

5.5 Discussion

Over the *t* ms rise time of an action potential (and approximating an instantaneous rise), we expect the SHG intensity of any dye to reach

$$\frac{\Delta S_{eff}}{S} = \frac{\Delta S_{100\,mV}}{S}\left(1 - exp\left(\frac{-tln2}{t_{1/2}}\right)\right)$$

per cent effective change from the baseline, where $t_{1/2}$ is the characteristic half-life of the dye. Consequently, an important metric when detecting sharp spikes in potential is $t/t_{1/2}$, which governs the proportion of the response that will be achieved over this time. Possessing a very fast response, **1b.2H** displays 20 % ($\Delta S_{\text{eff}}/S$ = 3.4%) of its sensitivity for a 100 mV potential spike within a 2 ms rise time. FM4-64 will only achieve 1.4 % ($\Delta S_{\text{eff}}/S$ = 0.062%) of its maximum value over the same timescale. Detection of IPSPs and EPSPs is more difficult than APs due to their inherently lower magnitude, however since they persist for a longer time (2–4 ms), the fast response of our porphyrinic dye should be able to detect them with sufficient sensitivity: $\Delta S_{\text{eff}}/S$ = 6.1%. For a 20 mV EPSP, this translates to a 1.2 % change in SHG intensity – a modulation which could easily be detected on a trial-by-trial basis.

In our previous study of push-pull amphiphilic porphyrins as SHG probes,[25] we established that the molecular first hyperpolarizability of **1b.2H** is significantly higher than commercially available styryl dyes. As voltage-sensitivity of a dye is linked to its molecular polarizability, we expect our porphyrins to be highly sensitive to transmembrane potential. In this study we show that **1b.2H** is about four times more sensitive to electric fields and ten times faster to respond than state of the art styryl dye FM4-64 which has already been used to image action potentials via SHG.[4-6] Dye sensitivities and kinetic responses are in agreement with literature values.[14, 38] We note that previous publications show styryl dyes with considerably higher sensitivities;[29, 31] however these studies use much longer time-windows and lower sampling rates than our technique. We postulate that the high sensitivity of di-4-ANEPPS (43% / 100 mV) previously recorded is a slow response and therefore is not observed over the faster time resolution we use in this study.[29, 31] Furthermore, the complexity of the kinetic behaviour of RH237 and di-4-ANEPPS reduces their usefulness as SHG probes of transmembrane potential.

These findings show the **1b.2H** porphyrinic chromophore is exceptionally well suited for measuring fast potential changes such as APs and PSPs.

5.6 References

1. J. Jiang and R. Yuste, *Microsc. Microanal.*, 2008, **14**, 526-531.
2. M. A. Popovic, A. J. Foust, D. A. McCormick and D. Zecevic, *J. Physiol.*, 2011, **589**, 4167-4187.
3. L. Sacconi, D. A. Dombeck and W. W. Webb, *Proc. Natl. Acad. Sci. U. S. A.*, 2006, **103**, 3124-3129.
4. D. A. Dombeck, M. Blanchard-Desce and W. W. Webb, *J. Neurosci.*, 2004, **24**, 999-1003.
5. D. A. Dombeck, L. Sacconi, M. Blanchard-Desce and W. W. Webb, *J. Neurophysiol.*, 2005, **94**, 3628-3636.
6. T. Sasaki, N. Takahashi, N. Matsuki and Y. Ikegaya, *J. Neurophysiol.*, 2008, **100**, 1668-1676.
7. T. J. Blanche and N. V. Swindale, *J. Neurosci. Methods*, 2006, **155**, 81-91.
8. L. Srinivasan, L. R. Varshney and J. Kusuma, 32nd Annual International Conference of the IEEE EMBS, Buenos Aires, 2010.
9. J. Bradley, R. Luo, T. S. Otis and D. A. DiGregorio, *J. Neurosci.*, 2009, **29**, 9197-9209.
10. L. Loew, L. Cohen, J. Dix, E. Fluhler, V. Montana, G. Salama and W. Jian-young, *J. Membr. Biol.*, 1992, **130**, 1-10.
11. E. W. Miller, J. Y. Lin, E. P. Frady, P. A. Steinbach, W. B. Kristan and R. Y. Tsien, *Proc. Natl. Acad. Sci. U. S. A.*, 2012, **109**, 2114-2119.
12. J. Erickson, A. Tooker, Y. C. Tai and J. Pine, *J. Neurosci. Methods*, 2008, **175**, 1-16.
13. M. Maher, J. Pine, J. Wright and Y.-C. Tai, *J. Neurosci. Methods*, 1999, **87**, 45-56.
14. A. C. Millard, L. Jin, J. P. Wuskell, D. M. Boudreau, A. Lewis and L. M. Loew, *J. Membr. Biol.*, 2005, **208**, 103-111.
15. R. Cossart, Y. Ikegaya and R. Yuste, *Cell Calcium*, 2005, **37**, 451-457.
16. J. J. Eggermont, *J. Neurophysiol.*, 1991, **66**, 1549-1563.
17. C. Grienberger and A. Konnerth, *Neuron*, 2012, **73**, 862-885.
18. D. Smetters, A. Majewska and R. Yuste, *Methods*, 1999, **18**, 215-221.
19. T. Berger, A. Borgdorff, S. Crochet, F. B. Neubauer, S. Lefort, B. Fauvet, I. Ferezou, A. Carleton, H.-R. Lüscher and C. C. H. Petersen, *J. Neurophysiol.*, 2007, **97**, 3751-3762.
20. C. B. Chien and J. Pine, *Biophys. J.*, 1991, **60**, 697-711.
21. F. Helmchen and W. Denk, *Nat. Methods*, 2005, **2**, 932-940.
22. J. Jiang, K. B. Eisenthal and R. Yuste, *Biophys. J.*, 2007, **93**, L26-L28.
23. R. Weissleder, *Nat. Biotechnol.*, 2001, **19**, 316-317.
24. A. Zoumi, A. Yeh and B. J. Tromberg, *Proc. Natl. Acad. Sci. U. S. A.*, 2002, **99**, 11014-11019.
25. J. E. Reeve, H. A. Collins, K. D. Mey, M. M. Kohl, K. J. Thorley, O. Paulsen, K. Clays and H. L. Anderson, *J. Am. Chem. Soc.*, 2009, **131**, 2758-2759.
26. I. Ben-Oren, G. Peleg, A. Lewis, B. Minke and L. Loew, *Biophys. J.*, 1996, **71**, 1616-1620.
27. O. Bouevitch, A. Lewis, I. Pinevsky, J. P. Wuskell and L. M. Loew, *Biophys. J.*, 1993, **65**, 672-679.
28. A. C. Millard, L. Jin, A. Lewis and L. M. Loew, *Opt. Lett.*, 2003, **28**, 1221-1223.
29. A. C. Millard, L. Jin, M.-d. Wei, J. P. Wuskell, A. Lewis and L. M. Loew, *Biophys. J.*, 2004, **86**, 1169-1176.
30. B. A. Nemet, V. Nikolenko and R. Yuste, *J. Biomed. Opt.*, 2004, **9**, 873-881.

31. M. Nuriya, J. Jiang, B. Nemet, K. B. Eisenthal and R. Yuste, *Proc. Natl. Acad. Sci. U. S. A.*, 2006, **103**, 786-790.
32. L. Sacconi, M. D'Amico, F. Vanzi, T. Biagiotti, R. Antolini, M. Olivotto and F. S. Pavone, *J. Biomed. Opt.*, 2005, **10**, 024014-024018.
33. P. R. Dragsten and W. W. Webb, *Biochemistry*, 1978, **17**, 5228-5240.
34. E. Fluhler, V. G. Burnham and L. M. Loew, *Biochemistry*, 1985, **24**, 5749-5755.
35. M. A. Holden, D. Needham and H. Bayley, *J. Am. Chem. Soc.*, 2007, **129**, 8650-8655.
36. G. Maglia, A. J. Heron, W. L. Hwang, M. A. Holden, E. Mikhailova, Q. Li, S. Cheley and H. Bayley, *Nat Nano*, 2009, **4**, 437-440.
37. W. L. Hwang, M. Chen, B. d. Cronin, M. A. Holden and H. Bayley, *J. Am. Chem. Soc.*, 2008, **130**, 5878-5879.
38. T. J. Ebner and G. Chen, *Prog. Neurobio.*, 1995, **46**, 463-506.

Chapter 6

A Water-Soluble Caging Group for Hydrophobic Biomolecules

Summary

N-Methyl-D-aspartate (NMDA) receptors are important for synaptic plasticity, the mechanism by which external stimuli are reinforced to facilitate learning and memory formation. We have synthesised two caged forms of the use-dependent NMDA receptor ion channel blocker MK801 and quantified the efficacy of this novel neurophysiological tool.[‡]

Here, I discuss considerations regarding the initial choice of caging group and refinements which increase water-solubility in our second generation design. I document the synthesis and testing of caged MK801 and then, in a demonstration of its use, we show that subcompartment-specific intracellular photolysis of this compound can be employed to establish the location of NMDA receptor ion channels involved in synaptic plasticity. Following initial synthesis of the proof-of-principle compound by Tom R. Eaton, I performed the synthesis, molecular design and biophysical characterisation of the water-soluble compound described. All neurophysiological experiments were performed by Dr. Rodríguez-Moreno and Dr. M. M Kohl, from the Department of Physiology, Development and Neuroscience, University of Cambridge.

[‡] Part of the work in this chapter was published in: A. Rodríguez-Moreno, M. M. Kohl, J. E. Reeve, T. R. Eaton, H. A. Collins, H. L. Anderson, O. Paulsen, *J. Neuroscience*, 2011, **31**, 8564-8569 which was accompanied by a paper on the synthesis and choice of caging group: J. E. Reeve, M. M. Kohl, A. Rodríguez-Moreno, O. Paulsen, H. L. Anderson, *Commun. Integr. Biol.*, 2012, **5**, 240-242

6.1 Introduction

In the study of excitable cells, such as neurons, drugs that block ion channels are of particular interest. In acute brain slices, drug effects are commonly restricted to three levels: (1), the whole tissue preparation through addition of the drug to the incubation medium; (2), a small volume of tissue through local pressure injection; or (3), a single cell through addition of the drug to the whole-cell patch clamp pipette. The photo-release of bioactive molecules with fine spatiotemporal resolution has revealed the more intricate, subcellular details of physiological systems. Propelled by their biological utility, many new molecular architectures are gaining credibility as molecular 'cages'.[1-3] The commercial availability of these compounds is also driving their utility, most notably the RuBi cage, synthesised by Yuste which allows two-photon activated uncaging of gamma-amino butyric acid (GABA).[4]

6.1.1 MK801, an NMDA receptor antagonist

MK801 (Figure 1, RHS) is a non-competitive antagonist of the NMDA receptor with a high affinity of binding (K_d = 37.2 ± 2.7 nM) in rat neurons.[5, 6] In order to target this action upon NMDA receptors in specific regions, it is important to have spatial selectivity over where a particular blocker is released.[3, 7] Microinjection of a blocking molecule into a cell does not have sufficient spatial selectivity, and in particular very small cellular structures (such as individual synapses) may not be targeted. If MK801 may be activated by uncaging with a tightly focused beam of light, it will be possible to study the blocking of receptors in individual synapses and therefore how NMDA currents drive interactions in small neural networks. [8, 9] Furthermore, it is possible to uncage a blocker protected with a photolabile group via two-photon absorption, allowing even finer (micrometre) spatial selectivity in three dimensions.[1, 4, 10] Furthermore, MK801 is a use-dependent NMDA receptor antagonist, meaning that if NMDA channels do not open following an activation (which is triggered by a membrane depolarisation), they

may not be blocked by MK801 (in this case, a Mg^{2+} cation which normally reversibly blocks the active site and which is displaced upon depolarisation stops MK801 from binding). Conservation of the use-dependence of MK801 in any caged form is important, since it is a phenomenon which can be exploited to later infer the nature of the membrane depolarisations taking place.

6.1.2 Biological implications for caged MK801

Long-term potentiation (LTP) is the mechanism which strengthens communication between synapses. This enhancement of signal transmission between two neurons allows synaptic plasticity – the ability of a neural network to learn and exhibit memory. Long-term depression (LTD) has the opposing effect, weakening the strength of signal transmission, which is essential for 'normalising' the effect of continued LTP in a network.[11-13] While the physical and biological basis of LTP and LTD is still poorly understood, some neurological theories [14, 15] have proposed mechanisms which translate LTP and LTD into the associative learning required for synaptic plasticity.

NMDA receptors are essential for LTD,[16-18] however the precise location and therefore the mechanism of their action remains unclear, with studies making weighty and often controversial assumptions on their locus of action.[19, 20] To find the location of NMDA receptors which are activated during timing-dependant LTD is to further refine the understanding of how LTD mediates synaptic plasticity. Selective deprotection of caged MK801 in a particular neuronal subcompartment before induction of LTD would confirm or refute the action of NMDA receptors in that subcompartment during LTD. By comparing the effect of uncaging on LTD in different subcompartments and different neuronal architectures, we can isolate the location and role of NMDA receptors in LTD.[9]

6.1.3 Caging Biomolecules

A caged biomolecule should fulfill a number of criteria, established in 1982 by Lester and Nerbonne,[21] which were revised as the technique has matured.[22] The caged molecule should (i) have no biological activity when in its caged form, (ii) release a bioavailable form of the caged substrate upon the application of a suitable wavelength of light with (iii) fast kinetics and (iv) a high photochemical quantum yield.

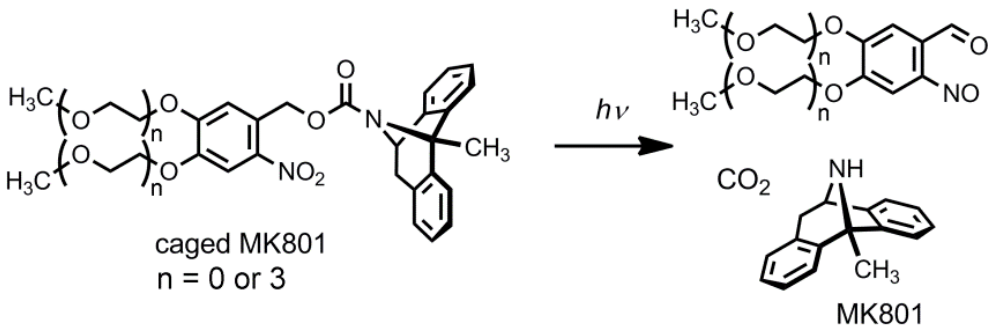

Figure 1. Exposure of caged MK801 to UV ($\lambda < 350$ nm) light leads to deprotection of MK801 via an intramolecular rearrangement. The use of a carbamate to facilitate a secondary amine leaving group results in the evolution of one molecule of CO_2 per uncaging event, and is a thermodynamic driving force for completion of the reaction.

The byproducts of the uncaging (Figure 1) should be (v) non-toxic and also (vi) not interfere with the physiological processes under investigation. Ideally, the caged molecule should also be (vii) water-soluble and (viii) inert to decomposition or attack under physiological conditions. In this chapter, I outline how the efficacy of a caged form of MK801 was established and then detail how the design was elaborated, increasing its suitability for *in* and *ex vivo* use.

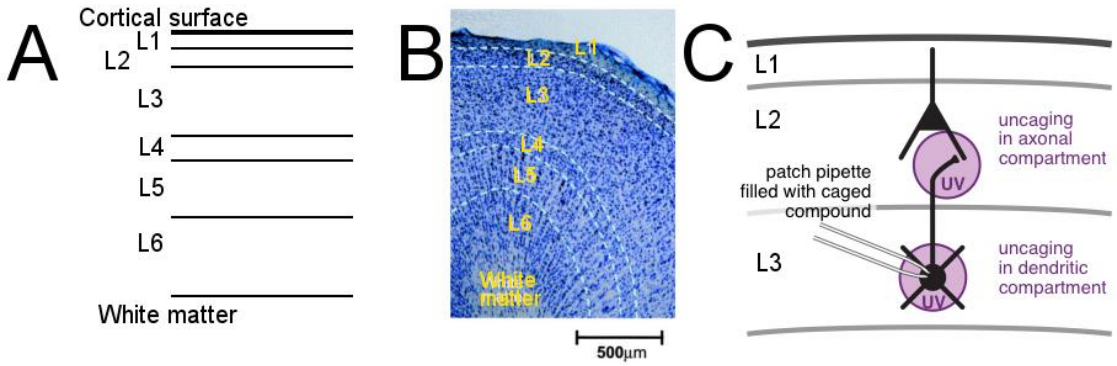

Figure 2. (A) Cartoon depicting layered structure of a typical mammalian brain. (B) Stained view of layered structure of cat visual cortex with six layers indicated. Dark dots indicate each neuron's soma. Reprinted from Maheswari *et al., J. Neurosci. Methods*, 2003, **124**, 83-92.[23] (C) Spot photolysis of a caged ion-channel blocker with UV light allows for precise temporal and spatial control of the drug effect, by uncaging only in either layer 2 or layer 3.[24]

The *o*-nitroveratryloxycarbonyl (NVOC) protecting group (Scheme 1) that we use in this chapter is widely applicable and has been used to solve numerous problems in chemistry and physiology. It was not long after its introduction by Woodward and coworkers[25] that it was first applied to biochemistry through the synthesis of caged ATP by Kaplan et al.[26] in 1978. Upon photolysis, NVOC protected amines decompose to release the caged molecule and form carbon dioxide and *o*-nitroso benzaldehyde photoproducts with photochemical quantum yields in the range 0.005-0.1%.

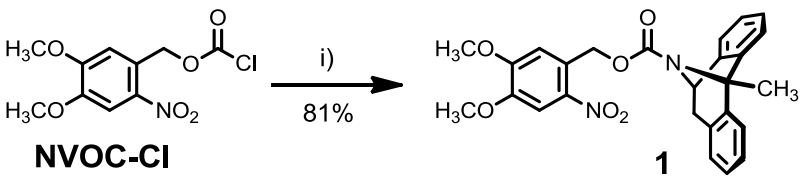

Scheme 1. Synthesis of NVOC caged MK801 (cMK801). i) Dizocilpine maleate (MK801), Na_2CO_3, dioxane, THF, water, rt, 48 h.

In this chapter, we aim to design, synthesise, characterise and test a caged form of NMDA receptor antagonist MK801 (Figure 1). We progress through two generations, the first of which is a proof of principle following a very simple synthesis, and the second of which employs a novel water-soluble caging group a TEG-substituted diphenoxy nitrobenzyl. Through photolysis of a novel caged NMDA receptor antagonist, introduced intracellularly via a patch pipette (Figure 2), we were able to demonstrate control of ion channel activity at the subcellular level (see Figure 4).[9, 24] This is of particular interest when studying the localisation of ion channel function in highly compartmentalised cells such as neurons.

6.2 First Generation: Design and Testing

Our first design used the common nitrophenyl photolabile protecting group motif[27] rather than other commonly employed cages such as methoxy nitroindolinyl (MNI)[28, 29] since it can be easily derivatised at its phenoxy positions. Synthesis from commercially available starting material was completed in 88% yield over one step by the combination of MK801 and NVOC-Cl. With the application of 350 nm UV light, excellent contrast can be achieved between subcellular compartments with low background. NVOC cages are neuropharmocologically compatible; we showed that the cage itself does not cause any channel blocking, unlike MNI which interacts with GABA-A receptors.[4] Formulation of cMK801 with Polysorbate 20 (Polyoxyethylene (20) sorbitan monolaurate) afforded sufficient water-solubility, but was detrimental to effective (high-resistance) patch-clamp seal formation.

Typically, when patched and activated (with neurotransmitters and a simultaneous voltage step 'stimulation'), a neuron will exhibit a transmembrane current, in the form of a postsynaptic potential (PSP), caused by ion flux through its NMDA receptor ion channels. This current can be measured, and is an indicator of the number of NMDA receptors which are both present and activatable. Binding of MK801 to a NMDA channel results in a block of the channel current and renders it permanently deactivated. By monitoring the ensemble NMDA receptor current, we can monitor the proportion of channels that have been blocked by MK801 (Figure 3).[17, 30]

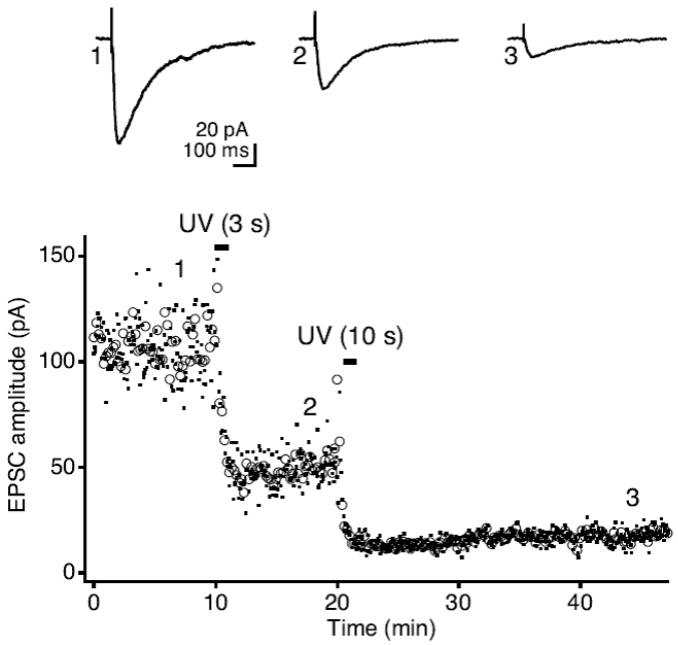

Figure 3 Excitatory post synaptic current (EPSC) traces from three regions within an uncaging experiment with cMK801. At position 1, no caged MK801 is released, and a full PSP response is activated by each stimulation. After a short UV flash, position 2 is rapidly reached in which about half of the NMDA receptors are blocked, resulting in a diminished NMDA receptor current. Finally, a 10 second flash blocks most remaining NMDA receptors, and causes the excitatory post synaptic current to fall to its baseline level. Figure courtesy of Dr. M. M. Kohl.

Our first caged derivative, cMK801 was sufficiently water-soluble for use as a proof of principle, and was employed in three experiments which demonstrate that MK801 may be effectively caged with a nitrobenzyl-type protecting group (Figure 4).

Firstly, the uncaging efficacy was established: Caged MK801 was loaded into an excitable neuron via a patch clamp and the normalised NMDA receptor current was measured at two minute intervals (Figure 4A). After 10 minutes, a UV flash at 350 nm was applied for one second, releasing MK801 from its caged form. The expected decay in normalised NMDA receptor current (Figure 4A) is observed; indicating that uncaging has taken place and that bioavailable MK801 is acting as an antagonist for the NMDA receptor.

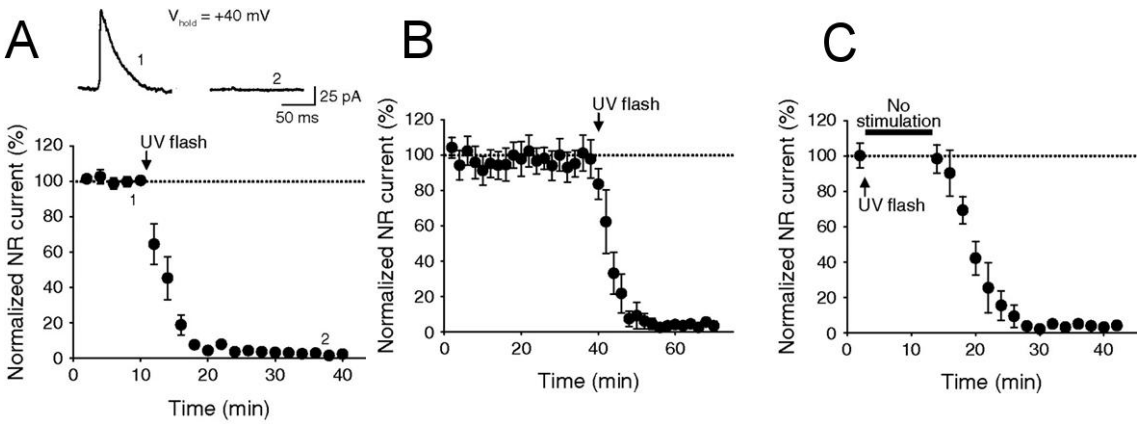

Figure 4 (A) A UV flash 10 minutes after loading causes MK801 uncaging and subsequent blocking of NMDA receptors, resulting in the normalised NMDA receptor (NR) current falling to zero. (B) The same is observed after 40 minutes, confirming that the dye is stable physiologically stable for the timescales necessary in the following experiments. (C) The use-dependence of MK801 is conserved when caged, even if MK801 is released and present in the cell for 10 minutes prior to stimulation, it does not result in an NMDA receptor block until stimulation is resumed.

The stability of cMK801 under physiological conditions was verified in a similar experiment, but in this case, cMK801 is loaded 40 minutes before a UV flash. The normalised NMDA receptor current before the flash is stable (Figure 4B), thus no MK801 is liberated in the absence of UV light.

Caged MK801 is shown to be use-dependent in a final proof-of-principle experiment. cMK801 is loaded into an excitable neuron and after verifying that a normalised NMDA receptor current exists, a UV flash was applied and stimulation was halted, preventing the opening of NMDA channels and subsequently preventing liberated MK801 from binding. After 10 minutes with no stimulation, postsynaptic potentials are again evoked and rapidly decay from their maximum level to zero with the same time constant as previous experiments, demonstrating that MK801 which is released in an uncaging experiment conserves its use-dependence (Figure 4C).

A key observation from these proof-of-principle experiments was that cMK801 has insufficient water-solubility, necessitating formulation with polysorbate 20, an amphiphilic molecule with a low critical micelle concentration. The action of this surfactant granted better aqueous solubility but often caused patching to fail due to leaks at the site of the seal. Since cMK801 was intended for use in pairing experiments, which requires the patching of two connected neurons and the chance of two successful patches is the chance of one successful patch, squared, a high patching failure rate makes patching two paired neurons near impossible. The design of a water soluble derivative of cMK801 which did not require formulation was therefore undertaken.

6.3 Second Generation: Design and Synthesis

NVOC-protected MK801 lacked water-solubility. Its hydrophobicity caused precipitation in aqueous solution, necessitating formulation before use. We therefore decided to elaborate the structure by the inclusion of triethylene glycol chains at the phenoxy positions. I synthesised a novel triethylene glycol substituted nitrophenyl cage-protected MK801 (TcMK801, Figure 1, n = 3).

The synthesis was completed from 3,4-dihydroxybenzaldehyde in seven steps, 7% overall yield to produce a water-soluble form of caged MK801, (Scheme 2). One notable feature is that the compounds are detected in ESI^+ MS exclusively with a sodium ion, suggesting complex formation of Na^+ with the TEG chains. This complexation of metal ions in solution may add solubility through the inclusion of charge.

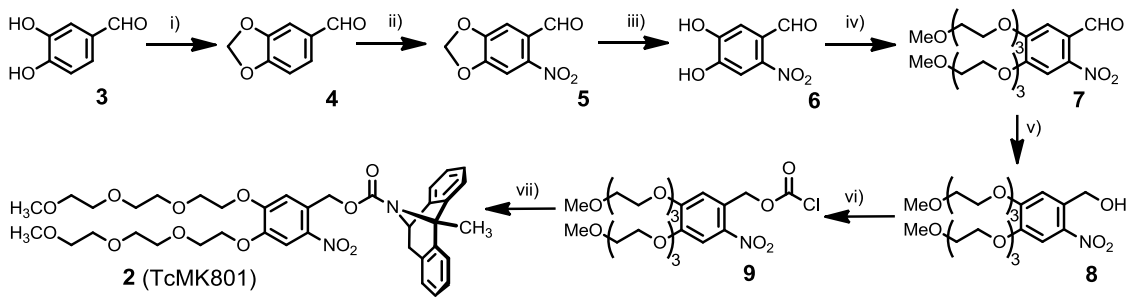

Scheme 2. Synthesis of TEG-substituted caged MK801 (TcMK801) **2**, from 4,5-dihydroxy 2-nitrobenzaldehyde. i) CH_2I_2, K_2CO_3, DMF, 60 ºC, 4 h ii) HNO_3, CH_2ClCH_2Cl, -30 ºC, 6.5 h. iii) AlCl3, CH_2ClCH_2Cl, -5ºC, 6.5 h, HBr, 2 days, rt. iv) Triethylene glycol monomethyl monotosylate ether, K_2CO_3, MeCN, reflux, 16 h. v) $NaBH_4$, MeOH, rt, 3 h. vi) $(Cl_3CO)_2CO$, Et_3N, $CHCl_3$, rt, 2.5 h. vii) Dizocilpine maleate (MK801), Na_2CO_3, dioxane, THF, water, rt, 48 h.

The concentration of a saturated solution of TcMK801 in pure water was measured by UV-vis absorption and found to be 9.8 μM, 50 times more soluble than cMK801, its methoxy precursor which saturated at 0.2 μM. The linear absorption properties of cMK801 and TcMK801 showed little variation (Figure 5), however the quantum yield of release was lower in the case of TcMK801, as measured by the uncaging time required for a full block of NMDA receptor current.

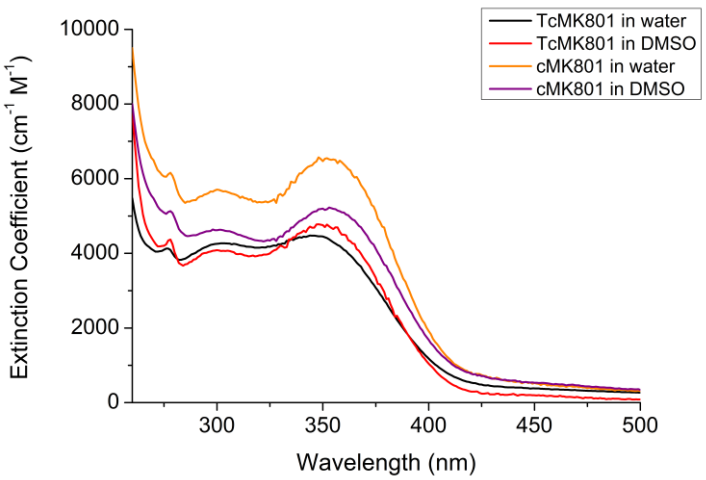

Figure 5. UV-vis absorption of cMK801 and TcMK801 in water and DMSO.

For patch clamping experiments, a 100 mM solution of TcMK801 in DMSO, was diluted one hundredfold with intracellular solution to yield a 1 mM aqueous solution with 1% DMSO by volume, which is tolerated well by cells in an established tissue or culture. Water solubility was therefore successfully conferred by triethylene glycol chains and permitted a formulation-free solution of caged MK801. Patch-clamping experiments confirmed that TcMK801 (which does not require polysorbate 20) permits quick and reproducible seal formation, and as such was carried through to use in neuron pairing experiments.

6.4 Suppression of LTP and LTD with caged NMDA antagonist MK801

Antonio Rodriguez-Moreno and Michael M. Kohl, under the supervision of Professor Ole Paulsen (Department of Physiology, Development and Neuroscience, University of Cambridge) used TcMK801 to identify the location of NMDA receptors responsible for LTP and LTD in mouse barrel cortex slices. The assumed postsynaptic somatodendritic location of NMDA receptors responsible for LTP was confirmed when release of MK801 in the somatodendritic subcompartment inhibited LTP whereas axonal uncaging had no impact (Figure 6A).[9, 24]

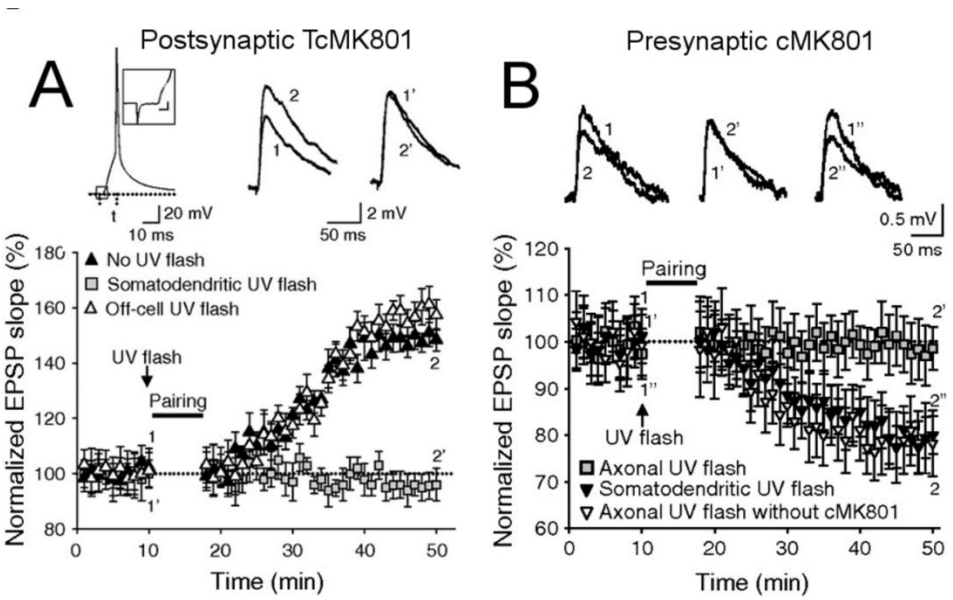

Figure 6 (A) Induction of LTP following pairing is inhibited by a somatodendritic flash, confirming the location of NMDA receptors on the postsynaptic cell. (B) LTD is inhibited by a presynaptic axonal flash on a pair of patched neurons indicating that the NMDA receptors responsible for LTD are located on the axon of the presynaptic cell.

The procedure for inducing LTD involves patching two paired (i.e. connected) neurons, then monitoring the NMDA receptor current in the presence and absence of MK801. We found that once TcMK801 was patched into the presynaptic cell, uncaging with an axonal flash (Figure 2)

inhibited LTD whereas a somatodendritic flash did not. This places the NMDA receptors responsible for LTD on the axon of the presynaptic neuron (Figure 6B).

In this study, cMK801 and TcMK801, photolabile caged forms of NMDA receptor antagonist MK801 were shown to be powerful tools for precise spatiotemporal control of neuronal ion channels. Testing and evaluation of cMK801 allowed the progression to a second generation molecule, TcMK801 was successfully used in paring protocols and demonstrated the location of NMDA receptors necessary for induction of both LTP and LTD. As a result of this study, cMK801 is now commercially available, and can be ordered from Sigma-Aldrich, who cite the study performed with Rodríguez-Moreno *et al*.[9] as the sole protocol and reference. TcMK801 was also passed on to Professor Matthew Larkum (Department of Physiology, University of Berne) where it was used in a two-photon uncaging study which confirms the participation of NMDA receptors in stimulating action potentials *in vivo* (MS in preparation). This work used pulsed NIR excitation at 690 nm, proving that TcMK801 may be uncaged in a multiphoton modality.

6.5 Experimental

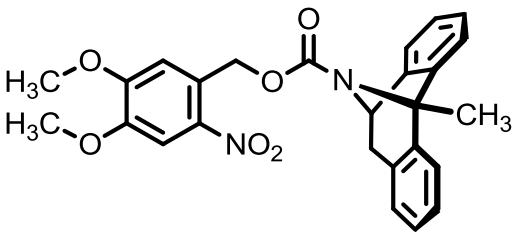

cMK801, **1**, was synthesised under my supervision by an undergraduate student, T. R. Eaton (Department of Chemistry, University of Oxford): MK801 malenate (30 mg, 89 μmol) and Na_2CO_3 (37.7 mg, 356 μmol) were dissolved in a mixture of water (1 mL) and dioxane (1 mL) to which 6-nitroveratryloxycarbonyl chloride (NVOC-Cl) (24.6 mg, 89.0 μmol) dissolved in THF (1 mL) and dioxane (1 mL) was added. The reaction was followed by TLC (1:50 EtOAc:CH_2Cl_2) and after 12 h was quenched with saturated $Na_2CO_{3(aq)}$ (50 mL). The organic-soluble products were extracted with $CHCl_3$ and the organic layer washed with water (2 × 20 mL). The product was isolated by flash chromatography on SiO_2 (1:50 EtOAc:CH_2Cl_2) and fractions were evaporated to give the product as a white wax. (33 mg, 81%). R_f = 0.29 (1:50 EtOAc:CH_2Cl_2). ^{1}H NMR (400 MHz, $CHCl_3$) δ_H 7.69 (s, 1H), 7.33 (m, 2H), 7.19 (m, 2H), 7.10 (m, 3H), 6.92 - 6.68 (m, 2H), 5.66 5.49 (m, 3H), 3.94 (s, 3H), 3.69 (m, 4H), 2.70 (d, J = 16.9 Hz, 1H), 2.32 (s, 3 H). ^{1}H NMR (400 MHz, CD_3CN) δ_H 7.67 (s, 1H), 7.41 (d, J = 6.7 Hz, 1H), 7.35 (d, J = 4.1 Hz, 1H), 7.21 (m, 3H), 7.12 (m, 3H), 6.94 (m, 1H), 5.49 (d, J = 5.3 Hz, 1H), 5.40 (s, 2H), 3.88 (s, 3H), 3.79 (m, 3H), 3.63 (dd, J = 17.3, 5.4 Hz, 1H), 2.68 (d, J = 17.3 Hz, 1H), 2.26 (s, 3H). ^{13}C NMR (125.7 MHz, CD_3CN, 338 K) δ_C 19.6, 34.1, 57.4, 57.4, 61.3, 64.7, 68.4, 109.0, 110.1, 112.8, 119.8, 122.9, 123.4, 127.4, 128.5, 128.8, 128.8, 128.9, 131.8, 133.5, 140.8, 145.1, 150.0, 151.3, 155.1, 155.6. m/z (MALDI+) 482.93, ($C_{26}H_{24}N_2O_6^+$, $[M+Na]^+$ 100%, requires 483.15).

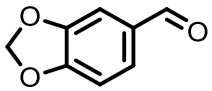

Benzo[d][1,3]dioxole-5-carbaldehyde (Piperonal), **3**, was prepared according to an adapted literature procedure.[31] 3,4-Dihydroxybenzaldehyde (5.00 g, 36.2 mmol) and K_2CO_3 (11.0 g, 79.6 mmol) were dissolved in *N*,*N*-dimethylformamide (10 mL) and diiodomethane (3 mL, 37.2 mmol) was added in one portion. The mixture was heated to 60 °C and stirred for 4 h then allowed to cool to room temperature. The mixture was poured onto a saturated solution of Na_2CO_3 (100 mL) and extracted with ether (2 × 200 mL). The combined organic layers were washed with saturated Na_2CO_3 solution (2 × 200 mL) and water (2 × 200 mL), dried over $MgSO_4$ and evaporated to yield a brown, aromatic solid (3.6 g, 66%). ^{1}H NMR (400 MHz, $CDCl_3$) δ_H 9.82 (s, 1H), 7.44 (d, J = 7.37 Hz, 1H), 7.35 (s, 1H), 6.95 (d, J = 8.19 Hz, 1H), 6.09 (s, 2H). m/z (ESI+) 151.05 ($[M+H]^+$, 100%, $C_8H_7O_3^+$ requires 151.04).

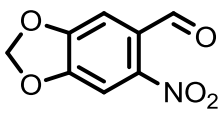

6-Nitrobenzo[d][1,3]dioxole-5-carbaldehyde (6-nitropiperonal), **4**, was synthesised according to a literature procedure.[32] Fuming HNO_3 (8 mL) was added to a stirred solution of piperonal (1.40 g, 9.33 mmol) in 1,2-dichloroethane (16 mL) at -30 °C. The mixture was stirred at -15 °C for 6.5 h until no starting material remained. The mixture was poured onto ice water (500 mL), extracted with EtOAc (2 × 100 mL) and dried over $MgSO_4$. The organic fractions were evaporated to dryness *in vacuo* to yield a brown amorphous solid (1.2 g, 66%). ^{1}H NMR (400 MHz, $CDCl_3$) δ_H 10.25 (s, 1H), 7.50 (s, 1H), 7.29 (s, 1H), 6.23 (s, 2H). *m/z* (ESI+) 218.00 ($[M+Na]^+$, 100%, $C_8H_5NO_5Na^+$ requires 218.01).

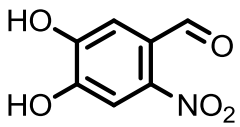

4,5-Dihydroxy-2-nitrobenzaldehyde, **5**, was synthesised according to a literature procedure.[32] 6-Nitropiperonal (1.20 g, 6.16 mmol) in 1,2-dichloroethane (4 mL) was added to a stirred solution of anhydrous $AlCl_3$ (2.4 g, 18 mmol) in 1,2-dichloroethane (6 mL) at -5 °C. The mixture was maintained at -5 °C for 2 h until no starting material remained. The mixture was poured onto a cooled solution of 48% HBr (250 mL) and stirred at room temperature for two days until no intermediate remained. The mixture was diluted with water (200 mL), extracted with EtOAc (2 × 100 mL), dried over $MgSO_4$ and evaporated to give a brown crystalline solid (120 mg, 11%). ^{1}H NMR (400 MHz, $CDCl_3$) δ_H 10.25 (s, 1H), 7.53 (s, 1H), 7.29 (s, 1H). *m/z* (ESI-) 181.99 ([M-H]$^-$, 100%, $C_7H_4NO_5^-$ requires 182.01).

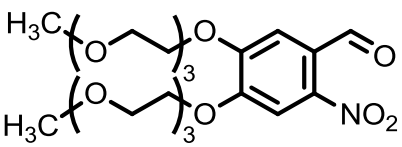

4,5-Bis(2-(2-(2-methoxyethoxy)ethoxy)ethoxy)-2-nitrobenzaldehyde, **6**, was prepared according to an adapted literature procedure.[33] A solution of 4,5-dihydroxy-2-nitrobenzaldehyde (60.0 mg, 327 μmol), 2-(2-(2-methoxyethoxy)ethoxy)ethyl tosylate (209 mg, 655 μmol) and K_2CO_3 (90.0 mg, 655 μmol) in anhydrous acetonitrile (5 mL) was refluxed for 16 h under N_2. The mixture was evaporated to dryness and purified by flash chromatography (EtOAc). The combined fractions were evaporated to dryness to yield **3** as a yellow oil (92 mg, 59%). ^{1}H NMR (400 MHz, $CDCl_3$) δ_H 10.43 (s, 1H), 7.71 (s, 1H), 7.45 (s, 1H), 4.32 (m, 4H), 3.94 (m, 4H), 3.75 (s, 4H), 3.66 (m, 8H), 3.55 (m, 4H), 3.38 (s, 6H). ^{13}C NMR (100 MHz, CDCl3) δ_C 188.16, 153.39, 152.23, 144.19, 125.99, 111.87, 109.61, 72.35, 71.43, 71.13, 71.03, 69.91, 69.71, 59.48. *m/z* (ESI+) 498.18 ([M+Na]$^+$ 100%, $C_{21}H_{33}ClNNaO_{11}^+$ requires 498.20)

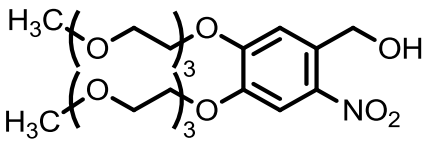

(4,5-Bis(2-(2-(2-methoxyethoxy)ethoxy)ethoxy)-2-nitrophenyl)methanol, **7**, was prepared according to an adapted literature procedure.[34] $NaBH_4$ (18.5 mg, 490 μmol) was added portionwise to a solution of 4,5-bis(2-(2-(2-methoxyethoxy)ethoxy)ethoxy)-2-nitrobenzaldehyde **3** (46.6 mg, 98.0 μmol) in anhydrous methanol (1.5 mL) at 5 °C. The reaction mixture was allowed to warm to room temperature and stirred for 3 h. The reaction was quenched with $HCl_{(aq)}$ (5 mL, 1 M) and extracted with chloroform (3 × 10 mL). The combined organic layers were washed with saturated NaCl solution (5 mL) and evaporated to dryness to yield **4** as a colourless oil (30 mg, 64%). ^{1}H NMR (400 MHz, $CDCl_3$) δ_H 7.76 (s, 1H), 7.35 (s, 1H), 4.95 (s, 2H), 4.33 (m, 2H), 4.23 (m, 2H), 3.90 (m, 4H), 3.74 (m, 4H), 3.66 (m, 8H), 3.55 (m, 4H), 3.37 (s, 3H), 3.36 (s, 3H), 1.25 (s, 1H). ^{13}C NMR (100 MHz, $CDCl_3$) δ_C 153.86, 147.25, 139.44, 133.19, 112.74, 110.56, 71.90, 71.87, 70.90, 70.79, 70.69, 70.65, 70.55, 70.43, 69.78, 69.51, 69.14, 68.89, 62.50, 59.01. *m/z* (ESI+) 500.16 ($[M+Na]^+$ 100%, $C_{21}H_{35}NNaO_{11}^+$ requires 500.21)

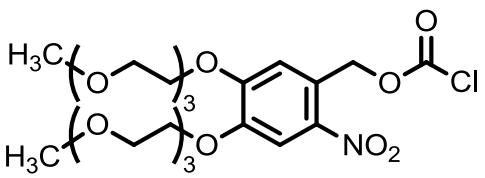

4,5-Bis(2-(2-(2-methoxyethoxy)ethoxy)ethoxy)-2-nitrobenzyl chloroformate, **8**, was prepared by mixture of (4,5-bis(2-(2-(2-methoxyethoxy)ethoxy)ethoxy)-2-nitrophenyl)methanol **4** (30 mg, 63 μmol) and triphosgene (28.0 mg, 94.5 μmol) in chloroform (5 mL) which was stirred for

2 h. Further triphosgene (18 mg, 63 μmol) was added and the mixture stirred for 30 min. When the reaction was complete by thin layer chromatography (TLC), the mixture was evaporated to dryness and purified by column chromatography on SiO_2 (1% MeOH in EtOAc). Combined fractions were evaporated and dried *in vacuo* to yield the product **5** as a colourless oil (20 mg, 59%). ^{1}H NMR (400 MHz, $CDCl_3$) δ_H 7.83 (s, 1H), 7.06 (s, 1H), 5.70 (s, 2H), 4.26 (m, 4H), 3.93 (m, 4H), 3.73 (m, 4H), 3.67 (m, 8H), 3.57 (m, 4H), 3.38 (s, 6H). *m/z* (ESI+) 562.18 ($[M+Na]^+$ 100%, $C_{22}H_{34}ClNNaO_{12}$+ requires 562.16)

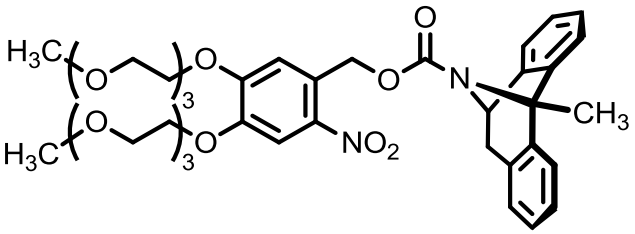

TcMK801, **2**, was prepared according to an adapted literature procedure.[35] A solution of 4,5-bis(2-(2-(2-methoxyethoxy)ethoxy)ethoxy)-2-nitrobenzyl chloroformate **5** (20 mg, 37 μmol) in THF (0.5 mL) was added to a solution of (+)-5-methyl-10,11-dihydro-5H-dibenzo[a,d]cyclohepten-5,10-imine maleate (MK801, 12.4 mg, 37.0 μmol), Na_2CO_3 monohydrate (18.4 mg, 148 μmol) and dioxane (0.5 mL) in water (1 mL). The mixture was stirred for 48 h. The reaction mixture was poured onto saturated $Na_2CO_{3(aq)}$ (2 mL), extracted with chloroform (2 × 5 mL) and washed with water (2 × 5 mL). The organic layer was evaporated to dryness and purified by column chromatography on SiO_2 (1% MeOH in ethyl acetate). Combined fractions were evaporated and dried *in vacuo* to yield the product **2** as a colourless oil (8 mg, 29%). ^{1}H NMR (400 MHz, $CDCl_3$) δ_H 7.75 (m, 1H), 7.33 (m, 1H), 7.31 (m, 2H), 7.19 (m, 2H), 7.10 (m, 2H), 7.08 (m, 1H), 6.92 (m, 1H), 5.51 (s, 1H), 5.49 (s, 1H), 4.22 (m, 2H), 3.88 (m, 2H), 3.82 (m, 4H), 3.74 (m, 4H), 3.65 (m, 8H), 3.55 (m, 4H), 3.38 (s, 3H), 3.37 (s, 3H), 2.69 (d, J = 17.1 Hz, 1H), 2.26 (s, 3H), 1.26 (s, 2H). ^{13}C NMR (100 MHz, $CDCl_3$)

δ_C 207.00, 167.75, 153.33, 143.27, 139.16, 130.86, 130.44, 128.78, 127.64, 127.52, 127.41, 126.13, 121.28, 118.60, 110.79, 71.90, 70.91, 70.66, 70.54, 69.47, 69.21, 68.79, 67.95, 67.06, 59.86, 59.01, 38.70, 30.91, 30.33, 29.67, 28.89, 25.58, 23.72, 22.96, 22.67, 14.03, 10.94. *m/z* (ESI+) 747.3100 ($[M+Na]^+$ 100%, $C_{38}H_{48}N_2NaO_{12}^+$ requires 747.3099)

6.6 References

1. I. Aujard, C. Benbrahim, M. Gouget, O. Ruel, J.-B. Baudin, P. Neveu and L. Jullien, *Chem.--Eur. J.*, 2006, **12**, 6865-6879.
2. F. F. Trigo, G. Papageorgiou, J. E. T. Corrie and D. Ogden, *J. Neurosci. Methods*, 2009, **181**, 159-169.
3. H. Yu, J. Li, D. Wu, Z. Qiu and Y. Zhang, *Chem. Soc. Rev.*, 2010, **39**, 464-473.
4. E. Fino, R. Araya, D. S. Peterka, M. Salierno, R. Etchenique and R. Yuste, *Front. Neu. Circ.*, 2009, **3**, 2.
5. E. J. Coan, W. Saywood and G. L. Collingridge, *Neurosci. Lett.*, 1987, **80**, 111-114.
6. E. H. Wong, J. A. Kemp, T. Priestley, A. R. Knight, G. N. Woodruff and L. L. Iversen, *Neuropharmacology*, 1986, **83**, 7104-7108.
7. A. P. Pelliccioli and J. Wirz, *Photochem. Photobiol. Sci.*, 2002, **1**, 441-458.
8. G. C. R. Ellis-Davies, *Nat Meth*, 2007, **4**, 619-628.
9. A. Rodrìguez-Moreno, M. M. Kohl, J. E. Reeve, T. R. Eaton, H. A. Collins, H. L. Anderson and O. Paulsen, *J. Neurosci.*, 2011, **31**, 8564-8569.
10. W. Denk, *J. Neurosci. Methods*, 1994, **91**, 6629-6633.
11. D. E. Feldman, *Annu. Rev. Neurosci.*, 2009, **32**, 33-55.
12. D. E. Feldman and M. Brecht, *Science*, 2005, **310**, 810-815.
13. S. Song and L. F. Abbott, *Neuron*, 2001, **32**, 339-350.
14. E. L. Bienenstock, L. N. Cooper and P. W. Munro, *J. Neurosci.*, 1982, **2**, 32-48.
15. D. O. Hebb, *Organization of behavior. New York: Wiley, 1949, pp. 335, $4.00*, Wiley & Sons, New York, 1949.
16. V. A. Bender, K. J. Bender, D. J. Brasier and D. E. Feldman, *J. Neurosci.*, 2006, **26**, 4166-4177.
17. G.-q. Bi and M.-m. Poo, *J. Neurosci.*, 1998, **18**, 10464-10472.
18. D. Debanne, B. H. Gāhwiler and S. M. Thompson, *Journal of Physiology*, 1998, **507**, 237-247.
19. J. M. Christie and C. E. Jahr, *Neuron*, 2008, **60**, 298-307.
20. R. Corlew, D. J. Brasier, D. E. Feldman and B. D. Philpot, *The Neuroscientist*, 2008, **14**, 609-625.
21. H. A. Lester and J. M. Nerbonne, *Ann. Rev. Biophys. Bioeng.*, 1982, **11**, 151-175.
22. S. R. Adams and R. Y. Tsien, *Annu. Rev. Physiol.*, 1993, **55**, 755-784.
23. R. U. Maheswari, H. Takaoka, H. Kadono, R. Homma and M. Tanifuji, *J. Neurosci. Methods*, 2003, **124**, 83-92.
24. J. E. Reeve, M. M. Kohl, A. Rodrìguez-Moreno, O. Paulsen and H. L. Anderson, *Comm. Inter. Bio.*, 2012, **5**, 240-242.
25. A. Patchornik, B. Amit and R. B. Woodward, *J. Am. Chem. Soc.*, 1970, **92**, 6333-6335.
26. J. H. Kaplan, B. Forbush and J. F. Hoffman, *Biochemistry*, 1978, **17**, 1929-1935.
27. G. Marriott, *Biochemistry*, 1994, **33**, 9092-9097.
28. M. Canepari, L. Nelson, G. Papageorgiou, J. E. T. Corrie and D. Ogden, *J. Neurosci. Methods*, 2001, **112**, 29-42.
29. G. Papageorgiou, D. C. Ogden, A. Barth and J. E. T. Corrie, *J. Am. Chem. Soc.*, 1999, **121**, 6503-6504.
30. H. Markram, J. Lübke, M. Frotscher and B. Sakmann, *Science*, 1997, **275**, 213-215.
31. D. Guay, P. Hamel, M. Blouin, C. Brideau, C. C. Chan, N. Chauret, Y. Ducharme, Z. Huang, M. Girard, T. R. Jones, F. Laliberté, P. Masson, M. McAuliffe, H. Piechuta, J. Silva, R. N. Young and Y. Girard, *Bioorg. Med. Chem. Lett.*, 2002, **12**, 1457-1461.
32. B. P. Murphy, *J. Org. Chem.*, 1985, **50**, 5873-5875.

33. M. Balaz, H. A. Collins, E. Dahlstedt and H. L. Anderson, *Org. Biomol. Chem.*, 2009, **7**, 874-888.
34. S. Ando, Y. Okamoto, M. Otsuka and K. Umezawa, *J. Heterocycl. Chem.*, 2008, **45**, 1803-1808.
35. L. E. Steward, C. S. Collins, M. A. Gilmore, J. E. Carlson, J. B. A. Ross and A. R. Chamberlin, *J. Am. Chem. Soc.*, 1997, **119**, 6-11.

Chapter 7

Conclusions: Functional Dyes as Tools for Neurophysiology

We began a research project to find out whether porphyrins could be used to generate second harmonic light. This resulted in the design, synthesis and testing of a diverse family of membrane probes which have the potential to revolutionise an entire field of neurophysiology. Their molecular hyperpolarisabilities and potential sensitivities are higher and more rapid in response than any other probe. The biological testing has already begun to see if these dyes are wholly suitable or whether a third round of redesign and refinement is needed.

Once we synthesised the very first amphiphilic SHG probes, we found that their optical and solubility properties were tunable by complexation of a divalent metal ion. This led to diversification and consequently to the wide variety of possible optimal structures which we investigate in dye families **1** and **2** which are detailed in Chapter 2. In order to understand how these molecules behave in membranes, we investigated their properties with a range of imaging techniques. The most commonly used was the droplet interface monolayer which presented us with the characteristic crescent shapes seen in Chapter 3.

Desiring a better understanding of the relationship between these crescents and molecular tilt, we went on to develop a new methodological tool for determining the orientational distribution of dipolar dyes in membranes from a range of imaging techniques.

Up to this point, we had only taken into account the dominant contribution to molecular hyperpolarisability β_{zzz} which is directed along the molecular axis. Chapter 4 explains how we exploit off-axis contributions to the hyperpolarisability tensor by means of a cis-5,10-substituted donor-acceptor porphyrin. HRS measurements could not be obtained in the biological window due to one-photon absorption arising from their extremely red-shifted absorption spectrum. Therefore, while these molecules may not be suitable for biological imaging, they are of photophysical interest and we also present a new iterative-recycling approach to their synthesis which outperforms even 'rational' syntheses in terms of actual yield.

Finally, after two years of method development, we were able to measure the electric-field sensitivity of some porphyrin dyes. We find that their response is more than four times larger than commercially available dyes, a consequence of their large second hyperpolarisability, γ_{dc}. Additionally, they appear to respond at least five times faster than their styryl counterparts, a phenomenon that we can only account for by assuming that our dye shows an electro-optical response whereas the styryl dyes do not. We await the results of biological testing in *ex vivo* brain slices with great anticipation.

I briefly describe a successful side-project in Chapter 6: by careful refinement and molecular design, we arrive at a water-soluble caged form of NMDA antagonist MK801. The functionality provided by these molecules has led to significant interest from the neurophysiological community who are now able to obtain the described material commercially.

To arrive at the final, optimised forms of each of these functional dyes, more redesigning may be required. However, exceptional functionality has been achieved in all of the cases where we apply our molecular design techniques. To further refine the SHG dyes, we look to upcoming publications from the group which will offer increased flexibility in the form of chromophore which may be used, and I await with great enthusiasm their application to voltage-sensitive imaging. I believe the the most promising avenues to explore will make use of the highly effective **1b.2H** chromophore but reduce the lipophilicity of the molecule to increase the water solubility whilst maintaining its amphiphilicity and membrane affinity.